Local Water Slamming of Nonlinear Elastic Sandwich Hulls, and Adiabatic Shear Banding in Simple Shearing Deformations of Thermoelastoviscoplastic Bodies

Jian Xiao

Dissertation submitted to the faculty of the Virginia Polytechnic Institute and State University in partial fulfillment of the requirements for the degree of

Doctor of Philosophy
in
Engineering Mechanics

Romesh C. Batra, Chair
David A. Dillard
Mark S. Cramer
Scott L. Hendricks
Slimane Adjerid

December 3, 2012
Blacksburg, VA

Keywords: Local slamming, Curved flexible hulls, Delamination, Fluid-structure interaction, Adiabatic shear bands

Local Water Slamming of Nonlinear Elastic Sandwich Hulls, and Adiabatic Shear Banding in Simple Shearing Deformations of Thermoelastoviscoplastic Bodies

Jian Xiao

ABSTRACT

Abstract

We have developed a third-order shear and normal deformable plate/shell theory (TSNDT) incorporating all geometric nonlinearities and used it to analyze, by the finite element method (FEM), transient finite deformations of a sandwich beam with two face sheets and the core made of St. Venant-Kirchhoff materials. A triangular cohesive zone model with stress based criterion for delamination initiation and energy based relation for complete separation is used to analyze delamination failure in a beam under mixed-mode loading. We have studied transient post-buckling deformations and delamination progression in an axially compressed and initially delaminated clamped-clamped sandwich beam. The buckling load for transient deformations exceeds that for static deformations and the increase depends upon the loading rate. This FE software for analyzing deformations of sandwich beam is coupled with that based on the boundary element method (BEM) for studying time-dependent deformations of water and the coupled software is used to analyze deformations of flexible curved hulls due to water slamming loads. The water is assumed to be inviscid and incompressible and undergo irrotational deformations. The Laplace equation for the velocity potential is numerically solved by the BEM with normal velocity and pressure assumed to be continuous across the interface between the hull and the water. Challenging issues resolved in this work include finding the wetted surface of the hull, nonlinear deformations of the fluid due to convective part of acceleration, effects of geometric nonlinearities on hull's deformations, resolution of the jet tip, as well as the initiation and propagation of delamination between the face sheets and the core. It is found that both delamination and geometric nonlinearities significantly affect the hydrodynamic pressure acting on the

hull, and transverse shear deformations contribute more to the strain energy absorbed by the core than its transverse normal deformations.

We have used the discontinuous basis functions to derive the Galerkin formulation of a nonlinear problem involving simple shearing deformations of a homogeneous and isotropic thermo-elasto-visco-plastic body with uniform deformations perturbed to simulate the effect of a defect. The resulting coupled nonlinear ordinary differential equations are integrated with respect to time by using the package, LSODE (Livermore Solver for Ordinary Differential Equations). Computed results showing localization of deformations into narrow regions are found to agree well with those found by the FEM, and spatial variations of the shear stress are smoother than those obtained by the FEM.

Key Words: Local slamming, Curved flexible hulls, Delamination, Fluid-structure interaction, Adiabatic shear bands

Acknowledgments

I would like to express my first acknowledgement to my advisor Prof. Romesh C. Batra. I deeply appreciate his support and guidance during my Ph. D. study. His passion and critical thinking for research will influence my future life. I want to thank Prof. Slimane Adjerid for his teaching and patiently discussing with me the Discontinuous Galerkin Method. I also would like to thank the committee members for their valuable suggestions and time.

I appreciate all the members in our group for their friendship, help and discussions during my study. I especially want to thank the help of Dr. Kaushik Das who helped me a lot at the beginning of my Ph.D. research.

Last but most importantly, I would like to express my appreciation to my wife Daiwei Liu and son Peilin Xiao for their love, encouragement and company. I also would like to thank my family members in China. Without their support and encouragement I could not have persisted in my study.

This work was supported by the Office of Naval Research grant N00014-11-1-0594 to Virginia Polytechnic Institute and State University with Dr. Y. D. S. Rajapakse as the Program Manager. Views expressed in the dissertation are those of the author and neither of the funding agency nor of author's Institution.

Table of contents

List of Figures

Chapter 1

Chapter 2

Chapter 3

Chapter 5

List of tables

Chapter 1

Chapter 1: Finite deformations of curved laminated St. Venant-Kirchhoff beam using layer-wise third order shear and normal deformable beam theory (TSNDT)

Abstract

A layer-wise third order shear and normal deformable plate/shell theory (TSNDT) incorporating all geometric nonlinearities is used to study finite transient deformations of a curved laminated beam composed of a St. Venant-Kirchhoff material. In the TSNDT all displacement components of a point are expressed as 3^{rd} order polynomials in the thickness coordinate in each layer while maintaining the displacement continuity across adjoining layers. No shear correction factor is used. Transverse shear and transverse normal stresses are found from the computed displacement fields and the constitutive relation (i.e., no stress recovery technique is employed). For the St. Venant-Kirchhoff material the strain energy density is a quadratic function of the Green-St. Venant strain tensor appropriate for finite deformations. The software based on the finite element method (FEM) capable of solving static and transient nonlinear problems has been verified by using the method of manufactured solutions. Furthermore, results computed with the TSNDT have been found to agree well with those obtained using the commercial software ABAQUS, and C3D20 elements. Significant contributions of the work include developing a TSNDT considering all geometric nonlinearities and a materially objective constitutive relation, using the method of manufactured solutions to verify the numerical solution of transient nonlinear problems, and showing that results from the plate theory agree well with those from the analysis of plane strain nonlinear problems using the finite elasticity theory. Plate problems using the TSNDT can be analyzed with piecewise linear basis functions in the FEM.

Key words: TSNDT, finite deformations, method of manufactured solutions, St. Venant-Kirchhoff elastic material

1. Introduction

Laminated composite structures are widely used in aerospace, automobile and marine industries. Numerous plate and shell theories have been developed to analyze

deformations of these structures, e.g., see the review articles [1-3]. The classical plate and shell theory (CPT) like the Kirchhoff thin plate theory does not correctly predict results when the plate is moderately thick and shear deformations are not negligible. The first order shear deformable plate theory (FSDT) such as the Reissner-Mindlin theory [4, 5] considers transverse shear deformations and gives good results for moderately thick plates but it needs a shear correction factor and the transverse shear and transverse normal stresses are generally computed by using a stress recovery technique. Reddy and Liu [6] proposed a higher-order shear deformable plate theory (HSDT) in which the transverse deflection is independent of the thickness coordinate, z, and the two in-plane displacement components have terms of degree zero, one and three in z. Coefficients of these terms are such that for infinitesimal deformations, the transverse shear strains vanish on the top and the bottom surfaces of the plate; thus boundary-value problems involving tangential loads on these surfaces may not be properly studied.

For laminated plates, in order for the transverse shear and the transverse normal stresses to be continuous across an interface between adjoining layers, the transverse shear and the transverse normal strains should, in general, be discontinuous. As pointed out by Carrerra [1], Lekhnitskii [7] was the first to propose a Zig-Zag theory that satisfied the continuity of the transverse shear and the transverse normal stresses in a layered beam. Assuming a plane state of stress, Lekhnitskii used the Airy stress function to satisfy equilibrium equations in each layer. Strains were derived from stresses by using Hooke's law and strain-displacement equations were integrated for displacements to ensure the continuity of displacements across interfaces between adjoining layers. Ren [8, 9] extended Lekhnitskii's theory to orthotropic and anisotropic plates, using this theory Ren and Owen [10] studied vibrations and buckling of beams. Ambartsumian [11] extended the Reissner-Mindlin plate theory to layered anisotropic plates and shells. The assumed displacement field in each layer involved transverse shear stresses in a layer and unknown functions of displacements. Whitney [12] applied and extended Ambartsumian's theory to anisotropic and symmetrical and nonsymmetrical plates. Reissner [13] used a mixed variational principle to derive the governing equations. The assumed stress and displacement fields a priori satisfy the continuity of displacements and transverse shear stresses across interfaces between adjoining layers. Carrerra [1] has

pointed out Koiter's [14] recommendation (KR) that effects of transverse shear and normal stresses be considered in a plate/shell theory. Rybov [15, 16] seems to be the first one to incorporate KR in a plate theory by assuming expressions for transverse displacement and transverse shear stresses. Rassakazov [17] adopted KR in plate and shell theories and analyzed analytically and numerically linear and nonlinear problems. The reader is referred to Carrerra's [1] review paper for a historical development and details of various Zig-Zag theories.

Carrera [18, 19] developed the equivalent single layer (ESL) and layer-wise Zig-Zag plate theories based on Reissner's work. Di Sciuva [20] proposed a through-the-thickness piece-wise linearly varying displacement field which satisfies the continuity of surface tractions between adjoining layers and the number of unknowns is independent of the number of layers. Cho and Parmerter [21] generalized Di Sciuva's work by superposing a cubic varying displacement field on a zig-zag varying displacement field. Wu and Chen [22] developed a higher order theory based on global-local superposition technique that can accurately predict transverse shear stresses directly from constitutive relations and displacement fields found using the plate theory.

The transverse normal deformation becomes important when the plate is either thick or differences in values of elastic constants of materials of adjoining layers are large or major surfaces of the plate are subjected to equal and opposite normal tractions or the plate material is soft. A typical sandwich structure is composed of stiff face sheets and a flexible core; thus elastic constants of materials of the core and the face sheets vary significantly. In order to ascertain damage and failure of sandwich structures, it is critical that stresses be accurately found. One way to do so is to adopt the KR and modify higher order plate or shell theories that do not consider the transverse normal deformation and incorporate in them effects of transverse deformations. Batra and Vidoli [23, 24] used the Reissner mixed variational principle to derive a K^{th} order plate theory in which the three displacement components are assumed to be complete polynomials of degree K in the thickness coordinate z. They considered infinitesimal deformations of a piezoelectric material in [23] and also analyzed deformations of a thick beam due to tangential tractions; they studied wave propagation in an orthotropic non-piezoelectric material in

[24]. Other higher-order plate theories have been deduced by Carrerra [1] and Demassi [25] to cite a few. Carrerra [26] has reviewed various plate theories for multi-layered anisotropic laminates. Vel and Batra [27-29] used the Eshelby-Stroh formalism to analytically analyze static deformations of laminated composites with each layer made of a linear elastic material. This approach satisfies the KR and the continuity of surface tractions and displacements at interfaces between adjacent plies.

Sandwich structures with a soft core undergo large deformations for which geometric and material nonlinear effects should be considered. Reddy [30], amongst others, studied deformations of laminated composite plates with a layer-wise theory considering von Kármán geometric nonlinearity. Dvorkin and Bathe [31] studied large deformations of plates and shells using four-node shell elements, and derived governing equations for incremental displacements with the virtual work principle. Arciniega and Reddy [32] used a first-order shell theory with seven parameters including thickness stretching, nonlinear strain-displacement relations, three-dimensional constitutive relations, and higher-order elements with Lagrange interpolations.

Here we use a materially objective constitutive relation to study finite deformations of a curved laminated beam, and express displacements in each layer by using the TSNDT ensuring that displacements are continuous across the interface between two adjoining layers, consider all nonlinear effects in strain-displacement relations, and assume that each layer is made of a St. Venant-Kirchhoff material. For this material and with the reference configuration stress free, the 2ndPiola-Kirchhoff stress tensor is a linear function of the Green-St. Venant strain tensor and satisfies the principle of material objectivity. We note that the expression for the first Piola-Kirchhoff stress involves terms that are at least cubic in displacement gradients and that for the Cauchy stress is a ratio of polynomials in displacement gradients. The continuity of surface tractions across an interface between two layers is implicitly satisfied by assuming that the total work done by these surface tractions in any virtual displacement is zero. We use the method of manufactured solutions (e.g., see the material just before and after Eq. (20) of [33]) to verify that numerical solutions of nonlinear problems solved herein are accurate. The present zig-zag TSNDT does not exhibit locking effects, incorporates the

KR, and transverse shear and transverse normal stresses are computed by using the 3-D constitutive relations and displacement fields found using the plate theory; thus no stress recovery technique is employed.

The rest of the paper is organized as follows. In Section 2, we summarize equations governing finite static and dynamic deformations of a curved beam in orthogonal curvilinear coordinates. The weak form of governing equations is derived in Section 3, and details of the FEM to numerically solve the initial-boundary-value problem are provided. The layer-wise TSNDT displacement field for a laminated beam is briefly summarized in Section 4. The method of manufactured solutions is used in Section 5 to verify the developed software, and results for several example problems are presented and discussed. Conclusions of this work are summarized in Section 6.

2. Problem Formulation

2.1 Kinematics

We study finite plane strain deformations of a curved beam of rectangular cross-section; a schematic sketch of the beam is shown in Fig. 1. Let y_1, y_2, y_3be orthogonal curvilinear coordinate axes in the reference configuration with y_1-axis along the tangent to the mid-surface of the beam, y_2-axis pointing into the plane of the paper, and y_3-axis pointing along the local thickness direction. Let X_1, X_2, X_3 be fixed rectangular Carstesian coordinate axes, and the y_2-axis be parallel to the x_2- and X_2- axes. Let position vectors, with respect to fixed rectangular Cartesian coordinate axes, of a point p located at (y_1, y_2, y_3) in the reference configuration be $\boldsymbol{x}$ and $\boldsymbol{X}$ in the current and the reference configurations, respectively. The displacement $\boldsymbol{u}$ of point p is given by

$$\boldsymbol{u} = \boldsymbol{x} - \boldsymbol{X} \tag{1}$$

Where $u_2 = 0$, $u_1 = u_1(y_1, y_3, t)$, $u_3 = u_3(y_1, y_3, t)$, t is the time

The components, G_{ij}, of the metric tensor in the reference configuration are given by

$$G_{ij} = \boldsymbol{A}_i \cdot \boldsymbol{A}_j \ , \ \boldsymbol{A}_i = \frac{\partial \boldsymbol{X}}{\partial y_i} \tag{2}$$

For orthogonal curvilinear coordinate axes $G_{ij}$is non-zero only when $i = j$. Let

$$H_1 = \sqrt{G_{11}},\quad H_2 = \sqrt{G_{22}} = 1,\quad H_3 = \sqrt{G_{33}} = 1, \tilde{e}_i = \frac{\boldsymbol{A}_i}{H_{(i)}} \text{ (no sum on } i\text{)} \tag{3}$$

Here $(\tilde{e}_1, \tilde{e}_2, \tilde{e}_3)$ are unit base vectors for the curvilinear coordinate axes in the reference configuration. We note that

$$H_1 = \left(1 + \frac{y_3}{R}\right),\ \frac{\partial \tilde{e}_1}{\partial y_1} = -\frac{\tilde{e}_3}{R}, \frac{\partial \tilde{e}_3}{\partial y_1} = \frac{\tilde{e}_1}{R} \tag{4}$$

where R is the radius of curvature at the point (y_1, y_2, y_3).

Following [34], physical components of the displacement gradient, $\boldsymbol{F}$, are given by

$$[F] = \begin{bmatrix} 1 + \frac{1}{H_1}\left(\frac{\partial u_1}{\partial y_1} + \frac{u_3}{R}\right) & 0 & \frac{\partial u_1}{\partial y_3} \\ 0 & 1 & 0 \\ \frac{1}{H_1}\left(\frac{\partial u_3}{\partial y_1} - \frac{u_1}{R}\right) & 0 & 1 + \frac{\partial u_3}{\partial y_3} \end{bmatrix} \tag{5}$$

The Green-St. Venant strain tensor, $\boldsymbol{E}$, defined by

$$\boldsymbol{E} = \frac{1}{2}(\boldsymbol{F}^T\boldsymbol{F} - \boldsymbol{1}) \tag{6}$$

where $\boldsymbol{1}$ is the identity tensor, has the following non-zero physical components:

$$\begin{aligned} E_{11} &= \frac{1}{H_1}\left(\frac{\partial u_1}{\partial y_1} + \frac{u_3}{R}\right) + \frac{1}{2{H_1}^2}\left[\left(\frac{\partial u_1}{\partial y_1} + \frac{u_3}{R}\right)^2 + \left(\frac{\partial u_3}{\partial y_1} - \frac{u_1}{R}\right)^2\right] \\ E_{33} &= \frac{\partial u_3}{\partial y_3} + \frac{1}{2}\left[\left(\frac{\partial u_1}{\partial y_3}\right)^2 + \left(\frac{\partial u_3}{\partial y_3}\right)^2\right] \\ 2E_{13} &= \frac{1}{H_1}\left(\frac{\partial u_3}{\partial y_1} - \frac{u_1}{R}\right) + \frac{\partial u_1}{\partial y_3} + \frac{1}{H_1}\left[\frac{\partial u_3}{\partial y_3}\left(\frac{\partial u_3}{\partial y_1} - \frac{u_1}{R}\right) + \frac{\partial u_1}{\partial y_3}\left(\frac{\partial u_1}{\partial y_1} + \frac{u_3}{R}\right)\right] \end{aligned} \tag{7}$$

We note that $\boldsymbol{E}$ incorporates all geometric nonlinearities including the von Kármán nonlinearity, and is valid for finite (or large) deformations of a beam. The strain tensor for infinitesimal deformations is obtained from Eq. (7) by neglecting the nonlinear terms included in brackets.

Recalling that beam's dimension along the y_3- (or the z-) axis is considerably smaller than that along the y_1-axis, we assume the following 3^{rd} order Taylor series expansion in y_3 for u_1 and u_3:

$$u_1(y_1, y_3, t) = \sum_{i=0}^{3}(y_3)^i\, u_{1i}(y_1, t) = L_i(y_3)u_{1i}(y_1, t) \tag{8.a}$$

$$u_3(y_1, y_3, t) = \sum_{i=0}^{3} (y_3)^i \, u_{3i}(y_1, t) = L_i(y_3) u_{3i}(y_1, t) \tag{8.b}$$

$$L_j(y_3) = (y_3)^j, j = 0,1,2,3 \tag{8.c}$$

$$L_j'(y_3) = \mathrm{D_{ji}} L_i(y_3) \text{ (summed on } i\text{; } i \text{ , } j\text{= 0, 1, 2, 3)} \tag{8.d}$$

$$[\mathrm{D}] = \begin{bmatrix} 0 & 0 & 0 & 0 \\ 1 & 0 & 0 & 0 \\ 0 & 2 & 0 & 0 \\ 0 & 0 & 3 & 0 \end{bmatrix} \tag{8.e}$$

Here and below a repeated index implies summation over the range of the index, and a repeated index enclosed in parentheses does not imply summation. In Eq. (8), u_{10} and u_{30} are, respectively, the axial and the transverse displacements of a point on beam's mid-surface, and u_{1i} and $u_{3i}(i = 1,2,3)$ may be interpreted as generalized axial and transverse displacements of a point. The first subscript on u corresponds to the displacement direction, and the second subscript to the power of y_3. For $u_{10} = u_{12} = u_{13} = u_{31} = u_{32} = u_{33} = 0$, we get the Euler-Bernoulli beam theory when $u_{11} = -\frac{\partial u_{30}}{\partial y_1}$ and the Timoshenko beam theory when u_{11} is an arbitrary function of y_1 and time *t*. The displacement field (8) is a special case of the K^{th} order displacement field considered, amongst others, by Batra and Vidoli [23, 24], Carerra [1], Lo et al. [35], and Cho et al. [36]. We call the beam theory based on Eq. (8) as the third-order shear and normal deformable theory (TSNDT). Note that it accounts for the transverse normal strain and does not assume the transverse shear strain at the top and the bottom surfaces to be zero. Substitution for u_1 and u_3 from Eq. (8) into Eqs. (5) and (7) gives the following expressions for physical components of deformation gradient $\boldsymbol{F}$ and non-zero physical components of the Green-St. Venant strain tensor $\boldsymbol{E}$:

$$[F] = \begin{bmatrix} 1 + L_j \frac{1}{H_1}\left(\frac{\partial u_{1j}}{\partial y_1} + \frac{u_{3j}}{R}\right) & 0 & L_j D_{bj} u_{1b} \\ 0 & 1 & 0 \\ L_j \frac{1}{H_1}\left(\frac{\partial u_{3j}}{\partial y_1} - \frac{u_{1j}}{R}\right) & 0 & 1 + L_j D_{bj} u_{3b} \end{bmatrix}$$

$$E_{11} = L_j \frac{1}{H_1}\left(\frac{\partial u_{1j}}{\partial y_1} + \frac{u_{3j}}{R}\right) + \frac{1}{2{H_1}^2} L_i L_j \left(\frac{\partial u_{1i}}{\partial y_1}\frac{\partial u_{1j}}{\partial y_1} + \frac{u_{3i}u_{3j}}{R^2} + 2\frac{u_{3i}}{R}\frac{\partial u_{1j}}{\partial y_1} + \frac{\partial u_{3i}}{\partial y_1}\frac{\partial u_{3j}}{\partial y_1} + \right.$$

$$\frac{u_{1i}u_{1j}}{R^2} - 2\frac{u_{1i}}{R}\frac{\partial u_{3j}}{\partial y_1}\Big)$$

$$E_{33} = L_j D_{bj} u_{3b} + \frac{1}{2} L_i L_j \left(D_{bi} u_{1b} D_{lj} u_{1l} + D_{bi} u_{3b} D_{lj} u_{3l}\right) \tag{9}$$

$$2E_{13} = L_j \frac{1}{H_1}\left(\frac{\partial u_{3j}}{\partial y_1} - \frac{u_{1j}}{R}\right) + L_j D_{bj} u_{1b} + \frac{1}{2H_1} L_i L_j \left[D_{bi} u_{3b}\left(\frac{\partial u_{3j}}{\partial y_1} - \frac{u_{1j}}{R}\right) + D_{bi} u_{1b}\left(\frac{\partial u_{1j}}{\partial y_1} + \frac{u_{3j}}{R}\right)\right]$$

where indices $i, j, b, d, l = 0,1,2,3,$, and summation on repeated indices is implied. We note that expressions for E_{11}, E_{33} and E_{13} have terms of order 6, 4 and 5, respectively, in y_3. Eq. (9) can be written in the index notation as follows:

$$F_{ma} = \delta_{ma} + \frac{1}{H_{(a)}} L_b e^b_{ma} \tag{10.a}$$

$$E_{\alpha\beta} = \frac{1}{2}\left[L_b\left(\frac{1}{H_{(\beta)}} e^b_{\alpha\beta} + \frac{1}{H_{(\alpha)}} e^b_{\beta\alpha}\right) + L_b L_d \frac{1}{H_{(\alpha)} H_{(\beta)}} \eta^{bd}_{\alpha\beta}\right] \tag{10.b}$$

$$\eta^{bd}_{\alpha\beta} = e^b_{i\alpha} e^d_{i\beta} \tag{10.c}$$

Here indices $b, d = 0,1,2,3$ and the other indices take values 1 and 3, δ_{ma} is the Kronecker delta, and the repeated index enclosed in parentheses is not summed. The non-zero components of $e^j_{\alpha\beta}$ are listed below.

$$e^j_{11} = \frac{\partial u_{1j}}{\partial y_1} + \frac{u_{3j}}{R},\ e^j_{13} = D_{bj} u_{1b},\ e^j_{31} = \frac{\partial u_{3j}}{\partial y_1} - \frac{u_{1j}}{R}, e^j_{33} = D_{bj} u_{3b};\ j, b = 0,1,2,3 \tag{11}$$

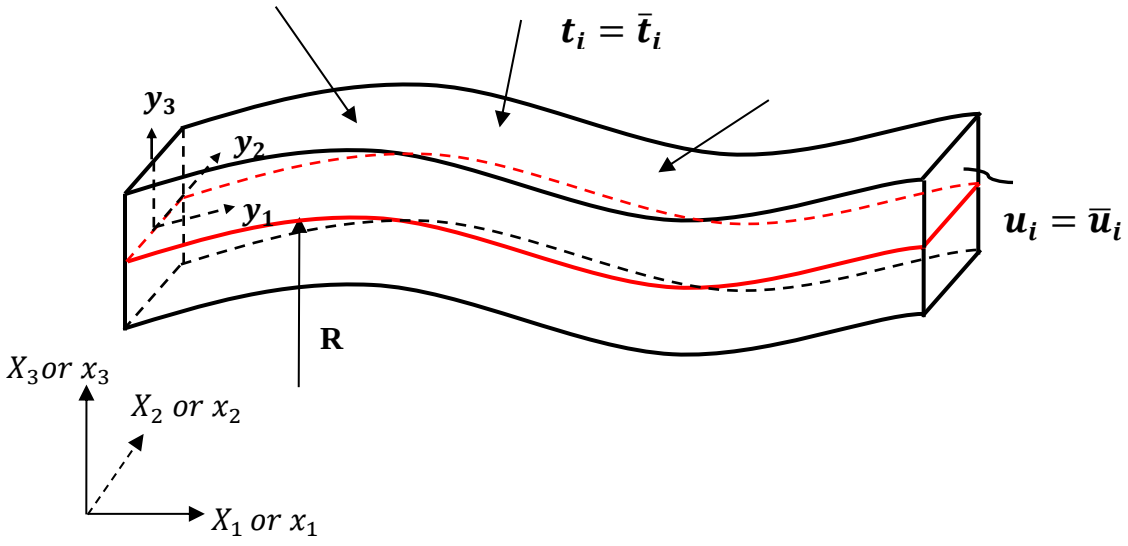

Fig. 1 Schematic sketch of a curved beam;

2.2 Kinetics

The in-plane displacements (u_1, u_3) of a point are governed by the following equations expressing the balance of linear momentum written in the Lagrangian description of motion using physical components $T_{11}, T_{13}, T_{31}, T_{33}$, of the first Piola-Kirchhoff stress tensor [34], and initial and boundary conditions .

$$\rho_0 \ddot{u}_1 = \frac{1}{H_1}\frac{\partial T_{11}}{\partial y_1} + \frac{1}{H_1}\frac{\partial (H_1 T_{13})}{\partial y_3} + \frac{1}{H_1 R} T_{31} + f_1 \tag{12.a}$$

$$\rho_0 \ddot{u}_3 = \frac{1}{H_1}\frac{\partial T_{31}}{\partial y_1} + \frac{1}{H_1}\frac{\partial (H_1 T_{33})}{\partial y_3} - \frac{1}{H_1 R} T_{11} + f_3 \tag{12.b}$$

$$u_i(y_1, y_3, 0) = u_i^0(y_1, y_3) \tag{12.c}$$

$$\dot{u}_i(y_1, y_3, 0) = \dot{u}_i^0(y_1, y_3) \tag{12.d}$$

$$T_{ij} N_j = \bar{t}_i(y_1, y_3, t) \text{ on } \Gamma_t \tag{12.e}$$

$$u_i(y_1, y_3, t) = \bar{u}_i(y_1, y_3, t) \text{ on } \Gamma_u \tag{12.f}$$

Here i and j equal 1 and 3. In Eq. (12) f_1 and f_3 are components of the body force per unit reference volume along the y_1- and the y_3- axes, respectively, $\rho_0$is the mass density in the reference configuration, and $\ddot{u}_i = \frac{\partial^2 u_i}{\partial t^2}$. The initial displacement u_i^0 and the initial velocity $\dot{u}_i^0$ are known functions of y_1 and y_3. Furthermore, $\boldsymbol{N}$ is a unit outward normal in the reference configuration at a point on the boundary Γ_t where surface tractions are prescribed as $\bar{t}_i$. On the remaining boundary, Γ_u, displacements are prescribed as $\bar{u}_i$.

Let $\omega_\alpha(y_1, y_3)(\alpha = 1, 3)$ be smooth functions that vanish on Γ_u. We multiply both sides of Eqs. (12.a) and (12.b) with ω_1 and ω_3, respectively, and integrate the resulting equations over the domain to obtain the following.

$$\begin{aligned}
\int_0^{\mathcal{L}} \int_{-H/2}^{H/2} \omega_1 \rho_0 \ddot{u}_1 H_1 dy_3 dy_1 &= \int_0^{\mathcal{L}} \int_{-H/2}^{H/2} \omega_1 \left[\frac{\partial T_{11}}{\partial y_1} + \frac{\partial (H_1 T_{13})}{\partial y_3} + \frac{1}{R} T_{31} + H_1 f_1\right] dy_3 dy_1 \\
\int_0^{\mathcal{L}} \int_{-H/2}^{H/2} \omega_3 \rho_0 \ddot{u}_3 H_1 dy_3 dy_1 &= \int_0^{\mathcal{L}} \int_{-H/2}^{H/2} \omega_3 \left[\frac{\partial T_{31}}{\partial y_1} + \frac{\partial (H_1 T_{33})}{\partial y_3} - \frac{1}{R} T_{11} + H_1 f_3\right] dy_3 dy_1
\end{aligned} \tag{13}$$

In Eq. (13), H and $\mathcal{L}$ are the thickness and the length of the beam, respectively. Recalling that functions ω_1, ω_3, u_1 and u_3 do not depend upon y_2, the integration with respect to y_2 has been carried out in Eq. (13) and the common factor (i.e., the width) has been cancelled out.

As for $u_\alpha(y_1, y_3)$ in Eq. (8), we write $\omega_\alpha(y_1, y_3)$ as

$$\omega_\alpha\left(y_1, y_3\right) = L_j(y_3)\omega_\alpha^j(y_1),\ \alpha = 1,3,\ j = 0,1,2,3 \tag{14}$$

Substituting from Eq. (14) into Eq. (13) and integrating with respect to y_3 , we get

$$\begin{aligned}
\int_0^{\mathcal{L}} \omega_1^j\left(A_{ji}\ddot{u}_{1i}\right)dy_1 &= \int_0^{\mathcal{L}} \omega_1^j\left(\frac{\partial M_{11}^j}{\partial y_1} - D_{ji}M_{13}^i + \frac{1}{R}M_{31}^j + \bar{f}_1^j + B_{13}^j\right)dy_1 \\
\int_0^{\mathcal{L}} \omega_3^j\left(A_{ji}\ddot{u}_{3i}\right)dy_1 &= \int_0^{\mathcal{L}} \omega_3^j\left(\frac{\partial M_{31}^j}{\partial y_1} - D_{ji}M_{33}^i - \frac{1}{R}M_{11}^j + \bar{f}_3^j + B_{33}^j\right)dy_1
\end{aligned} \tag{15}$$

where

$$M_{mn}^j(y_1, t) = \int_{-\mathrm{H}/2}^{\mathrm{H}/2} L_j(y_3)T_{mn}\mathcal{H}_{(n)}\,dy_3\ ,\mathcal{H}_{(1)} = 1, \mathcal{H}_{(3)} = H_1 \tag{16.a}$$

$$B_{13}^j(y_1, t) = L_j(H/2)H_1T_{13}(H/2, t) - L_j(-H/2)H_1T_{13}(-H/2, t) \tag{16.b}$$

$$B_{33}^j(y_1, t) = L_j(H/2)H_1T_{33}(H/2, t) - L_j(-H/2)H_1T_{33}(-H/2, t) \tag{16.c}$$

$$\bar{f}_\alpha^j(y_1, t) = \int_{-\mathrm{H}/2}^{\mathrm{H}/2} L_j(y_3)f_\alpha H_1\,dy_3 \tag{16.d}$$

$$A_{ji}(y_1, t) = \int_{-\mathrm{H}/2}^{\mathrm{H}/2} L_j(y_3)L_i(y_3)\rho_0 H_1\,dy_3 \tag{16.e}$$

and indices $m, n, \alpha = 1,3,$ and $i, j = 0,1,2,3$. The quantity M_{mn}^jequals j^{th} order moment of the stress T_{mn} about the y_2-axis; M_{mn}^0 is usually called the resultant force, and $M_{mn}^1$the bending moment. The quantities B_{13}^j and B_{33}^j equal j^{th} order moments about the y_2-axis of the tangential surface traction T_{13} and the normal surface traction T_{33} applied on the top and the bottom surfaces of the beam; for j = 0 these equal the resultant forces and for j = 1 their first-order moments about the y_2-axis. Similarly, $\bar{f}_\alpha^j$ equals j^{th} order moment of the body force f_α about the y_2-axis, and A_{ji} the inertia tensor associated with the generalized displacements u_{1i} and u_{3i}.

Requiring Eq. (15) to hold for all choices of ω_α^j, we obtain following eight equations governing transient deformations of the beam.

$$A_{ji}\ddot{u}_{1i} = \frac{\partial M_{11}^j}{\partial y_1} - D_{ji}M_{13}^i + \frac{1}{R}M_{31}^j + \bar{f}_1^j + B_{13}^j,\ j,i = 0,1,2,3 \tag{17.a}$$

$$A_{ji}\ddot{u}_{3i} = \frac{\partial M_{31}^j}{\partial y_1} - D_{ji}M_{33}^i - \frac{1}{R}M_{11}^j + \bar{f}_3^j + B_{33}^j,\ j,i = 0,1,2,3 \tag{17.b}$$

After expressions for moments M_{mn}^j in terms of displacements have been substituted in Eq. (17), we obtain "governing equations of motion" for the present shell theory which are nonlinear coupled partial differential equations (PDEs) for u_{1j} and u_{3j}. These PDEs involve second-order derivatives of u_{1j} and u_{3j} with respect to y_1 and time t and are to be solved under pertinent initial and boundary conditions.

The traction boundary conditions in Eq. (12.e) on the major surfaces (i.e., the top and the bottom) of the beam have been incorporated in Eq. (17); e.g., see Eqs. (16.b) and (16.c). At the beam edges, $y_1 = 0$, $y_1 = \mathcal{L}$, we specify a suitable combination of u_{1j}, u_{3j} and $M_{\alpha 1}^j$ given by

$$\int_{-\mathrm{H}/2}^{\mathrm{H}/2} L_j\, T_{\alpha 1} dy_3 = M_{\alpha 1}^j,\ \alpha = 1,3;\ j = 0,1,2,3 \tag{18}$$

We substitute from Eq. (8) into Eqs. (12.c) and (12.d), multiply both sides of the resulting equations with $\rho_0 L_j(y_3)$, and integrate with respect to y_3 on the domain $(-\mathrm{H}/2, \mathrm{H}/2)$ to obtain the following equations from which initial values $u_{\alpha i}(y_1, 0)$ and $\dot{u}_{\alpha i}(y_1, 0)$ are determined.

$$A_{ji}u_{\alpha i}(y_1, 0) = \int_{-\mathrm{H}/2}^{\mathrm{H}/2} \rho_0 L_j(y_3)\, u_\alpha^0(y_1, y_3) dy_3 = \mathcal{F}_{\alpha j}(y_1) \tag{19.a}$$

$$A_{ji}\dot{u}_{\alpha i}(y_1, 0) = \int_{-\mathrm{H}/2}^{\mathrm{H}/2} \rho_0 L_j(y_3)\, \dot{u}_\alpha^0(y_1, y_3) dy_3 = \dot{\mathcal{F}}_{\alpha j}(y_1) \tag{19.b}$$

Here α= 1,3 and $i, j = 0,1,2,3$.

2.3 Constitutive relation

We assume that the beam material is St. Venant-Kirchhoff for which the strain energy density, W, per unit reference volume is given by

$$W = \frac{1}{2}E_{mn}C_{mn\alpha\beta}E_{\alpha\beta}, C_{mn\alpha\beta} = C_{\alpha\beta mn} = C_{nm\alpha\beta} \tag{20}$$

Here $\boldsymbol{C}$ is the fourth-order elasticity tensor having 21 independent components for a general anisotropic material. The independent components of $\boldsymbol{C}$ reduce to 9, 5 and 2 for an orthotropic, transversely isotropic and isotropic material, respectively. The strain energy density for the St. Venant-Kirchhoff material reduces to that of a Hookean material if the finite strain tensor $\boldsymbol{E}$ is replaced in Eq. (20) by the strain tensor $e^{j}_{\alpha\beta}$ for infinitesimal deformations. Batra [37] has compared the response of four elastic materials for which a stress tensor is a linear function of an appropriate finite strain tensor (e.g., the Cauchy stress tensor is a linear function of the Almansi-Hamel strain tensor). For infinitesimal deformations the four constitutive relations give the same stress-strain curve, but their predictions for finite deformations are quite different.

For a nonlinear elastic material, physical components of the second Piola-Kirchhoff stress tensor $\boldsymbol{S}$ are related to those of $\boldsymbol{E}$ by

$$S_{mn} = \frac{\partial W}{\partial E_{mn}} \tag{21}$$

Eqs. (20) and (21) give

$$S_{mn} = C_{mn\alpha\beta} E_{\alpha\beta} \tag{22}$$

For plane strain deformations of an orthotropic material with the material principal axes coincident with the coordinate axes (y_1, y_2, y_3), Eq. (22) reduces to

$$\begin{Bmatrix} S_{11} \\ S_{33} \\ S_{13} \end{Bmatrix} = \begin{bmatrix} C_{1111} & C_{1133} & 0 \\ C_{3311} & C_{3333} & 0 \\ 0 & 0 & C_{1313} \end{bmatrix} \begin{Bmatrix} E_{11} \\ E_{33} \\ 2E_{13} \end{Bmatrix} \tag{23}$$

Recalling that

$$\boldsymbol{T} = \boldsymbol{F}\boldsymbol{S} \tag{24}$$

Where $\boldsymbol{T}$ is the 1st Piola-Kirchhoff stress tensor, we get

$$\begin{bmatrix} T_{11} & T_{13} \\ T_{31} & T_{33} \end{bmatrix} = \begin{bmatrix} F_{11}S_{11} + F_{13}S_{13} & F_{11}S_{13} + F_{13}S_{33} \\ F_{31}S_{11} + F_{33}S_{13} & F_{31}S_{13} + F_{33}S_{33} \end{bmatrix} \tag{25}$$

Substitution for $\boldsymbol{F}$ from Eq. (10.a) into Eq. (25), and for $\boldsymbol{E}$ from Eq. (10.b) into Eq. (23) and the result into Eq. (25) gives expressions for $\boldsymbol{T}$ in terms of generalized

displacements u_{1i} and u_{3i} and four elastic constants C_{1111}, C_{1133}, C_{3333}, and C_{1313}. It can be written as

$$T_{mn} = \frac{1}{2}\left(\delta_{m\mathrm{a}} + \frac{1}{H_{(\mathrm{a})}} L_i e^i_{m\mathrm{a}}\right) C_{\mathrm{an}\alpha\beta}\left[L_b\left(\frac{1}{H_{(\beta)}} e^b_{\alpha\beta} + \frac{1}{H_{(\alpha)}} e^b_{\beta\alpha}\right) + L_b L_d \frac{1}{H_{(\alpha)} H_{(\beta)}} \eta^{bd}_{\alpha\beta}\right] \qquad (26)$$

Here, indices $i, b, d = 0,1,2,3$ and other indices take values 1 and 3. Even though components of $\boldsymbol{S}$ are quadratic in displacement gradients those of $\boldsymbol{T}$ are cubic in displacement gradients. Thus constitutive relation (24) accounts for material nonlinearities in the sense that components of $\boldsymbol{T}$ are nonlinear functions of displacement gradients. We note that constitutive relations (21) and (24) are materially objective and are invariant under a rigid body motion superimposed upon the present configuration.

Substituting from Eq. (26) into Eq. (16.a), we obtain

$$M^j_{mn} = \int_{-\mathrm{H}/2}^{\mathrm{H}/2} L_j(y_3) T_{mn} \mathcal{H}_{(n)}\, dy_3 = \frac{1}{2}[\, C^{1jb}_{\mathrm{an}\alpha\beta}\delta_{m\mathrm{a}} e^b_{\alpha\beta} + C^{2jb}_{\mathrm{an}\alpha\beta}\delta_{m\mathrm{a}} e^b_{\beta\alpha} +$$

$$C^{3jbd}_{\mathrm{an}\alpha\beta}\delta_{m\mathrm{a}}\eta^{bd}_{\alpha\beta} + C^{4jib}_{\mathrm{an}\alpha\beta} e^i_{m\mathrm{a}} e^b_{\alpha\beta} + C^{5jib}_{\mathrm{an}\alpha\beta} e^i_{m\mathrm{a}} e^b_{\beta\alpha} + C^{6jibd}_{\mathrm{an}\alpha\beta}\, e^i_{m\mathrm{a}}\eta^{bd}_{\alpha\beta}] \qquad (27)$$

where

$$C^{1jb}_{\mathrm{an}\alpha\beta} = \int_{-\mathrm{H}/2}^{\mathrm{H}/2} L_j L_b C_{\mathrm{an}\alpha\beta} \frac{\mathcal{H}_{(n)}}{H_{(\beta)}} dy_3\,,\; C^{2jb}_{\mathrm{an}\alpha\beta} = \int_{-\mathrm{H}/2}^{\mathrm{H}/2} L_j L_b C_{\mathrm{an}\alpha\beta} \frac{\mathcal{H}_{(n)}}{H_{(\alpha)}} dy_3$$

$$C^{3jbd}_{\mathrm{an}\alpha\beta} = \int_{-\mathrm{H}/2}^{\mathrm{H}/2} L_j L_b L_d C_{\mathrm{an}\alpha\beta} \frac{\mathcal{H}_{(n)}}{H_{(\alpha)} H_{(\beta)}} dy_3, C^{4jib}_{\mathrm{an}\alpha\beta} = \int_{-\mathrm{H}/2}^{\mathrm{H}/2} L_j L_i L_b C_{\mathrm{an}\alpha\beta} \frac{\mathcal{H}_{(n)}}{H_{(\mathrm{a})} H_{(\beta)}} dy_3 \qquad (28)$$

$$C^{5jib}_{\mathrm{an}\alpha\beta} = \int_{-\mathrm{H}/2}^{\mathrm{H}/2} L_j L_i L_b C_{\mathrm{an}\alpha\beta} \frac{\mathcal{H}_{(n)}}{H_{(\mathrm{a})} H_{(\alpha)}} dy_3,\; C^{6jibd}_{\mathrm{an}\alpha\beta} = \int_{-\mathrm{H}/2}^{\mathrm{H}/2} L_j L_i L_b L_d C_{\mathrm{an}\alpha\beta} \frac{\mathcal{H}_{(n)}}{H_{(\mathrm{a})} H_{(\alpha)} H_{(\beta)}} dy_3$$

Here, indices $i, j, b, d = 0,1,2,3$ and other indices take values 1 and 3. The non-zero terms of M^j_{mn} for a beam made of isotropic material are listed in Appendix A.

The true stress or the Cauchy stress, $\boldsymbol{\sigma}$, is related to the 1st Piola-Kirchhoff stress by

$$\boldsymbol{\sigma} = \frac{1}{J}\boldsymbol{T}\boldsymbol{F}^T\,, \qquad (29)$$

where J is the determinant of the deformation gradient $\boldsymbol{F}$.

We are unable to analytically solve the above formulated nonlinear problem; thus we analyze it numerically.

3. Numerical Solution

3.1 Weak formulation

Let Θ_1^j and Θ_3^j be smooth functions of $y_1 \epsilon [0, \mathcal{L}]$. We take the inner product of both sides of Eqs. (17.a) and (17.b) with Θ_1^j and Θ_3^j, respectively, integrate the resulting equations with respect to $y_1$on $[0, \mathcal{L}]$, and then integrate by parts to arrive at the following equations:

$$\begin{aligned}
\int_0^{\mathcal{L}} \Theta_1^j \left(A_{ji} \ddot{u}_{1i}\right) dy_1 &= \int_0^{\mathcal{L}} \left(-\frac{\partial \Theta_1^j}{\partial y_1} M_{11}^j + \Theta_1^j \left(\frac{1}{R} M_{31}^j + \bar{f}_1^j + B_{13}^j - D_{ji} M_{13}^i \right) \right) dy_1 + B_{11}^j \\
\int_0^{\mathcal{L}} \Theta_3^j \left(A_{ji} \ddot{u}_{3i}\right) dy_1 &= \int_0^{\mathcal{L}} \left(-\frac{\partial \Theta_3^j}{\partial y_1} M_{31}^j + \Theta_3^j \left(\bar{f}_3^j + B_{33}^j - D_{ji} M_{33}^i - \frac{1}{R} M_{11}^j \right) \right) dy_1 + B_{31}^j
\end{aligned} \tag{30}$$

where

$$B_{11}^j = \Theta_1^j(\mathcal{L}) M_{11}^j(\mathcal{L}) - \Theta_1^j(0) M_{11}^j(0)\ , B_{31}^j = \Theta_3^j(\mathcal{L}) M_{31}^j(\mathcal{L}) - \Theta_3^j(0) M_{31}^j(0) \tag{31}$$

Here indices $i, j = 0,1,2,3$. If one thinks of $\Theta_1^j$and Θ_3^jas virtual displacements that vanish at boundary points where displacements are prescribed, then Eq. (30) states the principle of virtual work. Alternatively, Eq. (30) expresses a weak formulation of the problem since it involves first-order derivatives of u_1 and u_3 with respect to $y_1$whereas the PDEs (17) have second-order derivatives of u_1 and u_3 with respect to y_1. Since T_{11}, T_{13}, T_{31}andT_{33} are nonlinear functions of displacement gradients, Eq. (30) is nonlinear in u_1 and u_3.

3.2 Derivation of ordinary differential equations

We discretize the curve along the y_1-axis into one-dimensional finite elements (FEs) of not necessarily the same length. Let there be N nodes on this curve and $\Psi_1(y_1), \Psi_2(y_1), \cdots, \Psi_N(y_1)$ be the FE basis functions. We write

$$u_{\alpha j}(y_1, t) = \sum_{i=1}^{N} \Psi_i(y_1) \tilde{d}_{\alpha ij}(t), j = 0,1,2,3; \alpha = 1,3. \tag{32}$$

Substitution from Eq. (32) into Eq. (8) gives

$$u_\alpha(y_1, y_3, t) = \sum_{j=0}^{3} L_j(y_3) \sum_{i=1}^{N} \Psi_i(y_1) \tilde{d}_{\alpha ij}(t), j = 0,1,2,3; \alpha = 1,3 \tag{33}$$

Thus for N nodes along the y_1-axis, we have 8N unknown functions $\tilde{d}_{\alpha ij}(t)$, $\alpha = 1,3$; $i = 1,2,\cdots,N; j = 0,1,2,3$. We write these as the 8N-dimensional vector $\boldsymbol{d}(t)$, and the displacement field $u_{\alpha j}(y_1,t)$ as 8-dimensional vector $\tilde{\boldsymbol{u}}(y_1,t)$. These can be written as

$$\{\tilde{\boldsymbol{u}}(y_1,t)\} = [\emptyset(y_1)]\{\boldsymbol{d}(t)\} \tag{34}$$

$$\{\tilde{\boldsymbol{u}}(y_1,t)\} = \{u_{10} \quad u_{11} \quad u_{12} \quad u_{13} \quad u_{30} \quad u_{31} \quad u_{32} \quad u_{33}\}^T$$

where $[\emptyset]$ is 8×8N matrix and $\{\boldsymbol{d}\}$ is 8N×1 matrix. In index notation, Eq. (34) becomes

$$\tilde{u}_\beta(y_1,t) = \emptyset_{\beta j}(y_1) d_j(t), \quad \beta = 1,2,\ldots,8; j = 1,2,\cdots,8N \tag{35}$$

We can also write the displacement fields $u_1(y_1,y_3,t)$ and $u_3(y_1,y_3,t)$ as

$$\begin{Bmatrix} u_1(y_1,y_3,t) \\ u_3(y_1,y_3,t) \end{Bmatrix} = [\varphi(y_3)][\emptyset(y_1)]\{\boldsymbol{d}(t)\} = [\Phi(y_1,y_3)]\{\boldsymbol{d}(t)\} \tag{36}$$

where $[\varphi(y_3)]$ is 2×8 matrix, $[\emptyset(y_1)]$ is $8 \times 8N$ matrix and $[\Phi]$ is 2×8N matrix.

We use the Galerkin formulation and take the same basis functions for the test functions Θ_1^j, Θ_3^j as those for the trial solutions u_{1j}, u_{3j}; e.g., see Eq. (32). That is

$$\Theta_\alpha^j(y_1) = \sum_{i=1}^{N} \Psi_i(y_1)\, c_{\alpha i}^j\,, \quad \alpha = 1,3\,; \;\; j = 0,1,2,3 \tag{37}$$

where $c_{\alpha i}^j$ are constants.

Substitution from Eqs. (35) and (37) into Eq. (30) and requiring that the resulting equations hold for all values of constants $c_{\alpha i}^j$ gives the following set of coupled nonlinear ordinary differential equations (ODEs).

$$\boldsymbol{M}\ddot{\boldsymbol{d}} = \boldsymbol{F}^{ext} - \boldsymbol{F}^{int}(\boldsymbol{d}), \tag{38}$$

where

$$\boldsymbol{M} = \int_0^{\mathcal{L}} [\emptyset(y_1)]^T [\bar{A}][\emptyset(y_1)]\, dy_1\,, \; [\bar{A}] = \begin{bmatrix} A & 0 \\ 0 & A \end{bmatrix}$$

$$\boldsymbol{F}^{ext} = \int_0^{\mathcal{L}} [\emptyset(y_1)]^{\mathrm{T}} \begin{Bmatrix} vec\left(\bar{f}_1^j + B_{13}^j\right) \\ vec\left(\bar{f}_3^j + B_{33}^j\right) \end{Bmatrix} dy_1 + [\emptyset(\mathcal{L})]^{\mathrm{T}} \begin{Bmatrix} vec(M_{11}^j(\mathcal{L})) \\ vec(M_{31}^j(\mathcal{L})) \end{Bmatrix} - [\emptyset(0)]^{\mathrm{T}} \begin{Bmatrix} vec(M_{11}^j(0)) \\ vec(M_{31}^j(0)) \end{Bmatrix}$$

$$\boldsymbol{F}^{int} = \int_0^{\mathcal{L}} [BL1]^T \left\{ vec\left(M_{11}^j\right) \quad vec\left(M_{31}^j\right) \quad vec\left(D_{ji} M_{13}^i - \frac{1}{R} M_{31}^j\right) \quad vec\left(D_{ji} M_{33}^i + \frac{1}{R} M_{11}^j\right) \right\}^T dy_1$$

$$[BL1] = \begin{bmatrix} diag\left(\frac{\partial}{\partial y_1}\right) & 0 \\ 0 & diag\left(\frac{\partial}{\partial y_1}\right) \\ diag(1) & 0 \\ 0 & diag(1) \end{bmatrix} [\emptyset(y_1)], \; diag(\mathrm{f}) = \text{diagonal}\{\mathrm{f} \quad \mathrm{f} \quad \mathrm{f} \quad \mathrm{f}\} \tag{39}$$

$$diag(\mathrm{f}^{\mathrm{j}}) = \text{diagonal}(\mathrm{f}^0 \quad \mathrm{f}^1 \quad \mathrm{f}^2 \quad \mathrm{f}^3), \; vec(\mathrm{f}^{\mathrm{j}}) = \{\mathrm{f}^0 \quad \mathrm{f}^1 \quad \mathrm{f}^2 \quad \mathrm{f}^3\}$$

Here $\boldsymbol{M} = \boldsymbol{M}^T$ is the consistent mass matrix, $\boldsymbol{F}^{ext}$ represents the generalized 8N-dimensional nodal force ($\boldsymbol{F}^{ext}$ is 8N×1 matrix) equivalent to the externally applied surface tractions on boundaries and the body force (e.g., gravity). The 8N-dimensional vector $\boldsymbol{F}^{int}$ represents forces due to internal stresses, and is a nonlinear function of the generalized nodal displacement $\boldsymbol{d}$ since stresses T_{11}, T_{13}, T_{31} and T_{33} are nonlinear functions of u_1 and u_3. However, the weak formulation involves only first-order derivatives of generalized displacements. Thus lower order basis functions can be used to numerically analyze the problem. For example, for plates made of linear elastic materials, Qian et al. [38] and Xiao et al. [39] have used, respectively, basis functions derived by the moving least squares approximation and radial basis functions in meshless methods to study transient deformations of thick plates using K^{th} order shear and normal deformable plate theory. Here we consider material and geometric nonlinearities and use the TSNDT.

We now find initial values of $\boldsymbol{d}(0)$ from $\boldsymbol{u}(y_1, y_3, 0)$. Substituting time *t=0* in Eq. (36) and using Eq. (12.c) we get

$$\begin{Bmatrix} u_1(y_1, y_3, 0) \\ u_3(y_1, y_3, 0) \end{Bmatrix} = [\Phi(y_1, y_3)]\{d(0)\} = \begin{Bmatrix} u_1^0(y_1, y_3) \\ u_3^0(y_1, y_3) \end{Bmatrix} \tag{40}$$

Premultiplying both sides of Eq. (40) by $\rho_0[\Phi]^T(y_1, y_3)$ and integrating the result over Ω_0 yield

$$\boldsymbol{M}\boldsymbol{d}^0 = \boldsymbol{F}^0,\ \ \boldsymbol{d}^0 = \boldsymbol{d}(0), \boldsymbol{F}^0 = \int_{\Omega_0} \rho_0 [\Phi]^T \begin{Bmatrix} u_1^0 \\ u_3^0 \end{Bmatrix} H_1 dy_1 dy_3 \tag{41}$$

The solution of Eq. (41) gives $\boldsymbol{d}^0$. We follow a similar procedure to find $\dot{\boldsymbol{d}}^0$. The natural boundary conditions (12.e) are included in Eq. (18). The essential boundary conditions (12.f) in terms of $\tilde{d}_{\alpha ij}(t)$ are satisfied during the solution of Eq. (38).

If the edge, $y_1 = 0$, of the beam is simply supported, clamped or free, boundary conditions there are, respectively, given by Eqs. (42), (43) and (44).

$$\tilde{d}_{31j}(t) = 0,\ j = 0,1,2,3,\ M_{11}^j(0,t) = 0\ , j = 0,1,2,3; \tag{42.a, b,c}$$

$$\tilde{d}_{\alpha 1j}(t) = 0, j = 0,1,2,3;\ \alpha = 1,3; \tag{43}$$

$$M_{11}^j(0,t) = 0, M_{31}^j(0,t) = 0, j = 0,1,2,3\ . \tag{44}$$

That is, at a simply supported edge the transverse displacement and moments about the y_2-axis of tractions due to T_{11} of orders 0 through 3 vanish. The boundary condition (42.b) eliminates rigid body translation in the y_1-direction and is needed only if the other edge is either simply supported or free. At a clamped edge both the axial and the transverse displacements identically vanish. At a free edge, moments about the y_2-axis of orders 0 through 3 of tractions due to $T_{11}$and the transverse shear forces due to $T_{31}$of orders 0 through 3 vanish.

We note that the FE formulations for the Euler-Bernoulli and the Timoshenko beam theories involve two unknowns at a node, namely, the transverse displacement and the slope. Here, at a node we have 8 unknowns which may be associated with the displacement, the slope, the curvature, and the curvature gradient. The anticipated benefit of considering more unknowns at a node is improved solution for the transverse normal, the transverse shear and axial deformations of the beam. For a continuous elastodynamic problem, there are two unknowns at a node. Thus the numbers of degrees of freedom for the TSNDT and the 2-D elasticity problem would be the same if we take four nodes in the y_3-direction for the elasticity problem. The main benefit of using the TSNDT is savings in not generating a 2-D FE mesh. In the continuous problem one can

approximate displacements in the y_3-direction either with piecewise affine functions or piecewise quadratic functions or a cubic polynomial; the last case corresponds to the displacement field assumed in the TSNDT. Through numerical experiments, we will show in Section 5 that even for thick beams the TSNDT gives as accurate results as those obtained from the analysis of the continuum problem.

3.3 Solution of nonlinear ODEs

We use the conditionally stable central-difference method to integrate the coupled nonlinear ODEs (38). That is, with the notation

$$\boldsymbol{d}^{n+1} = \boldsymbol{d}\,(t_{n+1}), \tag{45}$$

we have

$$\boldsymbol{d}^{n+1} = \boldsymbol{d}^n + \Delta t\dot{\boldsymbol{d}}^n + \frac{\Delta t^2}{2}\ddot{\boldsymbol{d}}^n,\ \ddot{\boldsymbol{d}}^{n+1} = \boldsymbol{M}^{-1}\left[\boldsymbol{F}^{ext}(t_{n+1}) - \boldsymbol{F}^{int}(\boldsymbol{d}^{n+1})\right] \tag{46.a,b}$$

$$\dot{\boldsymbol{d}}^{n+1} = \dot{\boldsymbol{d}}^n + \frac{\Delta t}{2}\left(\ddot{\boldsymbol{d}}^{n+1} + \ddot{\boldsymbol{d}}^n\right) \tag{46.c}$$

The critical time step size to compute a stable solution is determined by finding the maximum frequency, ω_{max} , of free vibrations and taking $\Delta t \leq \Delta t_{crit}$, $\Delta t_{crit} = 2/\omega_{max}$. Ideally, ω_{max} should be found after every time step since frequencies of a structure change as it is deformed. The accuracy of the solution can be improved by taking $\Delta t \ll \Delta t_{crit}$ but at the cost of increasing the computational time.

Results presented in Section 5 have been computed with a consistent mass matrix and $\Delta t = 0.9\Delta t_{crit}$ for a linear problem but $\Delta t = 0.5\Delta t_{crit}$ for a nonlinear problem. For the nonlinear problems, ω_{max} found from analyzing frequencies of the undeformed beam is used to ascertain Δt_{crit}.

For a static problem, we use the modified Newton-Raphson method. That is, we iteratively solve

$$\boldsymbol{F}^{int}(\boldsymbol{d}) = \boldsymbol{F}^{ext}\ , \tag{47}$$

by first writing it as

$$\boldsymbol{K}\Delta\boldsymbol{d} = -\left(\boldsymbol{F}^{int}(\bar{\boldsymbol{d}}) - \boldsymbol{F}^{ext}\right),\ \boldsymbol{K} = \left.\frac{\partial \boldsymbol{F}^{int}}{\partial \boldsymbol{d}}\right|_{\boldsymbol{d}=\bar{\boldsymbol{d}}}\ ,\ \ \boldsymbol{d} = \bar{\boldsymbol{d}} + \Delta\boldsymbol{d} \tag{48.a}$$

$$\boldsymbol{K} = \int_0^{\mathcal{L}} \rho_0 [\mathrm{BL1}]^T [\mathbb{Q}][\kappa][\mathrm{BL2}] dy_1 \tag{48.b}$$

$$[BL2] = \begin{bmatrix} diag\left(\frac{\partial}{\partial y_1}\right) & diag\left(\frac{1}{R}\right) \\ 0 & D^T \\ D^T & 0 \\ diag\left(\frac{1}{R}\right) & diag\left(\frac{\partial}{\partial y_1}\right) \end{bmatrix} [\emptyset(y_1)] \tag{48.c}$$

$$[\kappa] = \begin{bmatrix} \kappa_{11} & \kappa_{12} & \kappa_{13} & \kappa_{14} \\ \kappa_{21} & \kappa_{22} & \kappa_{23} & \kappa_{24} \\ \kappa_{31} & \kappa_{32} & \kappa_{33} & \kappa_{34} \\ \kappa_{41} & \kappa_{42} & \kappa_{43} & \kappa_{44} \end{bmatrix}, [\mathbb{Q}] = \begin{bmatrix} \mathbb{Q}_{11} & \mathbb{Q}_{12} & \mathbb{Q}_{13} & \mathbb{Q}_{14} \\ \mathbb{Q}_{21} & \mathbb{Q}_{22} & \mathbb{Q}_{23} & \mathbb{Q}_{24} \\ \mathbb{Q}_{31} & \mathbb{Q}_{32} & \mathbb{Q}_{33} & \mathbb{Q}_{34} \\ \mathbb{Q}_{41} & \mathbb{Q}_{42} & \mathbb{Q}_{43} & \mathbb{Q}_{44} \end{bmatrix} \tag{48.d}$$

Here each term of $[\kappa]$ and $[\mathbb{Q}]$ like κ_{11}, $\mathbb{Q}_{11}$ etc. is 4×4 matrix. The non-zero terms of $[\mathbb{Q}]$ are

$$\mathbb{Q}_{11}^{jb} = \delta_{jb},\ \mathbb{Q}_{23}^{jb} = \delta_{jb}, \mathbb{Q}_{33}^{jb} = D_{jb}, \mathbb{Q}_{34}^{jb} = -\frac{1}{R}\delta_{jb}, \mathbb{Q}_{42}^{jb} = D_{jb}, \mathbb{Q}_{41}^{jb} = \frac{1}{R}\delta_{jb} \tag{49}$$

Here $j, b = 0,1,2,3$, D_{jb} is specified in Eq. (8.e). Expressions for elements of $[\kappa]$ are listed in Appendix B.

The iterative process is terminated when the norm of the residual load vector, $\bar{R}$, defined by

$$\boldsymbol{R} = \boldsymbol{F}^{int}(\boldsymbol{d}) - \boldsymbol{F}^{ext}, \bar{R} = max(|\boldsymbol{R}|)N/Sum(|\boldsymbol{F}^{ext}|) \tag{50.a,b}$$

is less than the prescribed value. During a given load step the stiffness matrix is evaluated only at the start of the load step. In Eq. 50, N equals the number of degrees of freedom

4. Curved laminated beam

For simplicity we consider a 3-layer curved laminated beam, and denote displacements of a point in the top, the central, and the bottom layers by superscripts *t, c* and *b*, respectively. With the origin of the curvilinear coordinate axes located at the geometric centroid of the rectangular cross-section (e.g., see Fig. 2), we assume the following displacement field in the beam.

$$u_\alpha^c(y_1, y_3, t) = \sum_{i=1}^{3} (y_3)^i \, l_{\alpha i}^c(y_1, t), \qquad \alpha = 1, 3, \qquad |y_3| \le H^c \tag{51.a}$$

$$u_\alpha^t(y_1, y_3, t) = u_\alpha^c(y_1, H^c, t) + \sum_{i=1}^{3} \left((y_3)^i - (H^c)^i\right) l_{\alpha i}^t(y_1, t), \quad \alpha = 1, 3, \qquad H^c < y_3 < H^c + H^t \tag{51.b}$$

$$u_\alpha^b(y_1, y_3, t) = u_\alpha^c(y_1, -H^c, t) + \sum_{i=1}^{3} \left((y_3)^i - (-H^c)^i\right) l_{\alpha i}^b(y_1, t), \quad \alpha = 1, 3, \quad -(H^b + H^c) \le y_3 \le -H^c \tag{51.c}$$

In Eq. (51) $2H^c$ equals the height of the central beam, and $H^t$and H^b heights of the top and the bottom beams, respectively. The assumed displacement field (51) is continuous across interfaces between the central and the top and the bottom beams. The continuity of surface tractions across these interfaces is implicitly satisfied during the derivation of the weak formulation of the problem.

For each displacement component, Eqs. (51.a) - (51.c) have four unknowns for the top, the central and the bottom layers. Thus in the TSNDT the number of degrees or unknowns for N nodes on the centroidal axis equals 20N. For studying plane strain deformations of a laminated beam composed of 3 plies using 4-node quadrilateral elements with 3 elements across the thickness in each ply, the number of degrees of freedom for N nodes along the y_1-axis will equal 20N.

The governing equations and the weak formulation derived, respectively, in Section 2 and subsection 3.1 remain unaffected by the number of plies. However, the displacement function L_j and the matrix $[D]$ need to be changed, and the material properties of the pertinent layer are used while evaluating integrals in Eq. (28).

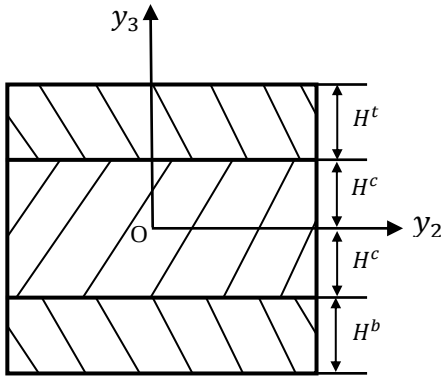

Fig.2 Cross-section of a 3-layer beam

5. Results for Example Problems

5.1 Linear problems

When analyzing linear elastic problems, we omit all nonlinear terms in expressions for the strain components, and note that differences among the three stress tensors, namely, the 1st and the 2nd Piola-Kirchhoff and the Cauchy are negligible. Also, we use the more common notation and replace y_1 and y_3 by x and z, respectively, and u_1 and u_3 by u and w, respectively. Unless otherwise stated, integrals in Eqs. (38) and (28) are numerically evaluated, respectively, by using 1 Gauss point in the x-direction, and 5 in each layer in the z-direction.

5.1.1 Static infinitesimal deformations of straight laminated beam

We study static infinitesimal deformations of a simply supported $(0^\circ/90^\circ/0^\circ)$ straight beam loaded by a uniformly distributed normal traction, $q = q_0 sin\left(\frac{\pi x}{\mathcal{L}}\right)$,on the top surface with the bottom surface traction free; a schematic sketch of the problem studied is shown in Fig. 3. Each layer is of the same thickness.

Values assigned to material parameters, taken from Pagano [40] who solved the problem analytically, are

$$E_L = 172\ GPa, E_T = 6.9\ GPa, G_{LT} = 3.4\ GPa, G_{TT} = 1.4\ GPa, \nu_{TL} = \nu_{TT} = 0.25 \qquad (52)$$

Here subscript L denotes the direction parallel to the fiber, subscript T the transverse direction, and ν is Poisson's ratio; i.e., E_T and E_L are elastic moduli in the transverse and the longitudinal directions, respectively, and G_{LT} is the shear modulus.

The percentage error, $\bar{\eta}$, in the TSNDT solution for variable σ is defined by

$$\bar{\eta} = 100(\int_0^{\mathcal{L}} |\sigma_{TSNDT} - \sigma_{ana}|dx) / \int_0^{\mathcal{L}} |\sigma_{ana}|dx \tag{53}$$

where subscripts $TSNDT$ and ana denote, respectively, numerical results computed by using the $TSNDT$ and the analytical approach. The deflection, w, is normalized by

$$\underline{w} = \frac{100 E_T H^3 w}{q_0 \mathcal{L}^4} \tag{54}$$

The normalized mid-point deflection of the beam from the TSNDT and the analytical approach as well as the percentage difference between the two results is listed in Table 1. It is clear that for $\mathcal{L}$ /H varying from 4 to 100 the mid-point deflection computed using the TSNDT differs from that found using the analytical approach by 0.04%. For $\mathcal{L}/H$ = 4 and 10, we have exhibited in Fig. 4a-f through-the-thickness variations of the axial, the transverse normal and the transverse shear stresses computed using the TSNDT and the analytical approach. Stresses using the TSNDT are found from the constitutive relations and the displacement fields. The difference $\bar{\eta}$ between stresses from the two approaches is less than 1% implying that the TSNDT gives accurate values of stresses including those of the transverse shear and the transverse normal stresses without using any stress recovery technique. We note that the transverse normal and the transverse shear stresses computed with the TSNDT are continuous across interfaces between adjoining plies. In Fig. 5 we have compared the presently computed values of the transverse shear stress for a beam with $\mathcal{L}/H$ = 4 with those given in [21] using an efficient higher order plate theory, EHOPT, that assumes a combination of zig-zag and a cubic variation in the z-direction of in-plane displacements. The transverse shear stresses denoted as EHOPT-C and EHOPT-E are computed, respectively, by using the constitutive equations and by integrating equilibrium equations. It is evident that the present results obtained without using any stress recovery technique are closer to the analytical solution than those derived from the EHOPT using the post-processing method.

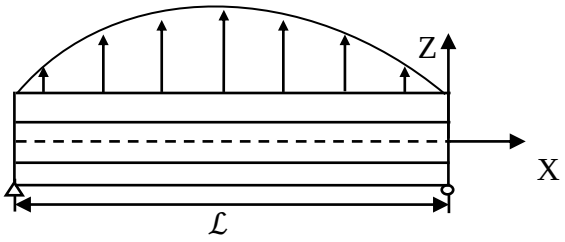

Fig. 3 Schematic sketch of the problem studied

Table 1 Comparison of beam centroid deflection $\underline{w}\left(\frac{\mathcal{L}}{2}, 0\right)$ (82 uniform elements with piecewise linear basis functions used to compute results with the TSNDT)

L/H	4	10	20	50	100
TSNDT	2.886	0.9312	0.6170	0.5268	0.5138
Elasticity	2.887	0.9316	0.6173	0.5270	0.5140
Difference	0.0346%	0.0429%	0.0486%	0.0380%	0.0389%

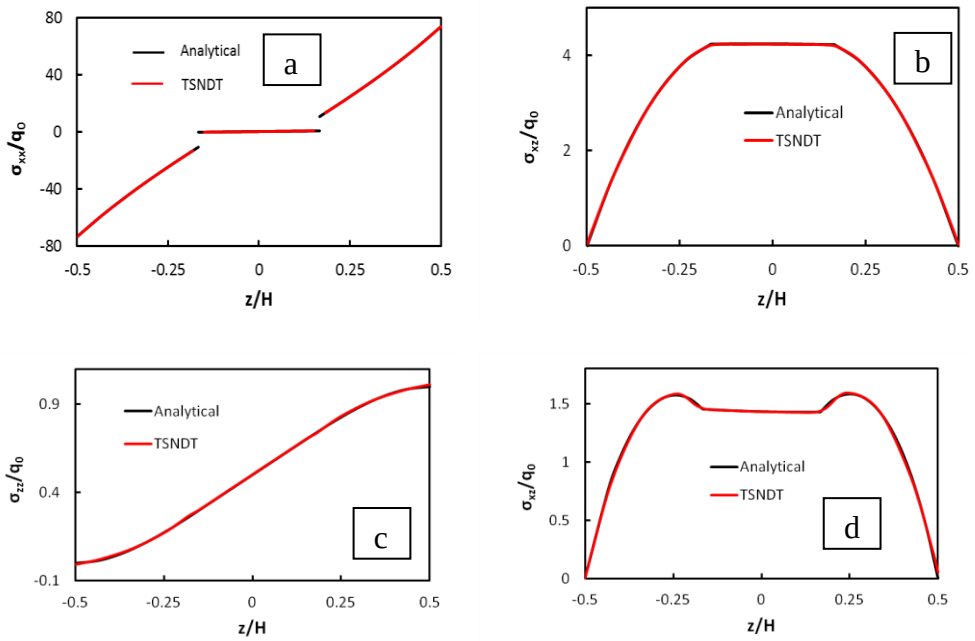

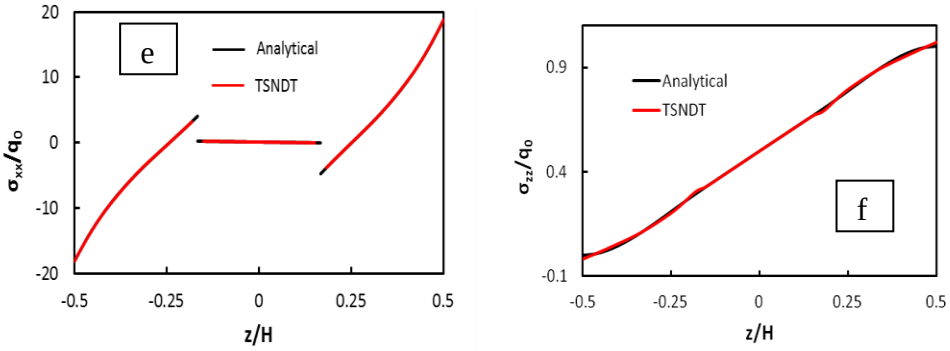

Fig. 4 Comparison of through-the-thickness distributions of stresses derived from the analytical solution based on the linear elasticity theory and the TSNDT solution for $(0^0/90\,\%0^0)$ laminates; black curves represent the elasticity solution and red curves the TSNDT solution; (a) σ_{xx} at $x = \mathcal{L}/2$ for $\mathcal{L}/H = 10$; difference, $\bar{\eta}$=0.062%; (b) σ_{xz} at $x = 0\ for\ \mathcal{L}/H = 10$; difference, $\bar{\eta}$=0.146% ; (c) σ_{zz} at $x = \mathcal{L}/2$ for $\mathcal{L}/H = 10$; difference, $\bar{\eta}$=0.439%; (d) σ_{xz} at $x = 0$ for $\mathcal{L}/H = 4$; difference, $\bar{\eta}$=0.742%; (e) σ_{xx} at $x = \mathcal{L}/2$ for $\mathcal{L}/H = 4$; difference, $\bar{\eta}$=0.439%; (f) σ_{zz} at $x = \mathcal{L}/2$ for $\mathcal{L}/H = 4$; difference, $\bar{\eta}$=0.941%

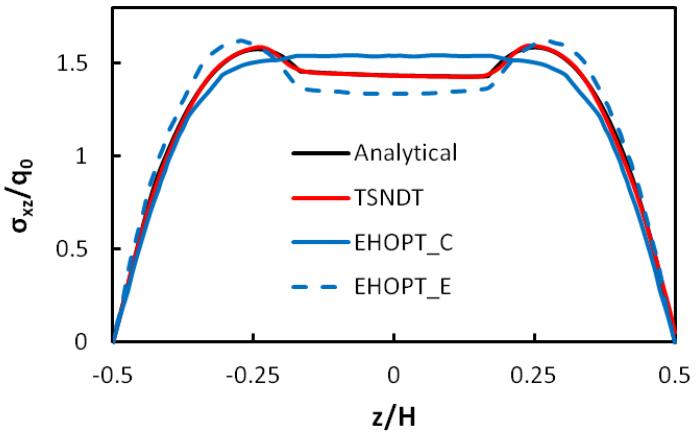

Fig. 5 Comparison of through-the-thickness variation of σ_{xz} at $x = 0$ for $\mathcal{L}/H = 4$ using the TSNDT, the EHOPT_C and the EHOPT_E; in EHOPT_C and EHOPT_E stresses are computed, respectively, by using constitutive equations and by integrating equilibrium equations.

5.1.2 Static infinitesimal deformations of curved laminated beam

The second problem studied is that of a simply supported $(0^\circ/90^\circ/0^\circ)$ beam of constant radius of curvature, $R = 25.4$ cm, length $\mathcal{L} = R\pi/3$, ply thickness = H/3, subjected to sinusoidal normal traction q_0 on the top surface as shown in Fig. 6, and

material properties given in Eq. (52). Results are presented in terms of the following non-dimensional variables:

$$\underline{w} = \frac{10E_T w}{q_0 H \chi^4},\ \underline{\sigma}_{xx} = \frac{\sigma_{xx}}{q_0 \chi^2},\ \underline{\sigma}_{xz} = \frac{\sigma_{xz}}{q_0 \chi},\ \underline{\sigma}_{zz} = \frac{\sigma_{zz}}{q_0},\ \chi = R/H \tag{55}$$

The analytical results obtained by digitizing plots in [41] are compared with those computed with the TSNDT, the CST [41], the FSDST [42], the HSDST [42], the EHOST [36], and the zig-zag [43] shell theory. The shell theory discussed in Section 2 that considers (does not consider) the variation of the radius of curvature through the shell thickness is called "thick (thin) shell theory". Deformations of a curved beam can also be analyzed by dividing it into small segments and approximating each segment as a straight line; the analysis based on this technique is called the "straight beam theory". This approach does not consider through-the-thickness variation of the radius of curvature.

The centroidal deflections and stresses at two points obtained with different theories are compared with the analytical solution in Tables 2 through 6. The TSNDT results presented in Table 2 with different number of integration points in the x- and the z-directions for evaluating integrals in Eqs. (38) and (28), respectively, suggest that using 1 Gauss point in the x-direction in each FE and 5 in each layer in the z-direction provides sufficiently accurate results for χ between 4 and 100. Unless otherwise specified, results presented below have been computed with 1 Gauss point in the x-direction in each 1-D FE. Values of centroidal deflection from the thick shell and the straight beam theories listed in Table 3 suggest that the deflection using the thick shell theory converges significantly faster than that derived from the straight beam theory.

For $\chi = 4, 10, 50$ and 100, converged values of stresses at critical points based on different shell theories are compared with their values from the analytical solution in Tables 4 through 6. For $\chi =$ 50 and 100, all theories give very good values of stresses. However, for $\chi = 4$ and 10, the thick shell theory gives superior results than those obtained with the other shell theories considered here. For $\chi = 4$ and 10, the through-the-thickness variations of stresses found with the thick shell TSNDT are compared in Figs. 7 and 8 with those from the analytical solution of Ren [41]. The maximum difference in the two values of a stress component is about 2% except for 5.1% for

$\underline{\sigma_{zz}}$ when χ= 10 which most likely is due to digitization errors as the plot of $\underline{\sigma_{zz}}$ in [41] is not clear. Results presented in subsection 5.5 will show that the thick shell TSNDT predicts $\underline{\sigma_{zz}}$ for $\chi = 10$ in agreement with that obtained using the commercial FE software, ABAQUS. In Fig. 8 we have exhibited through-the-thickness variation of the transverse shear stress found from three shell theories and the analytical solution of the boundary value problem. The three shell theories predict continuous variation of $\underline{\sigma_{xz}}$, and results from the thick shell TSNDT are in better agreement with the analytical values than those from the HSDST and EHOST that use post-processing methods.

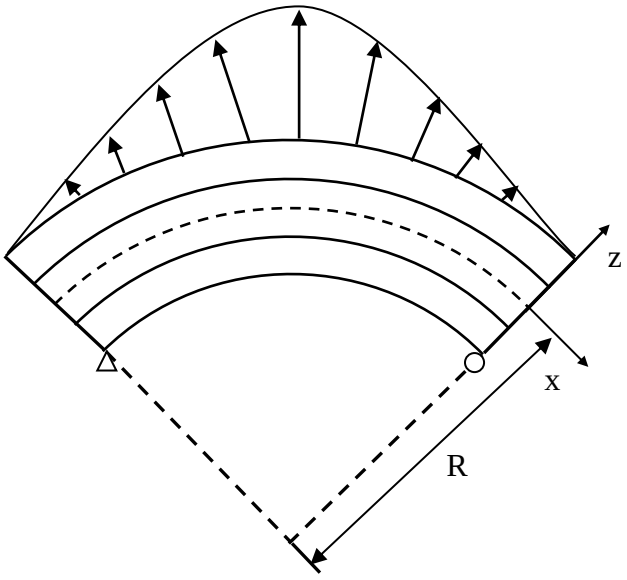

Fig. 6 Schematic sketch of a 3-layer laminated curved beam loaded by a sinusoidal normal traction on the top surface

Table 2 Comparison of the analytical solution of the shell centroid deflection, $\underline{w}\left(\frac{\mathcal{L}}{2}, 0\right)$, with those obtained by using different meshes and the number of integration points in the thick shell theory (the number of integration points in the z-direction are for each layer and are used to numerically evaluate integrals in Eq. (28))

χ	Number of Integration Points (x, z)	21 nodes	41 nodes	81 nodes	161 nodes	Exact[41]

4	1,5	0.457	0.458	0.458	------	0.457
	3,5	0.446	0.455	0.457	-----	
10	1,5	0.143	0.144	0.144	-----	0.144
	3,5	0.136	0.142	0.144	-----	
50	1,5	0.0804	0.0807	0.0808	------	0.0808
	3,5	-----	0.0666	0.0768	0.0798	
100	1,5	0.0782	0.0785	0.0785	------	0.0787
	3,5	------	0.0429	0.0653	0.0747	

Table 3 Comparison of the centroid deflection, $\underline{w}\left(\frac{\mathcal{L}}{2}, 0\right)$, from the straight beam and the thick shell theories computed with different number of nodes in the x-direction.

χ		5 nodes	11 nodes	21 nodes	41 nodes	Exact [41]
4	Thick shell	0.433	0.454	0.457	0.458	0.457
	Straight beam	0.333	0.385	0.397	0.405	
10	Thick shell	0.132	0.142	0.143	0.144	0.144
	Straight beam	0.109	0.127	0.132	0.135	
50	Thick shell	0.0710	0.0792	0.0804	0.0807	0.0808
	Straight beam	0.0600	0.0735	0.0768	0.0786	
100	Thick shell	0.0688	0.0770	0.0782	0.0785	0.0787

Straight beam	0.0582	0.0718	0.0750	0.0767

Table 4 Comparison of the deflection $\underline{w}\left(\frac{\mathcal{L}}{2}, 0\right)$ for the thin shell, the thick shell and the straight beam theories; Computed using 161 nodes for the straight beam theory when $\chi = 50$ and 100, and 81 nodes for all other theories and other values of χ.

χ	4	10	50	100
Exact [41]	0.457	0.144	0.0808	0.0787
TSNDT-Thick shell	0.458	0.144	0.0808	0.0785
TSNDT-Thin shell	0.412	0.137	0.0800	0.0781
TSNDT-Straight beam	0.409	0.136	0.0798	0.0779
CST	0.0781	0.0777	0.0776	0.0776
FSDST [42]	0.289	0.113	0.0786	0.0776
HSDST [42]	0.382	0.128	0.0793	0.0777
EHOST [36]	0.455	0.143	0.0808	0.0787
Zig-zag [43]	0.441	0.143	0.0810	0.0788

Table 5 Comparison of stress $\underline{\sigma}_{xx}\left(\frac{\mathcal{L}}{2}, \mp\frac{H}{2}\right)$ from different theories; 161 nodes in the x-direction for the straight beam theory when $\chi = 50$ and 100, and 81nodes for all other cases.

χ	4	10	50	100
Exact [41]	-1.772	-0.995	-0.798	-0.786
	1.367	0.897	0.782	0.781
TSNDT-Thick shell	-1.772	-0.995	-0.798	-0.786
	1.367	0.897	0.783	0.779
TSNDT-Thin shell	-1.378	-0.905	-0.784	-0.779
	1.398	0.895	0.781	0.778

TSNDT-Straight beam	-1.371	-0.901	-0.780	-0.776
	1.393	0.892	0.778	0.775
EHOST [36]	-1.702	-0.967	-0.794	-0.785
	1.599	0.928	0.786	0.780
Zig-zag [43]	-1.792	-1.003	-0.799	-0.787
	1.350	0.894	0.783	0.779

Table 6 Comparison of stress $\underline{\sigma}_{xz}(0,0)$ from different theories; 161 nodes in the x-direction for the straight beam theory when $\chi = 50$ and 100, and 81nodes for all other cases.

χ	4	10	50	100
Exact[41]	0.476	0.525	0.526	0.523
TSNDT-Thick shell	0.476	0.525	0.525	0.523
TSNDT-Thin shell	0.427	0.501	0.520	0.520
TSNDT-Straight beam	0.425	0.498	0.518	0.519
EHOST [36]	0.516	0.545	0.537	0.535
Zig-zag [43]	0.447	0.524	0.525	0.524

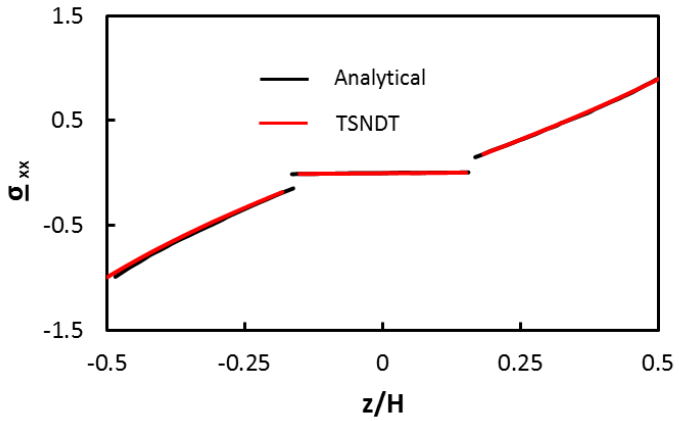

(a) $\underline{\sigma}_{xx}$ at $x = \mathcal{L}/2$ when $R/H = 10$; difference, $\bar{\eta}$=2.37 %

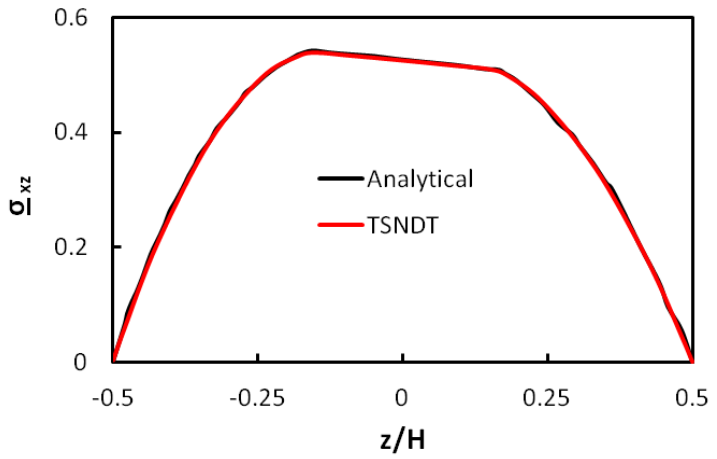

(b) $\underline{\sigma_{xz}}$ at $x = 0$ when $R/H = 10$; difference, $\bar{\eta}$=1.18 %

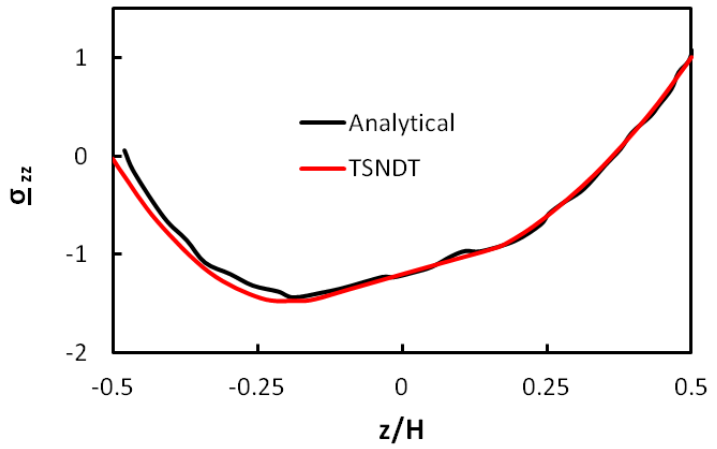

(c) $\underline{\sigma_{zz}}$ at $x = \mathcal{L}/2$ when$R/H = 10$; difference, $\bar{\eta}$=5.17 %

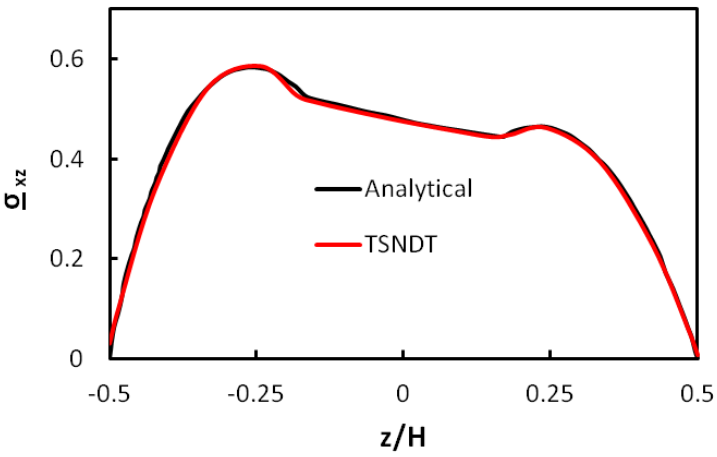

(d) $\underline{\sigma_{xz}}$ at $x = 0$ when $R/H = 4$; difference, $\bar{\eta}$=1.01%

Fig. 7 Comparison of through-the-thickness variation of stresses found from the analytical and the TSNDT solutions; black curve - analytical solution, red curve - TSNDT (thick shell theory)

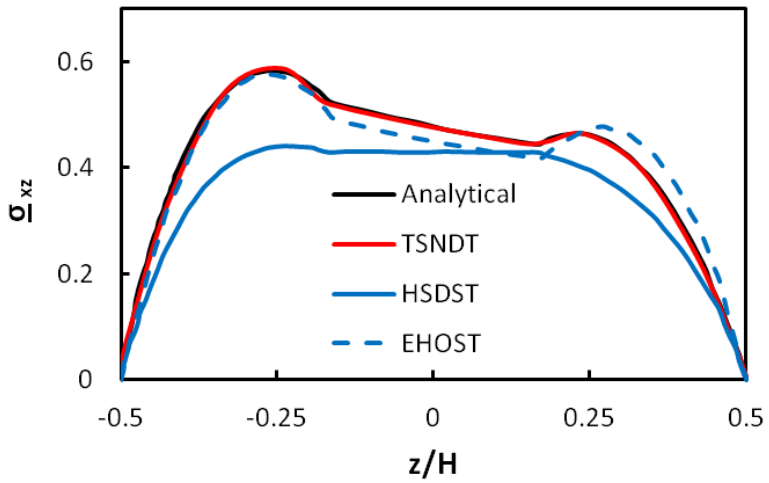

Fig. 8 Through-the-thickness variation of $\underline{\sigma}_{xz}$ at $x = 0$ when $R/H = 4$ for different theories, shear stresses in the HSDST and the EHOST are derived by integrating the equilibrium equations.

5.2 Finite static deformations of homogeneous straight beam

5.2.1 Comparison of results from the TSNDT with those from ABAQUS

Static finite deformations of clamped-clamped straight 15 cm thick beam with $\mathcal{L}/H = 20$, made of an isotropic and homogeneous St. Venant-Kirchhoff material having $E = 172.4\ GPa$ and $\nu = 0.3$ and loaded by a uniform pressure $q_0 = 30$ MPa on the bottom surface are analyzed as a plane strain problem with ABAQUS and with the TSNDT. We note that the direction of the normal pressure changes as the beam deforms. Values of the centroidal deflection and stresses at critical points from the two approaches and using linear and nonlinear theories are listed in Table 7. For both the linear and the nonlinear theories, converged values of the centroidal deflections and stresses at the point ($\mathcal{L}/4$, 0) found from the TSNDT and ABAQUS agree well with each other. The computed value of σ_{xx}/q_0 at the point $\left(\frac{\mathcal{L}}{2}, -\frac{H}{2}\right)$ from the linear theory in which the pressure always acts in the z-direction is nearly twice of that found from the nonlinear theory. The value of $\frac{\sigma_{xz}}{q_0}$ at the point $(\frac{\mathcal{L}}{4}, 0)$ from the linear theory is 11.6% higher than

that from the nonlinear theory. *Thus a stress based failure criterion will predict early failure of a material point if stresses from the linear theory are used in it*. Through-the-thickness variations of the axial stress, σ_{xx}, and the transverse stresses, σ_{xz} and σ_{zz}, from the TSNDT and ABAQUS are exhibited in Fig. 9; the percentage differences between the two values of the stress is defined as $100\int_{-H/2}^{H/2}|\sigma_{TSNDT}-\sigma_{ABA}|dz\,/\int_{-H/2}^{H/2}|\sigma_{ABA}|dz$ where subscripts TSNDT and ABA denote, respectively, values from the TSNDT and ABAQUS solutions. The two values of the percentage difference listed in the figure legends are for results from the linear and the nonlinear theories. With the error of 1.27%, it is clear that stresses computed from the TSNDT and ABAQUS are very close to each other. Whereas σ_{xx} is an affine function of z for both the linear and the nonlinear theories, the values of z where $\sigma_{xx} = 0$ are quite different. Through-the-thickness distributions of σ_{zz} from the linear and the nonlinear theories are both qualitatively and quantitatively quite different. Fig. 10 exhibits through-the-thickness variation of $\frac{\partial w}{\partial z}$ at the section $x = \mathcal{L}/4$ found from the linear and the nonlinear theories. Values of $\frac{\partial w}{\partial z}$ are always negative for the nonlinear theory but those from the linear theory are positive at points near the top surface and negative at points near the bottom surface. At a point along the thickness, the magnitude of $\frac{\partial w}{\partial z}$ for the nonlinear theory is more than that from the linear theory. The deformed positions of a line initially perpendicular to the centroidal axis at $x = \mathcal{L}/4$ found from the linear and the nonlinear theories are plotted in Fig. 11. It is evident that the linear and the nonlinear theories give quite different deformed positions of the line.

Table 7 For different node numbers along the x-axis in the TSNDT and for different FE meshes in ABAQUS, values at critical points of the centroidal deflection and stresses from the linear and the nonlinear theories.

L/H			Linear			Nonlinear		
		Nodes	w/H	σ_{xx}/q_0	σ_{xz}/q_0	w/H	σ_{xx}/q_0	σ_{xz}/q_0
			$(\mathcal{L}/2,0)$	$(\mathcal{L}/2,-H/2)$	$(\mathcal{L}/4,0)$	$(\mathcal{L}/2,0)$	$(\mathcal{L}/2,-H/2)$	$(\mathcal{L}/4,0)$
	TSNDT	21	0.8043	-96.3	7.851	0.6254	-57.49	6.910
		61	0.8147	-100.4	7.463	0.6270	-57.71	6.693

20		101	0.8147	-100.4	7.500	0.6271	-57.70	6.722
		161	0.8153	-100.4	7.500	0.6271	-57.70	6.722
	ABAQUS	11,161 (z,x)	0.8140	-100.4	7.520	0.6267	-57.70	6.730
		31, 61 (z,x)	0.8124	-100.4	7.101	0.6258	-57.71	6.445
		31,161 (z,x)	0.8147	-100.4	7.560	0.6270	-57.70	6.790
		61,301 (z,x)	0.8152	-100.4	7.489	0.6272	-57.70	6.714

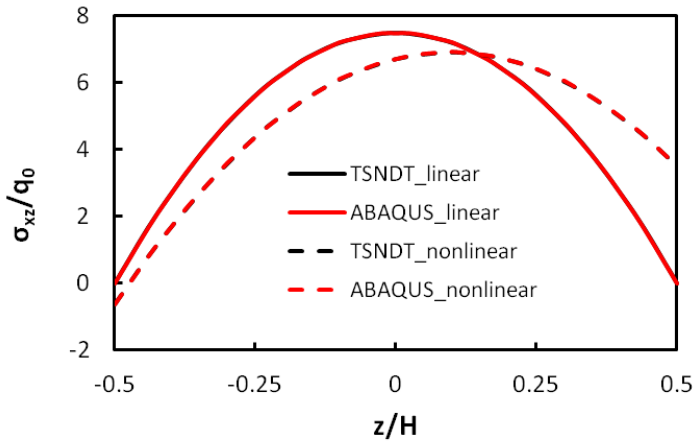

a. σ_{xz} at $x = \mathcal{L}/4$, $\mathcal{L}/H = 20$, $q_0 = 30\ MPa$; differences in the TSNDT and ABAQUS results from the linear and the nonlinear theories are 0.343% and 0.238%, respectively, and the two sets of results overlap in the Fig.

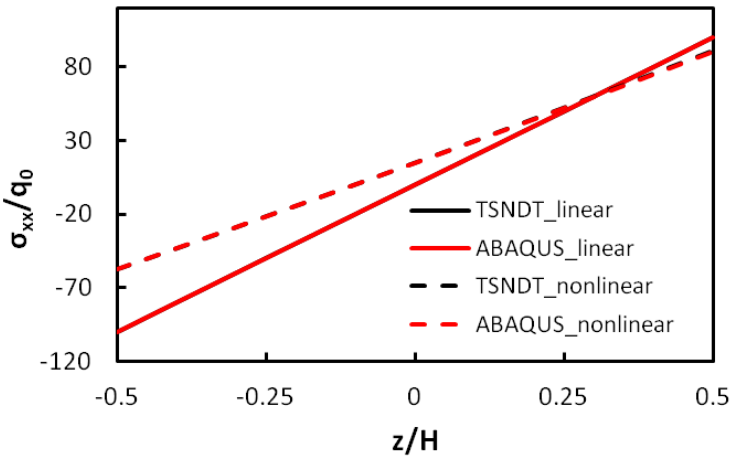

b. σ_{xx} at $x = \mathcal{L}/2$, $\mathcal{L}/H = 20$, $q_0 = 30\ MPa$; differences in the TSNDT and ABAQUS results from the linear and the nonlinear theories are 0.068% and 0.254%, respectively, and the two sets of results overlap in the Fig.

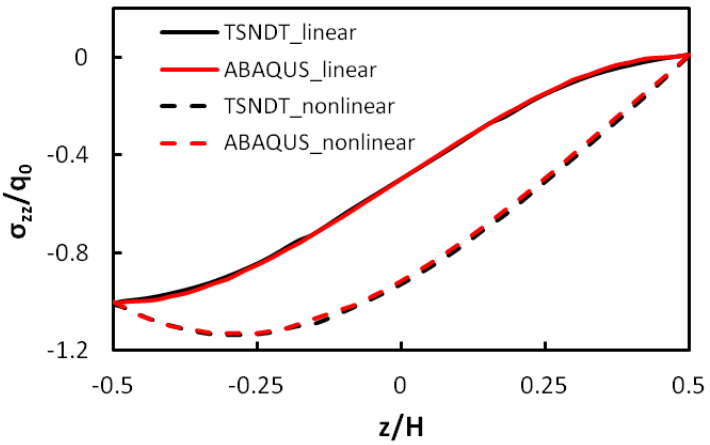

c. σ_{zz} at $x = \mathcal{L}/2$, $\mathcal{L}/H = 20$, $q_0 = 30\ MPa$; differences in the TSNDT and ABAQUS results from the linear and the nonlinear theories are 1.27% and 1.27%, respectively, and the two sets of results overlap in the Fig.

Fig. 9 Comparison of through-the-thickness variations of stresses computed from the linear and the nonlinear theories using the TSNDT and the elasticity (ABAQUS) theories.

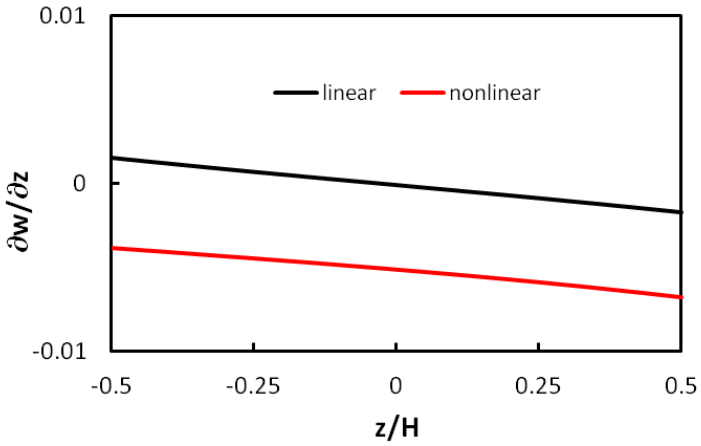

Fig. 10 Variation of $\frac{\partial w}{\partial z}$ through the thickness at x=$\mathcal{L}$/4 for the linear and the nonlinear theories found from the TSNDT solution.

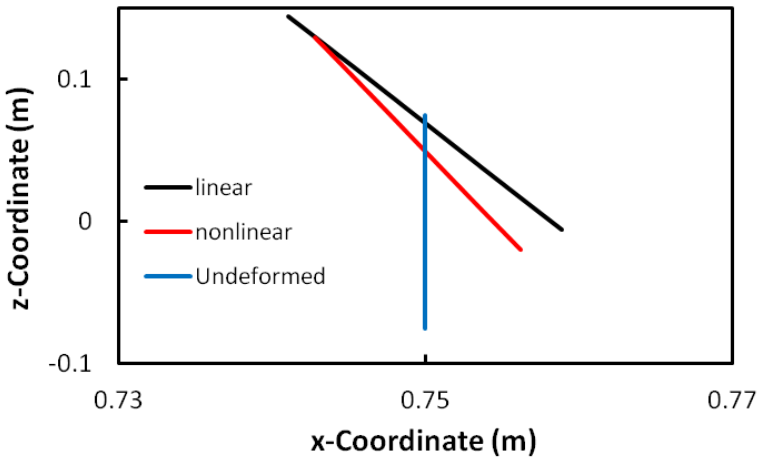

a. Deformed configurations of a line initially perpendicular to the centroidal axis at x = $\mathcal{L}$/4.

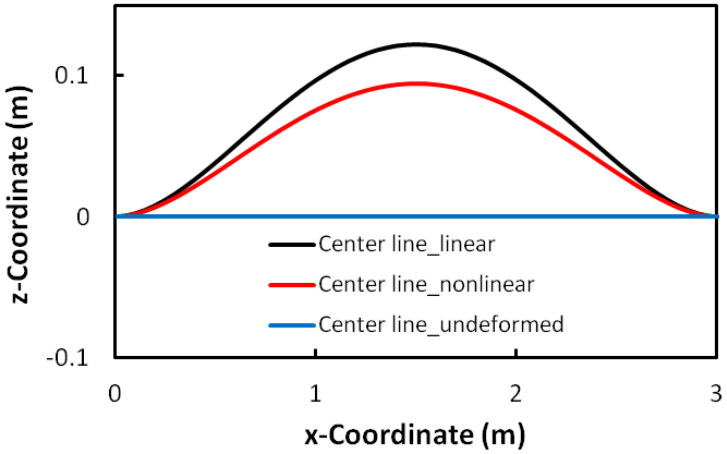

b. Deformed shapes of the beam centroidal axis

Fig. 11 Deformed and undeformed positions of lines computed using linear and nonlinear theories.

5.2.2 Verification of the software by the method of manufactured solutions

We use the method of manufactured solutions (e.g., see the material just before and following Eq. (20) of [33]) to verify the code developed for analyzing nonlinear deformations of the beam of subsection 5.2.1. For the clamped-clamped beam we begin by assuming the following displacement field

$$u = 0.2H\left(\left(\frac{z}{H}\right)^3 + \sin\left(4\frac{z}{H}\right)\right)\left(1-\frac{x}{\mathcal{L}}\right)\frac{x}{\mathcal{L}}e^{\frac{2x}{\mathcal{L}}} \tag{56.a}$$

$$w = 0.2H\left(\left(\frac{z}{H}\right)^4 + \cos\left(2\frac{z}{H}\right)\right)\left(1 - \frac{x}{\mathcal{L}}\right)\frac{x}{\mathcal{L}}e^{-\frac{x}{\mathcal{L}}} \tag{56.b}$$

and find strains from Eq. (7) and stresses from Eqs. (23) and (25). Substitution for stresses with acceleration terms set equal to zero in Eq. (12) gives expressions for the body force needed to satisfy equilibrium equations. We find surface tractions on the bounding surfaces from the computed stress field. We now numerically solve the problem with the in-house developed code by using the above found values of the body force and essential boundary conditions applied at both ends of beam and natural boundary conditions on the top and the bottom surfaces of the beam. For the displacement field (56), stress components in Eq. (12) were evaluated numerically by using Eqs. (5), (7), (23) and (25), the spatial derivatives of stresses in Eq. (12) were evaluated by the central difference method, and numerical values of the body force components at each node were read as input into the code.

For $\mathcal{L}/H$= 5 and $\mathcal{L} = 0.75m$, the computed centroidal deflection is compared with its analytical value in Table 8 for piecewise linear and piecewise quadratic basis functions along the x-axis, and using 8 integration points in the z-direction in Eq. (28).

Table 8 Non-dimensional deflection, w/H , of the beam centroid with different shape functions, number of nodes along the x-axis, and number of Gauss integration points along the x-axis which are indicated in parentheses.

	21 nodes	41 nodes	81 nodes	Analytical
Linear (1)	0.0321	0.0308	0.0306	0.0303
Linear (3)	0.0287	0.0300	0.0303	
Quadratic (3)	0.0304	0.0304	0.0305	

It is clear that the converged values of the centroidal deflection are in excellent agreement with the corresponding analytical value. In Fig. 12, the computed through-the-thickness variation of stresses and the deformed shape of the beam are compared with the corresponding ones obtained from the assumed analytical solution. These plots evince that the computed results match well with the corresponding analytical ones

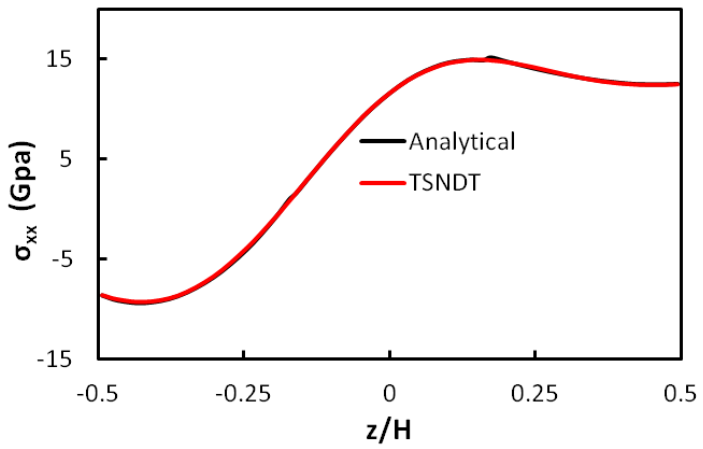

a. σ_{xx} at x=0.186 m; difference, $\bar{\eta}$=0.417%; the two solutions overlap each other.

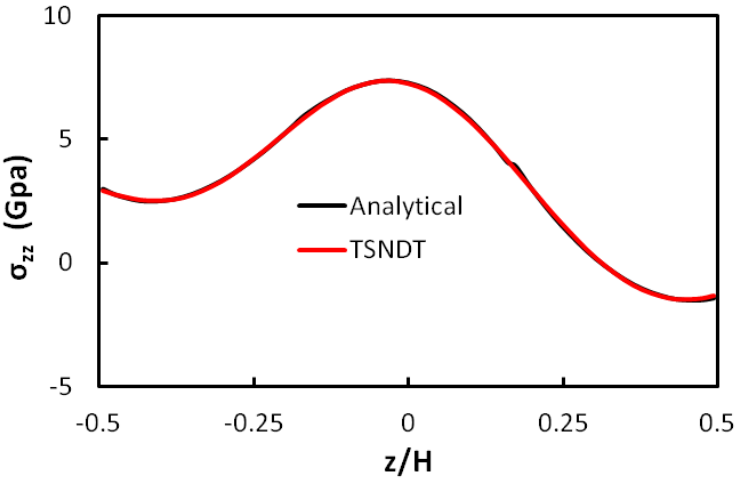

b. σ_{zz} at x=0.186 m; difference, $\bar{\eta}$=0.943%; the two solutions overlap each other.

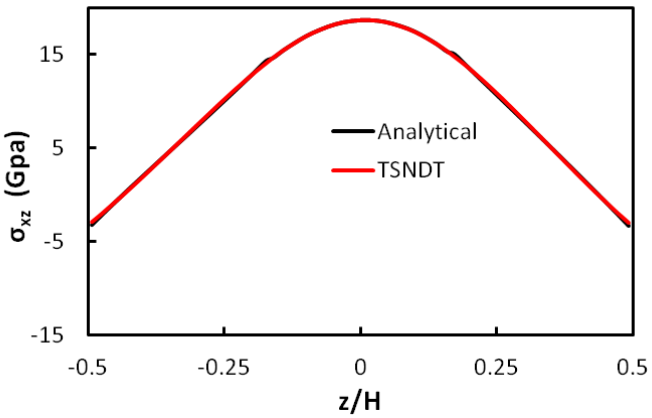

c. σ_{xz} at x=0.186 m; difference, $\bar{\eta}$=0.715%; the two solutions overlap each other.

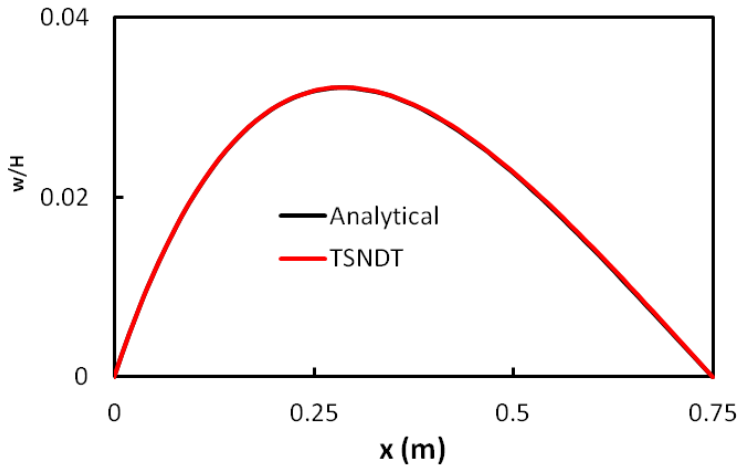

d. Deflection of the mid-surface, z = 0, of the beam; difference, $\bar{\eta}$ = 3.33%; the two curves overlap each other.

Fig .12 Comparison of the analytical and the numerical solutions computed using the TSNDT, 81 nodes along the x-axis and piecewise quadratic basis functions.

5.3 Finite static deformations of homogeneous curved beam with constant curvature

The clamped-clamped curved beam studied in subsection 5.1.2 is assumed to be made of an isotropic and homogeneous St. Venant-Kirchhoff material with Young's modulus $E = 172\ GPa$ and Poisson's ratio $\nu = 0.3$ and subjected to a uniformly distributed pressure q_0 on the bottom surface. The centroidal deflections and stresses at critical points from the TSNDT and ABAQUS solutions listed in Table 9 reveal the following. The centroidal deflection, the axial stress σ_{xx} at ($\mathcal{L}$/2, H/2), and the transverse shear stress σ_{xz} at ($\mathcal{L}$/4, H/2) from the linear theory equal 1.624, 1.422 and 0.857 times those from the nonlinear theory. Here $\mathcal{L}$ equals the beam length along the centroidal axis. Through-the-thickness stresses computed from the linear and the nonlinear theories are plotted in Fig. 13. The maximum difference between results from the TSNDT and the ABAQUS is less than 0.8% implying that the TSNDT gives results close to those obtained from the analysis of plane strain deformations of the curved beam using nonlinear elasticity theory. Fig. 14 exhibits through-the-thickness variation of $\frac{\partial w}{\partial z}$ at the section x = $\mathcal{L}$/2.

Table 9 Comparison of centroidal deflection and stresses at critical points of curved beam computed by using the TSNDT and ABAQUS

χ	q_0			Linear			Nonlinear		
			Nodes	w/H	σ_{xx}/q_0	σ_{xz}/q_0	w/H	σ_{xx}/q_0	σ_{xz}/q_0
				$(\mathcal{L}/2,0)$	$(\mathcal{L}/2,H/2)$	$(3\mathcal{L}/4,0)$	$(\mathcal{L}/2,0)$	$(\mathcal{L}/2,H/2)$	$(3\mathcal{L}/4,0)$
		TSNDT	21	0.9080	14.02	-1.144	0.5628	9.845	-1.338
			61	0.9126	14.06	-1.153	0.5622	9.885	-1.346
10	1.38 Gpa	ABAQUS	11, 161 (z, x)	0.9128	14.07	-1.114	0.5620	9.885	-1.343
			31, 161 (z, x)	0.9130	14.07	-1.156	0.5620	9.886	-1.347

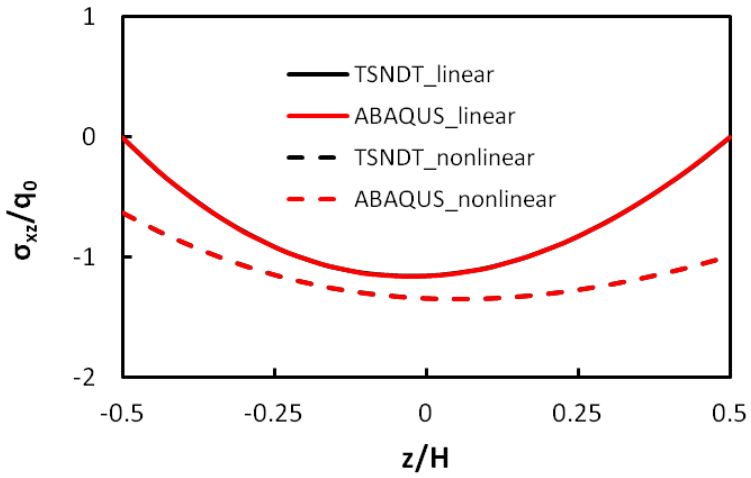

a. σ_{xz} at $x = 3\mathcal{L}/4$, $\chi = 10$, $q_0 = 1.38\,GPa$; differences in the TSNDT and the ABAQUS results from the linear and the nonlinear theories are 0.107% and 0.331%, respectively, and results computed using the TSNDT and ABAQUS overlap each other.

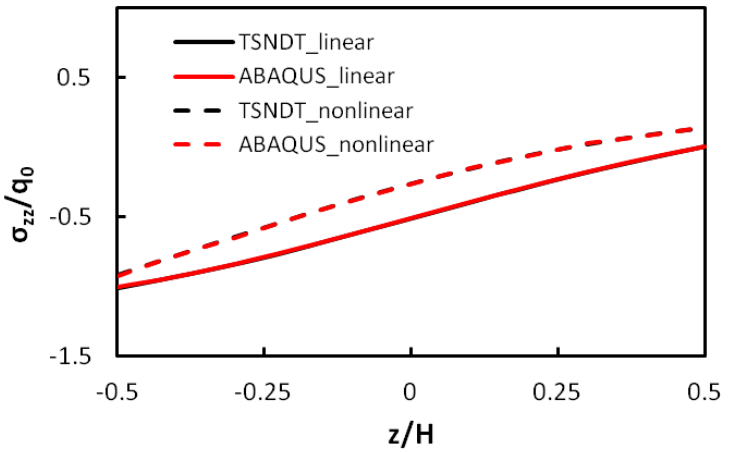

b. σ_{zz} at $x = 3\mathcal{L}/4$, $\chi = 10$, $q_0 = 1.38\,GPa$; differences in the TSNDT and the ABAQUS results from the linear and the nonlinear theories are 0.279% and 0.706%, respectively, and results computed using the TSNDT and ABAQUS overlap each other.

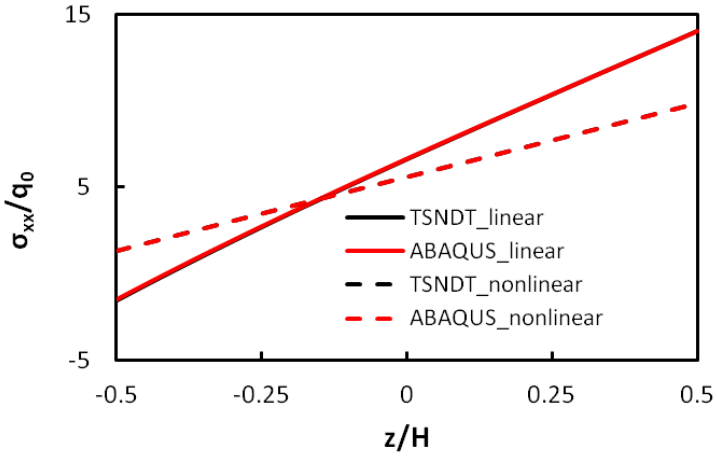

c. σ_{xx} at $= \mathcal{L}/2$, $\chi = 10$, $q_0 = 1.38\,GPa$; differences in the TSNDT and the ABAQUS results from the linear and the nonlinear theories are 0.190% and 0.122%, respectively, and the results computed using the TSNDT and ABAQUS overlap each other.

Fig. 13 Comparison of through-the-thickness variation of stresses for the curved beam computed from the linear and the nonlinear theories.

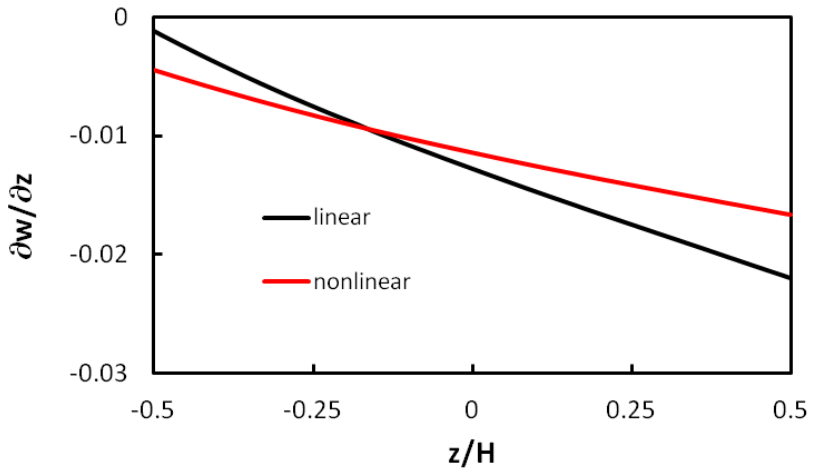

Fig. 14 For the curved beam, variation of $\frac{\partial w}{\partial z}$ through-the-thickness at x=$\mathcal{L}$/2 from the linear and the nonlinear theories.

5.4 Transient deformations

5.4.1 Homogeneous straight beam

5.4.1.1 Verification of the software by the method of manufactured solutions

We use the method of manufactured solutions described in subsection 5.2.2 for verifying the in-house developed code for a beam made of a homogeneous and isotropic material and set

$$E = 172.4\ GPa,\ \upsilon = 0.3,\ \rho = 4000\frac{kg}{m^3}, H = 0.15m,\ \mathcal{L}/H = 20 \tag{57}$$

We assume the following displacement field for a clamped-clamped beam

$$u = 2000H\left(\left(\frac{z}{H}\right)^3 + \sin\left(4\frac{z}{H}\right)\right)\left(1-\frac{x}{\mathcal{L}}\right)\frac{x}{\mathcal{L}}e^{2\frac{x}{L}}(e^t - t - 1.0) \tag{58.a}$$

$$w = 2000H\left(\left(\frac{z}{H}\right)^4 + \cos\left(2\frac{z}{H}\right)\right)\left(1-\frac{x}{\mathcal{L}}\right)\frac{x}{\mathcal{L}}e^{-\frac{x}{\mathcal{L}}}(e^t - t - 1.0) \tag{58.b}$$

The procedure outlined in subsection 5.3.2 is used to numerically solve the problem. The maximum frequency of the undeformed beam, $\omega_{max} = 1.97 \times 10^6\ rad/s$, and the time step used to integrate Eq. (46) is $5.0 \times 10^{-7} s$ which is less than the critical

time step, Δt_{crit}. The time history of the centroidal deflection and through-the-thickness variations of stresses from the numerical and the presumed solutions are shown in Fig. 15. The maximum difference for the centroidal deflection between the TSNDT and the analytical solutions is 3.38% mainly due to the numerical computation of the body forces and inputting those into the code. Through-the-thickness distributions of stresses from the two solutions are very close to each other.

5.4.1.2 Comparison of results from the TSNDT and ABAQUS

For uniformly distributed pressure $q_0 = 20\ MPa$ applied on the bottom surface of a homogeneous and isotropic straight beam, Fig. 16 shows the time history of the centroidal deflection and deformed positions of the centroidal axis computed using the linear and the nonlinear theories. For each theory, results from the TSNDT and ABAQUS are very close to each other.

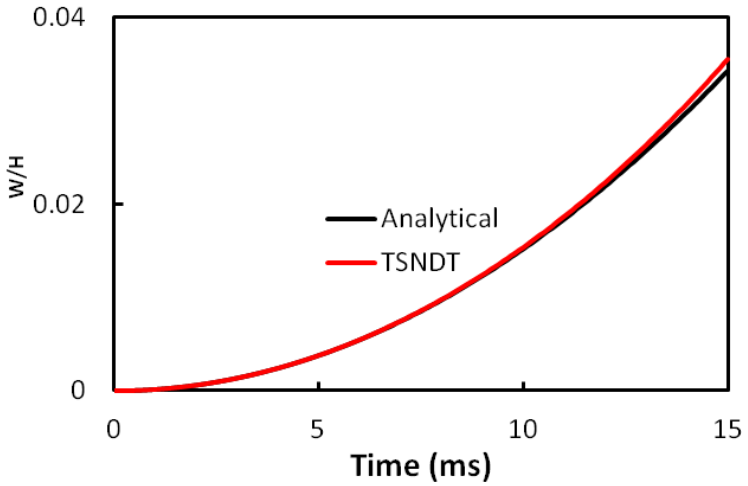

a. Time history of deflection at point $(\mathcal{L}/2,0)$; the difference in the TSNDT and the analytical results from the nonlinear theories is 3.48%, and results from the TSNDT are very close to analytical solution.

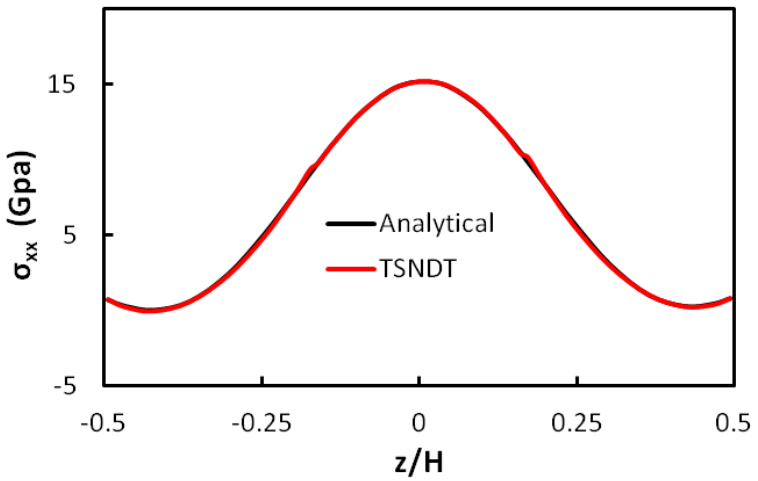

b. σ_{xx} at $x = 0.726m$ when $t = 15ms$; the difference in the TSNDT and the analytical results from the nonlinear theories equals 0.7% , and results from the TSNDT are very close to analytical solution.

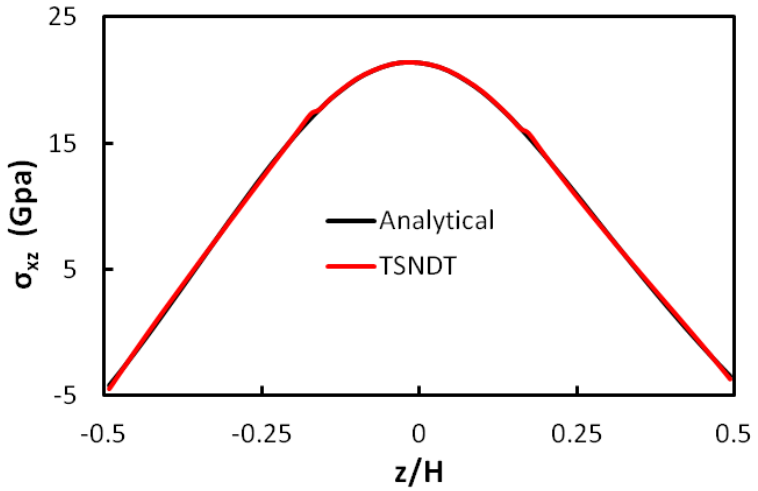

c. σ_{xz} at $x = 0.726m$ when $t = 15ms$; the difference in the TSNDT and the analytical results from the nonlinear theories equals 0.65% , and results from the TSNDT are very close to analytical solution.

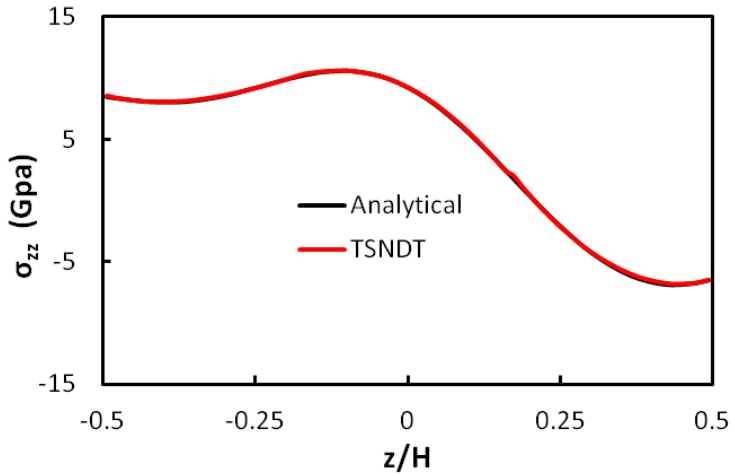

d. σ_{zz} at $x = 0.726m$ when $t = 15ms$; the difference in the TSNDT and the analytical results from the nonlinear theories equals 0.25% , and results from the TSNDT are very close to analytical solution.

Fig. 15 Comparison of results computed by using the TSNDT with 101 nodes in the x-direction and the analytical solution for the method of manufactured solutions

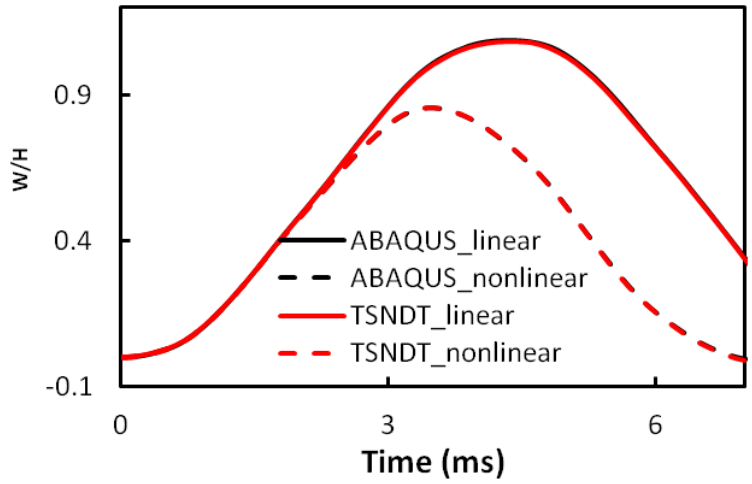

a. Time histories of the centroidal deflection from the linear and the nonlinear theories; for each theory results from the TSNDT and ABAQUS essentially overlap each other.

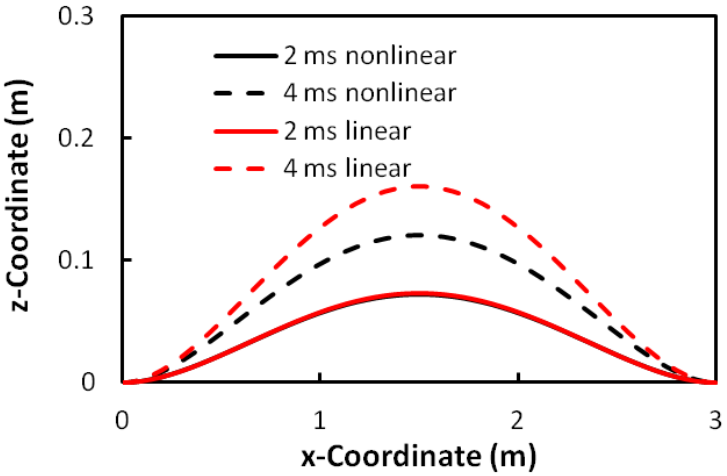

b. Deformed positions of the centroidal axis at t = 2 and 4 ms from the linear and the nonlinear theories computed using the TSNDT;

Fig. 16 Comparison of results computed by using the TSNDT and ABAQUS with and without considering geometric nonlinearities.

5.4.2 Homogeneous curved beam

For the clamped-clamped homogeneous curved beam of section 5.4 with χ = 10, mass density = 10684 kg/m^3, and uniformly distributed pressure, $q_0 = 689\ MPa$, we have exhibited in Fig. 17 time histories of the centroidal deflection computed using the linear and the nonlinear theories. One can see that results from the TSNDT agree well with those from ABAQUS, and the maximum deflection from the nonlinear theory is considerably less than that from the linear theory. The maximum frequency, ω_{max}, of the beam was found to be $8.43 \times 10^7\ rad/s$ and $\Delta t = 1.5 \times 10^{-8} s$, which is less than Δt_{crit}, was used to integrate Eq. (46).

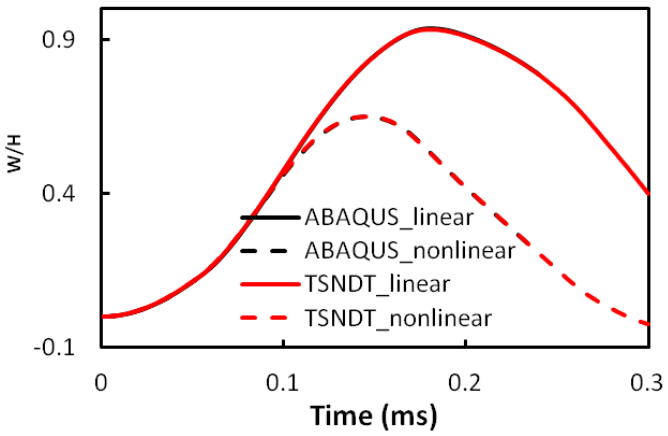

a. Time histories of the deflection of the beam centroid from the linear and the nonlinear theories; for each theory results from the TSNDT and ABAQUS essentially overlap each other.

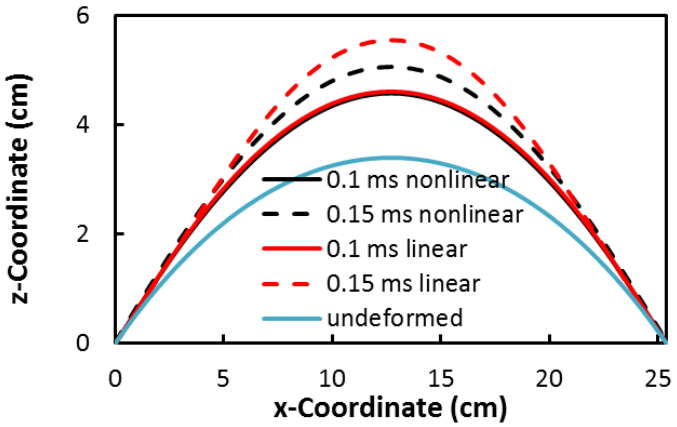

b. Deformed positions of the centroidal axis at t = 0.1 and 0.15 ms from the linear and the nonlinear theories computed using the TSNDT (x and z are global coordinate in this plot)

Fig. 17 Comparison of results computed by using the TSNDT (61 nodes) and ABAQUS with and without considering geometric nonlinearities.

6. Conclusions

A third order shear and normal deformable beam theory (TSNDT) for analyzing finite deformations of a curved laminated beam made of a St. Venant-Kirchhoff material has been developed. It has been used in combination with the finite element method (FEM) to analyze static and dynamic deformations of straight and curved beams by considering all geometric nonlinear effects. Equations governing deformations of the

beam are written in the Lagrangian description of motion using continuum mechanics principles, and a weak form of the governing equations has been derived. No shear correction factor is used, and stresses are derived from the displacement field and the constitutive relation without using any post-processing technique. The method of manufactured solutions has been used to verify the in-house developed software capable of analyzing static and dynamic problems. Furthermore, for both straight and curved beams, deflections and stresses computed using the TSNDT for linear and nonlinear theories agree very well with those obtained using the commercial FE software ABAQUS that analyzes plane strain deformations of the beam modeled as a continuum. For a curved beam made of a homogeneous and isotropic material and radius of curvature/beam thickness = 10, it is found that the maximum transverse deflections and axial stresses at critical points computed using the linear theory are nearly 60% and 40% more than those obtained from the nonlinear theory. However, the transverse shear stresses from the linear theory equal about 86% of those from the nonlinear theory. Thus a stress based failure criterion will predict premature failure of the beam if stresses are derived from the linear elasticity theory.

Appendix A

Expressions of non-zero terms of M_{mn}^{j} are listed below.

$$M_{11}^{j} = C_{1111}^{1jb}e_{11}^{b}+C_{1133}^{1jb}e_{33}^{b} + C_{1111}^{3jbd}\,\frac{1}{2}\eta_{11}^{bd}+C_{1133}^{3jbd}\,\frac{1}{2}\eta_{33}^{bd} + C_{1111}^{4jib}e_{11}^{i}e_{11}^{b} + C_{1133}^{4jib}e_{11}^{i}e_{33}^{b}$$
$$+C_{3113}^{4jib}e_{13}^{i}e_{13}^{b} + C_{3131}^{4jib}e_{13}^{i}e_{31}^{b} + C_{1111}^{6jibd}\,\frac{1}{2}e_{11}^{i}\eta_{11}^{bd} + C_{1133}^{6jibd}\,\frac{1}{2}e_{11}^{i}\eta_{33}^{bd} + C_{3113}^{6jibd}\,e_{13}^{i}\eta_{13}^{bd}$$

$$M_{33}^{j} = C_{3311}^{1jb}e_{11}^{b} + C_{3333}^{1jb}e_{33}^{b} + C_{3311}^{3jbd}\,\frac{1}{2}\eta_{11}^{bd} + C_{3333}^{3jbd}\,\frac{1}{2}\eta_{33}^{bd} + C_{3311}^{4jib}e_{33}^{i}e_{11}^{b} + C_{3333}^{4jib}e_{33}^{i}e_{33}^{b} \quad \text{(A.1)}$$
$$+C_{1313}^{4jib}e_{31}^{i}e_{13}^{b} + C_{1331}^{4jib}e_{31}^{i}e_{31}^{b} + C_{3311}^{6jibd}\,\frac{1}{2}e_{33}^{i}\eta_{11}^{bd} + C_{3333}^{6jibd}\,\frac{1}{2}e_{33}^{i}\eta_{33}^{bd} + C_{1313}^{6jibd}\,e_{31}^{i}\eta_{13}^{bd}$$

$$M_{13}^{j} = C_{1313}^{1jb}e_{13}^{b} + C_{1331}^{1jb}e_{31}^{b} + C_{1313}^{3jbd}\,\eta_{13}^{bd} + C_{3311}^{4jib}e_{13}^{i}e_{11}^{b} + C_{3333}^{4jib}e_{13}^{i}e_{33}^{b} + C_{1331}^{4jib}e_{11}^{i}e_{31}^{b}$$
$$+C_{1313}^{4jib}e_{11}^{i}e_{13}^{b} + C_{3311}^{6jibd}\,\frac{1}{2}e_{13}^{i}\eta_{11}^{bd} + C_{3333}^{6jibd}\,\frac{1}{2}e_{13}^{i}\eta_{33}^{bd} + C_{1313}^{6jibd}\,e_{11}^{i}\eta_{13}^{bd}$$

$$M_{31}^{j} = C_{3113}^{1jb}e_{13}^{b} + C_{3131}^{1jb}e_{31}^{b} + C_{3113}^{3jbd}\,\eta_{13}^{bd} + C_{1111}^{4jib}e_{31}^{i}e_{11}^{b} + C_{1133}^{4jib}e_{31}^{i}e_{33}^{b} + C_{3131}^{4jib}e_{33}^{i}e_{31}^{b}$$
$$+C_{3113}^{4jib}e_{33}^{i}e_{13}^{b} + C_{1111}^{6jibd}\,\frac{1}{2}e_{31}^{i}\eta_{11}^{bd} + C_{1133}^{6jibd}\,\frac{1}{2}e_{31}^{i}\eta_{33}^{bd} + C_{3113}^{6jibd}\,e_{33}^{i}\eta_{13}^{bd}$$

Here $i, j, b, d = 0,1,2,3$

For the beam made of an isotropic material with Young's modulus E and Poisson's ratio υ, we set

$$\mu_0 = \frac{E(1-\upsilon)}{(1-2\upsilon)(1+\upsilon)}, \mu_1 = \frac{E\upsilon}{(1-2\upsilon)(1+\upsilon)}, \mu_2 = \frac{E1}{2(1+\upsilon)} \tag{A.2}$$

When the beam is either straight or the curved beam is thin enough to neglect through-the-thickness variation of H_1, Eqs. (A.1) are simplified into Eq. (A.3).

$$\begin{aligned}
M_{11}^j &= C^{2jb}\left(\mu_0 e_{11}^b + \mu_1 e_{33}^b\right) + C^{3jbd}\left(\frac{1}{2}\mu_0\eta_{11}^{bd} + \frac{1}{2}\mu_1\eta_{33}^{bd} + \mu_0 e_{11}^b e_{11}^d + \mu_1 e_{11}^b e_{33}^d\right. \\
&\quad \left. + \mu_2 e_{13}^b e_{13}^d + \mu_2 e_{13}^b e_{31}^d\right) + C^{4jibd}\left(\frac{1}{2}\mu_0 e_{11}^i\eta_{11}^{bd} + \mu_1\frac{1}{2}e_{11}^i\eta_{33}^{bd} + \mu_2 e_{13}^i\eta_{13}^{bd}\right) \\
M_{33}^j &= C^{2jb}\left(\mu_1 e_{11}^b + \mu_0 e_{33}^b\right) + C^{3jbd}\left(\mu_1\frac{1}{2}\eta_{11}^{bd} + \mu_0\frac{1}{2}\eta_{33}^{bd} + \mu_1 e_{33}^b e_{11}^d + \mu_0 e_{33}^b e_{33}^d\right. \\
&\quad \left. + \mu_2 e_{31}^b e_{13}^d + \mu_2 e_{31}^b e_{31}^d\right) + C^{4jibd}\left(\mu_1\frac{1}{2}e_{33}^i\eta_{11}^{bd} + \frac{1}{2}\mu_0 e_{33}^i\eta_{33}^{bd} + \mu_2 e_{31}^i\eta_{13}^{bd}\right) \\
M_{13}^j &= C^{2jb}\,\mu_2\left(e_{13}^b + e_{31}^b\right) + C^{3jbd}\left(\mu_2\eta_{13}^{bd} + \mu_1 e_{13}^b e_{11}^d + \mu_0 e_{13}^b e_{33}^d + \mu_2 e_{11}^b e_{31}^d + \mu_2 e_{11}^b e_{13}^d\right) \\
&\quad + C^{4jibd}\left(\mu_1\frac{1}{2}e_{13}^i\eta_{11}^{bd} + \frac{1}{2}\mu_0 e_{13}^i\eta_{33}^{bd} + \mu_2 e_{11}^i\eta_{13}^{bd}\right) \\
M_{31}^j &= C^{2jb}\,\mu_2\left(e_{13}^b + e_{31}^b\right) + C^{3jbd}\left(\mu_2\eta_{13}^{bd} + \mu_0 e_{31}^b e_{11}^d + \mu_1 e_{31}^b e_{33}^d + \mu_2 e_{33}^b e_{31}^d +\right. \\
&\quad \left. \mu_2 e_{33}^b e_{13}^d\right) + C^{4jibd}\left(\mu_0\frac{1}{2}e_{31}^i\eta_{11}^{bd} + \mu_1\frac{1}{2}e_{31}^i\eta_{33}^{bd} + \mu_2 e_{33}^i\eta_{13}^{bd}\right)
\end{aligned}$$

where

$$\begin{aligned}
C^{2jb} &= \int_{-\mathrm{H}/2}^{\mathrm{H}/2} L_j L_b\, dy_3 = I^{j+b} \\
C^{3jbd} &= \int_{-\mathrm{H}/2}^{\mathrm{H}/2} L_j L_b L_d\, dy_3 = I^{j+b+d} \\
C^{4jibd} &= \int_{-\mathrm{H}/2}^{\mathrm{H}/2} L_j L_i L_b L_d\, dy_3 = I^{j+i+b+d}
\end{aligned} \tag{A.4}$$

$$I^\theta = \int_{-\mathrm{H}/2}^{\mathrm{H}/2} z^\theta\, dy_3,\ \theta = 0,1,\cdots 12$$

The seven non-zero terms of I^θ are

$$I^0 = \mathrm{H}\,, I^2 = \frac{\mathrm{H}^3}{12}, I^4 = \frac{\mathrm{H}^5}{80}, I^6 = \frac{\mathrm{H}^7}{448}, I^8 = \frac{\mathrm{H}^9}{2304}, I^{10} = \frac{\mathrm{H}^{11}}{11264}\,, I^{12} = \frac{\mathrm{H}^{13}}{53248} \tag{A.5}$$

In order to explicitly write constitutive equations (A.3) for the first order shear and normal deformable plate theory (FSNDT) for a thin shell made of an isotropic and homogeneous material, we set

$$\epsilon_{11}^{b} = \mu_0 e_{11}^{b} + \mu_1 e_{33}^{b}\ ,\ \epsilon_{33}^{b} = \mu_1 e_{11}^{b} + \mu_0 e_{33}^{b},\ \epsilon_{13}^{b} = \epsilon_{31}^{b} = \mu_2\left(e_{13}^{b} + e_{31}^{b}\right)$$

$$\Upsilon_{11}^{\mathrm{bd}} = \tfrac{1}{2}\mu_0\eta_{11}^{bd} + \tfrac{1}{2}\mu_1\eta_{33}^{bd} + \mu_0 e_{11}^{b}e_{11}^{d} + \mu_1 e_{11}^{b}e_{33}^{d} + \mu_2 e_{13}^{b}e_{13}^{d} + \mu_2 e_{13}^{b}e_{31}^{d}$$

$$\Upsilon_{33}^{\mathrm{bd}} = \mu_1\tfrac{1}{2}\eta_{11}^{bd} + \tfrac{1}{2}\mu_0\eta_{33}^{bd} + \mu_1 e_{33}^{b}e_{11}^{d} + \mu_0 e_{33}^{b}e_{33}^{d} + \mu_2 e_{31}^{b}e_{13}^{d} + \mu_2 e_{31}^{b}e_{31}^{d}$$

$$\Upsilon_{13}^{\mathrm{bd}} = \mu_2\eta_{13}^{bd} + \mu_1 e_{13}^{b}e_{11}^{d} + \mu_0 e_{13}^{b}e_{33}^{d} + \mu_2 e_{11}^{b}e_{31}^{d} + \mu_2 e_{11}^{b}e_{13}^{d} \qquad \text{(A.6)}$$

$$\Upsilon_{31}^{\mathrm{bd}} = \mu_2\eta_{13}^{bd} + \mu_0 e_{31}^{b}e_{11}^{d} + \mu_1 e_{31}^{b}e_{33}^{d} + \mu_2 e_{33}^{b}e_{31}^{d} + \mu_2 e_{33}^{b}e_{13}^{d}$$

$$\chi_{11}^{\mathrm{ibd}} = \mu_0\tfrac{1}{2}e_{11}^{i}\eta_{11}^{bd} + \mu_1\tfrac{1}{2}e_{11}^{i}\eta_{33}^{bd} + \mu_2 e_{13}^{i}\eta_{13}^{bd}$$

$$\chi_{33}^{\mathrm{ibd}} = \mu_1\tfrac{1}{2}e_{33}^{i}\eta_{11}^{bd} + \tfrac{1}{2}\mu_0 e_{33}^{i}\eta_{33}^{bd} + \mu_2 e_{31}^{i}\eta_{13}^{bd}$$

$$\chi_{13}^{\mathrm{ibd}} = \mu_1\tfrac{1}{2}e_{13}^{i}\eta_{11}^{bd} + \tfrac{1}{2}\mu_0 e_{13}^{i}\eta_{33}^{bd} + \mu_2 e_{11}^{i}\eta_{13}^{bd}$$

$$\chi_{31}^{\mathrm{ibd}} = \mu_0\tfrac{1}{2}e_{31}^{i}\eta_{11}^{bd} + \mu_1\tfrac{1}{2}e_{31}^{i}\eta_{33}^{bd} + \mu_2 e_{33}^{i}\eta_{13}^{bd}$$

where $\chi_{\mathrm{mn}}^{\mathrm{ibd}} = \chi_{\mathrm{mn}}^{\mathrm{idb}},\ m,n = 1,3.$

Thus constitutive equations (A.3) for the FSNDT become

$$M_{mn}^{0} = I^{0}\left(\epsilon_{mn}^{0} + \Upsilon_{\mathrm{mn}}^{00} + \chi_{\mathrm{mn}}^{000}\right) + I^{2}\left(\Upsilon_{\mathrm{mn}}^{11} + +\chi_{\mathrm{mn}}^{011} + 2\chi_{\mathrm{mn}}^{101}\right) \qquad \text{(A.7)}$$

$$M_{mn}^{1} = I^{2}\left(\epsilon_{mn}^{1} + \Upsilon_{\mathrm{mn}}^{01} + \Upsilon_{\mathrm{mn}}^{10} + \chi_{\mathrm{mn}}^{100} + 2\chi_{\mathrm{mn}}^{010}\right) + I^{4}\,\chi_{\mathrm{mn}}^{111}$$

where indices $m,n = 1,3$, and those for the TSNDT can be simplified into the following expressions.

$$M_{mn}^{0} = I^{0}\left(\epsilon_{mn}^{0} + \Upsilon_{\mathrm{mn}}^{00} + \chi_{\mathrm{mn}}^{000}\right) + I^{2}\left(\epsilon_{mn}^{2} + \Upsilon_{\mathrm{mn}}^{11} + \Upsilon_{\mathrm{mn}}^{20} + \Upsilon_{\mathrm{mn}}^{02} + 2\chi_{\mathrm{mn}}^{002} + \chi_{\mathrm{mn}}^{011} + 2\chi_{\mathrm{mn}}^{101} + \right.$$

$$\left.\chi_{\mathrm{mn}}^{200}\right) + I^{4}\left(\Upsilon_{\mathrm{mn}}^{13} + \Upsilon_{\mathrm{mn}}^{31} + \Upsilon_{\mathrm{mn}}^{22} + \chi_{\mathrm{mn}}^{022} + 2\chi_{\mathrm{mn}}^{031} + 2\chi_{\mathrm{mn}}^{130} + 2\chi_{\mathrm{mn}}^{121} + 2\chi_{\mathrm{mn}}^{220} + \chi_{\mathrm{mn}}^{211} + 2\chi_{\mathrm{mn}}^{310}\right)$$

$$+I^{6}\left(\Upsilon_{\mathrm{mn}}^{33} + \chi_{\mathrm{mn}}^{033} + 2\chi_{\mathrm{mn}}^{123} + \chi_{\mathrm{mn}}^{222} + 2\chi_{\mathrm{mn}}^{231} + 2\chi_{\mathrm{mn}}^{303}\right) + I^{8}\left(2\chi_{\mathrm{mn}}^{323} + \chi_{\mathrm{mn}}^{233}\right)$$

$$M_{mn}^{1} = I^{2}\left(\epsilon_{mn}^{1} + \Upsilon_{\mathrm{mn}}^{01} + \Upsilon_{\mathrm{mn}}^{10} + \chi_{\mathrm{mn}}^{100} + 2\chi_{\mathrm{mn}}^{010}\right) + I^{4}\left(\epsilon_{mn}^{3} + \Upsilon_{\mathrm{mn}}^{21} + \Upsilon_{\mathrm{mn}}^{12} + \Upsilon_{\mathrm{mn}}^{30} + \Upsilon_{\mathrm{mn}}^{03} + \chi_{\mathrm{mn}}^{300} + \right.$$

$$\left.2\chi_{\mathrm{mn}}^{030} + 2\chi_{\mathrm{mn}}^{021} + 2\chi_{\mathrm{mn}}^{120} + \chi_{\mathrm{mn}}^{111} + 2\chi_{\mathrm{mn}}^{210}\right) + I^{6}\left(\Upsilon_{\mathrm{mn}}^{23} + \Upsilon_{\mathrm{mn}}^{32} + 2\chi_{\mathrm{mn}}^{320} + \chi_{\mathrm{mn}}^{311} + 2\chi_{\mathrm{mn}}^{230} + \right.$$

$$2\chi_{\mathrm{mn}}^{212} + 2\chi_{\mathrm{mn}}^{131} + \chi_{\mathrm{mn}}^{122} + 2\chi_{\mathrm{mn}}^{023}) + I^8\left(2\chi_{\mathrm{mn}}^{313} + \chi_{\mathrm{mn}}^{322} + 2\chi_{\mathrm{mn}}^{232} + \chi_{\mathrm{mn}}^{133}\right) \quad \text{(A.8)}$$

$$M_{mn}^2 = I^2\,(\epsilon_{mn}^0 + \Upsilon_{\mathrm{mn}}^{00} + \chi_{\mathrm{mn}}^{000}) + I^4\,(\epsilon_{mn}^2 + \Upsilon_{\mathrm{mn}}^{11} + \Upsilon_{\mathrm{mn}}^{20} + \Upsilon_{\mathrm{mn}}^{02} + 2\chi_{\mathrm{mn}}^{002} + \chi_{\mathrm{mn}}^{011} + 2\chi_{\mathrm{mn}}^{101} + \chi_{\mathrm{mn}}^{200}) + I^6\,(\Upsilon_{\mathrm{mn}}^{13} + \Upsilon_{\mathrm{mn}}^{31} + \Upsilon_{\mathrm{mn}}^{22} + \chi_{\mathrm{mn}}^{022} + 2\chi_{\mathrm{mn}}^{031} + 2\chi_{\mathrm{mn}}^{130} + 2\chi_{\mathrm{mn}}^{121} + 2\chi_{\mathrm{mn}}^{220} + \chi_{\mathrm{mn}}^{211} + 2\chi_{\mathrm{mn}}^{310}) + I^8\,(\Upsilon_{\mathrm{mn}}^{33} + \chi_{\mathrm{mn}}^{033} + 2\chi_{\mathrm{mn}}^{123} + \chi_{\mathrm{mn}}^{222} + 2\chi_{\mathrm{mn}}^{231} + 2\chi_{\mathrm{mn}}^{303}) + I^{10}\,(2\chi_{\mathrm{mn}}^{323} + \chi_{\mathrm{mn}}^{233})$$

$$M_{mn}^3 = I^4\,(\epsilon_{mn}^1 + \Upsilon_{\mathrm{mn}}^{01} + \Upsilon_{\mathrm{mn}}^{10} + \chi_{\mathrm{mn}}^{100} + 2\chi_{\mathrm{mn}}^{010}) + I^6\,(\epsilon_{mn}^3 + \Upsilon_{\mathrm{mn}}^{21} + \Upsilon_{\mathrm{mn}}^{12} + \Upsilon_{\mathrm{mn}}^{30} + \Upsilon_{\mathrm{mn}}^{03} + \chi_{\mathrm{mn}}^{300} + 2\chi_{\mathrm{mn}}^{030} + 2\chi_{\mathrm{mn}}^{021} + 2\chi_{\mathrm{mn}}^{120} + \chi_{\mathrm{mn}}^{111} + 2\chi_{\mathrm{mn}}^{210}) + I^8\,(\Upsilon_{\mathrm{mn}}^{23} + \Upsilon_{\mathrm{mn}}^{32} + 2\chi_{\mathrm{mn}}^{320} + \chi_{\mathrm{mn}}^{311} + 2\chi_{\mathrm{mn}}^{230} + 2\chi_{\mathrm{mn}}^{212} + 2\chi_{\mathrm{mn}}^{131} + \chi_{\mathrm{mn}}^{122} + 2\chi_{\mathrm{mn}}^{023}) + I^{10}\,(2\chi_{\mathrm{mn}}^{313} + \chi_{\mathrm{mn}}^{322} + 2\chi_{\mathrm{mn}}^{232} + \chi_{\mathrm{mn}}^{133}) + I^{12}\,\chi_{\mathrm{mn}}^{333}$$

where $m, n = 1,3$.

Appendix B

Expressions of components of $[\kappa]$ are listed below.

$$k_{11}^{jb} = C_{1111}^{1jb} + C_{1111}^{3jib} e_{11}^{i} + 2C_{1111}^{4jib} e_{11}^{i} + C_{1133}^{4jib} e_{33}^{i} + C_{1111}^{6jbid}\ \tfrac{1}{2}\eta_{11}^{id} + C_{1111}^{6jibd}\ e_{11}^{i} e_{11}^{d} + C_{1133}^{6jbid}\ \tfrac{1}{2}\eta_{33}^{id} + C_{3113}^{6jibd}\ e_{13}^{i} e_{13}^{d}$$

$$k_{12}^{jb} = C_{1133}^{1jb} + C_{1133}^{3jib} e_{33}^{i} + C_{1133}^{4jib} e_{11}^{i} + C_{1133}^{6jibd}\ e_{11}^{i} e_{33}^{d} + C_{3113}^{6jibd}\ e_{13}^{i} e_{31}^{d}$$

$$k_{13}^{jb} = C_{1133}^{3jib} e_{13}^{i} + 2C_{3113}^{4jib} e_{13}^{i} + C_{3131}^{4jib} e_{31}^{i} + C_{1133}^{6jibd}\ e_{11}^{i} e_{13}^{d} + C_{3113}^{6jbid}\ \eta_{13}^{id} + C_{3113}^{6jibd}\ e_{13}^{i} e_{11}^{d}$$

$$k_{14}^{jb} = C_{1111}^{3jib} e_{31}^{i} + C_{3131}^{4jib} e_{13}^{i} + C_{1111}^{6jibd}\ \tfrac{1}{2} e_{11}^{i} e_{31}^{d} + C_{3113}^{6jibd}\ e_{13}^{i} e_{33}^{b}$$

$$\kappa_{21}^{jb} = C_{3311}^{1jb} + C_{3311}^{3jbd}\ e_{11}^{d} + C_{3311}^{4jib} e_{33}^{i} + C_{3311}^{6jibd}\ e_{33}^{i} e_{11}^{d} + C_{1313}^{6jibd}\ e_{31}^{i} e_{13}^{d}$$

$$\kappa_{22}^{jb} = C_{3333}^{1jb} + C_{3333}^{3jbd}\ e_{33}^{d} + C_{3311}^{4jbi} e_{11}^{i} + 2C_{3333}^{4jib} e_{33}^{i} + C_{3311}^{6jibd}\ \tfrac{1}{2}\eta_{11}^{bd} + C_{3333}^{6jbid}\ \tfrac{1}{2}\eta_{33}^{bd} + C_{3333}^{6jibd}\ e_{33}^{i} e_{33}^{d} + C_{1313}^{6jibd}\ e_{31}^{i} e_{31}^{d}$$

$$\kappa_{23}^{jb} = C_{3333}^{3jbd}\ e_{13}^{d} + C_{1313}^{4jib} e_{31}^{i} + 2C_{1331}^{4jib} e_{31}^{i} + C_{3333}^{6jibd}\ e_{33}^{i} e_{13}^{d} + C_{1313}^{6jibd}\ e_{31}^{i} e_{11}^{d}$$

$$\kappa_{24}^{jb} = C_{3311}^{3jbd}\ e_{31}^{d} + C_{1313}^{4jbi} e_{13}^{i} + C_{3311}^{6jibd}\ e_{33}^{i} e_{31}^{d} + C_{1313}^{6jbid}\ \eta_{13}^{id} + C_{1313}^{6jibd}\ e_{31}^{i} e_{33}^{d}$$

$$\kappa_{31}^{jb} = C_{1313}^{3jbd}\ e_{13}^{d} + C_{3311}^{4jib} e_{13}^{i} + C_{1331}^{4jbi} e_{31}^{i} + C_{1313}^{4jbi} e_{13}^{i} + C_{3311}^{6jibd}\ e_{13}^{i} e_{11}^{d} + C_{1313}^{6jbid}\ \eta_{13}^{id} + C_{1313}^{6jibd}\ e_{11}^{i} e_{13}^{d}$$

$$\kappa_{32}^{jb} = C_{1313}^{3jdb}\ e_{31}^{d} + C_{3333}^{4jib} e_{13}^{i} + C_{3333}^{6jibd}\ e_{13}^{i} e_{33}^{d} + C_{1313}^{6jibd}\ e_{11}^{i} e_{31}^{d}$$

$$\kappa_{33}^{jb} = C_{1313}^{1jb} + C_{1313}^{3jdb}\, e_{11}^{d} + C_{3311}^{4jbi} e_{11}^{i} + C_{3333}^{4jbi} e_{33}^{i} + C_{1313}^{4jib} e_{11}^{i} + C_{3311}^{6jbid}\, \frac{1}{2}\eta_{11}^{id} + C_{3333}^{6jbid}\, \frac{1}{2}\eta_{33}^{id} + C_{3333}^{6jibd}\, e_{13}^{i} e_{13}^{d} + C_{1313}^{6jibd}\, e_{11}^{i} e_{11}^{d}$$

$$\kappa_{34}^{jb} = C_{1331}^{1jb} + C_{1313}^{3jbd}\, e_{33}^{d} + C_{1331}^{4jib} e_{11}^{i} + C_{3311}^{6jibd}\, e_{13}^{i} e_{31}^{d} + C_{1313}^{6jibd}\, e_{11}^{i} e_{33}^{d}$$

$$\kappa_{41}^{jb} = C_{3113}^{3jbd}\, e_{13}^{d} + C_{1111}^{4jib} e_{31}^{i} + C_{1111}^{6jibd}\, e_{31}^{i} e_{11}^{d} + C_{3113}^{6jibd}\, \frac{1}{2} e_{33}^{i} e_{13}^{d}$$

$$\kappa_{42}^{jb} = C_{3113}^{3jbd}\, e_{31}^{d} + C_{1133}^{4jib} e_{31}^{i} + C_{3131}^{4jbi} e_{31}^{i} + C_{3113}^{4jib} e_{13}^{i} + C_{1133}^{6jibd}\, e_{31}^{i} e_{33}^{d} + C_{3113}^{6jbid}\, \frac{1}{2}\eta_{13}^{id} + C_{3113}^{6jibd}\, \frac{1}{2} e_{33}^{i} e_{31}^{d}$$

$$\kappa_{43}^{jb} = C_{3113}^{1jb} + C_{3113}^{3jdb}\, e_{11}^{d} + C_{3113}^{4jib} e_{33}^{i} + C_{1111}^{6jibd}\, e_{31}^{i} e_{31}^{d} + C_{1133}^{6jibd}\, e_{31}^{i} e_{13}^{d} + C_{3113}^{6jibd}\, \frac{1}{2} e_{33}^{i} e_{11}^{d}$$

$$\kappa_{44}^{jb} = C_{3131}^{1jb} + C_{3113}^{3jbd}\, e_{33}^{d} + C_{1111}^{4jbi} e_{11}^{i} + C_{1133}^{4jbi} e_{33}^{i} + C_{3131}^{4jib} e_{33}^{i} + C_{1111}^{6jbid}\, \frac{1}{2}\eta_{11}^{id} + C_{1133}^{6jbid}\, \frac{1}{2}\eta_{33}^{id} + C_{3113}^{6jibd}\, \frac{1}{2} e_{33}^{i} e_{33}^{d}$$

Here $i, j, b, d = 0,1,2,3$.

References

1. Carrera E., *Historical review of zig-zag theories for multilayered plates and shells.* Applied mechanics reviews, 2003. **56**(3): p. 287-308.
2. Reddy J.N. and R.A. Arciniega, *Shear deformation plate and shell theories: from Stavsky to present.* Mechanics of Advanced Materials and Structures, 2004. **11**(6): p. 535-582.
3. Kant T. and K. Swaminathan, *Estimation of transverse/interlaminar stresses in laminated composites–a selective review and survey of current developments.* Composite Structures, 2000. **49**(1): p. 65-75.
4. Reissner E., *The effect of transverse shear deformation on the bending of elastic plates.* Journal of Applied Mechanics, 1945. **12**(2): p. 69-77.
5. Mindlin R.D., *Influence of rotatory inertia and shear on flexural motions of isotropic, elastic plates.* Journal of Applied Mechanics, 1951. **18**(1): p. 31-38.
6. Reddy J.N. and C.F. Liu, *A higher-order shear deformation theory of laminated elastic shells.* International Journal of Engineering Science, 1985. **23**(3): p. 319-330.
7. Lekhnitskii S.G., *Strength calculation of composite beams.* Vestnik inzhen i tekhnikov, 1935. **9**.
8. Ren J.G., *A new theory of laminated plate.* Composites science and technology, 1986. **26**(3): p. 225-239.
9. Ren J.G., *Bending theory of laminated plate.* Composites science and technology, 1986. **27**(3): p. 225-248.

10. Ren J.G. and D.R.J. Owen, *Vibration and buckling of laminated plates.* International Journal of Solids and Structures, 1989. **25**(2): p. 95-106.
11. Ambartsumyan S.A., *Theory of anisotropic shells.* 1964.
12. Whitney J.M., *The effect of transverse shear deformation on the bending of laminated plates.* Journal of Composite Materials, 1969. **3**(3): p. 534-547.
13. Reissner E., *On a mixed variational theorem and on shear deformable plate theory.* International journal for numerical methods in engineering, 1986. **23**(2): p. 193-198.
14. Koiter W.T. *A consistent first approximation in the general theory of thin elastic shells*. in *Proc. IUTAM Symposium on the Theory on Thin Elastic Shells*. 1960.
15. Rybov A.F., *Fundamental equations of the theory of multilayered shells taking account of transverse shear strain.* Strength of Materials and Theory of Structures [in Russian], 1964. **3**.
16. Rybov A.F., *On the theory multilayered shell shells with filler*, in *Air Force Construction and Air Force Engeering*1967: Izd Khakosvsk, Univ, Kharkov.
17. Rasskazov A.O., *Theory of multilayer orthotropic shallow shells.* International Applied Mechanics, 1976. **12**(11): p. 1131-1136.
18. Carrera E. and E. Antona, *A class of two-dimensional theories for anisotropic multilayered plates analysis.* 1995. **19**: p. 1-39.
19. Carrera E., *Mixed layer-wise models for multilayered plates analysis.* Composite Structures, 1998. **43**(1): p. 57-70.
20. Di Sciuva M., *An improved shear-deformation theory for moderately thick multilayered anisotropic shells and plates.* Journal of Applied mechanics, 1987. **54**: p. 589-596.
21. Cho M. and R.R. Parmerter, *An efficient higher-order plate theory for laminated composites.* Composite Structures, 1992. **20**(2): p. 113-123.
22. Zhen W. and C. Wanji, *A global-local higher order theory for multilayered shells and the analysis of laminated cylindrical shell panels.* Composite Structures, 2008. **84**(4): p. 350-361.
23. Batra R.C. and S. Vidoli, *Higher-order piezoelectric plate theory derived from a three-dimensional variational principle.* AIAA journal, 2002. **40**(1): p. 91-104.
24. Vidoli S. and R.C. Batra, *Derivation of plate and rod equations for a piezoelectric body from a mixed three-dimensional variational principle.* Journal of elasticity, 2000. **59**(1): p. 23-50.
25. Demasi L., *Refined multilayered plate elements based on Murakami zig–zag functions.* Composite Structures, 2005. **70**(3): p. 308-316.
26. Carrera E., *Theories and finite elements for multilayered, anisotropic, composite plates and shells.* Archives of Computational Methods in Engineering, 2002. **9**(2): p. 87-140.
27. Vel S.S. and R.C. Batra, *The generalized plane strain deformations of thick anisotropic composite laminated plates.* International Journal of Solids and Structures, 2000. **37**(5): p. 715-733.
28. Batra R.C. and S.S. Vel, *Closure to'The generalized plane strain deformations of thick anisotropic composite laminated plates'.* International Journal of Solids and Structures(UK), 2001. **38**(3): p. 483-489.

29. Vel S.S. and R.C. Batra, *Analytical solution for rectangular thick laminated plates subjected to arbitrary boundary conditions.* AIAA journal, 1999. **37**(11): p. 1464-1473.
30. Reddy J.N., *Mechanics of laminated composite plates and shells: theory and analysis.*2004: CRC.
31. Dvorkin E.N. and K.J. Bathe, *A continuum mechanics based four-node shell element for general nonlinear analysis.* Engineering computations, 1984. **1**(1): p. 77-88.
32. Arciniega R.A. and J.N. Reddy, *Tensor-based finite element formulation for geometrically nonlinear analysis of shell structures.* Computer methods in applied mechanics and engineering, 2007. **196**(4-6): p. 1048-1073.
33. Batra R.C. and X.Q. Liang, *Finite dynamic deformations of smart structures.* Computational mechanics, 1997. **20**(5): p. 427-438.
34. Saada A.S., *Elasticity: theory and applications.*1993, Malabar,FL: Krieger.
35. Lo K.H., R.M. Christensen, and E.M. Wu, *A high-order theory of plate deformation—Part 1: Homogeneous plates.* Journal of Applied mechanics, 1977. **44**: p. 663.
36. Cho M., K.O. Kim, and M.H. Kim, *Efficient higher-order shell theory for laminated composites.* Composite Structures, 1996. **34**(2): p. 197-212.
37. Batra R.C., *Elements of continuum mechanics.*2006: AIAA.
38. Qian L.F. and R.C. Batra, *Three-dimensional transient heat conduction in a functionally graded thick plate with a higher-order plate theory and a meshless local Petrov-Galerkin method.* Computational mechanics, 2005. **35**(3): p. 214-226.
39. Xiao J.R., D.F. Gilhooley, R.C. Batra, J.W. Gillespie, and M.A. Mccarthy, *Analysis of thick composite laminates using a higher-order shear and normal deformable plate theory (HOSNDPT) and a meshless method.* Composites Part B: Engineering, 2008. **39**(2): p. 414-427.
40. Pagano N.J., *Exact solutions for composite laminates in cylindrical bending.* Journal of Composite Materials, 1969. **3**(3): p. 398-411.
41. Ren J.G., *Exact solutions for laminated cylindrical shells in cylindrical bending.* Composites science and technology, 1987. **29**(3): p. 169-187.
42. Icardi U. and R. Ruotolo, *Laminated shell model with second-order expansion of the reciprocals of Lamécoefficients H_α , H_β and interlayer continuities fulfilment.* Composite Structures, 2002. **56**(3): p. 293-313.
43. Xavier P.B., K.H. Lee, and C.H. Chew, *An improved zig-zag model for the bending of laminated composite shells.* Composite Structures, 1993. **26**(3): p. 123-138.

Chapter 2: Analysis of Post-buckling and Delamination in Laminated Composite Beams using CZM and Layer-wise TSNDT

Abstract

A layer-wise third order shear and normal deformable plate/shell theory (TSNDT) incorporating a cohesive zone model (CZM) is used to study the initiation and growth of delamination in straight and curved laminated beams. Upon satisfaction of the delamination criteria at a point on the interface between two layers, displacements there of two abutting points on the interface between the two layers are made discontinuous. Delaminations under mode-I, mode-II and mixed-mode static and transient loadings have been studied. All geometric nonlinearities, including the von Karman nonlinearity, are considered. The material of each layer is assumed to be St. Venant-Kirchhoff for which the second Piola-Kirchhoff stress tensor is a linear function of the Green-St. Venant strain tensor. Example problems studied also include delamination growth during axial buckling of a three-layer beam. It is found that the consideration of inertia forces noticeably delays the buckling load and significantly affects the deformed shape of an axially compressed laminated beam.

***Key words*:** TSNDT, cohesive zone model, delamination, geometric nonlinearities, St. Venant-Kirchhoff material, buckling

1. Introduction

Delamination is a common failure mode in sandwich structures because of low values of the interfacial strength. Methods employed to analyze delamination include linear elastic fracture mechanics (LEFM) such as the virtual crack closure technique [1], the strain energy release rate (SERR) or the J-integral [2], the virtual crack extension [3], and the cohesive zone model (CZM) [4]. Critical ingredients of these methods are the delamination initiation and growth criteria. Here we use the CZM mainly because it is easy to implement in software, one can readily compute the energy dissipated during delamination and relate it to the critical SERR and the interfacial strength. In the CZM surface tractions at a point on an interface are expressed as a non-monotonic function of

the jump in displacements there with the area under the curve equaling the critical SERR. These functions include cubic/exponential [4], bilinear [5], and trapezoidal [6]. Zou et al. [7] proposed a damage surface by combining the conventional stress-based and fracture mechanics-based criteria for mixed-mode failures. A scalar damage parameter is used to describe softening of the interface due to damage induced by delamination growth in laminated composites. Camanho and Dávila [8] described damage of the interface in terms of the mixed-mode relative displacement. Cohesive elements can be either continuum interface elements [9] or nonlinear springs connected to the corresponding nodes [10] on the two sides of the interface.

A layer-wise plate/beam theory can correctly predict through-the-thickness distributions of transverse shear and transverse normal stresses, and delamination can be simulated by using the CZM. For example, Allix and Corigliano [11] studied delamination of a laminated composite beam using the CZM and the layer-wise first order shear deformable beam theory (FSDT) considering all geometric nonlinearities. Zhang and Wang [12] incorporated the layer-wise FSDT and the crack closure method to study delamination growth in laminated composites.

Here we use the CZM and the layer-wise third order shear and normal deformable plate/shell theory (TSNDT) to study delamination in laminated composite beams. As shown by Batra and Xiao [13] the TSNDT correctly predicts all components of surface tractions on the interface. All geometric nonlinearities are considered in our formulation, and the initiation and propagation of delamination under mode-I, mode-II and mixed-mode static and dynamic loading are studied. The 2nd Piola-Kirchhoff stress tensor is expressed as a linear function of the Green-St. Venant strain tensor. Thus a materially objective constitutive relation is employed. Computed results are found to agree well with those available in the literature. Significant contributions of the work include studying post-delamination and post-buckling deformations of beams deformed under quasi-static and dynamic loadings.

The rest of the paper is organized as follows. In Section 2 we summarize governing equations, boundary conditions and the CZM. We derive governing equations and boundary conditions for the TSNDT as well as a weak form of governing equations

in Section 3. We also briefly review in Section 3 the finite element method (FEM) used to numerically solve the problem. Results for the delamination growth in double cantilever beams (DCBs) under pure and mixed-mode static and transient loadings are given in Section 4. The delamination growth in an initially delaminated composite beam under axial compression is also studied in this Section. Conclusions of this work are summarized in Section 5.

2. Formulation of the problem

2.1 Brief review of the continuum theory

2.1.1 Kinematics

A schematic sketch of the problem studied is shown in Fig. 1. The position vector of point p in the reference configuration is described by using orthogonal curvilinear coordinate axes y_1, y_2, y_3 in the reference configuration with y_1-axis along the tangent to the mid-surface of the beam, y_2-axis pointing into the plane of the paper, and y_3-axis pointing along the local thickness direction. Let X_1, X_2, X_3 be fixed rectangular Cartesian coordinate axes, and the y_2-axis be parallel to the X_2- axis. Let position vectors, with respect to fixed rectangular Cartesian coordinate axes, of point p located at (y_1, y_2, y_3) in the reference configuration be $\boldsymbol{x}$ and $\boldsymbol{X}$ in the current and the reference configurations, respectively.

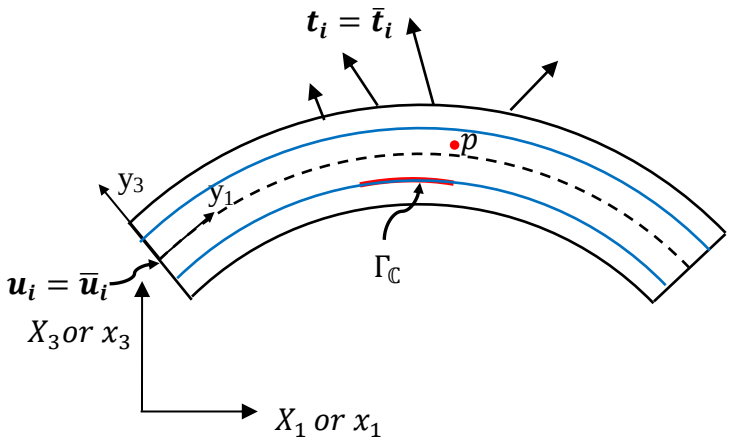

(a)

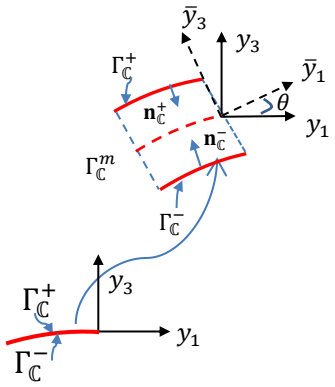

(b)

Fig. 1 Schematic sketches of a curved beam (a) and of cohesive interface $\Gamma_{\mathbb{C}}$ (b). X_2-, x_2- , y_2- and $\bar{y}_2$ -axes pointing into the plane of the paper are not shown in the Fig.

Components, G_{ij}, of the metric tensor in the reference configuration are given by [14]

$$G_{ij} = \boldsymbol{A}_i \cdot \boldsymbol{A}_j \,, \;\; \boldsymbol{A}_i = \frac{\partial \boldsymbol{X}}{\partial y_i} \tag{1}$$

For orthogonal curvilinear coordinate axes the metric tensor, G_{ij}, is non-zero only when $i = j$. We set

$$H_1 = \sqrt{G_{11}}, \quad H_2 = \sqrt{G_{22}} = 1, \quad H_3 = \sqrt{G_{33}} = 1, \tilde{\boldsymbol{e}}_i = \frac{\boldsymbol{A}_i}{H_{(i)}} \text{ (no sum on } i\text{)} \tag{2}$$

Here $(\tilde{\boldsymbol{e}}_1, \tilde{\boldsymbol{e}}_2, \tilde{\boldsymbol{e}}_3)$ are unit base vectors along the y_1, y_2 and y_3 axes, respectively, and

$$H_1 = \left(1 + \frac{y_3}{R}\right), \; \frac{\partial \tilde{\boldsymbol{e}}_1}{\partial y_1} = -\frac{\tilde{\boldsymbol{e}}_3}{R} \,, \; \frac{\partial \tilde{\boldsymbol{e}}_3}{\partial y_1} = \frac{\tilde{\boldsymbol{e}}_1}{R} \tag{3}$$

where R is the radius of curvature at the point (y_1, y_2, y_3).

We study finite plane strain deformations in the X_1X_3- plane, and for simplicity assume that the curved beam is of rectangular cross-section. The displacement $\boldsymbol{u}$ of point p is given by

$$\boldsymbol{u} = \boldsymbol{x} - \boldsymbol{X} \tag{4}$$

where $\boldsymbol{u}$ is a function of y_1 and y_3, and $u_2 = 0$. Physical components of the displacement gradient, $\boldsymbol{F}$, are given by [14]

$$[F] = \begin{bmatrix} 1 + \frac{1}{H_1}\left(\frac{\partial u_1}{\partial y_1} + \frac{u_3}{R}\right) & 0 & \frac{\partial u_1}{\partial y_3} \\ 0 & 1 & 0 \\ \frac{1}{H_1}\left(\frac{\partial u_3}{\partial y_1} - \frac{u_1}{R}\right) & 0 & 1 + \frac{\partial u_3}{\partial y_3} \end{bmatrix} \tag{5}$$

The Green-St. Venant strain tensor, $\boldsymbol{E}$, defined by

$$\boldsymbol{E} = \frac{1}{2}(\boldsymbol{F}^T\boldsymbol{F} - \mathbf{1}) \tag{6}$$

where $\mathbf{1}$ is the identity tensor, has following non-zero physical components:

$$E_{11} = \frac{1}{H_1}\left(\frac{\partial u_1}{\partial y_1} + \frac{u_3}{R}\right) + \frac{1}{2{H_1}^2}\left[\left(\frac{\partial u_1}{\partial y_1} + \frac{u_3}{R}\right)^2 + \left(\frac{\partial u_3}{\partial y_1} - \frac{u_1}{R}\right)^2\right]$$

$$E_{33} = \frac{\partial u_3}{\partial y_3} + \frac{1}{2}\left[\left(\frac{\partial u_1}{\partial y_3}\right)^2 + \left(\frac{\partial u_3}{\partial y_3}\right)^2\right] \tag{7}$$

$$2E_{13} = \frac{1}{H_1}\left(\frac{\partial u_3}{\partial y_1} - \frac{u_1}{R}\right) + \frac{\partial u_1}{\partial y_3} + \frac{1}{H_1}\left[\frac{\partial u_3}{\partial y_3}\left(\frac{\partial u_3}{\partial y_1} - \frac{u_1}{R}\right) + \frac{\partial u_1}{\partial y_3}\left(\frac{\partial u_1}{\partial y_1} + \frac{u_3}{R}\right)\right]$$

We note that $\boldsymbol{E}$ incorporates all geometric nonlinearities including the von Kármán nonlinearity, and is valid for finite (or large) deformations of a beam. The strain tensor for infinitesimal deformations is obtained from Eq. (7) by neglecting the nonlinear terms included in brackets.

2.1.2 Kinetics

The in-plane displacements (u_1, u_3) of a point are governed by the following equations expressing the balance of linear momentum written in the Lagrangian description of motion using physical components $T_{11}, T_{13}, T_{31}, T_{33}$, of the first (not necessarily symmetric) Piola-Kirchhoff stress tensor [14], and initial and boundary conditions.

$$\rho_0 \ddot{u}_1 = \frac{1}{H_1}\frac{\partial T_{11}}{\partial y_1} + \frac{1}{H_1}\frac{\partial (H_1 T_{13})}{\partial y_3} + \frac{1}{H_1 R}T_{31} + f_1 \tag{8.a}$$

$$\rho_0 \ddot{u}_3 = \frac{1}{H_1}\frac{\partial T_{31}}{\partial y_1} + \frac{1}{H_1}\frac{\partial (H_1 T_{33})}{\partial y_3} - \frac{1}{H_1 R}T_{11} + f_3 \tag{8.b}$$

$$u_i(y_1, y_3, 0) = u_i^0(y_1, y_3) \tag{8.a}$$

$$\dot{u}_i(y_1, y_3, 0) = \dot{u}_i^0(y_1, y_3) \tag{8.b}$$

$$T_{ij}N_j^t = \bar{t}_i(y_1, y_3, t) \quad \text{on} \quad \Gamma_t \tag{8.c}$$

$$u_i(y_1, y_3, t) = \bar{u}_i(y_1, y_3, t) \quad \text{on} \quad \Gamma_u \tag{8.d}$$

$$T_{ij}N_j^{\mathbb{C}+} = \bar{f}_i^{\mathbb{C}+}, \; T_{ij}N_j^{\mathbb{C}-} = \bar{f}_i^{\mathbb{C}-} \quad \text{on} \quad \Gamma_{\mathbb{C}} \tag{8.e}$$

$$\bar{f}_1^{\mathbb{C}-} = \hat{a}(\mathbb{R}_{11}\sigma_t + \mathbb{R}_{31}\sigma_n), \; \bar{f}_3^{\mathbb{C}-} = \hat{a}(\mathbb{R}_{13}\sigma_t + \mathbb{R}_{33}\sigma_n), \; \bar{f}_i^{\mathbb{C}+} = -\bar{f}_i^{\mathbb{C}-} \text{ on } \Gamma_{\mathbb{C}} \tag{8.f}$$

$$[\mathbb{R}] = \begin{bmatrix} \cos\theta & 0 & \sin\theta \\ 0 & 1 & 0 \\ -\sin\theta & 0 & \cos\theta \end{bmatrix} \tag{8.g}$$

In Eq. (8) i and j equal 1 and 3, f_1 and f_3 are components of the body force per unit reference volume along the y_1- and the y_3- axes, respectively, ρ_0 the mass density in the reference configuration, and $\ddot{u}_i = \frac{\partial^2 u_i}{\partial t^2}$. The initial displacement u_i^0 and the initial velocity $\dot{u}_i^0$ are known functions of y_1 and y_3. $\boldsymbol{N}^t$ is a unit outward normal in the reference configuration at a point on the boundary Γ_t where surface tractions are prescribed as $\bar{t}_i$. On boundary Γ_u, displacements are prescribed as $\bar{u}_i$. $\boldsymbol{N}^{\mathbb{C}\pm}$ is the outward unit normal on the corresponding interface $\Gamma_{\mathbb{C}}^{\pm}$, $\hat{a}$ equals the area into which a unit surface area in the reference configuration is deformed, $\mathbb{R}_{ij}$ the rotation matrix, θ the angle between y_1- and $\bar{y}_1$- axes, $\bar{f}_i^{\mathbb{C}\pm}$ the traction on the cohesive interface $\Gamma_{\mathbb{C}}^{\pm}$, and σ_t and σ_n the tangential and the normal tractions in the current configuration of the cohesive interface. Tractions σ_t and σ_n are related to jumps in displacements on the cohesive interface as discussed in subsection 2.1.4. As unit normals at corresponding points on the upper and the lower surfaces of a cohesive interface may not be parallel to each other, we use a mean cohesive interface $\Gamma_{\mathbb{C}}^m$ (see Fig. 1) to find surface tractions and jumps in tangential and normal displacements on the cohesive interface. Accordingly, we introduce local coordinate axes $\bar{y}_1$ and $\bar{y}_3$, respectively, along the tangent and the normal to the deformed mean cohesive interface $\Gamma_{\mathbb{C}}^m$. The unit outward normal $\mathbf{n}_{\mathbb{C}}^{\pm}$ on $\Gamma_{\mathbb{C}}^{\pm}$ in the current configuration is found from values of the deformation gradient on the corresponding interface. We assume that the rotation angle θ of the mean cohesive interface $\Gamma_{\mathbb{C}}^m$ equals the average of the rotation angles of unit normals $\mathbf{n}_{\mathbb{C}}^{\pm}$. The deformed area $\hat{a}$ of the mean cohesive interface $\Gamma_{\mathbb{C}}^m$ is taken equal to the average of areas into which

unit areas on $\Gamma_{\mathbb{C}}^{+}$ and $\Gamma_{\mathbb{C}}^{-}$ are deformed. We note that tractions on $\Gamma_{\mathbb{C}}^{+}$ and $\Gamma_{\mathbb{C}}^{-}$ are equal and opposite.

Using the transformation matrix $\mathbb{R}_{ij}$, the jump displacements δ_t and δ_n, of corresponding points on $\Gamma_{\mathbb{C}}^{+}$ and $\Gamma_{\mathbb{C}}^{-}$ are given by

$$\delta_t = \mathbb{R}_{1j}\left(u_j^{+}(y_1, y_3, t) - u_j^{-}(y_1, y_3, t)\right) \text{ on } \Gamma_{\mathbb{C}},\ j = 1,3 \tag{9.a}$$

$$\delta_n = \mathbb{R}_{3j}\left(u_j^{+}(y_1, y_3, t) - u_j^{-}(y_1, y_3, t)\right) \text{ on } \Gamma_{\mathbb{C}},\ j = 1,3 \tag{9.b}$$

where $u_i^{+}(y_1, y_3, t)$ and $u_i^{-}(y_1, y_3, t)$ represent, respectively, displacements of a point on $\Gamma_{\mathbb{C}}^{+}$ and $\Gamma_{\mathbb{C}}^{-}$ with respect to y_1 and y_3 coordinate axes, δ_t and δ_n equal jumps in the tangential and the normal displacements of corresponding points on $\Gamma_{\mathbb{C}}^{+}$ and $\Gamma_{\mathbb{C}}^{-}$ with respect to $\bar{y}_1$ and $\bar{y}_3$ coordinate axes on the mean cohesive interface $\Gamma_{\mathbb{C}}^{m}$.

2.1.3 Constitutive relations

We assume that the beam material is St. Venant-Kirchhoff for which the strain energy density, W, is given by

$$W = \frac{1}{2}E_{ij}C_{ijkl}E_{kl}, C_{ijkl} = C_{klij} = C_{jikl} \tag{10}$$

where $\boldsymbol{C}$ is the fourth-order elasticity tensor having 21 independent components for three-dimensional deformations of a general anisotropic material. The independent components of $\boldsymbol{C}$ with respect to the material principal axes reduce to 9, 5 and 2 for an orthotropic, transversely isotropic and isotropic material, respectively. The strain energy density for the St. Venant-Kirchhoff material reduces to that of a Hookean material if the finite strain tensor $\boldsymbol{E}$ is replaced in Eq. (10) by the strain tensor for infinitesimal deformations. Batra [15] has compared the response of four elastic materials for which a stress tensor is a linear function of an appropriate strain tensor (e.g., the Cauchy stress tensor is a linear function of the Almansi-Hamel strain tensor). For infinitesimal deformations the four constitutive relations give the same stress-strain curve for simple tensile and simple shear deformations, but their predictions for finite deformations are quite different.

For a nonlinear elastic material, physical components of the second Piola-Kirchhoff stress tensor $\boldsymbol{S}$ are related to $\boldsymbol{E}$ by

$$S_{ij} = \frac{\partial W}{\partial E_{ij}} = C_{ijkl}E_{kl} \tag{11}$$

However, $\boldsymbol{S}$ has no physical interpretation. Other stress tensors such as the Cauchy or the 1st Piola-Kirchhoff stress tensor can be determined from $\boldsymbol{S}$ only if the deformation gradient $\boldsymbol{F}$ is known. For plane strain deformations of an orthotropic material with the material principal axes coincident with the coordinate axes (y_1, y_2, y_3), Eq. (11) reduces to

$$\begin{Bmatrix} S_{11} \\ S_{33} \\ S_{13} \end{Bmatrix} = \begin{bmatrix} C_{1111} & C_{1133} & 0 \\ C_{3311} & C_{3333} & 0 \\ 0 & 0 & C_{1313} \end{bmatrix} \begin{Bmatrix} E_{11} \\ E_{33} \\ 2E_{13} \end{Bmatrix} \tag{12.a}$$

$$C_{1111} = \frac{1-\nu_{23}\nu_{32}}{E_2E_3\mathcal{D}}, C_{3333} = \frac{1-\nu_{12}\nu_{21}}{E_1E_2\mathcal{D}}, C_{1133} = C_{3311} = \frac{\nu_{31}+\nu_{21}\nu_{32}}{E_2E_3\mathcal{D}}, C_{1313} = G_{13} \tag{12.b}$$

$$\mathcal{D} = \frac{1}{E_1E_2E_3}\begin{vmatrix} 1 & -\nu_{21} & -\nu_{31} \\ -\nu_{12} & 1 & -\nu_{32} \\ -\nu_{13} & -\nu_{23} & 1 \end{vmatrix} \tag{12.c}$$

Here E_1, E_2 and E_3 represent, respectively, Young's moduli along the y_1-, the y_2- and the y_3-axes, G_{13} is the shear modulus in the y_1y_3-plane, $\upsilon_{12}, \upsilon_{13}$ and υ_{23} are Poisson's ratios.

Recalling that

$$\boldsymbol{T} = \boldsymbol{FS} \tag{13}$$

where $\boldsymbol{T}$ is the 1st Piola-Kirchhoff stress tensor, we get

$$\begin{bmatrix} T_{11} & T_{13} \\ T_{31} & T_{33} \end{bmatrix} = \begin{bmatrix} F_{11}S_{11} + F_{13}S_{13} & F_{11}S_{13} + F_{13}S_{33} \\ F_{31}S_{11} + F_{33}S_{13} & F_{31}S_{13} + F_{33}S_{33} \end{bmatrix} \tag{14}$$

Substitution for $\boldsymbol{F}$ from Eq. (5) into Eq. (14), for $\boldsymbol{E}$ from Eq. (7) into Eq. (12) and the result into Eq. (14) gives expressions for $\boldsymbol{T}$ in terms of displacements u_1 and u_3 and the four elastic constants C_{1111}, C_{1133}, C_{3333}, and C_{1313}. Even though components of $\boldsymbol{S}$ are quadratic in displacement gradients those of $\boldsymbol{T}$ are cubic in displacement gradients. We

note that constitutive relations (11) and (13) are materially objective, i.e., are invariant under a rigid body motion superimposed upon the present configuration.

The true stress or the Cauchy stress, $\boldsymbol{\sigma}$, is related to the 1st Piola-Kirchhoff stress by

$$\boldsymbol{\sigma} = \frac{1}{J}\boldsymbol{T}\boldsymbol{F}^{T}\,, \tag{15}$$

where J is the determinant of the deformation gradient $\boldsymbol{F}$. Thus $\boldsymbol{\sigma}$ need not be a polynomial function of the displacement gradients.

We now substitute for $\boldsymbol{T}$ into Eq. (8), and solve the resulting nonlinear coupled partial differential equations (PDEs) for u_1 and u_3 under pertinent initial and boundary conditions. These PDEs involve second-order derivatives of u_1 and u_3 with respect to y_1 and y_3 and time t.

2.1.4 Cohesive zone model

2.1.4.1 Mode-I or mode-II deformations

We first describe the CZM for mode-I and mode-II deformations, and then for mixed-mode deformations. We postulate the traction-separation relations depicted in Figs. 2a and 2b for mode-I and mode-II deformations, respectively.

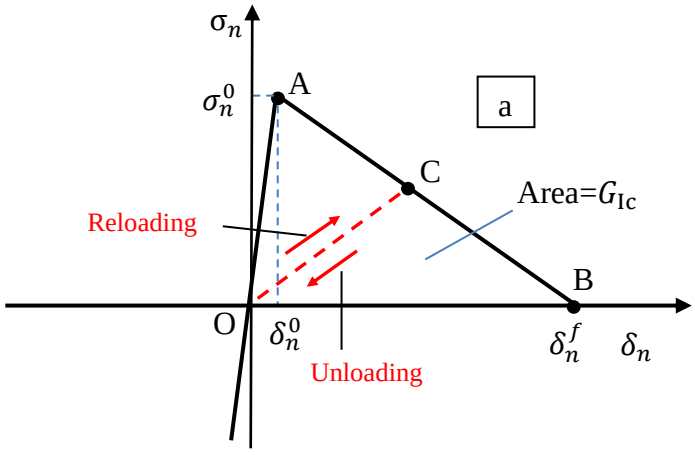

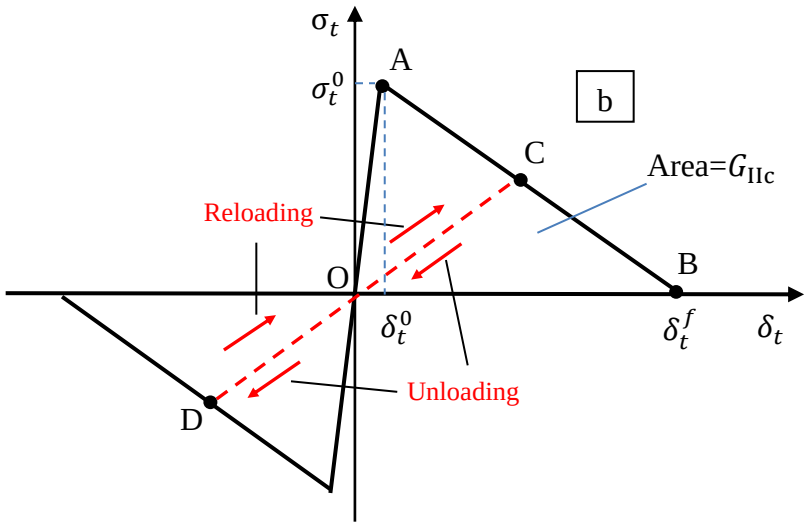

Fig. 2 Traction-separation relations at cohesive interface; (a) mode-I, (b) mode-II

For relative normal (tangential) displacement δ_n (δ_t) of adjoining points on the two sides of the interface less than δ_n^0 (δ_t^0) corresponding to point A in Fig. 2a (Fig. 2b), the traction-separation relation represented by straight line OA is completely reversible. For monotonically increasing values of δ_n (δ_t) greater than δ_n^0 (δ_t^0) the traction-separation relation is given by straight line AB. For $\delta_n = \delta_n^f$ $\left(\delta_t = \delta_t^f\right)$ there is complete separation (sliding) at the interface for mode-I (mode-II) deformations. For mode-I deformations, the separated surfaces are traction free and for mode-II deformations the sliding surfaces are assumed to be smooth or frictionless. Should the relative displacement δ_n (δ_t) exceeding δ_n^0 (δ_t^0) but less than δ_n^f (δ_t^f) begin to decrease, then the traction-separation relation follows the path CO for δ_n and COD for δ_t. The area of the triangle OAB equals the critical strain energy release rate G_{Ic} (G_{IIc}) for mode-I (mode-II) deformations. Values of G_{Ic} (G_{IIc}) and σ_n^0 (σ_t^0) characterize the interface. Here σ_n^0 (σ_t^0) equals the interface strength for mode-I (mode-II) deformations. The slope, k_s, of straight line OA is estimated. Then

$$\sigma_i = k_s \delta_i , \quad i = t \text{ and } n \tag{16.a}$$

$$\delta_i^0 = \frac{\sigma_i^0}{k_s}, \; i = t, n \tag{16.b}$$

where k_s is called the initial interface stiffness.

Thus, the delamination initiates when $\sigma_n = \sigma_n^0$ ($\sigma_t = \sigma_t^0$), and complete separation occurs when

$$\delta_n^f = \frac{2G_{Ic}}{\sigma_n^0},\ \delta_t^f = \frac{2G_{IIc}}{\sigma_t^0} \tag{17}$$

The interface stiffness k_s should be such that it does not make the system of simultaneous equations to be solved ill-conditioned and effectively prevents interpenetration between two contacting layers during compressive normal traction on the interface. For a beam of thickness H we use the relation

$$k_s = \frac{H}{\mathcal{K}} \max(\sigma_n^0, \sigma_t^0) \tag{18}$$

to find k_s, and set the nondimensional parameter $\mathcal{K} = 10^{-9}$.

2.1.4.2 Mixed mode deformations

For mixed-mode deformations, $\delta_n > 0$ and $\delta_t \neq 0$. We follow the approach of Ref. [8], and postulate that the delamination at a point on the interface initiates when

$$\left(\frac{\sigma_n}{\sigma_n^0}\right)^2 + \left(\frac{\sigma_t}{\sigma_t^0}\right)^2 = 1 \tag{19}$$

and complete separation occurs when

$$\left(\frac{G_I}{G_{Ic}}\right)^2 + \left(\frac{G_{II}}{G_{IIc}}\right)^2 = 1 \tag{20}$$

Here σ_n and σ_t are the normal and the tangential tractions on the interface under mixed-mode deformations. Similarly, G_I (G_{II}) are strain energy release rates for mode-I (mode-II) deformations for mixed-mode loading.

We define the equivalent mixed-mode relative displacement δ_e by

$$\delta_e = \sqrt{(\delta_t)^2 + (\delta_n)^2} = \frac{\delta_t}{\mu}\sqrt{1+\mu^2} = \delta_n\sqrt{1+\mu^2} \tag{21}$$

where $\mu\delta_n = \delta_t$, and note that $\mu = 0$ for mode-I, and $\mu \to \infty$ for mode-II deformations .

Assuming that under mixed-mode loading, the interface stiffness for the tangential and normal traction-separation modes also equals k_s, then substituting for σ_n and σ_t in terms of δ_t and δ_n into Eq. (19), the separation will initiate when

$$\left(\frac{\delta_n}{\sigma_n^0}\right)^2 + \left(\frac{\delta_t}{\sigma_t^0}\right)^2 = 1/(k_s)^2 \tag{22}$$

or equivalently,

$$\delta_e^0 = \delta_t^0 \delta_n^0 \sqrt{\frac{1+\mu^2}{(\delta_t^0)^2 + (\mu\delta_n^0)^2}} \tag{23}$$

where δ_t^0 and δ_n^0 are given by Eq. (16.b). We assume that the mode-mixity ratio μ at a point on the interface stays constant during the delamination process, however, the value of μ can vary from point to point. The value of μ at a point is determined at the instant δ_n becomes positive. Thus the mode-mixity at a point is assumed not to change during subsequent deformations at that point.

In order to find the value δ_e^f of δ_e at complete separation, we assume that the effective traction–effective separation relation under mixed-mode loading is also triangular, i.e., similar to that for mode-I and mode-II loadings. Thus values of G_I and G_{II} at complete separation are given by

$$G_I(1+\mu^2) = \frac{k_s \delta_e^0 \, \delta_e^f}{2}, \; G_{II} = \mu^2 G_I \tag{24}$$

Substitution from Eq. (24) into Eq. (20) gives

$$\delta_e^f = \frac{2(1+\mu^2)}{k_s \delta_e^0}\left[\left(\frac{1}{G_{Ic}}\right)^2 + \left(\frac{\mu^2}{G_{IIc}}\right)^2\right]^{-1/2} \tag{25}$$

Because of the assumption of μ staying constant at a point, should unloading occur for $\delta_e^0 < \delta_e < \delta_e^f$, the unloading curve follows a path similar to the straight line CO in Fig. 3a for mode-I deformations.

2.2 Equations for the layerwise TSNDT

2.2.1 Displacement field

For simplicity we consider a 3-layer curved sandwich beam and denote displacements of a point in the top, the central, and the bottom layers by superscripts *t, c* and *b*, respectively. With the origin of the curvilinear coordinate axes located at the geometric centroid of the rectangular cross-section (e.g., see Fig. 3), we assume the following displacement field in the three layers of the beam.

$$u_\alpha^c(y_1, y_3, t) = \sum_{i=0}^{3} (y_3)^i \, \mathcal{u}_{\alpha i}^c(y_1, t), \qquad \alpha = 1, 3, \qquad |y_3| < h^c \tag{26.a}$$

$$u_\alpha^t(y_1, y_3, t) = \mathcal{u}_\alpha^c(y_1, h^c, t) + \mathcal{u}_{\alpha 0}^t(y_1, t) + \sum_{i=1}^{3} \left((y_3)^i - (h^c)^i\right) \mathcal{u}_{\alpha i}^t(y_1, t), \tag{26.b}$$
$$\alpha = 1, 3, \qquad h^c \le y_3 \le h^c + h^t$$

$$u_\alpha^b(y_1, y_3, t) = \mathcal{u}_\alpha^c(y_1, -h^c, t) - \mathcal{u}_{\alpha 0}^b(y_1, t) + \sum_{i=1}^{3} \left((y_3)^i - (-h^c)^i\right) \mathcal{u}_{\alpha i}^b(y_1, t), \tag{26.c}$$
$$\alpha = 1, 3, \quad -(h^b + h^c) \le y_3 \le -h^c$$

Here $\mathcal{u}_{10}^c$ and $\mathcal{u}_{30}^c$ are, respectively, the axial and the transverse displacements of a point on the beam mid-surface, $\mathcal{u}_{\alpha i}^c$, $\mathcal{u}_{\alpha i}^b$ and $\mathcal{u}_{\alpha i}^t (\alpha = 1, 3, \ i = 1, 2, 3)$ may be interpreted as generalized axial and transverse displacements of a point, $\mathcal{u}_{\alpha 0}^t$ and $\mathcal{u}_{\alpha 0}^b (\alpha = 1, 3)$ equal jumps, if any, in displacements at the top and the bottom interfaces, respectively. The bottom interface is between the bottom layer and the core, and the top interface between the top layer and the core. We note that the displacement field given by Eq. (26) allows for the thickness of each layer to change, and incorporates both transverse normal and transverse shear strains. It can be written as

$$u_\alpha(y_1, y_3, t) = \sum_{j=0}^{3} \left(\ell_j^c(y_3) \, \mathcal{u}_{\alpha j}^c(y_1, t) + \ell_j^t(y_3) \, \mathcal{u}_{\alpha j}^t(y_1, t) + \ell_j^b(y_3) \, \mathcal{u}_{\alpha j}^b(y_1, t)\right), \tag{27}$$
$$\alpha = 1,3$$

where

$$\ell_j^c(y_3) = \begin{cases} (h^c)^j, & h^c \le y_3 \le h^c + h^t \\ (y_3)^j, & |y_3| < h^c \\ (-h^c)^j, & -(h^b + h^c) \le y_3 \le -h^c \end{cases}, j = 0,1,2,3 \quad (28.a)$$

$$\ell_j^t(y_3) = \begin{cases} (y_3)^j - (h^c)^j, & h^c \le y_3 \le h^c + h^t \\ 0, & -(h^b + h^c) \le y_3 \le h^c \end{cases}, j = 1,2,3 \quad (28.b)$$

$$\ell_j^b(y_3) = \begin{cases} 0, & -h^c \le y_3 \le h^c + h^t \\ (y_3)^j - (-h^c)^j, & -(h^b + h^c) \le y_3 \le -h^c \end{cases}, j = 1,2,3 \quad (28.c)$$

$$\ell_0^t(y_3) = \begin{cases} 1, & h^c \le y_3 \le h^c + h^t \\ 0, & -(h^b + h^c) \le y_3 \le h^c \end{cases}, \ell_0^b = \begin{cases} 0, & -h^c \le y_3 \le h^c + h^t \\ -1, & -(h^b + h^c) \le y_3 \le -h^c \end{cases} \quad (28.d)$$

We can thus rewrite Eq. (26) as

$$u_\alpha(y_1, y_3, t) = \sum_{j=1}^{12} L_j(y_3)\, u_{\alpha j}(y_1, t), \alpha = 1,3 \quad (29)$$

where

$$L_j = \begin{cases} \ell_{j-1}^c, j = 1,2,3,4 \\ \ell_{j-5}^t, j = 5,6,7,8 \\ \ell_{j-9}^b, j = 9,10,11,12 \end{cases} ; \quad u_{\alpha j} = \begin{cases} u_{\alpha(j-1)}^c, & j = 1,2,34 \\ u_{\alpha(j-5)}^t, & j = 5,6,7,8 \\ u_{\alpha(j-9)}^b, & j = 9,10,11,12 \end{cases} \quad (30)$$

Displacements δ_n and δ_t at the interface between the top layers and the core appearing in Eq. (16.a) are related to the displacement field $u_\alpha(y_1, y_3, t)$ by substituting from Eq. (29) into Eq. (9). Thus

$$\delta_t = \mathbb{R}_{1\alpha} u_{\alpha 0}^t, \ \delta_n = \mathbb{R}_{3\alpha} u_{\alpha 0}^t, \ \alpha = 1,3, \text{ summed on } \alpha \quad (31)$$

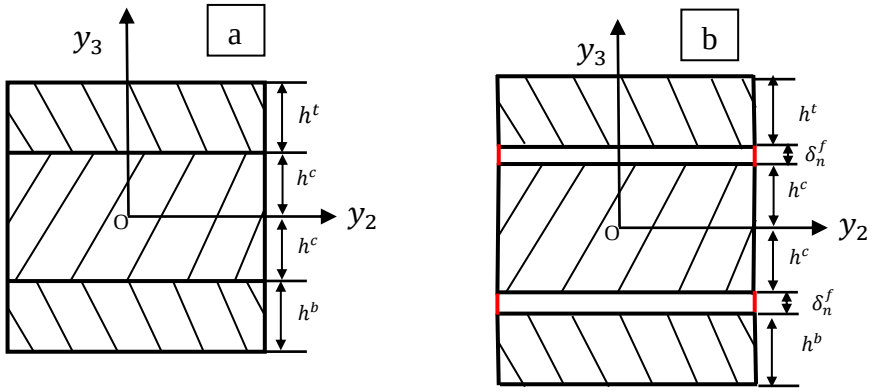

Fig. 3 Cross-section of a 3-layer beam ((a) before delamination, (b) after separation)

2.2.2 Governing equations

We multiply both sides of Eq. (8a,b) with $L_j(y_3)$ (j = 1, 2,…, 12), integrate both sides of the resulting equation over the beam thickness (i.e., with respect to y_3), and obtain

$$\begin{aligned}\int_{-h^c-h^b}^{h^c+h^t} L_j(y_3)\rho_0\ddot{u}_1 H_1 dy_3 &= \int_{-h^c-h^b}^{h^c+h^t} L_j(y_3)\left[\frac{\partial T_{11}}{\partial y_1}+\frac{\partial(H_1T_{13})}{\partial y_3}+\frac{1}{R}T_{31}+H_1f_1\right]dy_3\\ \int_{-h^c-h^b}^{h^c+h^t} L_j(y_3)\rho_0\ddot{u}_3 H_1 dy_3 &= \int_{-h^c-h^b}^{h^c+h^t} L_j(y_3)\left[\frac{\partial T_{31}}{\partial y_1}+\frac{\partial(H_1T_{33})}{\partial y_3}-\frac{1}{R}T_{11}+H_1f_3\right]dy_3\end{aligned} \tag{32}$$

Substituting from Eq. (30) into Eq. (32) and integrating by parts the 2nd term in brackets in the integrand on the right-hand side of Eq. (32) with respect to y_3 , we get

$$A_{ji}\ddot{u}_{1i} = \frac{\partial M_{11}^j}{\partial y_1} - \bar{M}_{13}^j + \frac{1}{R}M_{31}^j + \bar{f}_1^j + B_{13}^j + \mathcal{C}_{13}^j,\ \ i,j = 1,2,\cdots,12 \tag{33.a}$$

$$A_{ji}\ddot{u}_{3i} = \frac{\partial M_{31}^j}{\partial y_1} - \bar{M}_{33}^j - \frac{1}{R}M_{11}^j + \bar{f}_3^j + B_{33}^j + \mathcal{C}_{33}^j,\ \ i,j = 1,2,\cdots,12 \tag{33.b}$$

where

$$M_{mn}^j(y_1,t) = \int_{-h^c-h^b}^{h^c+h^t} L_j(y_3)T_{mn}\mathcal{H}_{(n)}\,dy_3\ ,\ \mathcal{H}_{(1)}=1,\mathcal{H}_{(3)}=H_1,m,n=1,3 \tag{34.a}$$

$$\bar{M}_{mn}^j(y_1,t) = \int_{-h^c-h^b}^{h^c+h^t} \frac{dL_j(y_3)}{dy_3}T_{mn}\mathcal{H}_{(n)}\,dy_3,\ \mathcal{H}_{(1)}=1,\mathcal{H}_{(3)}=H_1,\ \ m,n=1,3 \tag{34.b}$$

$$B_{13}^j(y_1,t) = L_j(h^c+h^t)H_1T_{13}(h^c+h^t,t) - L_j\left(-h^c-h^b\right)H_1T_{13}\left(-h^c-h^b,t\right) \tag{34.c}$$

$$B_{33}^j(y_1,t) = L_j(h^c+h^t)H_1T_{33}(h^c+h^t,t) - L_j\left(-h^c-h^b\right)H_1T_{33}\left(-h^c-h^b,t\right) \tag{34.d}$$

$$\mathcal{C}_{13}^{j}(y_1,t)=\left(L_j(h^{c-})-L_j(h^{c+})\right)H_1\bar{f}_1^{\mathbb{C}-}(h^c)+\left(L_j(-h^{c-})-L_j(-h^{c+})\right)H_1\bar{f}_1^{\mathbb{C}-}(-h^c) \quad (34.e)$$

$$\mathcal{C}_{33}^{j}(y_1,t)=\left(L_j(h^{c-})-L_j(h^{c+})\right)H_1\bar{f}_3^{\mathbb{C}-}(h^c)+\left(L_j(-h^{c-})-L_j(-h^{c+})\right)H_1\bar{f}_3^{\mathbb{C}-}(-h^c) \quad (34.f)$$

$$\bar{f}_\alpha^{j}(y_1,t)=\int_{-h^c-h^b}^{h^c+h^t}L_j(y_3)f_\alpha H_1\,dy_3\,,\alpha=1,3 \quad (34.g)$$

$$A_{ji}(y_1,t)=\int_{-h^c-h^b}^{h^c+h^t}L_j(y_3)L_i(y_3)\rho_0 H_1\,dy_3 \quad (34.h)$$

The quantity M_{mn}^{j}equals j^{th} order moment of the stress T_{mn} about the y_2-axis. Quantities B_{13}^{j} and B_{33}^{j} equal, respectively, j^{th} order moments about the y_2-axis of the tangential surface traction T_{13} and the normal surface traction T_{33} applied on the top and the bottom surfaces of the beam, and quantities $\mathcal{C}_{13}^{j}$ and $\mathcal{C}_{33}^{j}$ equal, respectively, j^{th} order moments about the y_2-axis of the tangential surface traction $\bar{f}_1^{\mathbb{C}\pm}$ and the normal surface traction $\bar{f}_3^{\mathbb{C}\pm}$ acting on the cohesive interface of the beam. Similarly, $\bar{f}_\alpha^{j}$ equals j^{th} order moment of the body force f_α about the y_2-axis, and $A_{ji}$is the inertia tensor associated with the generalized displacements u_{1i} and u_{3i}. The quantity $L_j(-h^{c\pm})$ equals the value of the function $L_j(y_3)$ at the interface between the core and the bottom layer, and $h^{c\pm}$ equals the value of y_3 on $\Gamma_{\mathbb{C}}^{\pm}$.

Assuming that we have cohesive surfaces at the two interfaces between the core and the two surrounding layers, $\bar{f}_1^{\mathbb{C}-}(h^c)$ and $\bar{f}_3^{\mathbb{C}-}(h^c)$ represent, respectively, the tangential and the normal tractions on the cohesive interface between top layer and core. Similarly, $\bar{f}_1^{\mathbb{C}-}(-h^c)$ and $\bar{f}_3^{\mathbb{C}-}(-h^c)$ represent, respectively, the tangential and the normal tractions on the cohesive interface between the bottom layer and the core. These tractions are measured per unit area in the reference configuration, and are related to the cohesive stresses σ_n and σ_t given by Eq. (8.f). Substituting for $\bar{f}_1^{\mathbb{C}\pm}$ and $\bar{f}_3^{\mathbb{C}\pm}$from the traction-separation relations similar to those in Eq. (16.a) into Eqs. (34.e) and (34.f) we express $\mathcal{C}_{13}^{j}$ and $\mathcal{C}_{33}^{j}$ in terms of displacements δ_n and δ_t , or equivalently in terms of $u_{\alpha0}^{t}$ and $u_{\alpha0}^{b}$ because of Eq. (31)

Equation (33a, b) governing deformations of the beam incorporates surface tractions acting on the top and the bottom surfaces of the beam.

Substitution for T_{mn} in terms of displacement gradients from Eqs. (12) and (14) into Eq. (34) gives expressions for moments $M_{mn}^{j}, \bar{M}_{mn}^{j}$ and $\mathcal{C}_{mn}^{j}$ in terms of displacements. Substituting these in Eq. (33), we obtain nonlinear coupled partial differential equations (PDEs) for u_{1j} and u_{3j} for the TSNDT. These 24 PDEs involve second-order derivatives of u_{1j} and u_{3j} with respect to y_1 and time *t*, and are to be solved under pertinent initial and boundary conditions.

We consider the case of zero initial displacements and velocities. Thus

$$u_{\alpha j}^{0}(y_1, t) = 0, \ \alpha = 1,3, j = 1,2,\cdots,12 \tag{35.a}$$

$$\dot{u}_{\alpha j}^{0}(y_1, t) = 0 \tag{35.b}$$

Boundary conditions at a clamped, simply supported and traction free edge, say $y_1 = 0$, are

$$u_{\alpha j}(0, t) = 0, \alpha = 1,3, j = 1,2,\cdots,12 \tag{36.a}$$

$$u_{3j}(0, t) = 0, M_{11}^{j}(0, t) = 0, \tag{36.b}$$

$$M_{11}^{j}(0, t) = 0, M_{31}^{j}(0, t) = 0, \tag{36.c}$$

respectively.

3. Finite element formulation of the problem

3.1 Weak formulation

Let Θ_1^{j} and Θ_3^{j} be smooth functions of $y_1 \epsilon [0, \mathcal{L}]$. We take the inner product of both sides of Eqs. (33.a) and (33.b) with Θ_1^{j} and Θ_3^{j}, respectively, integrate the resulting equations with respect to y_1 on $[0, \mathcal{L}]$, and then integrate by parts the terms involving $\frac{\partial M_{11}^{j}}{\partial y_1}$ and $\frac{\partial M_{31}^{j}}{\partial y_1}$ to arrive at the following equations:

$$\int_0^{\mathcal{L}} \Theta_1^j (A_{ji}\ddot{u}_{1i})dy_1 = \int_0^{\mathcal{L}} \left(-\frac{\partial \Theta_1^j}{\partial y_1} M_{11}^j + \Theta_1^j \left(\frac{1}{R} M_{31}^j + \bar{f}_1^j + B_{13}^j + \mathcal{C}_{13}^j - \bar{M}_{13}^j \right) \right) dy_1 + B_{11}^j$$
$$\int_0^{\mathcal{L}} \Theta_3^j (A_{ji}\ddot{u}_{3i})dy_1 = \int_0^{\mathcal{L}} \left(-\frac{\partial \Theta_3^j}{\partial y_1} M_{31}^j + \Theta_3^j \left(\bar{f}_3^j + B_{33}^j + \mathcal{C}_{33}^j - \bar{M}_{33}^j - \frac{1}{R} M_{11}^j \right) \right) dy_1 + B_{31}^j \quad (37)$$

where

$$B_{11}^j = \Theta_1^j(\mathcal{L}) M_{11}^j(\mathcal{L}) - \Theta_1^j(0) M_{11}^j(0)\,,\; B_{31}^j = \Theta_3^j(\mathcal{L}) M_{31}^j(\mathcal{L}) - \Theta_3^j(0) M_{31}^j(0) \quad (38)$$

Here indices $i, j = 1,2,\ldots,12$. If one thinks of Θ_1^j and Θ_3^j as virtual displacements that vanish at boundary points where displacements are prescribed, then Eq. (37) states the principle of virtual work. Alternatively, Eq. (37) expresses a weak formulation of the problem since it involves first-order derivatives of u_1 and u_3 with respect to y_1 whereas the PDEs (33) have second-order derivatives of u_1 and u_3 with respect to y_1. Since T_{11}, T_{13}, T_{31} and T_{33} are nonlinear functions of displacement gradients, Eq. (37) is nonlinear in u_1 and u_3.

3.2 Derivation of ordinary differential equations

We discretize the curve along the y_1-axis into one-dimensional finite elements (FEs) of not necessarily the same length. Let there be N nodes on this curve and $\Psi_1(y_1), \Psi_2(y_1), \cdots, \Psi_N(y_1)$ be the FE basis functions. We write

$$u_{\alpha j}(y_1, t) = \sum_{i=1}^{N} \Psi_i(y_1) \tilde{d}_{\alpha i j}(t), j = 1,2,\ldots,12;\;\; \alpha = 1,3 \quad (39)$$

Thus we have 24N unknown functions $\tilde{d}_{\alpha ij}(t)$, $\alpha = 1,3$; $i = 1,2,\cdots,N; j = 1,2,\ldots,12$. We write these as the 24N-dimensional vector $\boldsymbol{d}(t)$, and the displacement field $u_{\alpha j}(y_1, t)$ as 24-dimensional vector $\tilde{\boldsymbol{u}}(y_1, t)$. These can be written as

$$\{\tilde{\boldsymbol{u}}(y_1, t)\} = [\emptyset(y_1)]\{\boldsymbol{d}(t)\} \quad (40)$$

$$\{\tilde{\boldsymbol{u}}(y_1, t)\} = \{u_{1j} \quad u_{3j}\}^T, j = 1,2,\ldots,12$$

where $[\emptyset]$ is 24×24N matrix and $\{\boldsymbol{d}\}$ is 24N×1 matrix. In index notation, Eq. (40) becomes

$$\tilde{u}_{\mathrm{i}}(y_1,t)=\emptyset_{\mathrm{ij}}(y_1)d_j(t),\quad i=1,2,\dots,24;\ j=1,2,\cdots,24N \tag{41}$$

We can also write the displacement fields $u_1(y_1,y_3,t)$ and $u_3(y_1,y_3,t)$ as

$$\begin{Bmatrix}u_1(y_1,y_3,t)\\u_3(y_1,y_3,t)\end{Bmatrix}=[\varphi(y_3)][\emptyset(y_1)]\{\boldsymbol{d}(t)\}=[\Phi(y_1,y_3)]\{\boldsymbol{d}(t)\} \tag{42}$$

where $[\varphi(y_3)]=\begin{bmatrix}L(y_3) & 0\\ 0 & L(y_3)\end{bmatrix}$ is 2×24 matrix, $[\emptyset(y_1)]$ is $24\times 24\mathrm{N}$ matrix and $[\Phi]$ is 2×24N matrix.

We use the Galerkin formulation and take the same basis functions for the test functions Θ_1^j, Θ_3^j as those for the trial solutions u_{1j}, u_{3j}; e.g., see Eq. (39). That is

$$\Theta_\alpha^j(y_1)=\sum_{i=1}^{N}\Psi_{\mathrm{i}}(y_1)\,c_{\alpha i}^j\,,\quad \alpha=1,3\,;\ \ j=1,2,\dots,12 \tag{43}$$

where $c_{\alpha i}^j$ are 24N constants.

Substitution from Eqs. (40) and (43) into Eq. (37) and requiring that the resulting equations hold for all values of constants $c_{\alpha i}^j$ gives the following set of coupled nonlinear ordinary differential equations (ODEs).

$$\boldsymbol{M}\ddot{\boldsymbol{d}}=\boldsymbol{F}^{ext}+\boldsymbol{F}^{c}-\boldsymbol{F}^{int}(\boldsymbol{d}), \tag{44}$$

where

$$\boldsymbol{M}=\int_0^{\mathcal{L}}[\emptyset(y_1)]^{\mathrm{T}}[\bar{A}][\emptyset(y_1)]\,dy_1\ ,\ [\bar{A}]=\begin{bmatrix}A & 0\\ 0 & A\end{bmatrix} \tag{45.a}$$

$$\boldsymbol{F}^{ext}=\int_0^{\mathcal{L}}[\emptyset(y_1)]^{\mathrm{T}}\begin{Bmatrix}vec\left(\bar{f}_1^{\,j}+B_{13}^j\right)\\ vec\left(\bar{f}_3^{\,j}+B_{33}^j\right)\end{Bmatrix}dy_1+[\emptyset(\mathcal{L})]^{\mathrm{T}}\begin{Bmatrix}vec(M_{11}^j(\mathcal{L}))\\ vec(M_{31}^j(\mathcal{L}))\end{Bmatrix}-[\emptyset(0)]^{\mathrm{T}}\begin{Bmatrix}vec(M_{11}^j(0))\\ vec(M_{31}^j(0))\end{Bmatrix} \tag{45.b}$$

$$\boldsymbol{F}^{c}=\int_0^{\mathcal{L}}[\emptyset(y_1)]^{\mathrm{T}}\begin{Bmatrix}vec\left(\mathcal{C}_{13}^j\right)\\ vec\left(\mathcal{C}_{33}^j\right)\end{Bmatrix}dy_1 \tag{45.c}$$

$$\boldsymbol{F}^{int}=\int_0^{\mathcal{L}}[BL1]^T\left\{vec(M_{11}^j)\quad vec(M_{31}^j)\quad vec\left(\bar{M}_{13}^j-\tfrac{1}{R}M_{31}^j\right)\quad vec\left(\bar{M}_{33}^j+\tfrac{1}{R}M_{11}^j\right)\right\}^T dy_1 \tag{45.d}$$

$$[BL1] = \begin{bmatrix} diag\left(\frac{\partial}{\partial y_1}\right) & 0 \\ 0 & diag\left(\frac{\partial}{\partial y_1}\right) \\ diag(1) & 0 \\ 0 & diag(1) \end{bmatrix} [\emptyset(y_1)],\ diag(\mathrm{f}) = \text{diagonal}\{\mathrm{f} \quad \mathrm{f} \quad \ldots \quad \mathrm{f}\},\ (12 \text{ terms}) \tag{45.e}$$

$$diag(\mathrm{f}^{\mathrm{j}}) = \text{diagonal}(\mathrm{f}^{1} \quad \mathrm{f}^{2} \quad \ldots \quad \mathrm{f}^{12}),\ vec(\mathrm{f}^{\mathrm{j}}) = \{\mathrm{f}^{1} \quad \mathrm{f}^{2} \quad \ldots \quad \mathrm{f}^{12}\} \tag{45.f}$$

Here $\boldsymbol{M} = \boldsymbol{M}^T$ is the consistent mass matrix, $\boldsymbol{F}^{ext}$ represents the generalized 24N-dimensional nodal force ($\boldsymbol{F}^{ext}$ is 24N×1 matrix) equivalent to the externally applied surface tractions on boundaries and the body force (e.g., gravity). The 24N-dimensional vector $\boldsymbol{F}^{int}$ represents forces due to internal stresses, and is a nonlinear function of the generalized nodal displacement $\boldsymbol{d}$ since stresses T_{11}, T_{13}, T_{31} and T_{33} are nonlinear functions of u_1 and u_3. $\boldsymbol{F}^c$ represents the force vector due to tractions applied on the cohesive interface. The weak formulation involves only first-order derivatives of generalized displacements. Thus C^0 basis functions can be used to numerically analyze the problem. For example, for plates made of linear elastic materials, Qian et al. [16] and Xiao et al. [17] have used, respectively, basis functions derived by the moving least squares approximation and radial basis functions in meshless methods to study transient deformations of thick plates using K^{th} order shear and normal deformable plate theory. Here we consider material and geometric nonlinearities and use the TSNDT.

Integrals in Eq. (45) are numerically evaluated by using three Gauss integration points in each FE along the y_1-axis except in Eqs. (45.c) and (45.d) where we use only one Gauss point in a FE along the y_1-axis. Recall that jump displacements at nodes on the cohesive interface are included in $\boldsymbol{d}$.

If the edge, $y_1 = 0$, where node 1 is located, of the beam is clamped, simply supported or free, boundary conditions there are, respectively, given by Eqs. (46), (47) and (48).

$$\tilde{\mathrm{d}}_{\alpha 1 j}(t) = 0, j = 1,2,\ldots,12;\ \alpha = 1,3; \tag{46}$$

$$\tilde{\mathrm{d}}_{31 j}(t) = 0,\ M_{11}^{j}(0,t) = 0\ , j = 1,2,\ldots,12; \tag{47.a, b}$$

$$M_{11}^{j}(0,t) = 0\ , M_{31}^{j}(0,t) = 0,\ j = 1,2,\ldots,12. \tag{48}$$

3.3 Solution of nonlinear ODEs

We use the conditionally stable central-difference method to integrate the coupled nonlinear ODEs (44). That is, with the notation

$$\boldsymbol{d}^{n+1} = \boldsymbol{d}\,(t_{n+1}), \tag{49}$$

we have

$$\boldsymbol{d}^{n+1} = \boldsymbol{d}^{n} + \Delta t\dot{\boldsymbol{d}}^{n} + \frac{\Delta t^2}{2}\ddot{\boldsymbol{d}}^{n}, \tag{50.a}$$

$$\ddot{\boldsymbol{d}}^{n+1} = \boldsymbol{M}^{-1}\left[\boldsymbol{F}^{ext}(t_{n+1}) + \boldsymbol{F}^{c}(\boldsymbol{d}^{n+1}) - \boldsymbol{F}^{int}(\boldsymbol{d}^{n+1})\right], \tag{50.b}$$

$$\dot{\boldsymbol{d}}^{n+1} = \dot{\boldsymbol{d}}^{n} + \frac{\Delta t}{2}\left(\ddot{\boldsymbol{d}}^{n+1} + \ddot{\boldsymbol{d}}^{n}\right). \tag{50.c}$$

The critical time step size to compute a stable solution is determined by finding the maximum frequency, ω_{max} , of free vibrations and taking $\Delta t \leq \Delta t_{crit}$, $\Delta t_{crit} = 2/\omega_{max}$. Ideally, ω_{max} should be found after every time step since frequencies of a structure change as it is deformed. The accuracy of the solution can be improved by taking $\Delta t \ll \Delta t_{crit}$ but at the cost of increasing the computational time.

Results presented in Section 4 have been computed with a consistent mass matrix and $\Delta t = 0.9\Delta t_{crit}$ for a linear problem but $\Delta t = 0.5\Delta t_{crit}$ for a nonlinear problem. For the nonlinear problems, ω_{max} found from analyzing frequencies of the undeformed beam is used to ascertain Δt_{crit}.

For a static problem, the nonlinear algebraic Eq. (44) is solved for $\boldsymbol{d}$ by the modified Newton-Raphson method. That is, we iteratively solve

$$\boldsymbol{F}^{int}(\boldsymbol{d}) - \boldsymbol{F}^{c}(\boldsymbol{d}) = \boldsymbol{F}^{ext} \tag{51}$$

by first writing it as

$$\boldsymbol{K}\Delta\boldsymbol{d} = -\left(\boldsymbol{F}^{int}(\bar{\boldsymbol{d}}) - \boldsymbol{F}^{c}(\bar{\boldsymbol{d}}) - \boldsymbol{F}^{ext}\right),\ \boldsymbol{K} = \left.\frac{\partial\left(\boldsymbol{F}^{int} - \boldsymbol{F}^{c}\right)}{\partial\boldsymbol{d}}\right|_{\boldsymbol{d}=\bar{\boldsymbol{d}}}\ ,\ \boldsymbol{d} = \bar{\boldsymbol{d}} + \Delta\boldsymbol{d} \tag{52}$$

The iterative process is terminated when the norm of the residual load vector, $\bar{R}$, defined by

$$\boldsymbol{R} = \boldsymbol{F}^{int}(\boldsymbol{d}) - \boldsymbol{F}^{c}(\boldsymbol{d}) - \boldsymbol{F}^{ext}, \;\; \bar{R} = max(|\boldsymbol{R}|)N/Sum(|\boldsymbol{F}^{ext}|) \tag{53}$$

is less than 0.05%. Recall that N equals the number of nodes. For every load step the stiffness matrix $\boldsymbol{K}$ is evaluated only once.

4. Example problems

We use the more common notation and replace y_1 and y_3 by x and z, respectively. Subscripts 1, 2 and 3 represent directions along the x-, the y- and the z-axes, respectively. When analyzing problems without considering geometric nonlinearities, we omit all nonlinear terms in expressions for the strain components and rotation of the cohesive interface, and note that differences among the three stress tensors, namely, the 1st and the 2nd Piola-Kirchhoff and the Cauchy stress tensors are negligible.

4.1 Delamination in straight DCB neglecting effects of geometric nonlinearities and inertia forces

4.1.1 Mode-I deformations under monotonically increasing load

We study the initiation and propagation of delamination in a double cantilever beam (DCB) shown in Fig. 4a and compare computed results with the numerical results of Ref. [7], and experimental findings of Ref. [18]. Thus this example also verifies our code for linear quasi-static problems. We divide the bottom layer of the DCB into two layers of equal thickness, and introduce the cohesive interface only between the top beam and the upper layer of the bottom beam. The thickness of the top, the middle and the bottom layers of the beam are given by $h^t = h$, $2h^c = \frac{h}{2}$ and $h^b = \frac{h}{2}$, respectively. Thus the z-coordinate of points on the bottom and the top surfaces of the DCB equal -0.75 h and 1.25 h, respectively.

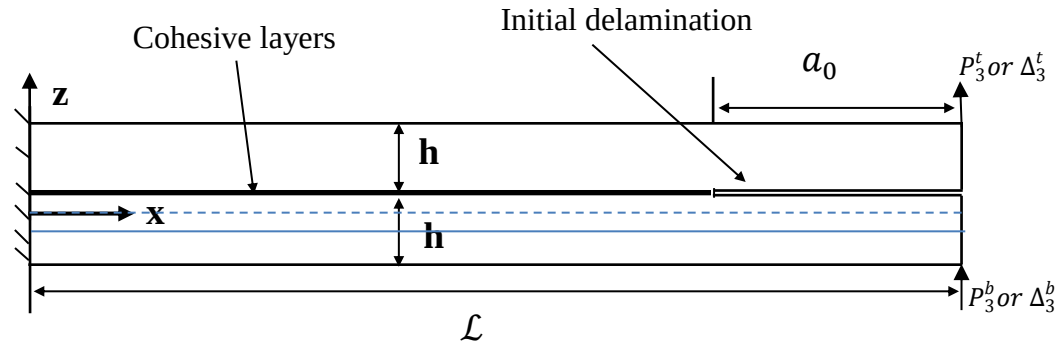

(a)

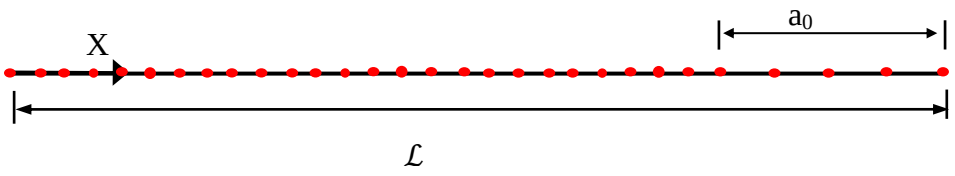

(b)

Fig. 4 (a) Sketch of DCB with either point loads or transverse displacements applied at the ends, (b) finite element mesh on the mid-surface of the beam.

Boundary conditions at the clamped edge x = 0 are given by Eq. (46). For studying mode-I deformations, we set $-\Delta_3^b = \Delta_3^t = \Delta_3$, and apply the following boundary conditions at $x = \mathcal{L}$.

$$u_{30}^c(\mathcal{L}) = -\Delta_3, u_{30}^t(\mathcal{L}) = 2\Delta_3, u_{30}^b(\mathcal{L}) = 0 \tag{54.a}$$

$$u_{3i}^c(\mathcal{L}) = u_{3i}^b(\mathcal{L}) = u_{3i}^t(\mathcal{L}) = 0,\ i = 1,2,3 \tag{54.b}$$

$$M_{11}^j(\mathcal{L}) = 0, j = 1,2,\dots,12 \tag{54.c}$$

The displacement Δ_3 is applied in increments of 0.01 mm. Forces P_3^t and P_3^b are evaluated by integrating computed values of $T_{31}(\mathcal{L}) = \sigma_{xz}(\mathcal{L})$ for the upper and the lower layers of the DCB, respectively, and multiplying the result with the beam width B. For this problem, $\delta_n(y_1) = u_{30}^t(y_1)$.

Material and geometric parameters are assigned following values taken from [7].

$E_1 = 130\ GPa$, $G_{13} = 2.0\ GPa, G_{Ic} = 275\ Jm^{-2}, \sigma_n^0 = 60\ MPa$

$$E_2 = E_3 = 7.5\ GPa,\quad \upsilon_{12} = \upsilon_{13} = 0.3, \upsilon_{23} = 0.3 \tag{55}$$

$$\mathcal{L} = 100\ mm,\quad a_0 = 45\ mm,\quad h = 2\ mm, B = 15\ mm$$

Here a_0 equals the initial delaminated length and $2h$ the total thickness of the DCB. The FE mesh shown in Fig. 4b has 2-node elements with element size in the undelaminated region equal to half of that in the initial delaminated region. Thus it can only support a compressive load. The experimental value of the tensile strength σ_n^0 was not provided in [18] and was assumed to be 60 MPa in [7]. Here results have been computed for two values, 30 and 60 MPa, of σ_n^0 that are representative of the strength of the matrix.

In the delaminated region, integrals in Eq. (31) over the thickness are written as the sum of two integrals, one from $-(h^c + h^b)$ to h^c and the other from h^c to $(h^c + h^t)$ with the interface between the core and the top layer regarded as traction free. Thus the effective stiffness of the delaminated beam is less than that of the in-tact beam.

The computed load vs. edge displacement curves for $\sigma_n^0 = 30$ and 60 MPa, two FE meshes and two values of the initial stiffness $\mathrm{k_s}$ of the cohesive traction-separation relation are compared in Fig. 5 with those reported in Refs [7] and [18]. Furthermore, in Fig. 6, the presently computed load vs. the delaminated length curve is compared with that given in [7]. It is clear from these plots that the present work accurately analyzes mode-I delamination of a DCB specimen. Effects of the initial stiffness ($\mathcal{K} = 10^{-8}$ or 10^{-9} in Eq. (18)) in the cohesive traction separation relation and of the interfacial strength (30 or 60 MPa) on the computed load-displacement curves are insignificant.

The variations with the edge displacement of the strain energy W_e stored in the DCB, the work done by external forces and the energy dissipated during delamination are exhibited in Fig. 7. The energy W_e is evaluated by integrating the elastic energy density W (cf. Eq. 10) over the beam domain, the work W_p of external forces equals $\int P_3^t d\Delta_3^t + \int P_3^b d\Delta_3^b$, and the energy W_d dissipated during delamination equals $\int_{\Gamma_{\mathbb{C}}} BG_{Ic}\, dy_1$. It is clear that the delamination begins to grow when the edge displacement and the load equal about 1.5 mm and 45 N, respectively. The energy dissipated during delamination is comparable to the elastic energy stored in the beam. The maximum percentage difference

$100(W_p - W_e - W_d)/W_p$ equals 0.6% signifying that the balance of energy is well satisfied.

The line PQR perpendicular to the centroidal axis at $x = 40$ mm in the reference configuration is deformed into line segments P'Q' and Q"R' shown in Fig. 8. Thus abutting particles of the lower and the upper layers that occupied the place Q in the reference configuration are deformed into places Q" and Q' respectively, and Q'Q" equals the jump $\delta_n(x) = \jmath_{30}^t(x)$ at $x = 40$ mm. It is also evident that segments PQ and QR are rotated, respectively, into lines P'Q' and Q"R' that have slopes of opposite signs.

4.1.2 Mode-I deformations under cyclic load

We now study mode-I deformations of the DCB analyzed in subsection 4.1.1 during loading, unloading and reloading. We use increments of 0.01 mm to first increase Δ_3 at the edge $x = \mathcal{L}$ from 0 to 2 mm, then decrease Δ_3 to zero, and finally increase Δ_3 to 3 mm. Variations with Δ_3 of the load and different components of energy are shown in Figs. 9 and 10, respectively. The load vs. displacement curve in Fig. 9 is given by OAB during initial loading, by BO during unloading to zero value of Δ_3, and by OBC during subsequent reloading. From results depicted in Fig. 10 we see that the energy dissipated because of delamination during unloading is zero (e.g., the curve AE in Fig. 10) and no additional energy is dissipated till the specimen has been reloaded to the state (corresponding to point A in Fig. 10) from which it was unloaded. The work done by external force follows the path OC during initial loading and CDE during unloading. It is clear that during the full cycle of loading and unloading the net work done by external forces corresponding to point E in Fig. 10 equals the energy used to damage the cohesive layer of the DCB as evidenced by a decrease in its stiffness from the slope of line OA to the slope of line OB in Fig. 9. The area of triangle OAB equals the energy corresponding to point E in Fig. 10. The strain energy of deformation follows the path OFB during initial loading and the path BO during unloading. Thus all of the energy stored in the body is recovered during unloading as should be the case for an elastic problem. The curve BO is essential parallel to the curve CDE with the vertical distance between the two curves equaling the energy corresponding to point A or that used to damage the

cohesive layer. These results suggest that the present software correctly predicts deformations during the loading, unloading and reloading process.

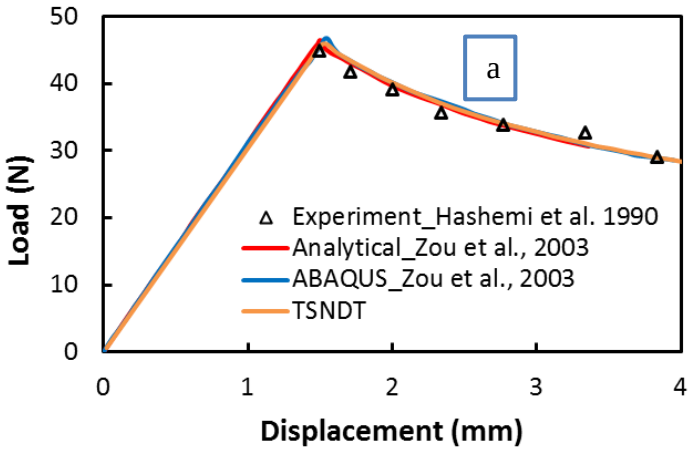

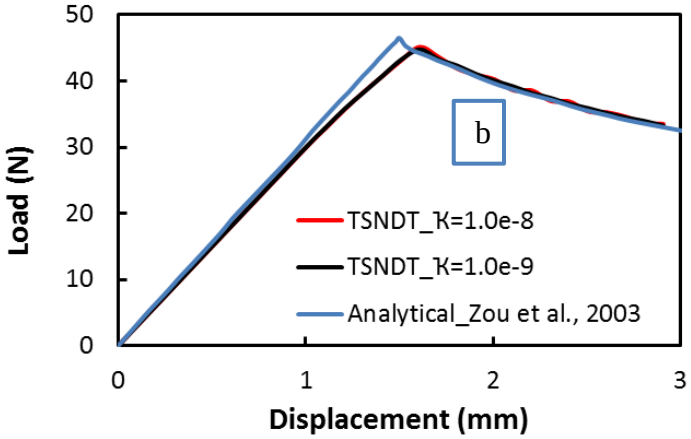

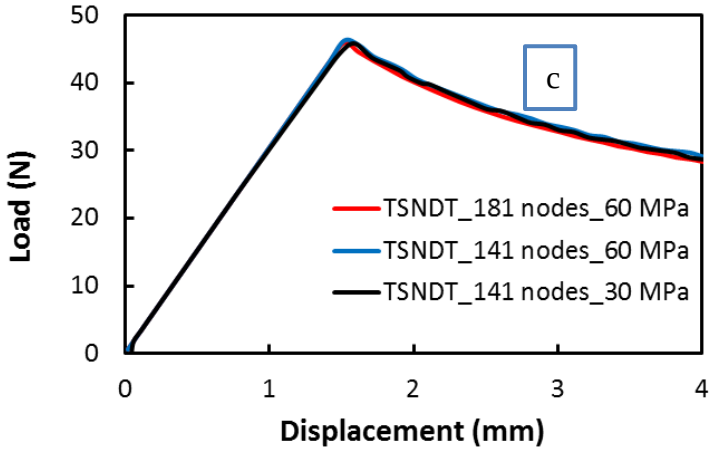

Fig. 5 For quasistatic mode-I deformations of the DCB specimen, comparison of the presently computed load (P_3^t) - end displacement (Δ_3^t) curves with numerical results of Ref. [7] and experimental findings of Ref. [18] . (a) and (b) $\sigma_n^0 = 60\ MPa$ (181 nodes), (c) load vs. displacement curves for two values, 60 and 30 MPa, of the cohesive strength σ_n^0.

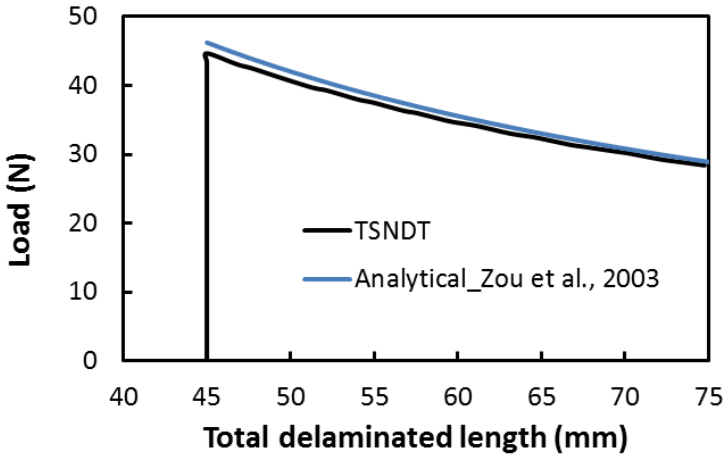

Fig. 6 Load P_3^t vs. delaminated length, $\sigma_n^0 = 60\ MPa$ (181 nodes)

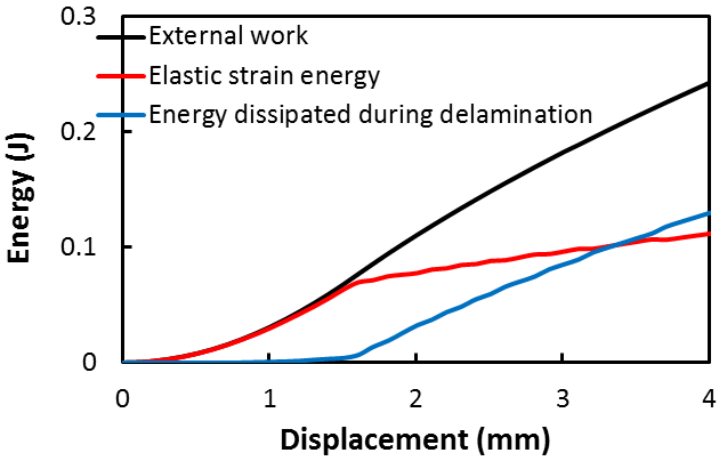

Fig. 7 Variation with the edge displacement of the work done by external forces, strain energy stored in the beam and energy dissipated during delamination, $\sigma_n^0 = 60\ MPa$ (181 nodes)

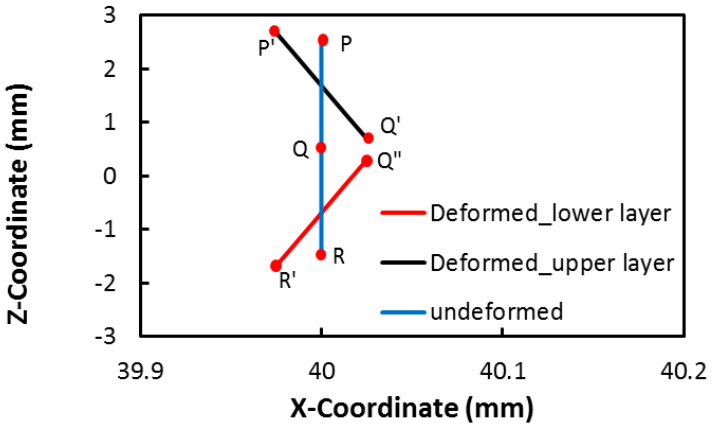

Fig. 8 Deformed configurations of a line initially perpendicular to the centroidal axis at x = 40 mm when $\Delta_3 = 3.42\ mm$.

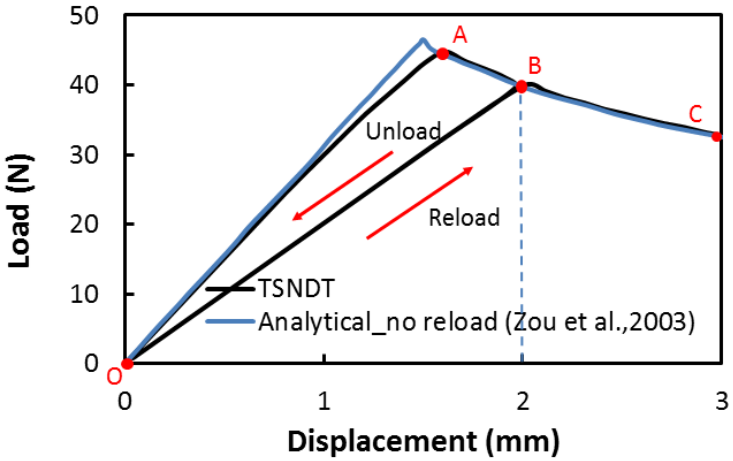

Fig. 9 For $\sigma_n^0 = 60\ MPa$ and quasistatic mode-I deformations of the DCB, load (P_3^t)-edge displacement (Δ_3^t) curves during loading, unloading and reloading. The analytical results are obtained by using equations given in [7], and numerical results were computed using 181 nodes.

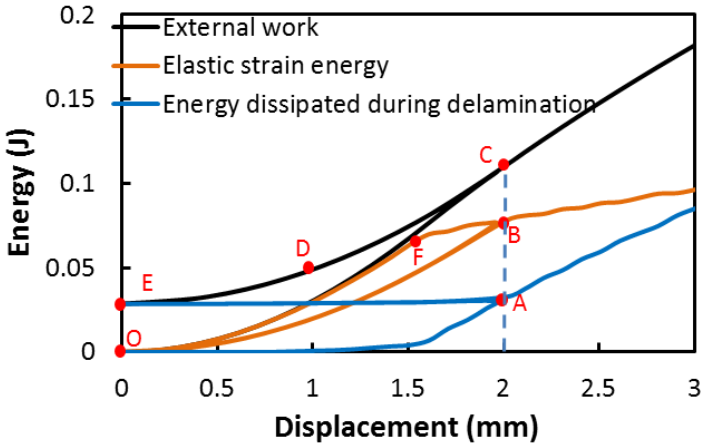

Fig. 10 Variation with the edge displacement of the work done by external forces, strain energy stored in the beam and energy dissipated during delamination.

4.1.3 Mode-II deformations under monotonically increasing load

We now study mode-II deformations of the DCB made of an isotropic material with following values of material and geometric parameters taken from [19, 20].

$$E = 150\ GPa\ ,\quad \nu = 0.25\ ,\quad G_{IIc} = 1.45\ kJm^{-2},\quad \sigma_t^0 = 80\ MPa$$

$$\mathcal{L} = 100\ mm,\quad a_0 = 50\ mm,\quad 2h = 3\ mm, B = 10\ mm \tag{56}$$

Numerical results computed with the presently developed software are compared with the analytical results based on the LEFM approach reported in [19] and numerical results given in [20] that were computed with a user defined cohesive element subroutine implemented in ABAQUS.

Boundary conditions $\Delta_3^b = \Delta_3^t = \Delta_3$ in Fig. 4a for mode-II deformations are satisfied by setting

$$u_{30}^c(\mathcal{L}) = \Delta_3, u_{30}^t(\mathcal{L}) = 0, u_{30}^b(\mathcal{L}) = 0 \tag{57.a}$$

$$u_{3i}^c(\mathcal{L}) = u_{3i}^b(\mathcal{L}) = u_{3i}^t(\mathcal{L}) = 0,\ i = 1,2,3 \tag{57.b}$$

$$M_{11}^j(\mathcal{L}) = 0, j = 1,2,\ldots,12 \tag{57.c}$$

The displacement Δ_3 is applied in increments of 0.05 mm and values of $P_3 = P_3^t + P_3^b$ are found as mentioned in subsection 4.1.1 by integrating over the thickness

computed values of $T_{31}(\mathcal{L}) = \sigma_{xz}(\mathcal{L})$ for the upper and the lower layers of the DCB, respectively, and multiplying the result with the beam width B. The presently computed load P_3 - displacement Δ_3 curves for mode-II delamination exhibited in Fig. 11 are close to those reported in Refs. [19] and [20]. The load vs. displacement curves in Fig. 11b for two values, 60 and 80 MPa, of σ_t^0, and two different FE meshes, are essentially identical to each other signifying negligible effect of the precise value of σ_t^0 used to compute results, and whether 81 or 121 nodes are used to discretize the length $\mathcal{L}$ of the beam. The beam begins to delaminate when Δ_3= 14.8 mm as signified by a drop in the load in Fig. 12a. The presently computed peak load differs from that reported in Refs. [19] and [20] by 2.7% and 1.8%, respectively. With an increase in the delamination length the load continues to drop till Δ_3= 23 mm at which instant the load begins to increase because the delamination has propagated to the end of the beam as depicted in Fig. 12.

The delaminated lengths for Δ_3 equal to 14.3 mm and 17.5 mm are 50 mm and 77 mm, respectively. That is, the interface between the lower surface of the top beam and the upper surface of the bottom beam at x = 40 mm is not delaminated when $\Delta_3 = 14.3$ mm but is delaminated when $\Delta_3 = 17.5$ mm. We have plotted in Figs. 13 and 14, respectively, the variation at x = 40 mm of σ_{xz} and σ_{xx} for Δ_3 = 14.3 mm and 17.5 mm. It is clear that σ_{xz} and σ_{xx} are continuous across the interface before delamination. The axial stress σ_{xx} continuously varies from +422 MPa to -422 MPa from the bottom to the top surface. Subsequent to delamination, the two layers deform independently and σ_{xz} equals zero on the interface since the contacting smooth delaminated surfaces have zero tangential tractions. The through-the-thickness variations of σ_{xx} in the two layers of the beam are identical to each other since they have the same bending stiffness and curvature.

The deformed configurations of line PQR initially perpendicular to the centroidal axis at x = 40 mm when $\Delta_3 = 17.5$ mm are shown in Fig. 15. Segments PQ and QR of line PQR are deformed into P'Q' and Q"R' that are parallel to each other. The distance Q'Q" equals the jump $\delta_t(x) = \mathcal{u}_{10}^t(x)$ at $x = 40$ mm.

4.1.4 Mixed-mode deformations under monotonically increasing load

For the DCB studied in subsection 4.1.3 we assume the following values of material and geometric parameters which are the same as those used in Refs. [19] and [20]

$$E_1 = 150\ GPa\ ,\quad G_{13} = 6.0\ GPa,\ G_{Ic} = 352\ Jm^{-2}, G_{IIc} = 1.45k\ Jm^{-2}$$

$$E_2 = E_3 = 11.0\ GPa,\ \upsilon_{12} = \upsilon_{13} = 0.25, \upsilon_{23} = 0.45 \tag{58}$$

$$\mathcal{L} = 100\ mm,\quad a_0 = 40\ mm,\quad 2h = 3\ mm, B = 10\ mm$$

$$\sigma_n^0 = 60\ MPa,\ \sigma_t^0 = 80\ MPa$$

For studying mixed-mode deformations of the DCB displayed in Fig. 4a, we set $\Delta_3^b = -\Delta_3$ and $P_3^t = 0$. Thus the following boundary conditions at x = $\mathcal{L}$ are imposed.

$$\mathcal{u}_{30}^c(\mathcal{L}) = -\Delta_3\ , \mathcal{u}_{3i}^c(\mathcal{L}) = \mathcal{u}_{3i}^b(\mathcal{L}) = 0,\ i = 1,2,3 \tag{59.a}$$

$$\mathcal{u}_{30}^b(\mathcal{L}) = 0 \tag{59.b}$$

$$M_{11}^j(\mathcal{L}) = 0, j = 1,2,\ldots,12, \tag{59.c}$$

$$M_{31}^j(\mathcal{L}) = 0, j = 5,6,7,8 \tag{59.d}$$

We define shear load $\overline{\mathrm{P}}_3 = -\mathrm{P}_3^b$. In Fig. 16 we have compared the presently computed load ($\overline{\mathrm{P}}_3$) - edge displacement (Δ_3) curve with those of Refs. [19] and [20]. We note that results computed using FE meshes with 121 and 161 nodes are very close to each other and the two values of the peak load are virtually identical. The presently computed peak value of the shear load differs from that of Refs. [19] and [20] by 8.6% and 9.1%, respectively. The ratio of $G_{\mathrm{I}}/G_{\mathrm{II}}$ versus the delamination length shown in Fig. 17 is nearly constant and equals 1.35 which agrees with the analytical result of [7]. Values of G_{I} and G_{II} are calculated from Eq. (24).

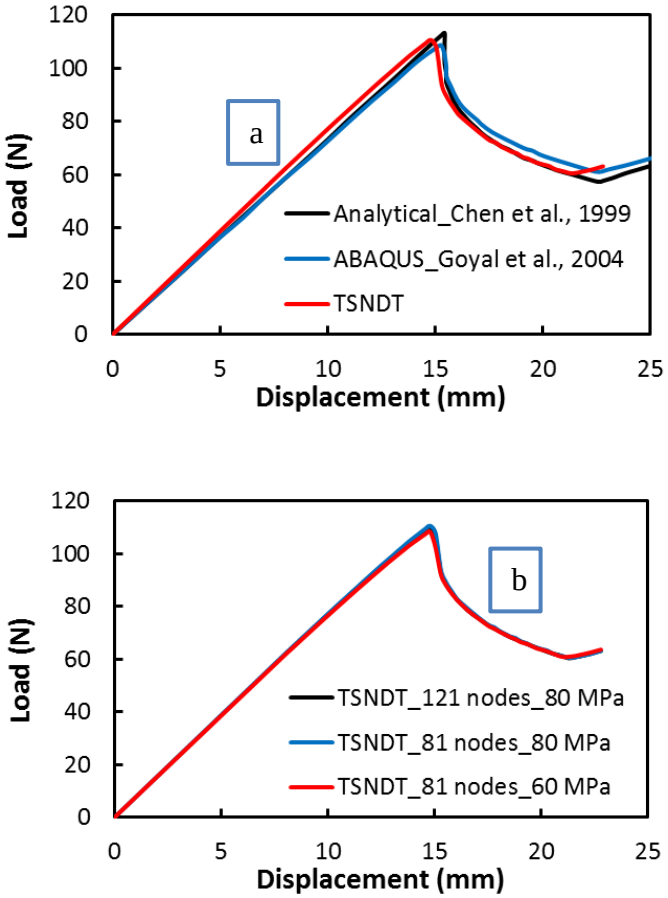

Fig. 11 Load (P_3) - edge displacement (Δ_3) curves for mode-II deformations using 81 nodes. (a) Comparison of present results with those of [19] and [20] (121 nodes), (b) load vs. displacement curves for two values, 60 and 80 MPa, of the cohesive strength σ_t^0, and two FE meshes having 81 and 121 nodes.

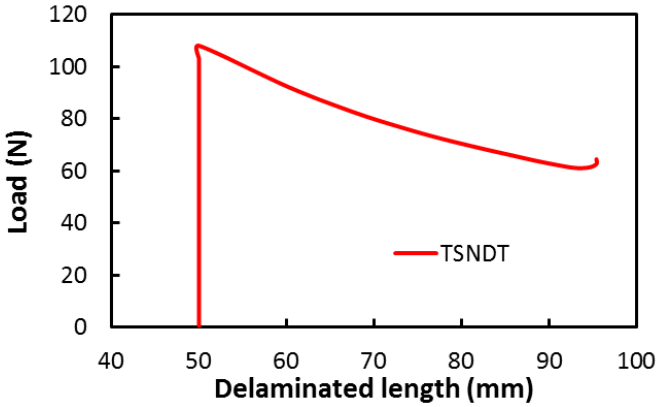

Fig. 12 Load P_3^t vs. delaminated length, $\sigma_t^0 = 80\ MPa$ (121 nodes).

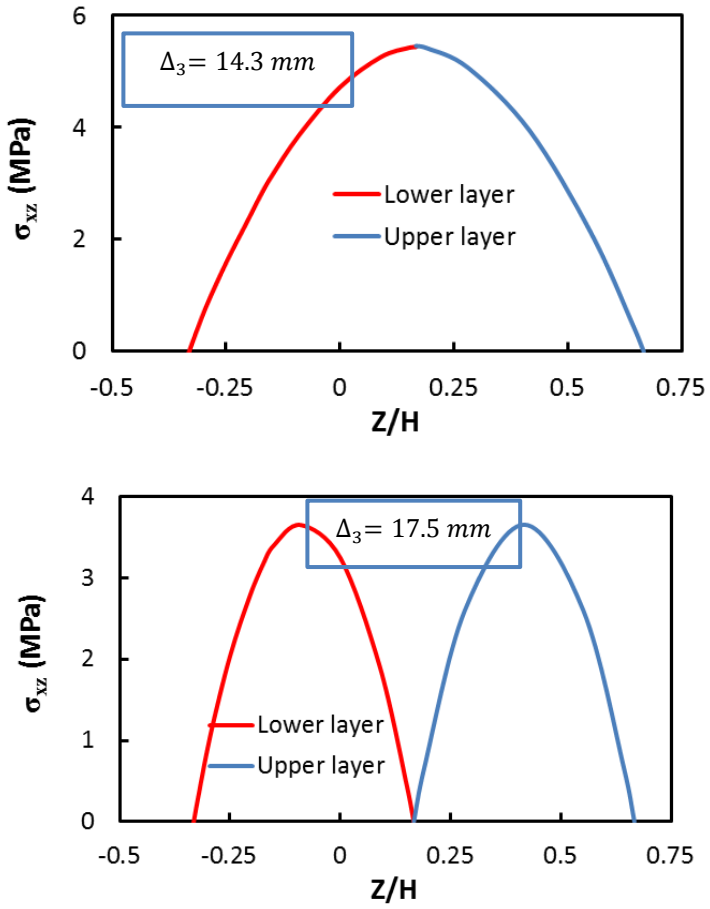

Fig. 13 Variation of σ_{xz} at x = 40 mm for two different values of the edge displacement, Δ_3 (H=2h).

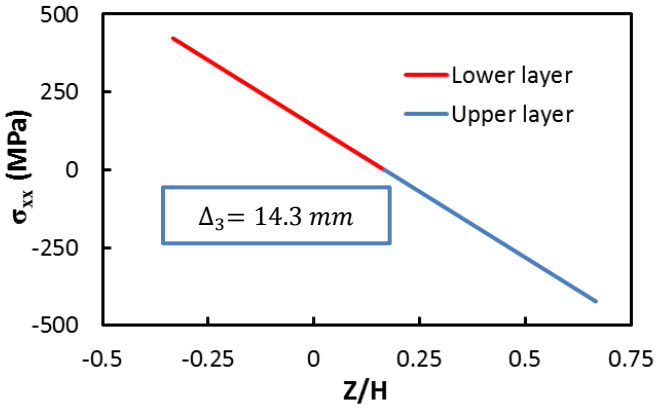

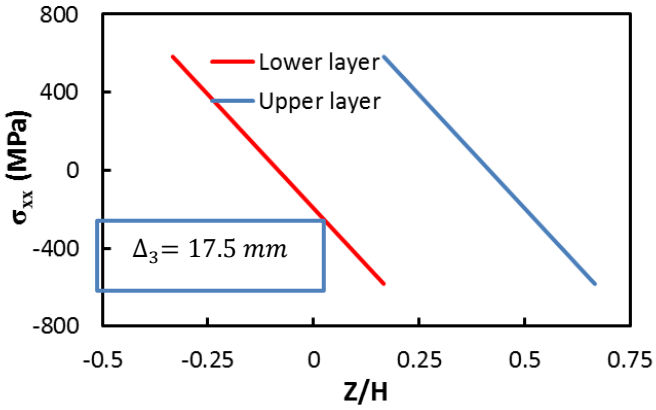

Fig. 14 Variation of σ_{xx} at x = 40 mm for two different values of the edge displacement, Δ_3(H=2h).

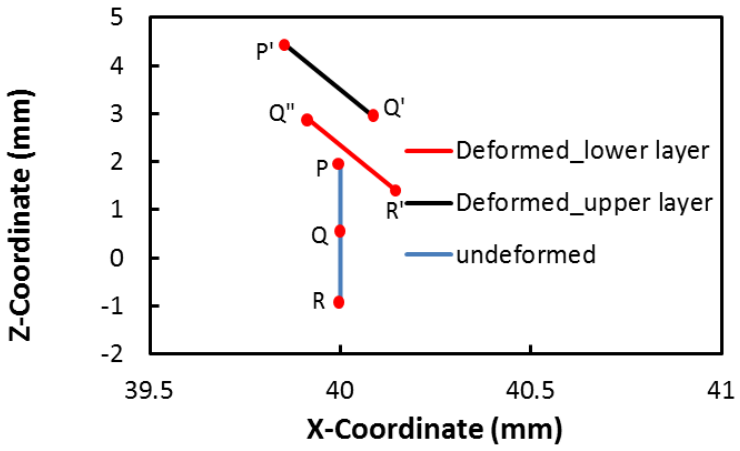

Fig. 15 For Δ_3= 17.5 mm, deformed configurations of a line initially perpendicular to the centroidal axis at x = 40 mm (121 nodes).

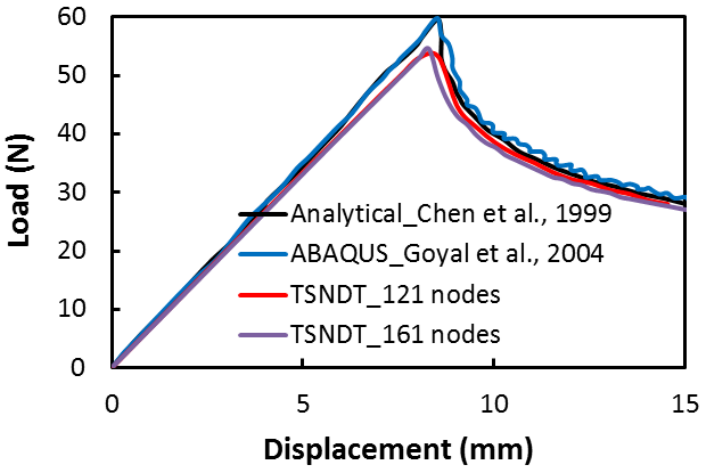

Fig.16 Comparison of presently computed load ($\overline{P}_3$) - edge displacement (Δ_3) curves for mixed-mode deformations with those of [19] and [20] when $\sigma_n^0 = 60\ MPa$ using two FE meshes with 121 and 161 nodes.

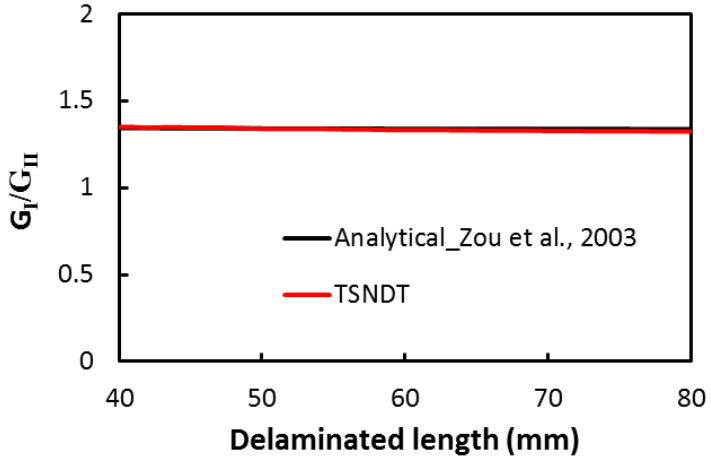

Fig.17 Mode - mixity ratio vs. the delaminated length for mixed-mode delamination for $\sigma_n^0 = 60$ MPa.

4.2 Delamination in curved DCB neglecting effects of geometric nonlinearities and inertia forces

We now study delamination growth in mode-I deformations of the curved DCB shown in Fig. 18 also studied by Guedes et al. [21] and compare our results with those of [21]. The beam is deformed by applying displacements $\Delta_3^t = -\Delta_3^b = \Delta_3$ at points on the right edge. Values of material and geometric parameters used to compute results are listed below.

$$E_1 = 4.5\ GPa\ ,\quad G_{13} = 1.0\ GPa,\ E_2 = E_3 = 1.7\ GPa, \upsilon_{12} = \upsilon_{13} = 0.3, \upsilon_{23} = 0.4$$

$$G_{Ic} = 800\ Jm^{-2}\ , G_{IIc} = 1200\ Jm^{-2}, \sigma_n^0 = \sigma_t^0 = 20\ MPa \tag{60}$$

$$\theta_T = 0.182\pi,\quad \theta_D = 0.063\pi,\quad 2h = 11.6\ mm, B = 22.8\ mm, R = 40h$$

Here θ_T is the central angle of the entire beam, θ_D the central angle of the initially delaminated part of the beam, and R is the radius of the mid-surface. Boundary conditions for this problem are identical to those of the problem studied in subsection 4.1.1.

The presently computed load (P_3^t) vs. end displacement (Δ_3^t) curve shown in Fig. 19 agrees well with that of [21]. Whereas the two FE meshes with 81 and 121 nodes give basically the same load – displacement curves, the presently computed value of the peak load differs from that of Ref. [21] by 4.1% and the two end displacements when the peak loads occur differ by 1.3%. The load versus delaminated length curve exhibited in Fig. 20 indicates that the load monotonically decreases with an increase in the delamination length. The variation with Δ_3 of the strain energy W_e stored in the DCB, the work done by external forces and the energy dissipated during delamination are displayed in Fig. 21. The maximum difference $100(W_p - W_e - W_d)/W_p$ equals 0.6% signifying that the balance of energy is well satisfied.

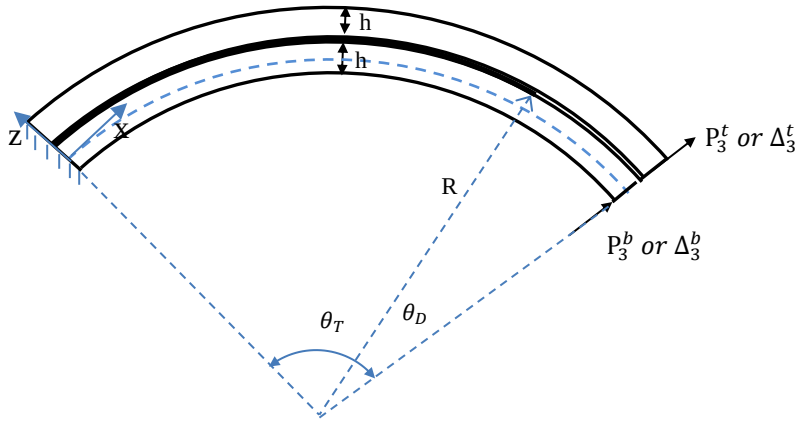

Fig. 18 Curved DCB beam clamped at the left end and loaded by applying radial displacements at the right end.

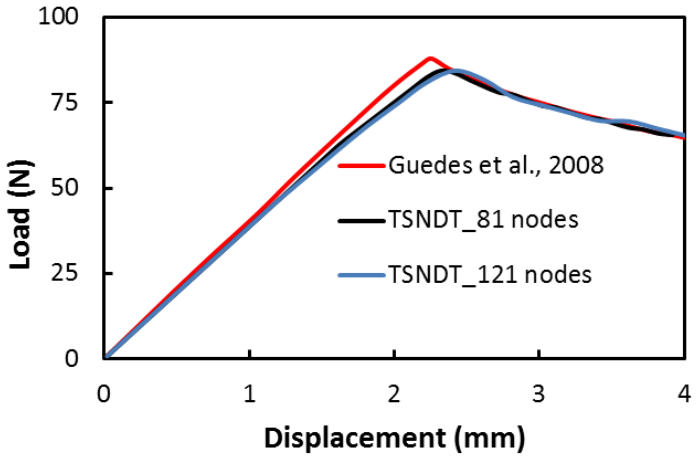

Fig.19 Load (P_3^t)-crosshead displacement (Δ_3^t) curves for the curved beam of Fig. 18.

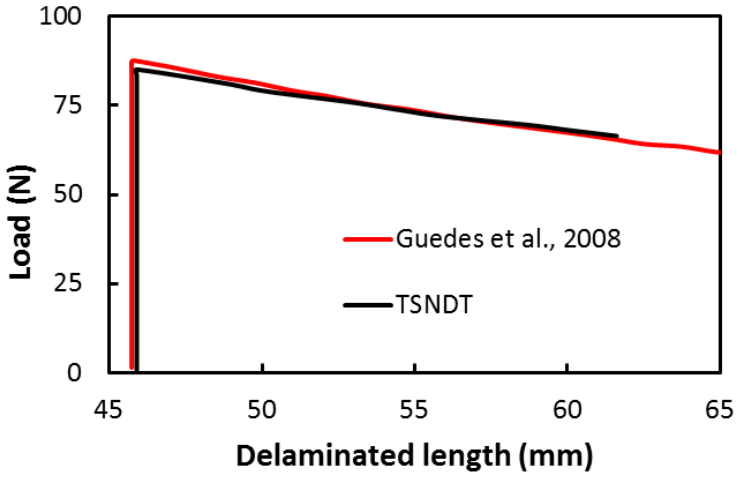

Fig. 20 Load (P_3^t) vs. delaminated length (121 nodes) for the curved beam of Fig. 18.

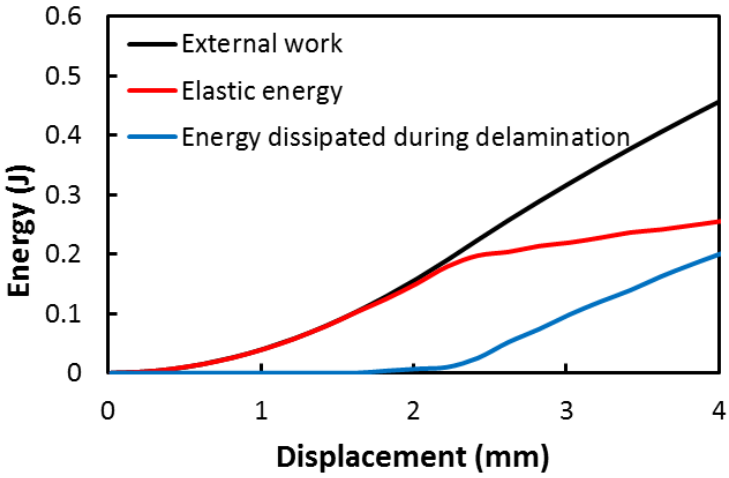

Fig. 21 For the curved beam of Fig. 18, variation with the delamination length of the work done by external forces, strain energy stored in the beam and energy dissipated during delamination (121 nodes).

4.3 Delamination growth in mode-I deformations of straight DCB with consideration of geometric nonlinearities

We study the same problem as that analyzed by Allix and Corigliano [11]. Whereas they used the displacement field of the Timoshenko beam theory we use that of the TSNDT. We note that the Timoshenko beam theory neglects transverse normal

strains and assumes the transverse shear strain to be constant. However, the TSNDT assumes quadratic variation through-the-thickness of the transverse normal strain and cubic variation of the transverse shear strain. Values assigned to material and geometric parameters taken from Ref. [11] are listed below.

$$E_1 = 135\ GPa\ ,\quad G_{13} = 5.7\ GPa,\quad E_2 = E_3 = 10.0\ GPa$$

$$\upsilon_{12} = \upsilon_{13} = 0.3,\ \upsilon_{23} = 0.3,\ G_{Ic} = 400\ Jm^{-2} \tag{61}$$

$$\mathcal{L} = 20\ mm,\quad a_0 = 5.5\ mm,\quad 2h = 0.4\ mm,\ B = 1\ mm,\ \sigma_n^0 = 20\ \text{MPa}.$$

Values of E_2, E_3 and Poisson's ratios are not given in [11], and have been estimated in the present work. Boundary conditions for this problem are the same as those for the problem studied in subsection 4.1.1.

From the load (P_3^t) vs. the edge displacement (Δ_3^t) curves plotted in Fig. 22, we conclude that the presently computed peak loads for the linear and the nonlinear problems are essentially equal to each other. However, for Δ_3^t = 1.5 mm, the presently computed load from the nonlinear analysis exceeds that from the linear analysis by about 3%. Whereas delamination initiates for the same value of Δ_3^t for the Timoshenko beam theory used by Allix and Carigliano [11] and the TSNDT used here, the two peak loads differ by 5.9%. For post-delamination deformations the P_3^t vs. Δ_3^t curves from the present work are close to that from the analytical solution of Zou et al. [7] based on linear theory, however, these differ noticeably from those reported by Allix and Corigliano [11].

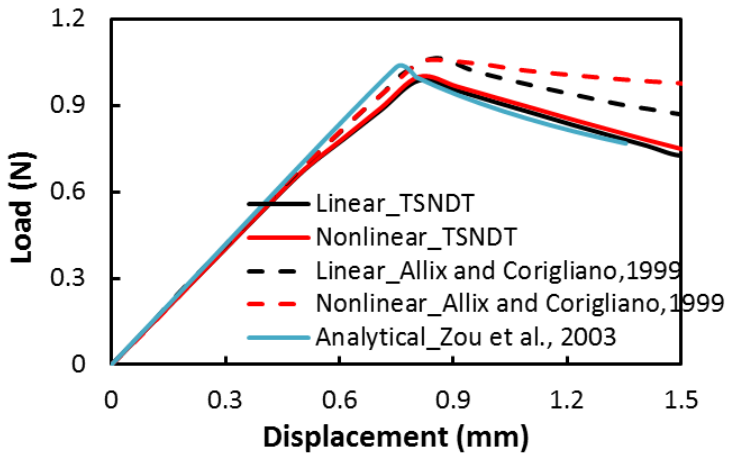

Fig. 22 For mode-I deformations of the DCB, comparison of load (P_3^t) vs. the edge displacement (Δ_3^t) curves for the linear and the nonlinear analyses using 81 nodes.

4.4 Post-buckling deformations of predelaminated beam deformed in axial compression

Pre- and post-buckling deformations of an initially debonded [$0_4/0_{12}/0_4$] beam shown in Fig. 23a and analyzed in [22] are simulated considering all geometric nonlinearities. The initial debonded length located at the mid-span between the top face sheet and the core equals a_1. The nonsymmetrical perturbation shown in Fig. 23a with P_0 = 0.01N is applied, and the beam is deformed by keeping the right edge clamped and applying axial displacement Δ_1 on the left edge. Thus boundary conditions applied on the left edge are

$$u_{3i}^c(0) = u_{3i}^b(0) = u_{3i}^t(0) = 0,\ i = 0,1,2,3 \tag{62.a}$$

$$u_{1i}^c(0) = u_{1i}^b(0) = u_{1i}^t(0) = 0,\ i = 1,2,3 \tag{62.b}$$

$$u_{10}^b(0) = u_{10}^t(0) = 0,\ u_{10}^c(0) = \Delta_1 \tag{62.c}$$

The displacement Δ_1 is applied in increments of 0.001 mm. The point load P_0 at ($\mathcal{L}$/2, H/2) is replaced by the surface traction T_{31} (x, H/2) = (P_0/ε) $\delta(\mathcal{L}/2-\varepsilon/2, H/2)$ where δ(x, H/2) is the delta function centered at (x, H/2).

The compressive axial load P is found by integrating $T_{11}(0, z)$ over the thickness, multiplying the result with the beam width, and taking the absolute value.

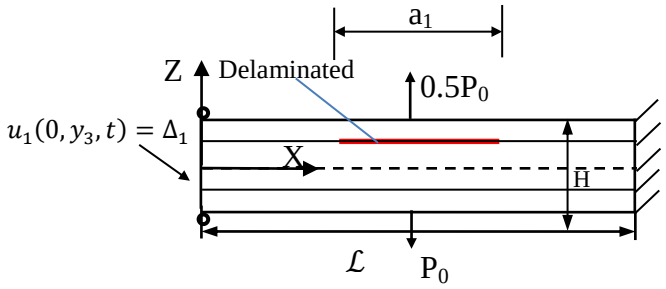

(a)

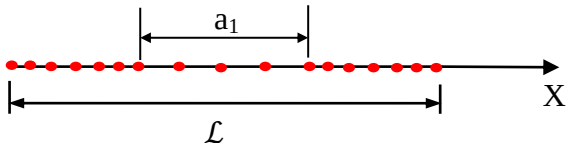

(b)

Fig. 23 (a) Sketch of initially delaminated beam deformed in uniaxial compression and unsymmetrical perturbations applied at the top and the bottom surfaces; (b) sketch of the FE mesh (not to scale).

Values of geometric and material parameters taken from [22] are

$$E_1 = 139.3\ GPa,\ G_{13} = 5.58\ GPa,\ E_2 = E_3 = 9.72\ GPa,\ \upsilon_{12} = \upsilon_{13} = 0.29,\ \upsilon_{23} = 0.4$$

$$G_{Ic} = 87.6\ Jm^{-2},\ G_{IIc} = 315.2\ Jm^{-2},\ \sigma_n^0 = 44.54\ \text{MPa},\ \sigma_t^0 = 106.9\ MPa \qquad (63)$$

$$\mathcal{L} = 50.8\ mm,\quad a_1 = 19.05\ mm,\quad H = 2.59\ mm,\ B = 5.08\ mm$$

The presently computed results are compared with the numerical solution of [22] and the experimental findings of [23]. In Figs. 24 and 25 we have exhibited the axial load vs. the engineering axial strain, and the axial load vs. the mid-span deflections (or z-displacements) of the top and the bottom surfaces. Results computed with two FE meshes having 120 and 160 two-node elements are close to each other. The drop in the

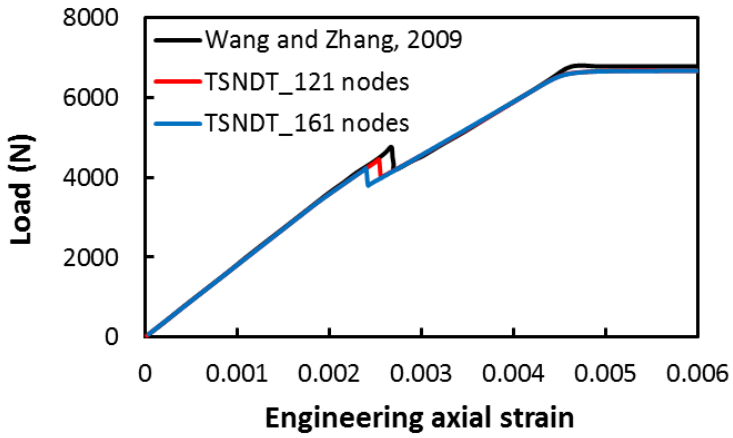

Fig. 24 Axial compressive load P vs. the engineering axial strain.

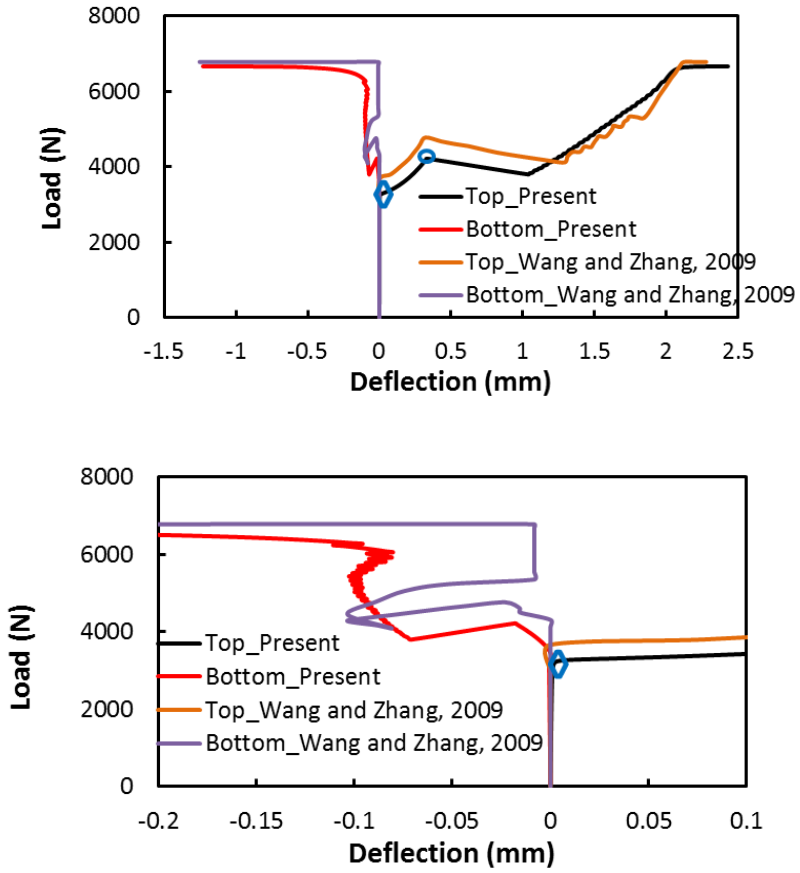

Fig. 25 Axial compressive load P vs. the mid-span deflection of the top and the bottom surfaces, symbol ◊ represents the local buckling load (3404 N), symbol ○ represents the load when the delamination begins to propagate (4226 N).

axial load at an axial strain of about 0.25% indicates that the delamination begins to propagate. The value of this load for the 121-node mesh exceeds that for the 161-node mesh by 5.0%, and the corresponding values of the axial strains differ by 5.6%. The axial load and the axial strain for the 161-node mesh at the instant of delamination propagation differ from the corresponding values found by Wang and Zhang [22] by 11 % and 10%, respectively.

Whereas the presently computed axial load vs. the axial engineering strain curve is close to that of Ref. [22], the axial load vs. the mid-span deflection curves exhibited in Fig. 25 show some deviations. With an increase in the axial compression, the upper sub-laminate buckles locally and its mid-span deflection increases significantly. The initiation of local buckling at an axial load of 3.4 kN is indicated by the symbol ◊. With

continued axial compression, both the axial load and the lateral deflections of the top and the bottom surfaces monotonically increase till delamination begins to propagate between the top layer and the core. As should be clear from the plot of the axial load vs. the delaminated length given in Fig. 26, the axial load slowly decreases from 4.2 kN with an increase in the delaminated length, and the delamination is unstable till the delaminated length equals about 34.4 mm. Subsequently, the axial load increases even though more of the interface is being delaminated which indicates stable delamination growth.

The lower sub-laminate begins to buckle when the load reaches the collapse load of 6.7 kN. The difference between the presently computed collapse load and that reported in [22] is 1.55%, however, both these values exceed the experimental value [23] of the collapse load by about 24% as should be clear from the variation of the axial load with the axial strain at the mid-span of the top surface displayed in Fig. 27. One possible reason for this difference is the failure of the material near the clamped ends that is not considered in both the present study and in [22]. The initiations of local buckling and unstable delamination growth agree with the experimental results of [23] except that we overestimate the collapse load.

Variations with the axial strain of the strain energy stored in the beam, the work done by external forces and the energy dissipated due to delamination are exhibited in Fig. 28. The total energy dissipated during delamination is only about 4% of the work done by external forces which is mostly stored as strain energy in the beam. We have plotted in Fig. 29 the deformed shapes of laminated beam corresponding to two values of the axial compressive strain.

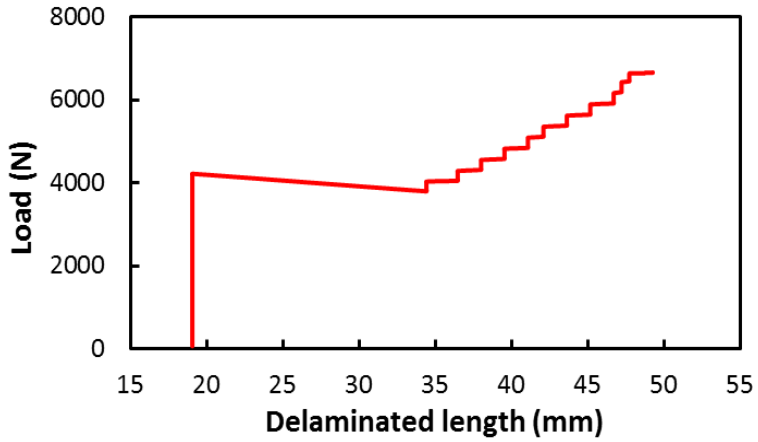

Fig. 26 Axial compressive load P vs. delaminated length during axial compression of an initially delaminated composite beam.

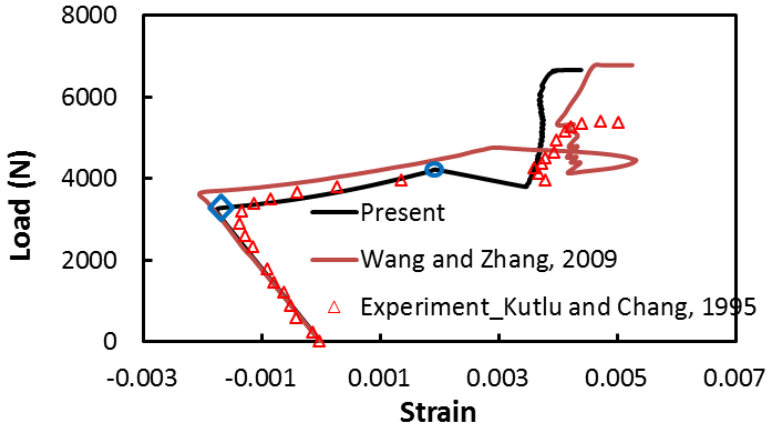

Fig. 27 Axial compressive load P vs. axial engineering strain, du/dx, at the mid-span of the top surface of the beam, symbol ◊ represents the local buckling load (3404 N), and symbol ○ represents the load when the delamination begins to propagate (4226 N).

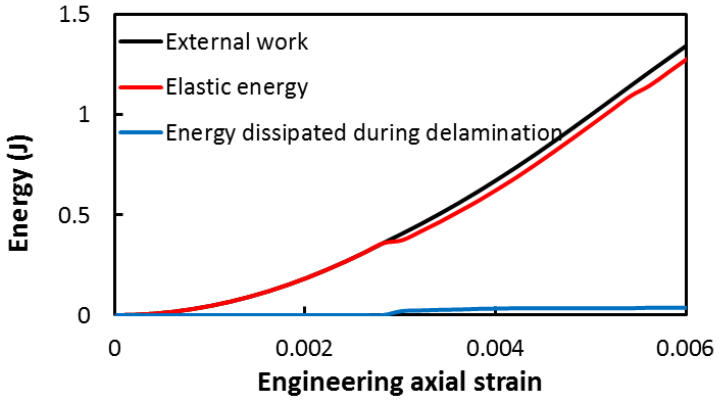

Fig. 28 Variation with the engineering axial strain of the work done by external forces, strain energy stored in the beam, and the energy dissipated during delamination.

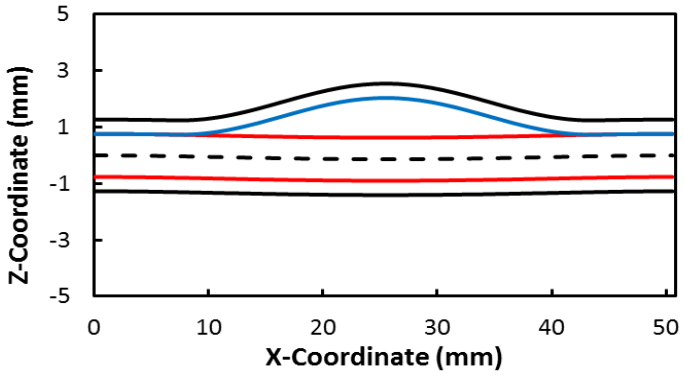

(a)

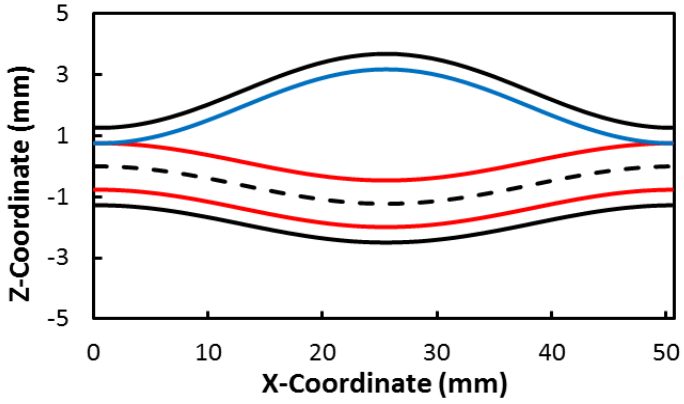

(b)

Fig. 29 Deformed shapes of the beam corresponding to engineering axial strain of (a) 0.33 %, and (b) 0.6 %.

4.5 Transient deformations

4.5.1 Transient deformations of DCB

We study delamination growth in dynamic mode-II deformations of the DCB specimen studied in subsection 4.1.3, take mass density equal to 2000 kg/m^3 , employ the same FE mesh (121 nodes) as that used in subsection 4.1.3, neglect effects of geometric nonlinearities, and compute results for Δ_3 = 2.5 m/s and 0.25 m/s. The load (P_3) - displacement (Δ_3) curves plotted in Fig. 30 reveal that inertial effects are insignificant for Δ_3 = 0.25 m/s but the larger value 2.5 m/s of Δ_3 results in oscillatory P_3 - Δ_3 curve suggesting that inertial effects are noticeable. The peak load for the transient problem with Δ_3 = 2.5 m/s is about 14% higher than that for the static problem. The time step used to compute results found by using the criterion discussed in Section 3.3 equaled $8 \times 10^{-9}\ s$.

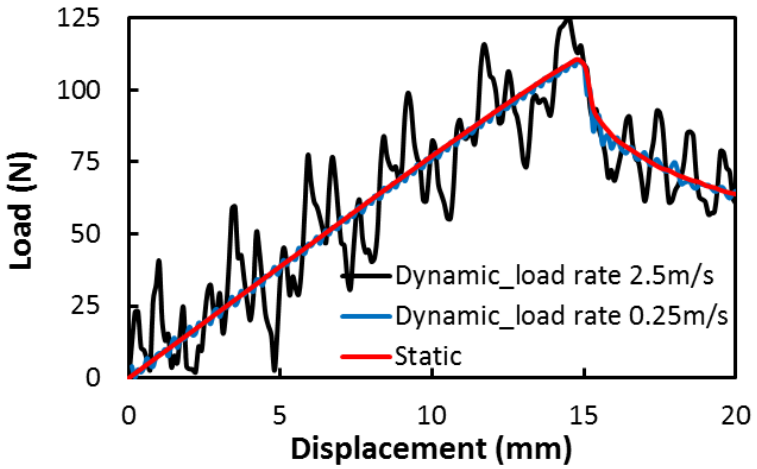

Fig. 30 Load P_3versus edge displacement Δ_3 curves for mode-II deformations with Δ_3 = 0.25 and 2.5 m/s (121 nodes).

4.5.2 Dynamic post-buckling deformations of pre-delaminated beam deformed in axial compression

We delineate the effect of inertia forces on post-buckling deformations of an initially debonded beam deformed in axial compression by restudying the problem of subsection 4.4 using the FE mesh with 121 nodes, taking mass density = 2000 kg/m^3 , and Δ_1 = 2.03 m/s and 0.203 m/s or equivalently axial strain rates of 40/s and 4/s,

respectively. The time step used to compute results found by using the criterion discussed in Section 3.3 equaled $1.4 \times 10^{-8}\ s$. The axial load vs. the engineering axial strain curves displayed in Fig. 31 reveal that, for Δ_1 = 2.03 m/s, the consideration of inertia effects increases the buckling load from 6.1 kN for the static analysis to 10.5 kN for the dynamic problem, i.e., by about 65%. Thus the dynamic load amplification factor (DLAF) equals 1.65. Batra and Geng [24] found that for a pinned-pinned column the DLAF varied from 1.69 to 8.59 when loading rate was increased from 20 kN/s to 1000 kN/s.

Variations of the axial compressive load P vs. the delaminated length for the two loading rates of Δ_1 are shown in Fig. 32. The load corresponding to the initiation of the unstable delamination growth increases with an increase in the loading rate, it equals 4.2, 5.5 and 10.5 kN for the quasistatic problem, Δ_1 = 0.203 m/s and Δ_1 = 2.03 m/s, respectively. The delaminated length that grows unstably changes from about 15 mm for the quasistatic problem to 32 and 25 mm for Δ_1= 0.203 and 2.03 m/s, respectively. We recall that present results have been computed by prescribing displacements at the end faces.

Fig. 33 shows deformed shapes of the beam for different loading rates when the engineering axial strain equals 0.8 %. Whereas delamination propagated to the ends of the beam for Δ_1= 0.203 m/s, it did not propagate to the end faces of the beam for Δ_1= 2.03 m/s because the beam buckled globally. In Fig. 34 we have plotted variation with the engineering axial strain of the mid-span deflections of the top and the bottom surfaces of the beam. These results suggest that an increase in the loading rate smoothens out the rate of increase of deflections of the two surfaces. The unstable growth of delamination could not be detected by studying the growth in the deformed shapes of the top and the bottom surfaces.

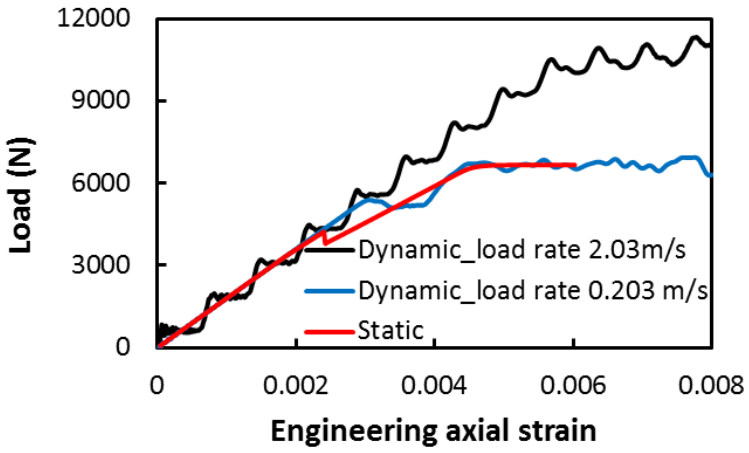

Fig. 31 Axial compressive load P vs. engineering axial strain for Δ_1 = 0.203 and 2.03 m/s.

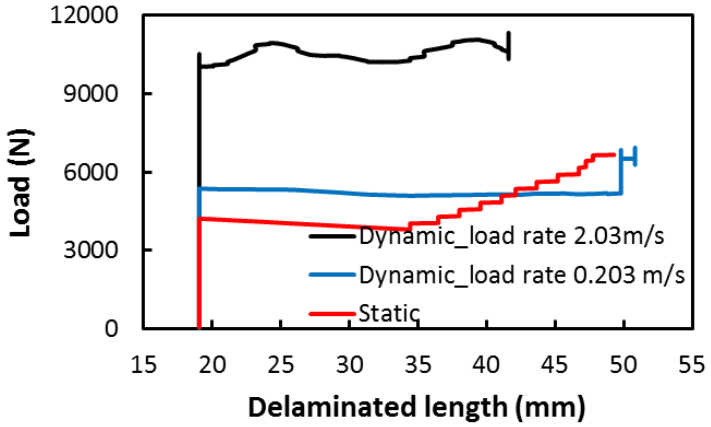

Fig. 32 Axial compressive load P vs. delaminated length for Δ_1 = 0.203 and 2.03 m/s.

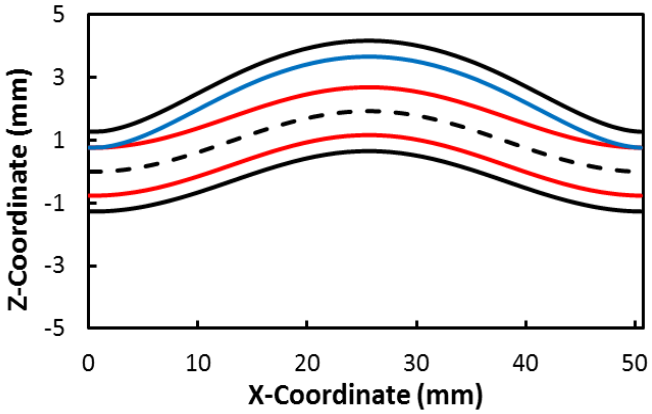

(a)

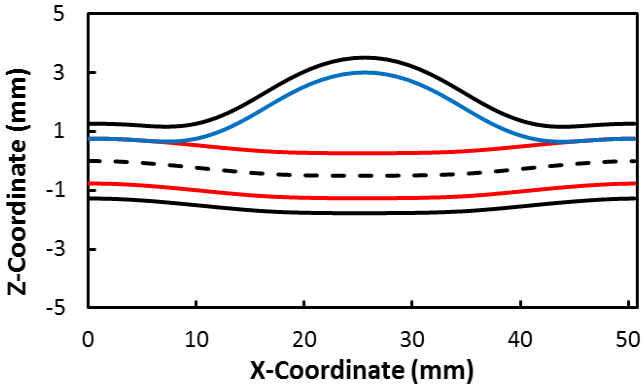

(b)

Fig. 33 At an engineering axial strain of 0.8%, deformed shapes of the beam for (a) Δ_1= 0.203 m/s, and (b) Δ_1 = 2.03 m/s.

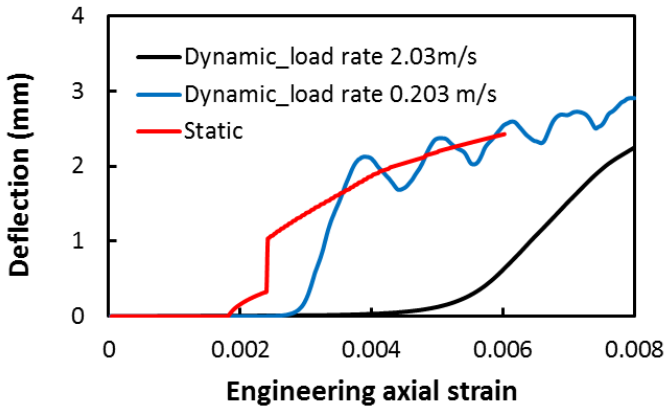

(a)

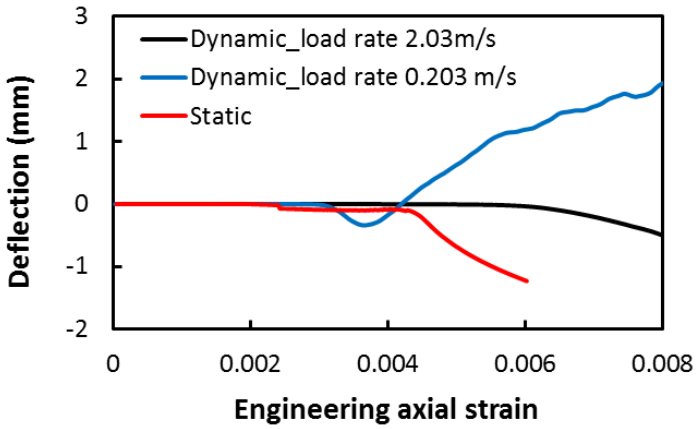

(b)

Fig. 34 For Δ_1 = 0.203 and 2.03 m/s, variation with the engineering axial strain of the mid-span deflection of (a) the top and (b) the bottom surfaces.

5. Conclusions

We have used a cohesive zone model (CZM) and a layer-wise shear and normal deformable beam theory (TSNDT) to analyze the delamination growth in a laminated composite beam, and compared our results with those available in the literature for four problems. The TSNDT used here accounts for all geometric nonlinearities including the von Karman nonlinearitiy. Presently computed results for mode-I, mode-II and mixed-mode deformations of straight and curved double cantilever beams (DCBs) under the assumption of infinitesimal deformations have been found to agree well with those of other investigators including results obtained using the linear elastic fracture mechanics approach. During the analysis of delamination growth in axial compression of an initially delaminated beam we found that local buckling ensues first and it is followed by global buckling. Because of the geometric nonlinearities considered, we could also analyze the post-buckling response of the beam which is found to agree well with experimental results reported in the literature. We have also studied the effect of inertia forces on the delamination growth in a predelaminated beam. It is found that for the applied axial strain rate of 40/s, the buckling load increases by 65% over that for the static problem, and the length of the unstably grown delaminated region decreases by 30%.

References

1. Irwin G.R., *Analysis of stresses and strains near the end of a crack traversing a plate.* Journal of Applied Mechanics, 1957.
2. Rice J.R., *A path independent integral and the approximate analysis of strain concentration by notches and cracks*, 1967, DTIC Document.
3. Hellen T.K., *On the method of virtual crack extensions.* International journal for numerical methods in engineering, 1975. **9**(1): p. 187-207.
4. Needleman A., *A continuum model for void nucleation by inclusion debonding.* Journal of Applied mechanics, 1987. **54**(3): p. 525-531.

5. Mi Y., M.A. Crisfield, G.A.O. Davies, and H.B. Hellweg, *Progressive delamination using interface elements.* Journal of Composite Materials, 1998. **32**(14): p. 1246-1272.
6. Tvergaard V. and J.W. Hutchinson, *The relation between crack growth resistance and fracture process parameters in elastic-plastic solids.* Journal of the Mechanics and Physics of Solids, 1992. **40**(6): p. 1377-1397.
7. Zou Z., S. Reid, and S. Li, *A continuum damage model for delaminations in laminated composites.* Journal of the Mechanics and Physics of Solids, 2003. **51**(2): p. 333-356.
8. Camanho P.P. and C.G. Dávila, *Mixed-mode decohesion finite elements for the simulation of delamination in composite materials.* NASA-Technical Paper, 2002. **211737**.
9. Balzani C. and W. Wagner, *An interface element for the simulation of delamination in unidirectional fiber-reinforced composite laminates.* Engineering Fracture Mechanics, 2008. **75**(9): p. 2597-2615.
10. Xie D. and A.M. Waas, *Discrete cohesive zone model for mixed-mode fracture using finite element analysis.* Engineering Fracture Mechanics, 2006. **73**(13): p. 1783-1796.
11. Allix O. and A. Corigliano, *Geometrical and interfacial non-linearities in the analysis of delamination in composites.* International Journal of Solids and Structures, 1999. **36**(15): p. 2189-2216.
12. Zhang Y. and S. Wang, *Buckling, post-buckling and delamination propagation in debonded composite laminates: Part 1: Theoretical development.* Composite Structures, 2009. **88**(1): p. 121-130.
13. Batra R.C. and J. Xiao, *Finite deformations of curved laminated St. Venant-Kirchhoff beam using layer-wise third order shear and normal deformable beam theory (TSNDT)* Composite structures 2013. **97**: p. 147-164.
14. Saada A.S., *Elasticity: theory and applications.*1993, Malabar,FL: Krieger.
15. Batra R.C., *Elements of continuum mechanics.*2006: AIAA.
16. Qian L.F. and R.C. Batra, *Three-dimensional transient heat conduction in a functionally graded thick plate with a higher-order plate theory and a meshless local Petrov-Galerkin method.* Computational mechanics, 2005. **35**(3): p. 214-226.
17. Xiao J.R., D.F. Gilhooley, R.C. Batra, J.W. Gillespie, and M.A. Mccarthy, *Analysis of thick composite laminates using a higher-order shear and normal deformable plate theory (HOSNDPT) and a meshless method.* Composites Part B: Engineering, 2008. **39**(2): p. 414-427.
18. Hashemi S., A.J. Kinloch, and J.G. Williams, *The analysis of interlaminar fracture in uniaxial fibre-polymer composites.* Proceedings of the Royal Society of London. A. Mathematical and Physical Sciences, 1990. **427**(1872): p. 173-199.
19. Chen J., M. Crisfield, A. Kinloch, E. Busso, F. Matthews, and Y. Qiu, *Predicting progressive delamination of composite material specimens via interface elements.* Mechanics of composite materials and structures, 1999. **6**(4): p. 301-317.
20. Goyal V.K., E.R. Johnson, and C.G. Dávila, *Irreversible constitutive law for modeling the delamination process using interfacial surface discontinuities.* Composite Structures, 2004. **65**(3): p. 289-305.

21. Guedes R.M., A. S á and M. De Moura, *An experimental and numerical assessment of DCB tests on glass/polyester curved beams cut out from pipes.* Polymer Testing, 2008. **27**(8): p. 985-994.
22. Wang S. and Y. Zhang, *Buckling, post-buckling and delamination propagation in debonded composite laminates Part 2: Numerical applications.* Composite Structures, 2009. **88**(1): p. 131-146.
23. Kutlu Z. and F.K. Chang, *Composite panels containing multiple through-the-width delaminations and subjected to compression. Part II: experiments & verification.* Composite Structures, 1995. **31**(4): p. 297-314.
24. Batra R.C. and T.S. Geng, *Enhancement of the dynamic buckling load for a plate by using piezoceramic actuators.* Smart Materials and Structures, 2001. **10**(5): p. 925.

Chapter 3: Local water slamming of curved rigid hulls

Abstract

We use the boundary element method (BEM) to study transient plane strain deformations of water induced by a rigid hull impacting at normal incidence initially stationary water occupying a half space with the goal of finding the hydrodynamic pressure acting on the hull. Water is assumed to be incompressible and inviscid, and its deformations to have zero vorticity. Thus deformations of water are governed by the Laplace equation. Challenging issues addressed are finding the free surface of water whose evolution is governed by a nonlinear partial differential equation, determining the *a priori* unknown wetted length, and ensuring that water maintains contact with the hull without penetrating into it. The solution of the problem using the commercial software, LSDYNA, resulted in water penetrating into a rigid hull. The developed BEM code has been verified by using the method of manufactured solutions. Computed results for the hydrostatic pressure on straight hulls and ship bow section are found to compare well with the corresponding experimental findings. It is found that the peak pressure acting near the terminus of the wetted length decreases with an increase in the radius of the circular hull.

Key Words: Water slamming, curved hulls, ship bow section

1. Introduction

Local water slamming is characterized by large hydrodynamic loads of short duration which can cause significant structural damage, e.g., see Faltinsen [1]. The water entry of a rigid V-shaped wedge of small deadrise angle β was first studied by von Kármán [2]. Subsequently, Wagner [3] generalized von Kármán's work by including effects of water splash-up on the body. Similarity solutions for water slamming of a rigid wedge were developed by Dobrovol'skaya [4] for β greater than 30° and by Zhao and Faltinsen [5] for $4^{\circ} \leq \beta \leq 81^{\circ}$. Zhao et al. [6] generalized Wagner's solution for arbitrary values of β and numerically solved the problem using the boundary integral

method. Effects of jet flow were neglected and computed results were found to agree with the corresponding experimental findings. Mei et al. [7] analytically and numerically solved the two-dimensional water impact problem for wedges and circular cylinders including effects of jet flow. Yettou et al. [8] experimentally measured hydrodynamic pressures acting on rigid wedges during their free fall into stationary water and also analytically solved the problem.

Fluid motions of water entry problems have been simulated by several numerical techniques such as the finite element method (FEM) [9], the FEM with Arbitrary-Lagrangian-Eulerian (ALE) formulation [10], smoothed particle hydrodynamics (SPH) method [11] and the boundary element method (BEM) [5], [12], [13]. Zhao and Faltinsen [5] analyzed the water entry of a rigid wedge using the BEM and compared computed results with those obtained by the similarity method. Lin and Ho [12] used the BEM to study the influence of water depth on the slamming pressure acting on a rigid wedge. They found that the maximum impact pressure is larger for shallow water than that for deep water which agreed with their experimental observations. Battistin and Iafrati [13] used the BEM to simulate two-dimensional water entry problems of arbitrary shaped bodies.

In practical water slamming problems, the hull is curved and deformable. Hull's deformations affect the motion of the fluid and the hydroelastic pressure acting on the solid-fluid interface. Sun [14] and Sun and Faltinsen [15, 16] numerically analyzed water slamming problems for arbitrary geometries using the BEM for studying deformations of water that was modeled as non-viscous and incompressible, and modal analysis for deformations of the cylindrical shell. They considered effects of gravity and flow separation from the solid surface. Qin and Batra [17] studied the hydroelastic problem using $\{3,2\}$-order plate theory for a sandwich hull of small deadrise angle and modified Wagner's water impact theory to consider the fluid-structure interaction during slamming. The plate theory incorporates the transverse shear and the transverse normal deformations of the core, but not of the face sheets which were modeled as Kirchhoff plates. Das and Batra [18] studied the water slamming of deformable sandwich hulls using the commercial FE software LSDYNA with the ALE formulation. They considered all

geometric nonlinearities when studying hull's deformations, assumed the fluid to be compressible, accounted for inertia effects in the fluid and the solid, and examined delamination between the core and the face sheets. They pointed out that boundary conditions at the fluid/solid interface were not well satisfied since the fluid penetrated into the rigid hull. Stenius et al. [19] used LSDYNA to study hydroelastic effects for deformable hulls considering different boundary conditions, impact velocities, deadrise angles, membrane effects and hull materials. Lu et al. [20] employed the coupled BEM and the FEM for studying hydroelastic effects with the hull modeled as a Timoshenko beam. Panciroli et al. [21] experimentally and numerically analyzed the water slamming of linear elastic wedges. The experimental results for different values of the panel thickness, deadrise angle and entry velocity were compared with those obtained by using the SPH formulation in LSDYNA. Oger et al. [11] used twenty million particles to correctly predict the pressure on the wedge. Experimental results for the failure of deformable sandwich composite panels including core shear, delamination and damage of the face sheets due to water slamming are reported in [22, 23]. Hu et al. [24] approximated the slamming pressure by equivalent bending moment to study delamination of a composite hull using the FE software ANSYS and the cohesive zone model. Water slamming problem for a composite hull of a rather complex shape has been analyzed by Paepegem et al. [25] both numerically using ABAQUS and experimentally. Aureli et al. [26] have exploited deformations due to fluid structure interaction to harvest energy.

We focus here on delineating the effect of hull curvature on pressure acting on the hull. Even though hulls deform due to water slamming loads and the maximum hydrodynamic pressures acting on rigid and deformable hulls may be different, estimates of the maximum pressure on rigid hulls will provide useful guidelines for designers.

2. Problem Formulation

A schematic sketch of the problem studied is shown in Fig. 1. At time t = 0, the ship hull keel impacts at normal incidence with vertically downward velocity V stationary water occupying the semi-infinite domain $Z \leq 0$ when rectangular Cartesian

coordinates (X, Y, Z) fixed to the earth are used to describe deformations of the fluid. We simplify the problem by assuming that the hull dimensions in the Y-direction are very large so that a plane strain state of deformation in the XZ-plane can be assumed and the problem can be solved as 2-dimensional (2-D). Furthermore, we assume that the hull geometry is symmetric about the plane X = 0 and it initially impacts water along the line X = Z = 0. Thus deformations of water in the region $X \geq 0$ and $Z \leq 0$ and motion of the right-half of the hull are analyzed.

We note that the hydrodynamic load acting on the hull is highly localized; thus the slamming problem is idealized as that of either straight or curved wedge entering water with a vertically downward speed (see Fig. 1) that may change due to the force exerted by water on the hull and the consideration of gravity forces. Even though gravity and surface tension effects are not considered in studying deformations of water, the analysis could be modified to account for gravitational forces. We derive equations governing deformations of water using balance laws of mass, linear momentum and moment of momentum, and the continuity of velocity and surface tractions at the hull/water interface. Sources of nonlinearities include (i) the *a priori* unknown length of the wetted surface, (ii) dependence of pressure at a point on the square of the velocity potential gradient, and (iii) the *a priori* unknown deformed shape of the free surface of water. Both the wetted length and the shape of the free surface of water are to be determined as a part of the solution of the problem.

2.1 Equations governing deformations of the fluid

For hull speeds of the order of 10 m/s, viscous effects in water are often neglected. Also, the time duration during which the compressibility of water likely plays a noticeable role is considerably smaller than that of interest in the water slamming problem. We thus assume the water to be incompressible, homogeneous and inviscid and its deformations to be irrotational. The assumption of null vorticity implies that there exists a velocity potential φ such that velocity $\boldsymbol{v} = -\nabla\varphi$, where ∇ is the spatial gradient operator in the XZ-plane. The assumption of incompressibility requires that φ satisfy the Laplace equation:

$$\frac{\partial^2\varphi}{\partial Z^2}+\frac{\partial^2\varphi}{\partial X^2}=0\ , \qquad \text{in the water domain.} \tag{1}$$

Eq. (1) expresses the balance of mass. In the absence of gravity force, the balance of linear momentum for an inviscid fluid gives

$$\rho\frac{D\boldsymbol{v}}{Dt}=-\nabla p, \tag{2}$$

Where ρ is the mass density of water, D/Dt is the total time derivative, and the hydrostatic pressure p is determined by solving Eq. (2) under the following boundary conditions.

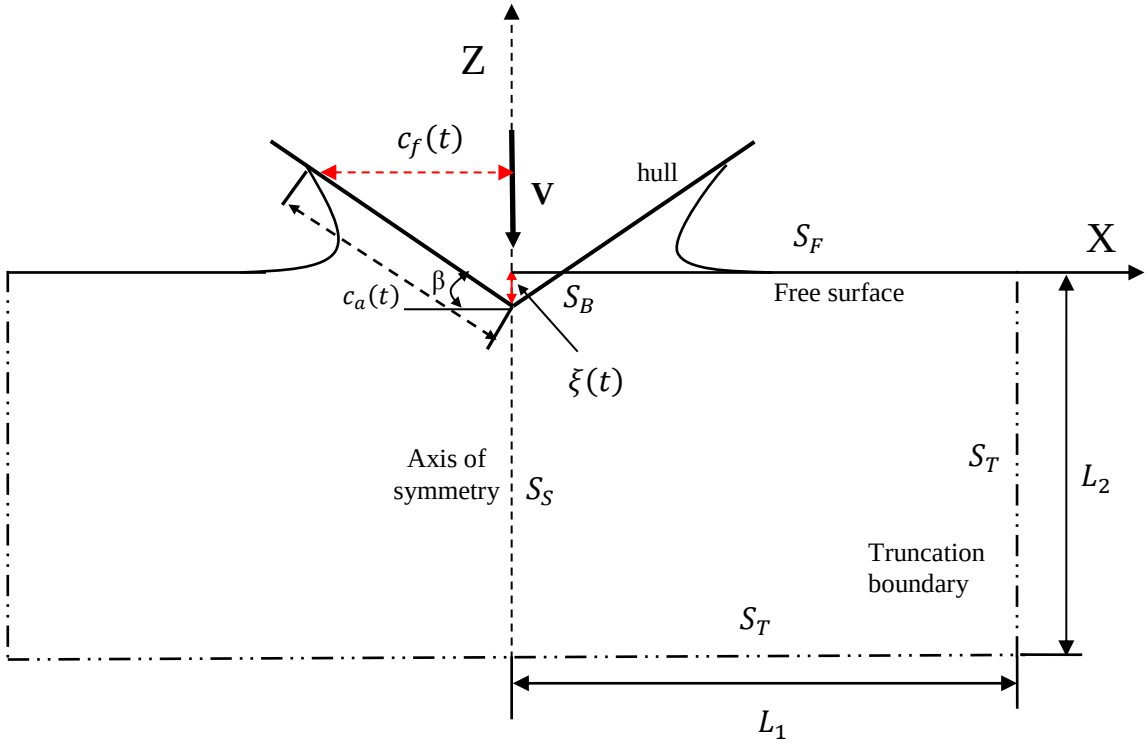

Fig. 1 Schematic sketch of the water slamming problem studied

$p = p_a$, $\frac{DX}{Dt}=-\frac{\partial\varphi}{\partial X}$, $\frac{DZ}{Dt}=-\frac{\partial\varphi}{\partial Z}$, $\frac{D\varphi}{Dt}=-\frac{1}{2}|\nabla\varphi|^2$ on the free surface of water, (3.a)

$|\boldsymbol{v}| \to 0$ as $(X^2 + Z^2)^{1/2} \to \infty$ for $X > 0$ and $Z \leq 0$, (3.b)

$\frac{\partial\varphi}{\partial X}=0$ on $X = 0$. (3.c)

Here p_a is the atmospheric pressure. In writing boundary condition (3.a) we have tacitly neglected the surface tension effect. These equations imply that the velocity of a point on the free surface equals that of the fluid particle instantaneously occupying it. Eq. $(3.a)_4$ following from Eq. $(3.a)_1$ and the Bernoulli Eq. (5) is used to update the function φ on the free surface after every time step. Ideally one should specify in Eq. (3.b) the rate of decay of the speed of water at infinity. However, we do not do so since the domain occupied by the fluid will be truncated to a finite one when numerically solving the problem. The boundary condition (3.c) follows from the assumption that deformations are symmetric about the plane X = 0. At the fluid/hull interface the non-penetration of the fluid into the solid is satisfied if

$$\frac{\partial \varphi}{\partial \mathrm{n}} = -\mathbf{V} \cdot \boldsymbol{n} \tag{4}$$

where **V** is velocity of the hull particle and $\boldsymbol{n}$ is a unit vector normal to the fluid/hull interface (pointing into hull).

We note that Eqs. (1) – (4) for finding p and $\boldsymbol{v}$ are coupled, Eq. $(3.a)_4$ is nonlinear in φ, and the free surface of water and the wetted surface of hull are to be determined as parts of the solution of the problem.

Recalling that $\boldsymbol{v} = -\nabla\varphi$, Eq. (2) can be integrated to give the following Bernoulli equation:

$$\mathrm{p} - \mathrm{p_a} = -\rho\left(-\frac{\partial \varphi}{\partial \mathrm{t}} + \frac{1}{2}|\nabla\varphi|^2\right) \tag{5}$$

2.2 Numerical Solution of the Problem

2.2.1 Analysis of fluid's deformations by the BEM

We use the BEM to solve Laplace Eq. (1) and truncate the domain occupied by the fluid to lengths L_1 and L_2 in the X- and Z- directions, respectively (cf. Fig. 1). Values of L_1 and L_2 will be determined iteratively to compute a converged solution near the hull/water interface.

Using Green's second identity, the velocity potential at point *j* in the fluid (either in the interior or on the boundary) can be written as [27] :

$$c(j)\varphi(j) = \int_{\partial\Omega} G(\boldsymbol{\xi}, j)\frac{\partial\varphi(\boldsymbol{\xi})}{\partial n}ds(\boldsymbol{\xi}) - \int_{\partial\Omega}\varphi(\boldsymbol{\xi})\frac{\partial G(\boldsymbol{\xi},j)}{\partial n}ds(\boldsymbol{\xi}) \quad (6)$$

where $G(\boldsymbol{\xi}, j) = \ln r(\boldsymbol{\xi}, j)$, $r(\boldsymbol{\xi}, j)$ is the distance between source point $\boldsymbol{\xi}$ on the fluid boundary and point *j* , c(j) is a constant, $\boldsymbol{n}$ is a unit normal pointing out of the fluid domain, and Ω equals the region occupied by the fluid. We note that c, φ, Ω and $\boldsymbol{n}$ vary with time t; this dependence is not exhibited to simplify the notation. Since Eq. (6) holds even when the velocity potential is a constant, we get

$$c(j) = -\int_{\partial\Omega}\frac{\partial G(\boldsymbol{\xi},j)}{\partial n}ds(\boldsymbol{\xi}) \quad (7)$$

The integral Eq. (6) is converted into a system of simultaneous linear algebraic equations by using piecewise linear basis functions, i.e., the boundary of the fluid domain is discretized by using 2-node 1-D elements. Since $G(\boldsymbol{\xi}, j) = \ln r(\boldsymbol{\xi}, j)$ the integrals in Eq. (6) are numerically evaluated by using 6 Gauss points in each element. Thus Eq. (6) can be written as

$$[H]\begin{Bmatrix}\varphi^{F}\\ \varphi^{B}\\ \varphi^{T+S}\end{Bmatrix} = [G]\begin{Bmatrix}\frac{\partial\varphi^{F}}{\partial n}\\ \frac{\partial\varphi^{B}}{\partial n}\\ \frac{\partial\varphi^{T+S}}{\partial n}\end{Bmatrix} \quad (8)$$

where elements of matrices $[H]$ and $[G]$ depend upon coordinates of nodes, and superscripts F, B, T and S on a quantity represent, respectively, its value at a node on the free surface, the hull/water interface, the truncation boundaries and the axis of symmetry.

Recalling that at time *t* we know at every point on the fluid boundary either φ or $\frac{\partial\varphi}{\partial n}$ we can solve for the other variable at that point. Transforming unknowns in Eq. (8) to the left hand side, we rewrite Eq. (8) as

$$[A]\begin{Bmatrix} \frac{\partial \varphi^{F}}{\partial n} \\ \varphi^{B} \\ \varphi^{T+S} \end{Bmatrix} = [B]\begin{Bmatrix} \varphi^{F} \\ \frac{\partial \varphi^{B}}{\partial n} \\ \frac{\partial \varphi^{T+S}}{\partial n} \end{Bmatrix} \tag{9}$$

In writing Eq. (9) we have used boundary conditions listed in Eq. (4) and taken the velocity of hull particles to be known. After having solved Eq. (9) we know φ and $\frac{\partial \varphi}{\partial n}$ at every point on the fluid boundary at time *t*. Thus the tangential derivative $\frac{\partial \varphi}{\partial s}$ of φ at points on the boundary $\partial\Omega$ can be computed; here *s* is the arc length along $\partial\Omega$. Combining $\frac{\partial \varphi}{\partial s}$ with the computed $\frac{\partial \varphi}{\partial n}$ on $\partial\Omega$, the gradient vector $\nabla\varphi$ at points on the hull/water interface and on the free surface of water is determined, and the free surface profile, and values of φ at points on the free surface are updated using Eq. (3.a). Eq. (6) is used to determine the velocity potential φ at any point in the fluid domain.

We need to determine $\frac{\partial \varphi}{\partial t}$ to obtain the pressure field in the fluid domain from Eq. (5). It is found by introducing a new variable Ψ defined by

$$\Psi = \frac{\partial \varphi}{\partial t} + \mathbf{V} \cdot \nabla\varphi \tag{10}$$

It has been proved by Greco [28] that Ψ also satisfies the 2-D Laplace equation

$$\frac{\partial^2 \Psi}{\partial X^2} + \frac{\partial^2 \Psi}{\partial Z^2} = 0 \tag{11}$$

Following Sun [14] and deferring details to the Appendix, boundary conditions for Ψ are

$$\Psi = \mathbf{V} \cdot \nabla\varphi + \frac{1}{2}|\nabla\varphi|^2 \qquad \text{on the free surface,} \tag{12.a}$$

$$\frac{\partial \Psi}{\partial n} = -\boldsymbol{n} \cdot \dot{\mathbf{V}} \qquad \text{on the solid body/fluid interface,} \tag{12.b}$$

$$\frac{\partial \Psi}{\partial n} = 0 \qquad \text{on the axis of symmetry and on truncation boundaries.} \tag{12.c}$$

here $\dot{\mathbf{V}}$ is the acceleration of the rigid body motion of particles on the hull surface.

At every time *t*, the boundary value problem defined by Eqs. (11) and (12) is numerically solved by the BEM. The algebraic equation for the determination of Ψ and $\frac{\partial \Psi}{\partial n}$ at boundary points is

$$[A]\begin{Bmatrix} \frac{\partial \Psi^{\mathrm{F}}}{\partial n} \\ \Psi^{\mathrm{B}} \\ \Psi^{\mathrm{T+S}} \end{Bmatrix} = [B]\begin{Bmatrix} \Psi^{\mathrm{F}} \\ \frac{\partial \Psi^{\mathrm{B}}}{\partial n} \\ \frac{\partial \Psi^{\mathrm{T+S}}}{\partial n} \end{Bmatrix} \tag{13}$$

where matrices $[A]$ and $[B]$ are the same as those in Eq. (9). Knowing Ψ and φ, from Eq. (10) $\frac{\partial \varphi}{\partial t}$ can be evaluated at all points on the fluid boundary including those on the fluid/solid interface. This approach avoids finding $\frac{\partial \varphi}{\partial t}$ by the backward difference method at the computational cost of solving twice the boundary value problem for the fluid. Recall that the value of φ at any point in the fluid domain is found from Eqs. (6) and (7).

2.2.2 Analysis of the motion of free surface of water

The free surface of stationary water changes rapidly when a solid body enters it at time $t = 0$. For small values of time *t* Sun [14] proposed that the free surface profile for the water entry of a straight solid body can be approximated by

$$Z(t) = \frac{X\xi(t)}{c_f(t)} arcsin\left(\frac{c_f(t)}{X}\right) - \xi(t) \quad for \;\; X > c_f(t), \tag{14}$$

where $\xi(t)$ is the submergence of the solid body apex relative to the undisturbed free surface,

$$c_f(\delta t) = \frac{\pi\xi(\delta t)}{2tan\beta}, \tag{15}$$

is the absolute value of X-coordinate of jet tip, and β is the deadrise angle; $\xi(t)$ and $c_f(t)$ are shown in Fig. 1. Eq. (15) is Wagner's [3] approximation and is generally valid for small values of β.

For water slamming of a circular hull with the deadrise angle at $X = 0$ not equal to zero, we assume that the hull region close to the apex can be regarded as straight and

approximate the free surface of water near the apex using Eq. (14). For an arbitrary shaped hull with deadrise angle at $X = 0$ equal to zero, we assume that the free surface of water is undisturbed for the first time step. The velocity potential on the free surface is assumed to be zero at the initial time. Assuming that the downward velocity at the apex of the hull will not change during a short period of time, the first time step size δt is obtained from Eq. (14) with $c_f(\delta t) = 0.005\mathcal{L}$ where $\mathcal{L}$ is the hull arc length, and $\xi(\delta t) = V\delta t$.

A very thin jet in the water surface is generally formed where water separates from the solid hull surface. Capturing this jet is computationally expensive. One way to alleviate this problem is to truncate the jet. For example, Zhao and Faltinsen [5] as well as Battistin and Iafrati [13] accomplish this by putting an element perpendicular to the wedge when the angle between the water surface and the wedge is smaller than a threshold value. This usually results in oscillatory pressure distribution on the wedge. As shown in Fig. 2a, Sun [14] introduced a new segment on the free surface when the jet became too thin, i.e., when distance from point B to the solid body becomes smaller than a threshold value d_0, the point is projected on the wedge and a new segment CD replaces the free water surface CA. Point B is found by starting from a point away from the jet tip, and evaluating the distance of this point from the hull. Point B is the first node on the free surface of water whose distance from the hull is less than the threshold value d_0. We note that Sun [16] did not elaborate upon the method to find point B. This method reduces oscillations in the pressure distribution on the hull; we name this approach of truncating the jet as "distance cut method". We adopt a similar method and call it "angle cut method". Referring to Fig. 2b, we find the tangent at every point of the free surface of water and the tangent at the corresponding point to the solid body surface. The angle θ between the two tangents at the abutting points of the fluid and the solid is calculated. Starting from the jet tip A, we find the first point E on the jet surface for which θ is larger than the threshold value θ_0. When the length between points E and A becomes more than the jet cut threshold length λ_0, point B is projected on the wedge to point D. λ_0 is equal to $0.01\mathcal{L}$ in present study and $\mathcal{L}$ is the arc length of the hull. The length between points E and B is called the jet keep length λ_1, and it is taken to equal $0.8\lambda_0$. Point C on the jet is

selected such that length CB, called the jet smoothing length λ_2 equals $0.1\lambda_0$. A new section CD replaces CA and values of the velocity potential at points on CD are derived by interpolating and extrapolating from those on the section CB. Battistin and Iafrati [13] suggested that the threshold angle, θ_0, should be between 4^o and 10^o depending upon the hull shape; here we take $\theta_0 = 4^0$. Thus we first find the jet starting point E as described above, and then locate points B and C according to the values of the jet keep length and the jet smoothing length, respectively, point D is the projection of point B onto the solid body.

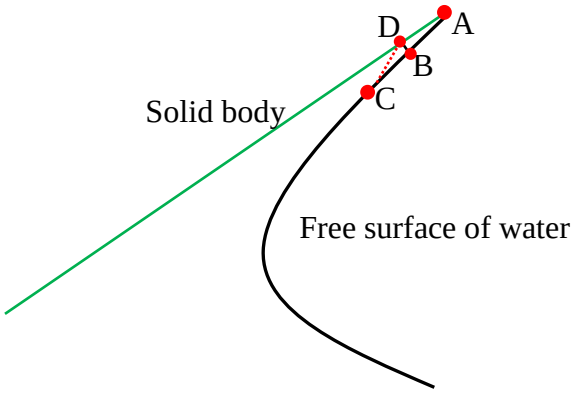

a. Distance cut method for truncating a thin jet

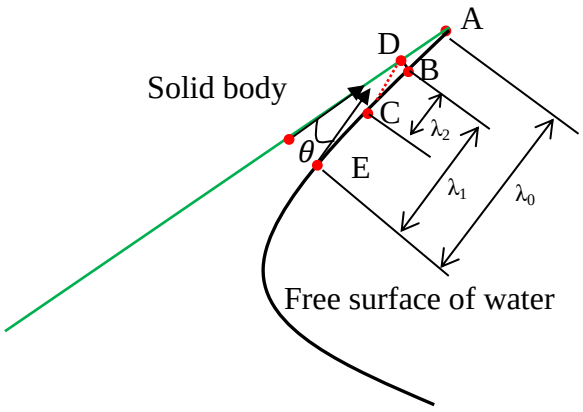

b. Angle cut method for truncating a thin jet (λ_1=0.8 λ_0, $\lambda_{2=}$=0.1λ_0)

Fig. 2 Two techniques for truncating a thin jet

Even with the truncating of a thin jet the numerical solution becomes unstable due to the free surface profile becoming non-smooth after the solution has been computed for several time steps. Many smoothing methods have been proposed to remove the saw-tooth instability in the free surface. We smooth the X – and $Z-$ coordinates and the velocity potential φ using the smooth function defined in Longuet and Cokelet [29]. A function $\mathcal{F}(s)$ defined at points s_j (j=1, 2,…, N) can be locally approximated by the function

$$f(s) = (a_0 + a_1 s + a_2 s^2) + (-1)^j (b_0 + b_1 s) \tag{16}$$

Here s is the arc length along the water surface, and a_0 , a_1…, b_0 , b_1… are coefficients which can be chosen uniquely by setting $f(s) = \mathcal{F}(s)$ at nodes s_{j-2}, s_{j-1}, s_j, s_{j+1}, and s_{j+2} when j=3,4,…,N-2. These coefficients for end nodes j=1, 2 and j=N, N-1 can be evaluated uniquely by setting $f(s) = \mathcal{F}(s)$ at the first and the last 5 nodes, respectively. Terms in the first parentheses in Eq. (16) give the smoothed mean curve, and those in the second parentheses represent oscillations in the data. Omitting terms in the second parentheses we get the smooth function

$$\bar{f}(s) = a_0 + a_1 s + a_2 s^2 \tag{17}$$

as the approximation of $\mathcal{F}(s)$.

Assuming the nodes are uniformly distributed when j=1, 2, N-1, N, and non-uniformly distributed for other values of j, the five-point smoothing function can be written as

$$\bar{f}_1 = \frac{11f_1+12f_2-6f_3-4f_4+3f_5}{16} \ , \tag{18.a}$$

$$\bar{f}_2 = \frac{3f_1+8f_2+6f_3-f_5}{16} , \tag{18.b}$$

$$\bar{f}_j = c_{j-2}f_{j-2} + c_{j-1}f_{j-1} + c_j f_j + c_{j+1}f_{j+1} + c_{j+2}f_{j+2} \ , \tag{18.c}$$

$$\bar{f}_{N-1} = \frac{3f_N + 8f_{N-1} + 6f_{N-2} - f_{N-4}}{16} , \tag{18.d}$$

$$\bar{f}_N = \frac{11f_N + 12f_{N-1} - 6f_{N-2} - 4f_{N-3} + 3f_{N-4}}{16} \ , \tag{18.e}$$

where

$$c_{j-2} = -\frac{\mathrm{h_j h_{j-1}}}{2(\mathrm{h_{j-1}+h_{j-2}})(\mathrm{h_{j-1}+h_{j-2}+h_j+h_{j+1}})} \ , \ c_{j-1} = \frac{\mathrm{h_j}}{2(\mathrm{h_{j-1}+h_j})} \ ,$$

$$c_j = \frac{(\mathrm{h_{j-1}+h_{j-2}})(2\mathrm{h_j+h_{j+1}})-\mathrm{h_j h_{j-2}}}{2(\mathrm{h_{j-1}+h_{j-2}})(\mathrm{h_j+h_{j+1}})} \ , \quad c_{j+1} = \frac{\mathrm{h_{j-1}}}{2(\mathrm{h_{j-1}+h_j})} \ ,$$

$$c_{j+2} = -\frac{\mathrm{h_j h_{j-1}}}{2(\mathrm{h_j+h_{j+1}})(\mathrm{h_{j-1}+h_{j-2}+h_j+h_{j+1}})} \ ,$$

and $\mathrm{h_j}$ is the distance between nodes j and j+1, i.e.,

$$h_j = \sqrt{\left(X_{j+1} - X_j\right)^2 + \left(Z_{j+1} - Z_j\right)^2} \tag{19}$$

Here, N is the total number of nodes on the free surface to be smoothed.

By approximating the arc length between nodes i and $i+1$ by h_i we find the arc length of any point on the free surface of water. The corresponding X- and Z-coordinates and the potential φ near the jet are found by using Eq. (18)**.**

Matrices A and B in Eqs. (9) and (13) whose elements depend upon current coordinates of node points are evaluated after every time step. Thus we refine the mesh after every time step, and evaluate values of variables at the nodes of the new mesh from their values at the nodes of the previous mesh by using three-point spline functions, e.g., see Pozrikidis [30].

2.2.3 Numerical integration of governing equations

The fourth-order Runge-Kutta method is used to numerically integrate the system of first order ordinary differential equations included in Eq. (3.a) for $X, \quad Z$ and φ with $\frac{\partial \varphi}{\partial n}$ on the boundaries regarded as known and kept fixed. Using the notation $\Xi = \{X, \quad Z, \quad \varphi\}$, we write these three equations as

$$\frac{d\Xi}{dt} = f\left(\Xi, \ \frac{\partial \varphi}{\partial n}\right) \tag{20}$$

The fourth-order Runge-Kutta integration method [14] gives

$$\Xi^{i+1} = \Xi^i + (k_1 + 2k_2 + 2k_3 + k_4)\delta t/6 \,, \tag{21}$$

where

$$k_1 = f\left(\Xi^i,\ \frac{\partial\varphi^i}{\partial n}\right) \,, \qquad k_2 = f\left(\Xi^i + k_1\delta t/2,\ \frac{\partial\varphi^i}{\partial n}\right),$$

$$k_3 = f\left(\Xi^i + k_2\delta t/2,\ \frac{\partial\varphi^i}{\partial n}\right) \,, \qquad k_4 = f\left(\Xi^i + k_3\delta t,\ \frac{\partial\varphi^i}{\partial n}\right),$$

and Ξ^i is the value of Ξ at time step i. Battistin and Iafrati [13] used one node per element and suggested that the time step size should be such that the maximum displacement of a point during a time step is less than one fourth of the corresponding element length. Here we approximate the jet tip velocity by the time derivative of $c_f(t)$ defined in Eq. (15) and select the time step size by requiring that it takes γ_t time steps for the jet tip to travel the length of one element. Thus

$$\delta t = \frac{h_{min} 2tan\beta}{V\pi\gamma_t} \tag{22}$$

where h_{min} is minimum element length near the jet tip, γ_t is assigned values between 2 and 20; here we use γ_t= 5. For the water slamming of a curved hull shown in Fig. 19, we choose β as the minimum of the local deadrise angles at nodes on the water/fluid interface, slope of the free water surface at nodes on it, and the local angle at the jet tip.

2.2.4 Analysis of hull's rigid body motion

Let $V(t)$ be the projection of the rigid body velocity $\boldsymbol{V}$ along the Z-direction and $\dot{V}(t)$ be the corresponding acceleration, the rigid body acceleration of the hull in the Z-direction is calculated from

$$\dot{V}(t) = \frac{F_Z}{M^*} - g \tag{23.a}$$

$$F_Z = -M_a^*\dot{\mathrm{V}} + F_Z' \tag{23.b}$$

here M^* is the total mass of the hull, g the acceleration due to gravity, and F_Z the total upward force due to water slamming. We note that F_Z is an implicit function of the acceleration of fluid particles contacting the hull, and we decompose it into two parts; the upward force $F_Z^{'}$ without considering acceleration of fluid particles and $M_a^*\dot{\mathrm{V}}$ that depends upon the acceleration of fluid particles abutting the hull. The quantity M_a^* is called the added mass since the term $M_a^*\dot{\mathrm{V}}$ is usually transferred to the left hand side and lumped with the inertia force of the structure. Thus the net effect is equal to considering a larger mass of the structure than its true mass.

Young [30] studied the hydroelastic problem for propulsors by coupled BE and FE methods and the added mass matrix for the FE analysis of the solid body was obtained from the solution of the fluid problem by the BEM. We separate the pressure term due to fluid particles' acceleration and calculate the added mass effect for rigid body motion. It can successfully simulate the free drop test of light weight rigid wedge and rigid ship bow section.

Substituting for $\frac{\partial \Psi^{\mathrm{B}}}{\partial n}$ from Eqs. (12.b) and (12.c) into Eq. (13) we get

$$[A]\begin{Bmatrix} \frac{\partial \Psi^{\mathrm{F}}}{\partial n} \\ \Psi^{\mathrm{B}} \\ \Psi^{\mathrm{T+S}} \end{Bmatrix} = [B]\begin{Bmatrix} \Psi^{\mathrm{F}} \\ -\boldsymbol{n}\cdot\dot{\mathbf{V}} \\ 0 \end{Bmatrix} \tag{24}$$

With the notation

$$[\mathbb{Q}] = \begin{bmatrix} \mathbb{Q}_{11} & \mathbb{Q}_{12} & \mathbb{Q}_{13} \\ \mathbb{Q}_{21} & \mathbb{Q}_{22} & \mathbb{Q}_{23} \\ \mathbb{Q}_{31} & \mathbb{Q}_{32} & \mathbb{Q}_{33} \end{bmatrix} = [A]^{-1}[B] \tag{25}$$

we write

$$\{\Psi^{\mathrm{B}}\} = [\mathbb{Q}_{21} \quad \mathbb{Q}_{22} \quad \mathbb{Q}_{23}]\begin{Bmatrix} \Psi^{\mathrm{F}} \\ -\boldsymbol{n}\cdot\dot{\mathbf{V}} \\ 0 \end{Bmatrix} = \{\Psi_2^{\mathrm{B}}\} + \{\Psi_1^{\mathrm{B}}\} \tag{26.a}$$

$$\{\Psi_2^{\mathrm{B}}\} = -[\mathbb{Q}_{22}]\{\boldsymbol{n}\cdot\dot{\mathbf{V}}\} \tag{26.b}$$

$$\{\Psi_1^{\mathrm{B}}\} = [\mathbb{Q}_{21}]\{\Psi^{\mathrm{F}}\} \tag{26.c}$$

It is clear from Eq. (25) that the coefficient matrix $[\mathbb{Q}]$ is derived from matrices A and B appearing in the BE formulation of the fluid problem.

By substituting Eq. (10) for $\frac{\partial \varphi}{\partial t}$ from Eqs. (5) and (26), we get the following equations for the pressure acting on the solid/fluid interface:

$$\mathrm{p} - \mathrm{p_a} = -\rho\left(-\Psi^{\mathrm{B}} + \mathbf{V}\cdot\nabla\varphi + \frac{1}{2}|\nabla\varphi|^2\right) = \mathrm{p}_2 + \mathrm{p}_1 \tag{27.a}$$

$$\mathrm{p}_2 = \rho\Psi_2^{\mathrm{B}} = -\rho[\overline{\mathbb{Q}}_{22}]\{n_Z\}\dot{\boldsymbol{V}} \tag{27.b}$$

$$\mathrm{p}_1 = -\rho\left(-\Psi_1^{\mathrm{B}} + \mathbf{V}\cdot\nabla\varphi + \frac{1}{2}|\nabla\varphi|^2\right) \tag{27.c}$$

$$\overline{\mathbb{Q}}_{22}(j) = \mathbb{Q}_{22}(i,j)\left(\frac{s_{i+1}-s}{s_{i+1}-s_i}\right) + \mathbb{Q}_{22}(i+1,j)\left(\frac{s-s_i}{s_{i+1}-s_i}\right), j = 1,\mathcal{N} \tag{27.d}$$

Here $\{n_Z\}$ is the Z-component of the unit normal to the fluid/solid interface with the unit normal pointing out of the fluid, p_2 is the pressure due to rigid body acceleration, and p_1 is the pressure without considering acceleration of the rigid body motion. The coefficient matrix $\overline{\mathbb{Q}}_{22}$ for point $\mathscr{p}$ between nodes i and $i+1$ is evaluated by using the following Eq. (27.d). s, s_i and s_{i+1} are, respectively, the arc length of point $\mathscr{p}$, node i and node $i+1$, and $\mathcal{N}$ equals the number of nodes on the fluid structure interface.

Integrating component of the pressure in the Z-direction over the solid/fluid interface gives the total Z-force acting on the hull. Thus using Eq. (23.b) we get

$$F_Z = \int_0^{\ell}(\mathrm{p}_2 + \mathrm{p}_1)n_Z \mathrm{ds} = -M_a^*\dot{\mathrm{V}} + F_Z' \tag{28}$$

where

$$M_a^* = \int_0^{\ell}\rho n_Z[\overline{\mathbb{Q}}_{22}]\{n_Z\}\mathrm{ds}\,, \qquad F_Z' = \int_0^{\ell}\mathrm{p}_1 n_Z \mathrm{ds} \tag{29}$$

Here ℓ is the total arc length of the fluid/structure interface, and s is the arc length from the keel to a point of the hull.

Substitution from Eq. (28) into Eq. (23.a) gives

$$(M^* + M_a^*)\dot{V}(t) = F_Z^{'} - M^* g \tag{30}$$

Eq. (30) is numerically integrated by using the following central-difference algorithm:

$$(M^* + M_a^*)\dot{V}^{n+1} = F_Z^{'}(t_{n+1}) - M^* g \tag{31.a}$$

$$V^{n+1} = V^n + \frac{1}{2}\left(\dot{V}^{n+1} + \dot{V}^n\right)\delta t \tag{31.b}$$

$$\xi^{n+1} = \xi^n + V^n \delta t + \frac{1}{2}\dot{V}^n \delta t^2 \tag{31.c}$$

where

$$V^{n+1} = V\,(t_{n+1})\,,\ \xi^{n+1} = \xi\,(t_{n+1}) \tag{32}$$

here ξ is the submergence of the solid body with respect to the undisturbed water surface shown in Fig. 1. The velocity and acceleration of the hull keel is assumed to be equal to the rigid body velocity and acceleration since the edge at the keel is assumed not to deform. The time step δt in Eq. (31) equals that used to integrate equations for fluid's deformations.

The flow chart for iteratively solving the fluid structure interaction (FSI) problem is given in Fig. 6. Using the known solution at time t_n, ξ^{n+1}, $\dot{V}^{n+1}$ and V^{n+1} can be evaluated by using Eq. (31). These are used to update φ and Ψ for the next iteration. The iterative process is terminated when the normalized difference, $\int_0^{\mathcal{L}} |p_4^{I+1} - p_4^I| ds \,/\, \int_0^{\mathcal{L}} |p_4^{I+1}| ds$, of the computed total pressure between two successive iterations $I+1$ and I is less than the prescribed tolerance of 1E-4; here $p_4 = p_1 + p_2$. The FSI procedure discussed above is called the added mass method.

2.2.5 Verification of the code

The developed BEM software has been verified by using the method of manufactured solutions (e.g., see the material just preceding and following Eq. (20) of [31]). In cylindrical coordinates, we assume that

$$\varphi = -a(r + \frac{b^2}{r})\sin\theta\,, \tag{33}$$

where a and b are constants. The function φ given by Eq. (33) identically satisfies the Laplace equation. For $a = 2$ and $b = 1$, we use the software to numerically solve the Laplace equation on the domain Ω_0 depicted in Fig. 3 under the following boundary conditions:

$$\varphi = 0 \;\; on\; BD \tag{34.a}$$

$$\frac{\partial \varphi}{\partial n} = Z \;\; on\; DA \tag{34.b}$$

$$\frac{\partial \varphi}{\partial n} = 0 \;\; on\; AB \tag{34.c}$$

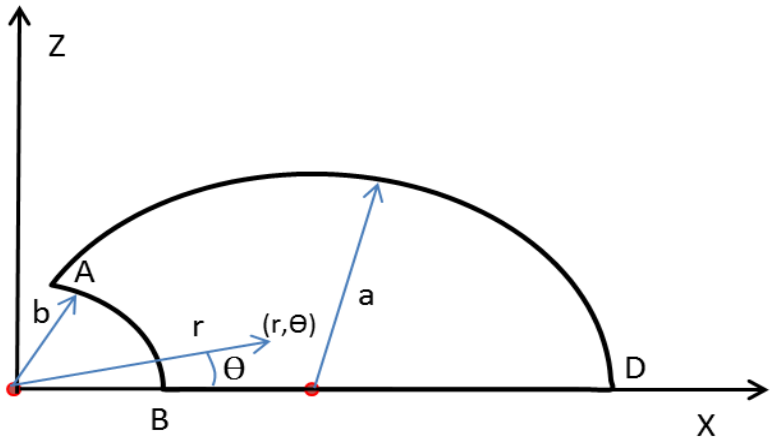

Fig. 3 Domain Ω_0 for solving the Laplace equation

The BEM software is used to find values of φ on boundaries DA and AB, and of $\frac{\partial \varphi}{\partial n}$ on boundary BD. We discretized each edge AB, BD and DA with 50 and 100 uniform elements for meshes 1 and 2, respectively, and found the difference, $\bar{\eta}$, in the computed and the analytical values of $\frac{\partial \varphi}{\partial n}$ and φ by using the following equation:

$$\bar{\eta} = \frac{\int_0^{\mathcal{L}} |f_{num} - f_{ana}| ds}{\int_0^{\mathcal{L}} |f_{ana}| ds} \tag{35}$$

here subscripts ana and num on f represent its values from the analytical and the numerical solutions, and $\mathcal{L}$ is the total arc length of the boundary.

In Figs. 4 and 5 we have compared, respectively, the analytical and the numerically computed values of the flux $\frac{\partial \varphi}{\partial n}$ on BD and of φ on the boundary ABDA. In each case the two curves essentially overlap each other. Values of the error norm, $\bar{\eta}$, defined by Eq. (35) and listed in Table 1 for the two meshes, are less than 0.13 %. Thus the developed BEM software gives very good solution of the Laplace equation.

Table 1 For the two meshes used, values of $\bar{\eta}$ for $\frac{\partial \varphi}{\partial n}$ and φ on the boundary

	$\frac{\partial \varphi}{\partial n}$	φ
Mesh 1	0.00122	0.000430
Mesh 2	0.000322	0.000110

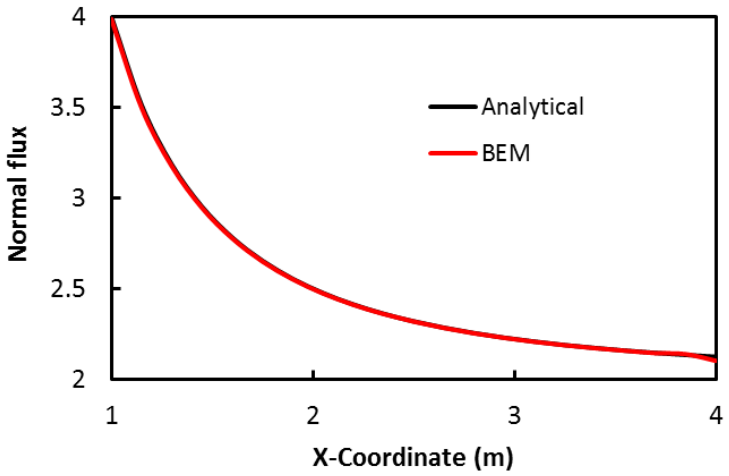

Fig. 4 Comparison of variations of the analytical and the numerically computed values of $\frac{\partial \varphi}{\partial n}$ on boundary BD; the two curves overlap each other.

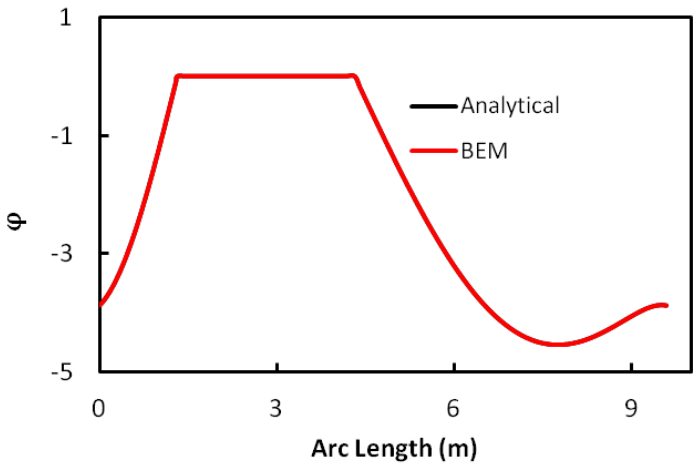

Fig. 5 Comparison of variations of the analytical and the numerically computed values of φ on the boundary ABDA traversed counter-clockwise; the two curves overlap each other.

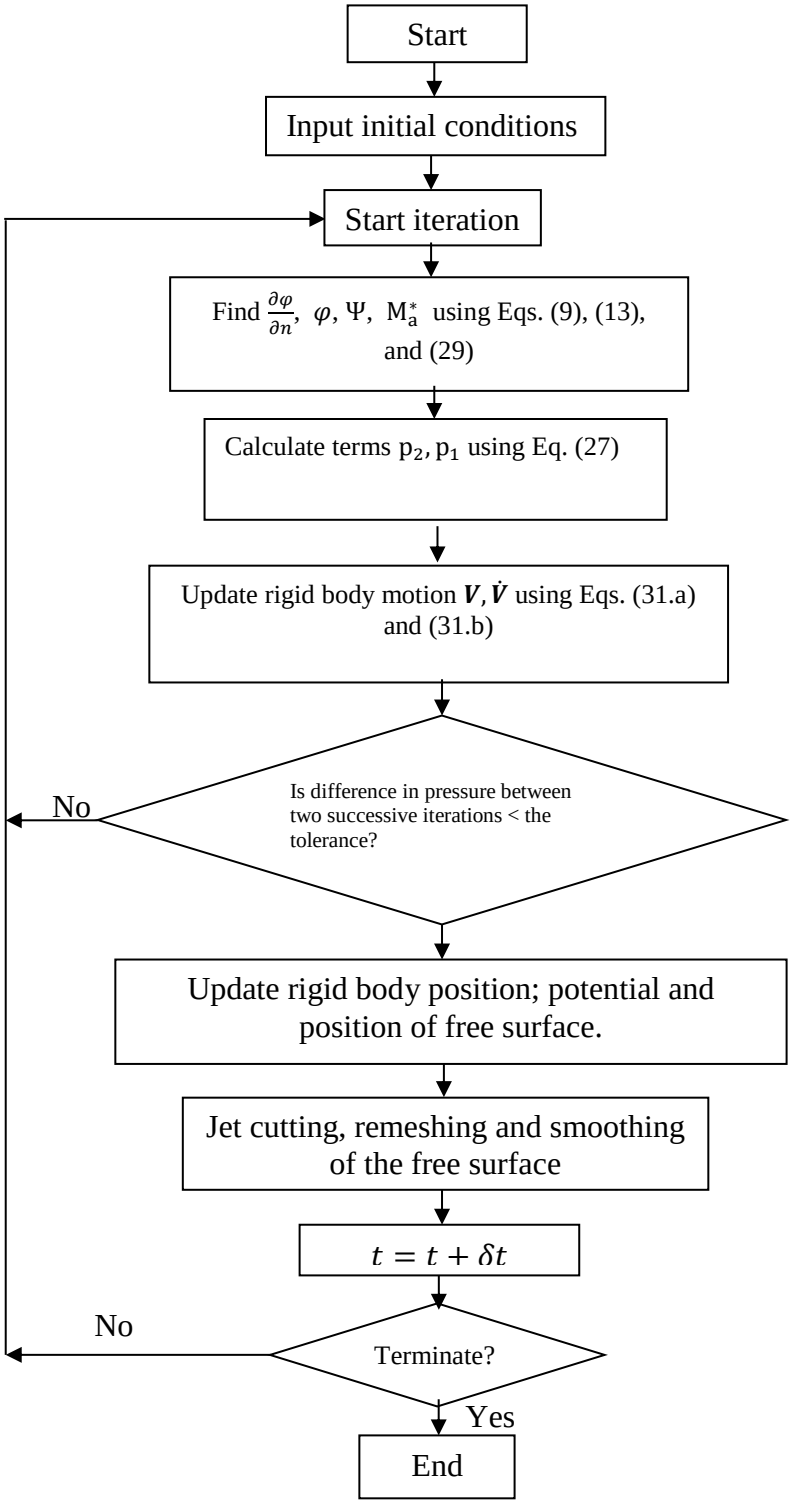

Fig. 6 Flow chart of the fluid structure interaction analysis.

3. Example Problems

3.1 Straight wedge impacting water at uniform velocity

The first problem studied is that of water slamming of a straight rigid wedge moving downwards along the Z-axis with constant velocity in which we have neglected effects of the gravity force. The problem has been investigated, amongst others, by Zhao and Faltinsen [5] who presented a similarity solution, Sun [14] who used the BEM, Mei et al. [7] who considered the jet flow, and Das and Batra [18] who employed the commercial FE software LSDYNA. We have followed the procedure detailed in Sun's [9] dissertation; however, techniques of smoothing the free surface and truncating the jet are different from her approach.

We discretize the fluid domain boundary into two-node elements with node numbers starting from the point $\mathcal{C}$ in Fig. 7 and going counter-clockwise ($\mathcal{CDEABC}$), and denote the length of element *j* with nodes *j* and *j+1* by h_j. Non-uniform meshes are used to discretize the free surface of water near the jet tip $\mathcal{A}$, fluid boundary $\mathcal{AB}$ on the hull and also fluid boundary $\mathcal{BC}$ on the symmetry axis. In Fig. 7 the free surface of water near the wedge edge is exhibited in which points $\mathcal{A}$ and $\mathcal{B}$ are, respectively, points of intersection between the free surface and the hull, and the hull and the symmetry axis. The length, h_j, of element j for mesh 1 is chosen according to the following empirical criteria.

The length of an element on the free surface boundary $\mathcal{EA}$ is given by

$$h_j = \begin{cases} d_{34}\,, & \bar{N}_{\mathcal{A}} - 100 \le j < \bar{N}_{\mathcal{A}} \\ \min\left(d_{33}, 1.05^{\bar{N}_A - 100 - j} d_{34}\right), & j < \bar{N}_{\mathcal{A}} - 100 \text{ and } \zeta_{\mathcal{A}j} \le 1.0\mathcal{L} \\ d_{32}, & 1.0\mathcal{L} < \zeta_{\mathcal{A}j} \le 2.0\mathcal{L} \\ d_{31}, & \zeta_{\mathcal{A}j} > 2.0\mathcal{L} \end{cases} \tag{36}$$

$d_{31} = L_1/40$, $d_{32} = 1/75$, $d_{33} = d_{32}/5$, $d_{34} = d_{32}/b_r$.

Here b_r is the mesh refinement parameter whose value depends upon the deadrise angle, $\zeta_{\mathcal{A}j}$ is the arc length between points $\mathcal{A}$ and j, and $\bar{N}_{\mathcal{A}}$ is the node number of point $\mathcal{A}$.

A non-uniform mesh with element size h_j given by Eq. (37) is used to discretize the water surface $\mathcal{AB}$ contacting the hull with finer meshes near points $\mathcal{A}$ and $\mathcal{B}$.

$$h_j = \begin{cases} d_{34}\,, & \bar{N}_{\mathcal{A}} \le j \le \bar{N}_{\mathcal{A}} + 100 \\ \min\left(d_{32}, 1.05^{j-(\bar{N}_A+100)} d_{34}\right), & \bar{N}_{\mathcal{A}} + 100 \text{ and } \zeta_{\mathcal{A}j} \le \zeta_{\mathcal{AB}} - 0.1\mathcal{L} \\ 0.5 d_{32}\,, & j > \bar{N}_{\mathcal{A}} + 100 \text{ and } \zeta_{\mathcal{A}j} > \zeta_{\mathcal{AB}} - 0.1\mathcal{L} \end{cases} \tag{37}$$

It is clear that this scheme generates finer meshes near points $\mathcal{A}$ and $\mathcal{B}$. The length h_j of element j on the axis of symmetry boundary $\mathcal{BC}$ is taken to be given by

$$h_j = \min\left(d_{31}, 1.2^{j-\bar{N}_{\mathcal{B}}} h_{\bar{N}_{\mathcal{B}}-1}\right). \tag{38}$$

Here, $\bar{N}_{\mathcal{B}}$ is the node number of point $\mathcal{B}$. The element length on each one of the two truncation boundaries $\mathcal{CD}$ and $\mathcal{DE}$ equals d_{31}. Lengths of elements for mesh 2 are the same as those for mesh 1 except that $d_{31} = L_1/80$ and $d_{32} = 1/150$; thus the element length for mesh 2 is one-half of that for mesh 1 in most of the region on the boundary. Unless otherwise specified, results presented below have been computed with mesh 2 and $b_r = 2$.

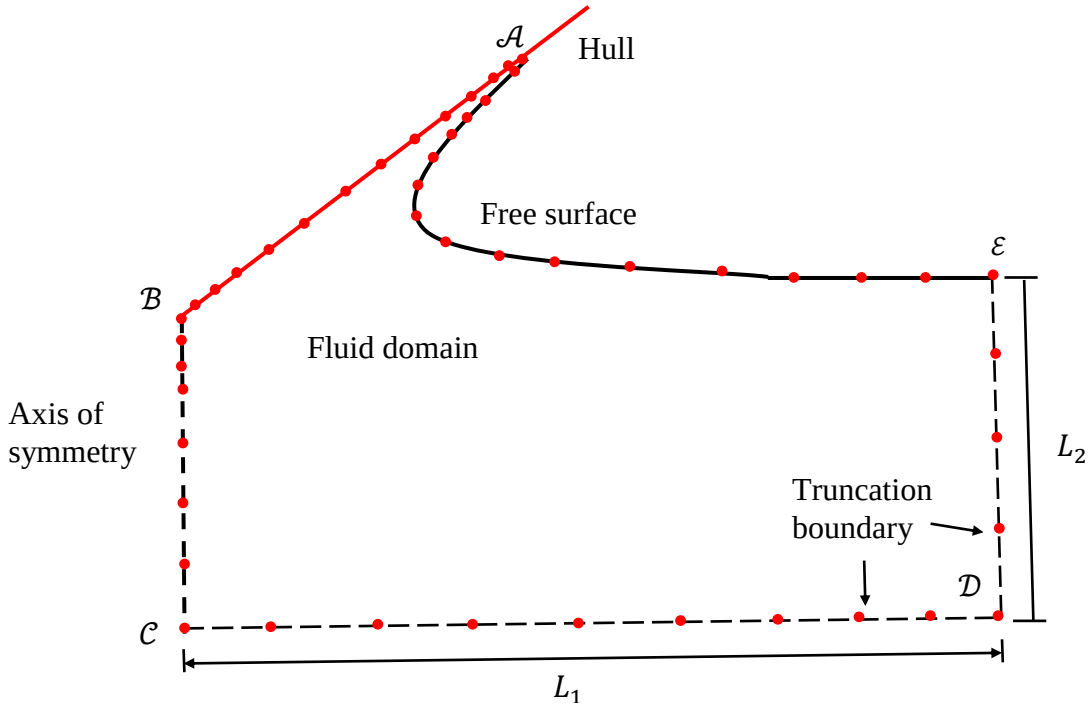

Fig. 7 Regions on the fluid boundary (Not to scale).

The percentage difference, $\bar{e}$, between quantities f_1 and f_2 computed with two different meshes or between the present work and that of other investigators for the same problem is defined as

$$\bar{e} = 100 \frac{\int_{-1}^{\bar{Z}_{max}} |f_1 - f_2| d\bar{Z}}{\int_{-1}^{\bar{Z}_{max}} |f_1| d\bar{Z}} \tag{39}$$

Here $\bar{Z} = Z/Vt$, $\bar{Z}_{max} = \frac{c_f(t)tan(\beta)}{Vt} - 1$, which is the maximum value at time *t* of $\bar{Z}$ for the wetted wedge.

We have delineated the influence of different jet cut parameters, time step size, BE mesh size and the size of the fluid domain considered on results for the water slamming of a 1 m long rigid straight wedge of different deadrise angles β impacting stationary water at uniform vertically downward velocity V = 10 m/s. While computing results, the time step δt is found from Eq. (22) with $\gamma_t = 5$. In an incompressible material only shear waves that do not change volume can propagate. However, here the fluid has been assumed to be inviscid implying that there are no shear waves. Thus traditional criteria for finding the time step size in the central-difference algorithm cannot be used. Problems are designated as B1, B2, and B3, respectively, for L_1 = L_2 = 5, 10 and 15 m, and computations are ceased when the jet tip reaches the other edge of the wedge, i.e., the entire wedge has been wetted. The variation of pressure normalized by the kinetic energy density of water moving at speed V (i.e., $\bar{p} = \frac{2p}{\rho V^2}$) on the non-dimensional length of the wedge computed by different time steps and truncation boundaries is shown in Fig. 8. The percentage difference, $\bar{e}$, between pressures on the wedge computed with time steps $\delta t/2$ (used as reference for computing $\bar{e}$ in Eq. (39)) and δt is 0.2%. Results of problems B1 and B2 differ from those of problem B3 (used as reference for computing $\bar{e}$) by 1.81% and 0.286%, respectively. Unless otherwise specified, we use L_1 = $L_2 = 15m$ to analyze problems discussed below.

For rigid wedges of deadrise angles $\beta = 45^\circ, 30^\circ, 10^\circ, 4^\circ$ results have been computed by taking the refinement number $b_r = 2, 2, 10, 60$, respectively, and the jet cut

threshold length $\lambda_0 = 0.1\mathcal{L}$ for all four cases. In Fig. 9 we have compared the computed pressure distributions on the wedge and the water surface profiles with those reported by Sun [14] and Zhao and Faltinsen [5], and have listed values of the difference $\bar{e}$ in Table 2. The maximum difference, $\bar{e}$, between our computed pressure and that reported in [5] is 6%. Thus the pressure distributions obtained using the present technique are close to those found by Zhao and Faltinsen [5] who employed the similarity solution.

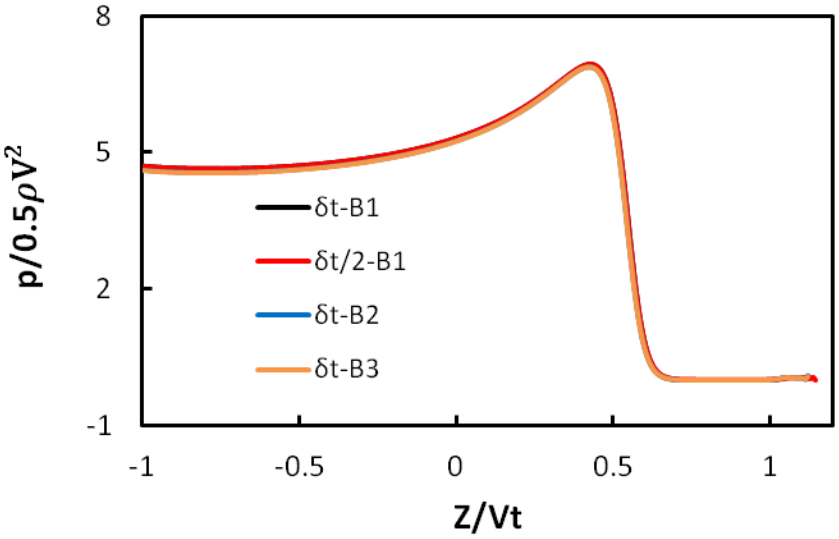

Fig. 8 Distribution of the normalized slamming pressure on the wedge of deadrise angle β = 30° for different truncation boundaries and time step sizes; the four curves essentially overlap each other.

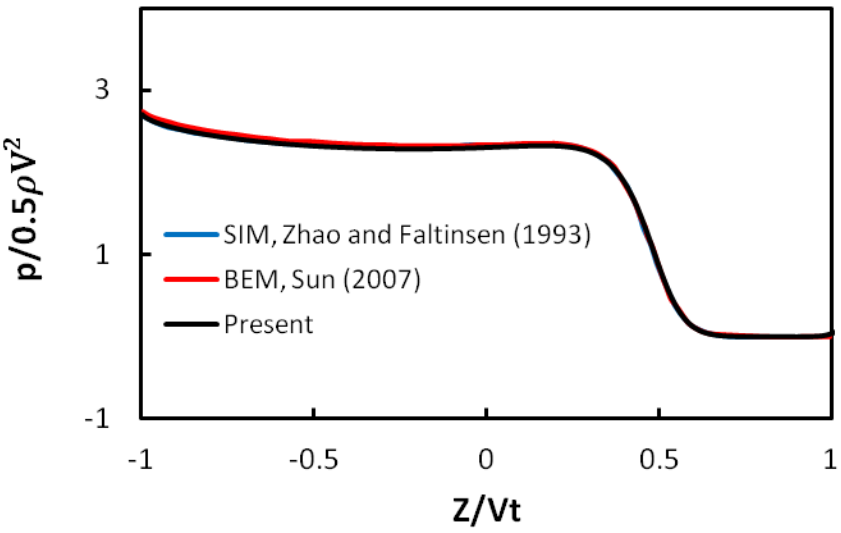

a. Distribution of the normalized slamming pressure on the wedge of deadrise angle $\beta = 45^{\circ}$

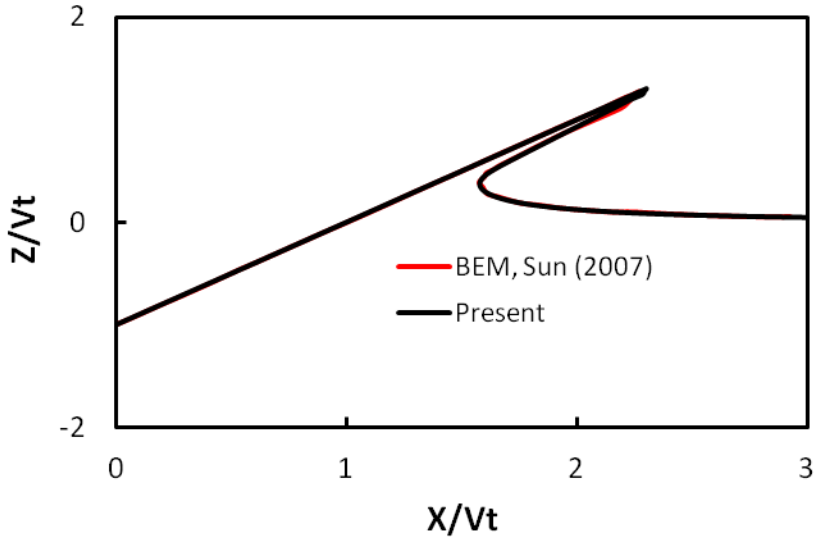

b. Free surface of water for the rigid wedge of deadrise angle $\beta = 45^{\circ}$ slamming stationary water at uniform speed of 10 m/s.

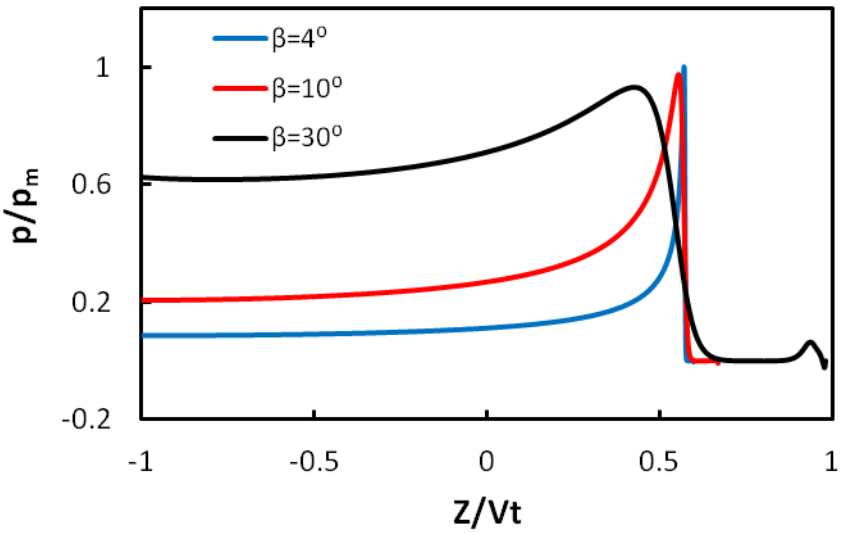

c. Distribution of the normalized slamming pressure on the wedge for deadrise angle $= 30°, 10°, 4°$; $p_m = \frac{1}{2}\rho\left(\frac{\pi V}{2tan\beta}\right)^2$

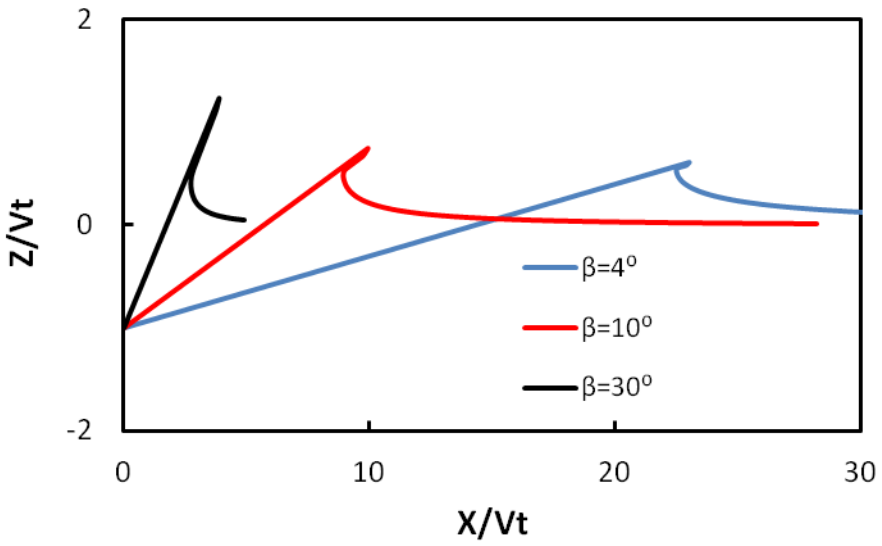

d. Free surfaces of water for rigid wedges of deadrise angles $\beta = 30°, 10°, 4°$ slamming stationary water at the uniform speed of 10 m/s

Fig. 9 Distribution of the normalized slamming pressure on the wedge and free surface of water for deadrise angles $\beta = 45^{\circ}, 30^{\circ}, 10^{\circ}, 4^{\circ}$.

Table 2 For the pressure computed on rigid straight wedge of different deadrise angles, the percentage difference $\bar{e}$ between the similarity solution of [5] and present results and those reported in [14]

Deadrise angle	45 °	30 °	10 °	4 °
BEM_Sun [14]	1.21%	3.15%	6.36%	11.6%
Present_mesh1	0.706%	1.17%	2.55%	5.94%
Present_mesh2	0.799%	1.63%	2.14%	3.09%

Results plotted in Fig. 9 illustrate that the deadrise angle β significantly influences the pressure distribution on the wetted hull surface. An increase in β results in more uniform distribution of pressure. The peak value of the normalized pressure (recall that the normalization pressure depends upon β) is essentially independent of β.

3.2 Freely falling straight wedge

We now analyze the problem studied in subsection 3.1 but consider the effect of gravitational forces acting on the wedge. The problem has been studied both analytically and numerically by Yettou et al. [8] for straight 1.2 m long wedges of different masses, entry speeds and deadrise angles; however, we study only two cases, namely that of the 94 kg wedge of deadrise angle 25°, and of 153 kg wedge of deadrise angle 30°. Each wedge enters water at $5.047\ m/s$. While simulating deformations, we used mesh 2 with refinement number $b_r = 5$, jet cut parameter = the default value, and the time step sizes are found from Eq. (22), γ_t= 10 for each case with its corresponding deadrise angle. For $c_f(t) \leq 0.005\ m$, Wagner's [3] solution

$$p_w(X) = min\left(\rho V \frac{c_f(t)}{\sqrt{c_f(t)^2 - X^2}} \frac{dc_f(t)}{dt}, \frac{1}{2}\rho\left(\frac{dc_f(t)}{dt}\right)^2\right), \quad X \leq c_f(t) \tag{40}$$

is used to find the initial slamming pressure p_w and hence the resultant force on the wedge, and the water surface profile is computed using Eq. (14). For $c_f(t) \geq 0.005$ m, deformations of the water are analyzed by the BEM described above.

As the influence of thin jet on the total slamming pressure is negligible, we consider a wedge of length greater than 1.2 m to compute results until the 1.2 m length of the wedge completely enters the water. The presently computed time history of the Z-velocity of the 94 kg wedge is compared in Fig. 10 with that found experimentally by Yettou et al. [8], analytically by Zhao and Faltinsen [5] and numerically by Das and Batra [18] who used the commercial FE software LSDYNA. For $t \leq 40$ ms, the maximum percentage differences $100|V^{pre} - V^{ana}|/V^{ana}$ and $100|V^{pre} - V^{exp}|/V^{exp}$ equal 3.32% and 6.89%, respectively; here V^{pre}, V^{exp} and V^{ana} denote, respectively, values of the axial velocity computed from the present work, the experimental work of [8] and the analytical solution of [5]. Thus the present approach gives good results for $t \leq 40$ ms. For $t > 40$ ms, the difference between the present and the experimental values of the axial velocity increases because of possible flow separation from the wedge. The time history of the presently computed upward force acting on the wedge is compared with that of Ref. [18] in Fig. 11; the corresponding experimental results are not included in [8]. It is clear that forces acting on the rigid wedge from the two approaches are nearly the same, and

the present results are smoother than those given in [18] in the sense that the amplitude of oscillations in the pressure are nearly non-existent. We note that Das and Batra [21] reported water penetrating into the rigid wedge because of the difficulty in finding values of parameters in the contact algorithm that will eliminate this interpenetration. They tried several values of these parameters and found the values that reduced oscillations in the hydrodynamic pressure acting on the wedge.

For the 153 kg wedge, the presently computed time histories of the upward total force acting on the wedge are compared with those of Yettou et al. [8] and Das and Batra [18] in Fig. 12. These evince that the present approach gives results close to those of Das and Batra [18]. Das [32] found that the total force computed by integrating the pressure reported by Yettou et al. [8] was significantly different from the value of the total upward force reported in [8]. The spatial variation of the hydrodynamic pressure on the wedge at three different times is exhibited in Fig. 13. Whereas our results agree well with those of Das and Batra, they noticeably differ from those of Yettou et al. [8]. One way to find the total upward force acting on the hull is to integrate with respect to X the pressure distribution shown in Fig. 13a and multiply it with the wetted length and $cos(30°)$. The axial force so found from Yettou et al.'s [8] pressure distribution differs from their values exhibited in Fig. 10 by 19.0%, 18.8% and 15.3% for time t = 14.7, 23.7 and 35.5 ms, respectively. However, the difference, $100|F^{Das} - F^{Pre}|/F^{Das}$, between the present total upward force F^{Pre} and the total upward force F^{Das} computed using LSDYNA by Das and Batra [18] equals 3.80%, 1.35% and 1.49% for time t = 14.7, 23.7 and 35.5 ms, respectively. Time histories of the added mass M_a^* for the two hulls of masse 94 kg (wedge of deadrise angle 25°) , and of 153 kg (wedge of deadrise angle 30°) are exhibited in Fig. 13b. It is clear that the added mass does not depend upon the wedge mass but on the mass of the water displaced and the average acceleration of this body of displaced water.

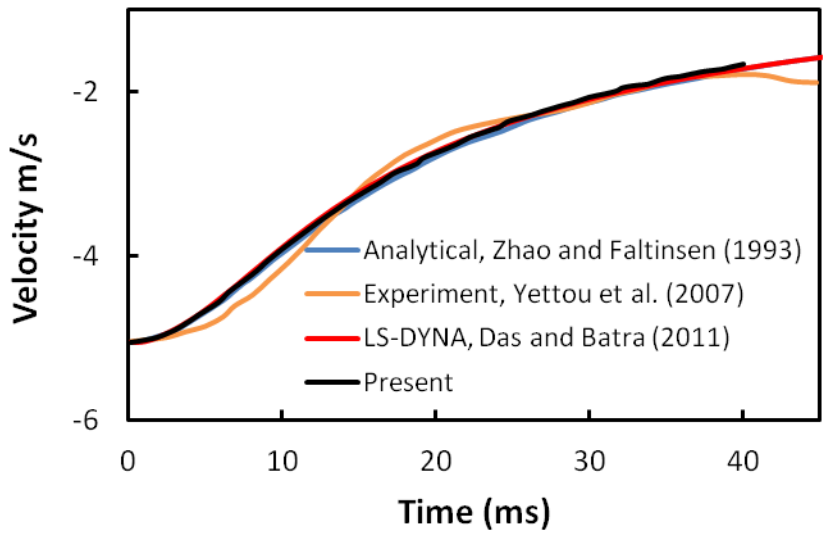

Fig. 10 Time histories of the downward velocity of the 94 kg wedge

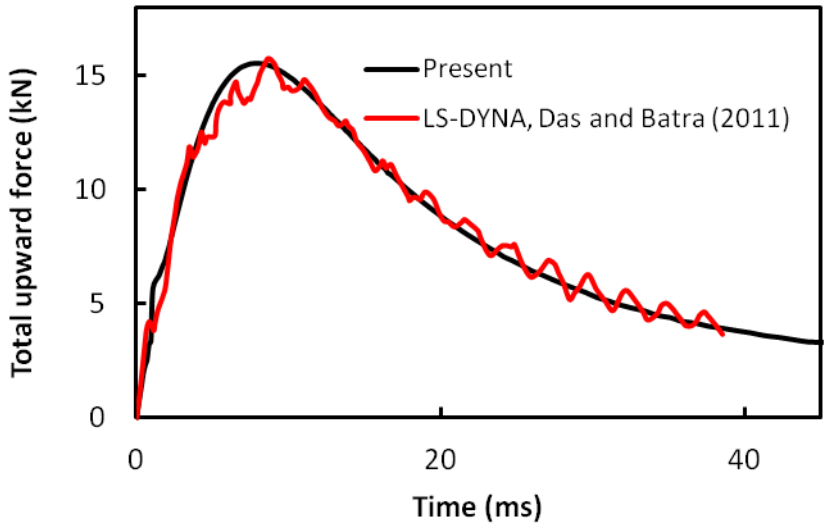

Fig. 11 Time histories of the total upward force on the 94 kg wedge

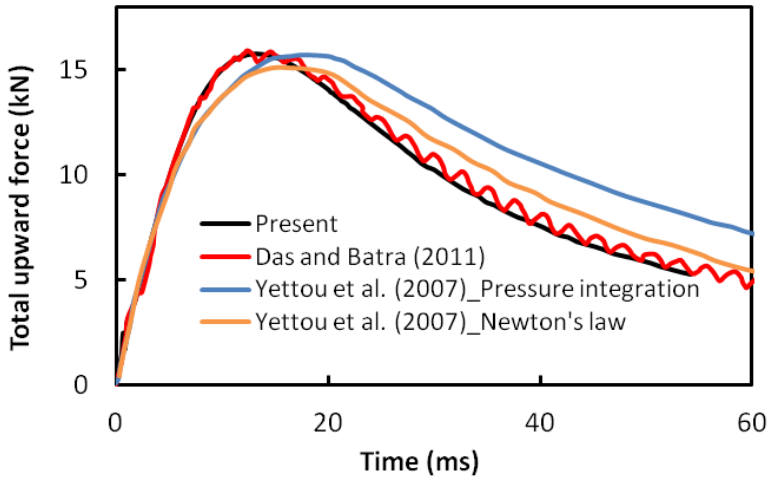

Fig. 12 Time histories of the upward force on the 153 kg wedge

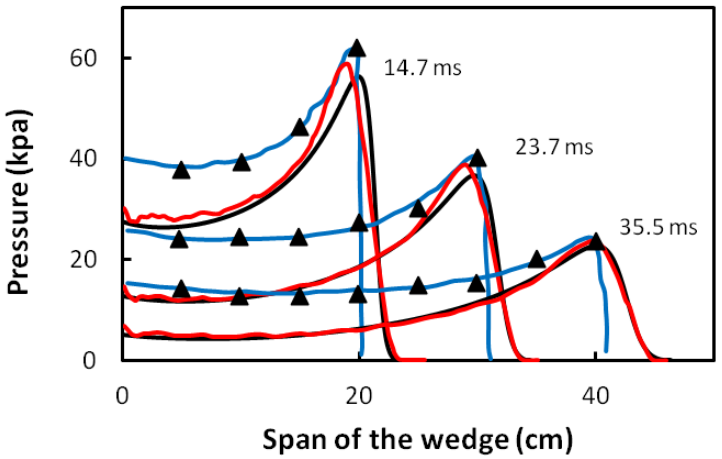

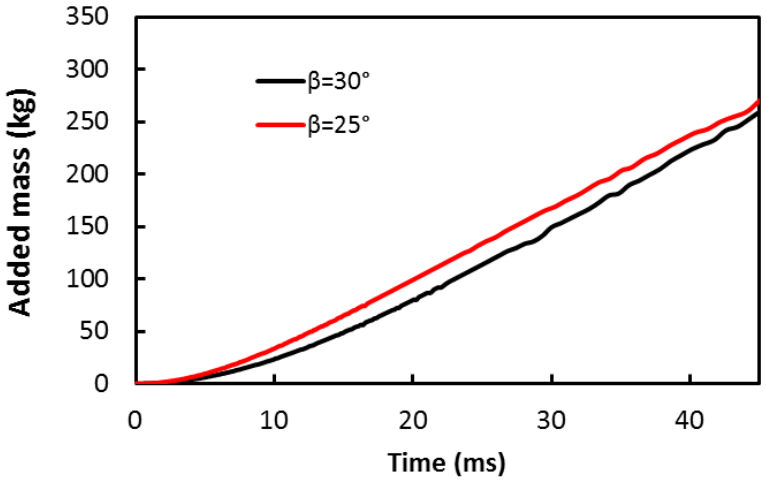

Fig. 13 (a) Variations of the slamming pressure on the 153 kg rigid wedge at three different times; blue lines and solid black triangles represent, respectively, analytical and experimental results of Yettou et al. [8]; black solid and red solid curves represent, respectively, present results and those of Das and Batra [18]. (b) Time histories of the added mass matrix for the wedges of deadrise angles 25^o and 30^o.

3.3 Freely falling bow section

The drop test into stationary water of ship bow section conducted by Aarsnes [33] has been simulated in this section and computed results have been compared with experimental findings of Aarsnes [33] and numerical results reported in Sun [14]. The shape of the ship bow section of total length 1 m and weight 261 kg is shown in Fig 14. The roll angle equals 0, and the initial entry velocity is $2.43m/s$. The initial time is assumed to be 0.1ms. As the total upward force is small for t < 0.1 ms, the slamming pressure is assumed to be zero for t < 0.1 ms. While simulating deformations, we used mesh 2 with refinement number $b_r = 4$, jet cut parameter = the default value, and the time step size is found from Eq. (22) with $\beta = 30°$, γ_t= 10 and V = $2.43m/s$. We note that the local deadrise angle varies along the length of the bow section and is greater than $30°$ except for points near the hull apex P1. Because the ship bow profile between two adjacent nodes is approximated by a straight line, the pressure distribution on it may exhibit oscillations as pointed out by Sun [9].

Time histories of the total upward force and the Z-velocity plotted in Figs. 15 and 16 evince that our computed results are close to those of Sun [14] and also to the experimental findings of Aarsnes. Reasons for the difference between the computed and the experimental results include errors in approximating the ship bow section profile, 3-D effects not considered in the 2-D simulations, neglecting effects of the fluid viscosity, surface tension and gravity, and assuming fluid deformations to be irrotational.

Time histories of the pressure at points P1 (0, 0), P2 $(0.041, 0.111)$ and P3 $(0.072, 0.149)$ are exhibited in Fig. 17a,b,c, those of the added mass in Fig. 17d, and the spatial variations of the pressure on the ship bow section at time t = 20.6 ms, 29.6 ms, 37.2 ms, 44.8 ms and 50.8 ms are plotted in Fig. 18. It is clear that the pressure distributions on the ship bow section are quite different from those on the straight wedge section. For the straight wedge, the high pressure region is narrow and distributed near

the jet flow while that for the ship bow section the high pressure region is quite broad as also reported by Arai and Matsunaga [34]. The maximum added mass of 15 kg is much less than 261 kg weight of the ship bow section.

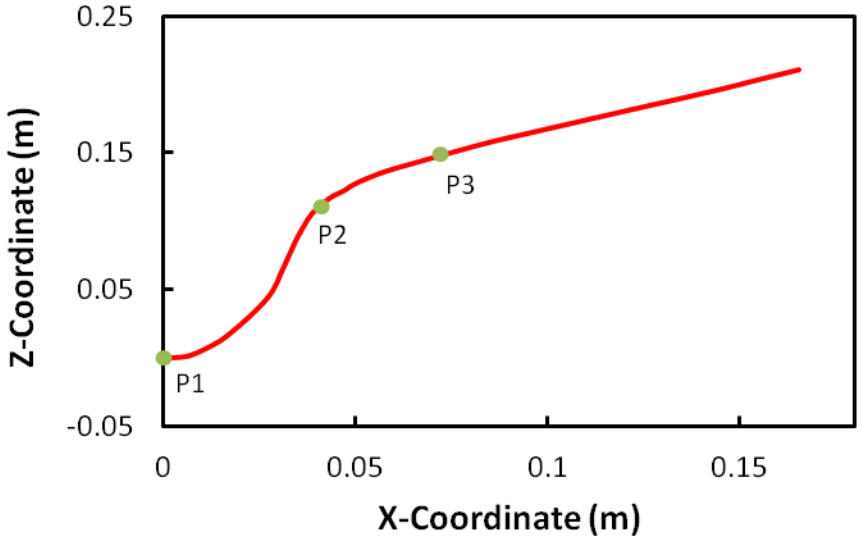

Fig. 14 Cross section of the ship bow studied

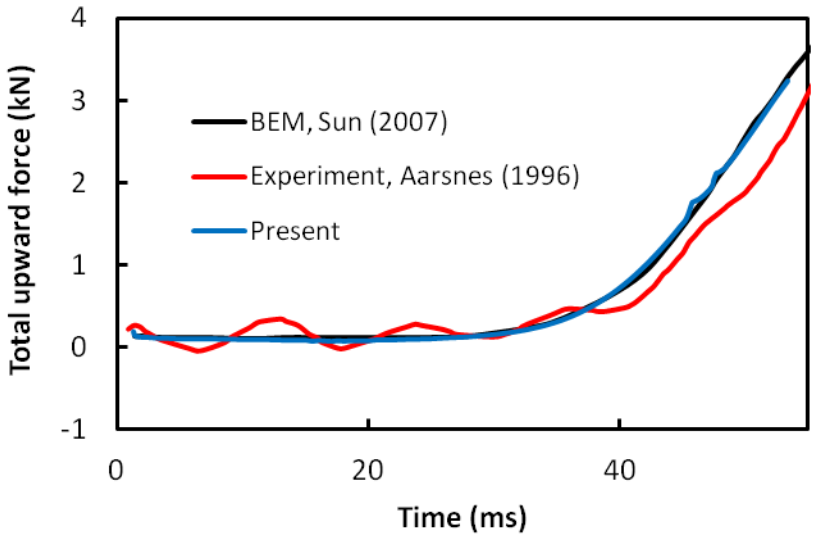

Fig. 15 Time histories of the total upward force for the rigid ship bow section

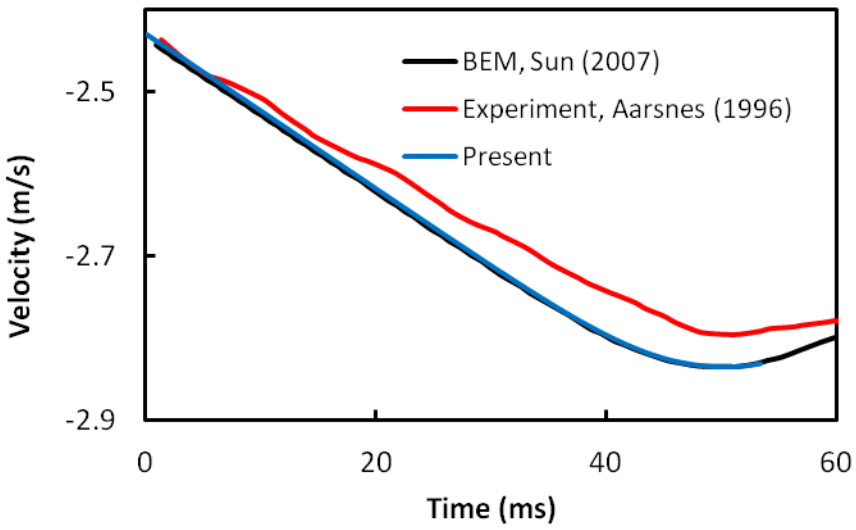

Fig. 16 Time histories of the Z-velocity of the rigid ship bow section

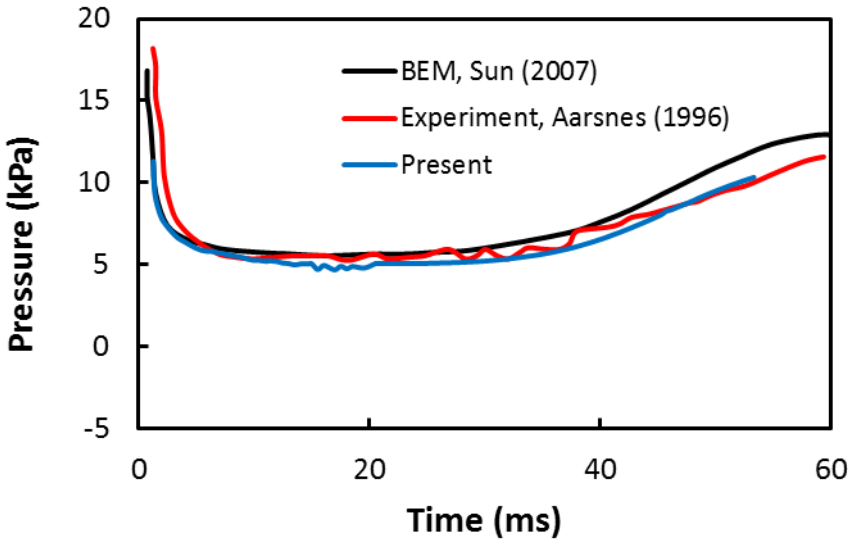

(a) Time histories of the slamming pressure at point P1

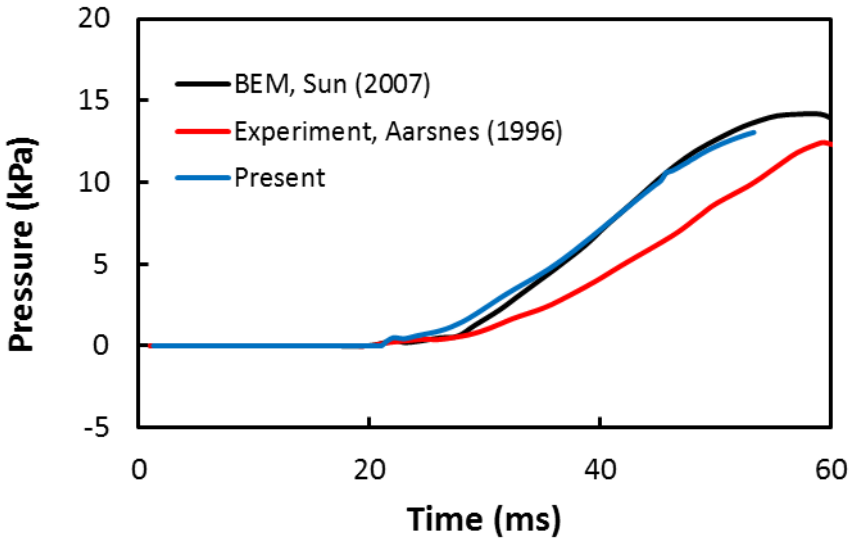

(b) Time histories of the slamming pressure at point P2

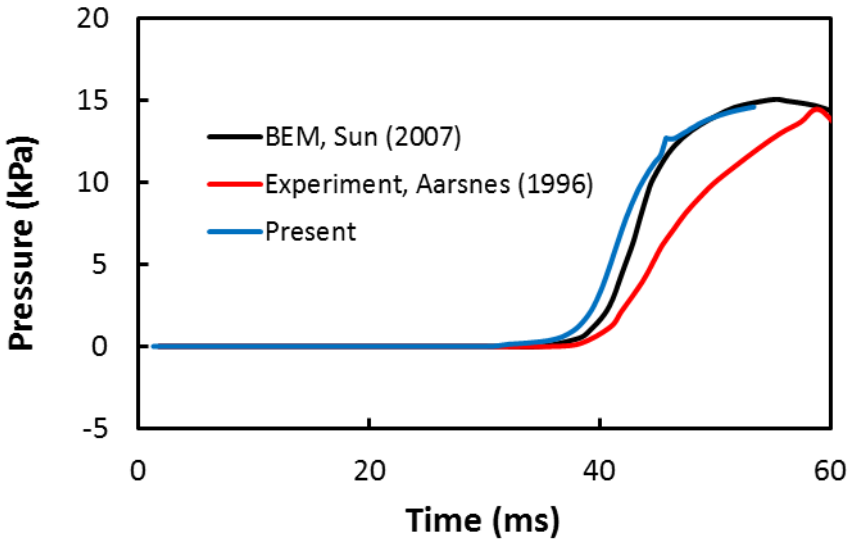

(c) Time histories of the slamming pressure at point P3

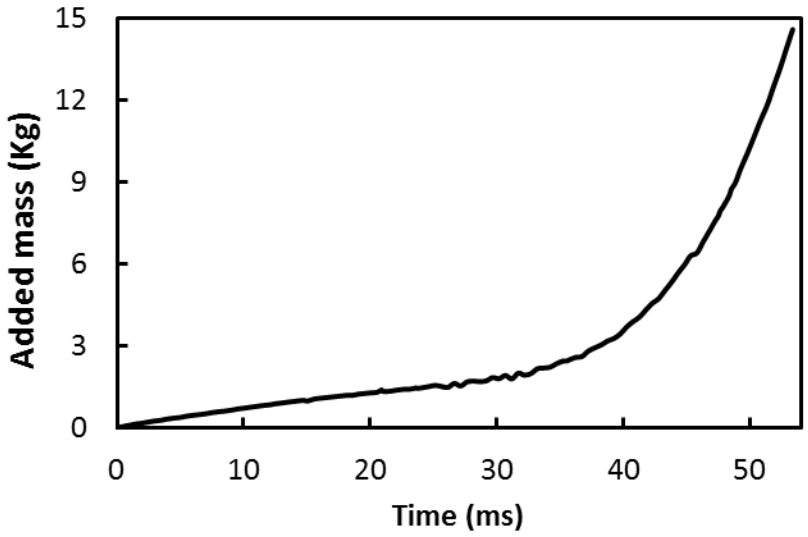

(d) Time history of the added mass

Fig. 17 Time histories of the slamming pressure at points P1, P2 and P3, and time history of the added mass

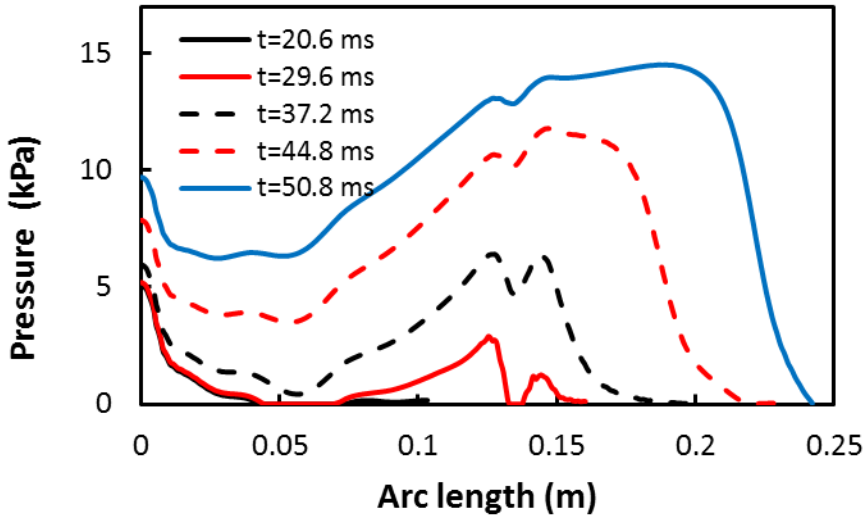

Fig. 18 Variations of the pressure on the ship bow section at times t = 20.6 ms, 29.6 ms, 37.2 ms, 44.8 ms, and 50.8 ms.

3.4 Circular hull

In an attempt to delineate effects of local hull curvature on the hydrodynamic pressure acting on the hull, we consider hulls of different radii and off-set their centers so

as to have an initial deadrise angle of 5^o; e.g., see Fig. 19. We assume uniform entry velocity of 10 m/s and arc length of the hull equal to 1m. We use mesh 2 with refinement number $b_r = 30$, jet cut parameter = the default value, and the time step size is found from Eq. (22) with $\beta = 5°$, $\gamma_t = 10$. For R = 5, 8, 20 and 50 m, we have exhibited in Fig. 20 the variation of the hydrodynamic pressure on curved and straight hulls at t = 2.7, 4.8 and 5.4 ms after the hull contacts stationary water. Hull's velocity is assumed to be constant and equal 10 m/s. For comparison purposes, we have also plotted the pressure distribution on a straight hull of deadrise angle = 5^o. It is clear that the curvature of the hull noticeably affects the magnitude of the peak pressure and the pressure distribution on the hull. Whereas for a straight hull the peak pressure stays constant as the wetted length increases, for the curved hull the peak pressure decreases with an increase in the wetted length. In each case the peak pressure occurs near the terminus of the wetted length.

The time history of the wetted arc length is exhibited in Fig. 21. If we interpret the slope of these curves as the speed of the wetted arc length terminus, then this speed slowly decreases with an increase in the arc length.

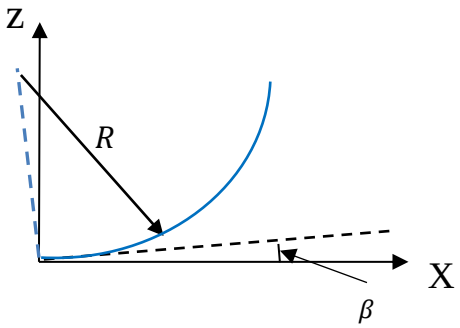

Fig. 19 Sketch of circular hull and the definition of deadrise angle at X = Z = 0.

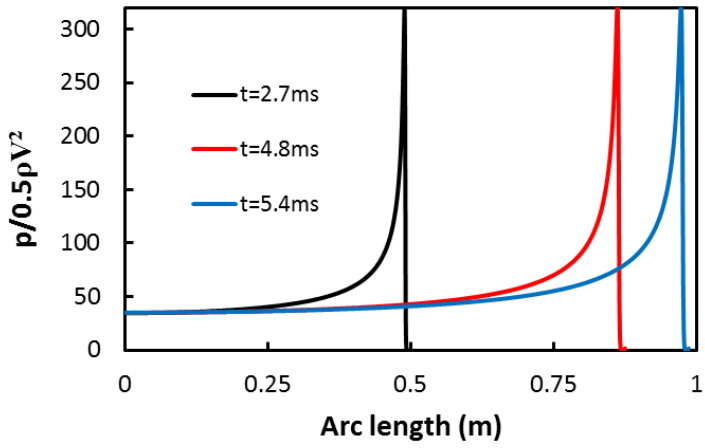

a. Straight hull (β=5°)

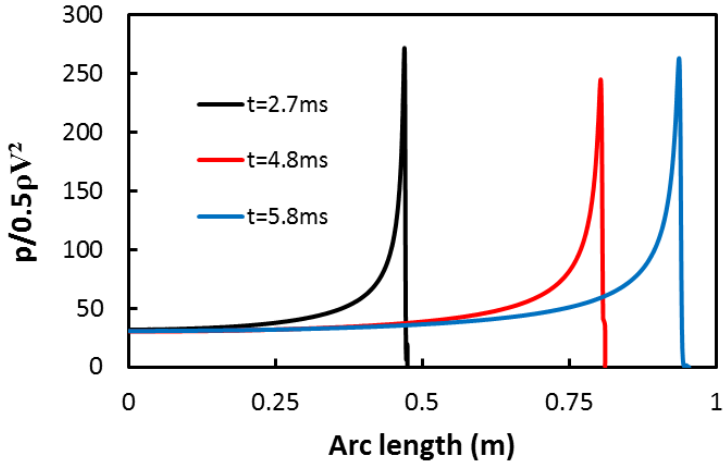

b. R=50m

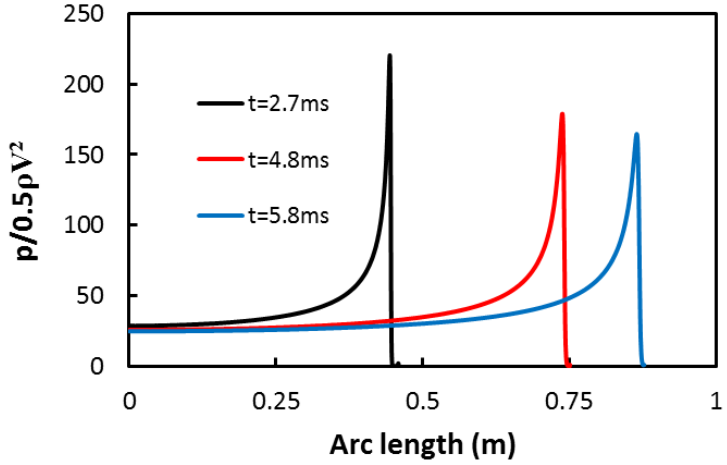

c. R=20m

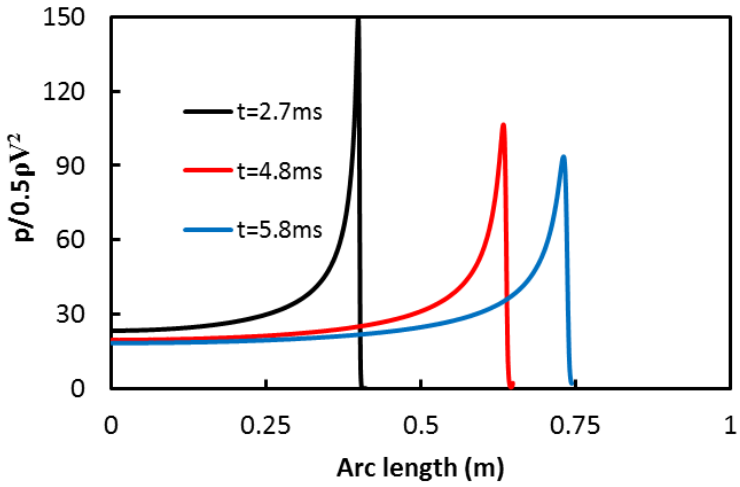

d. R=8m

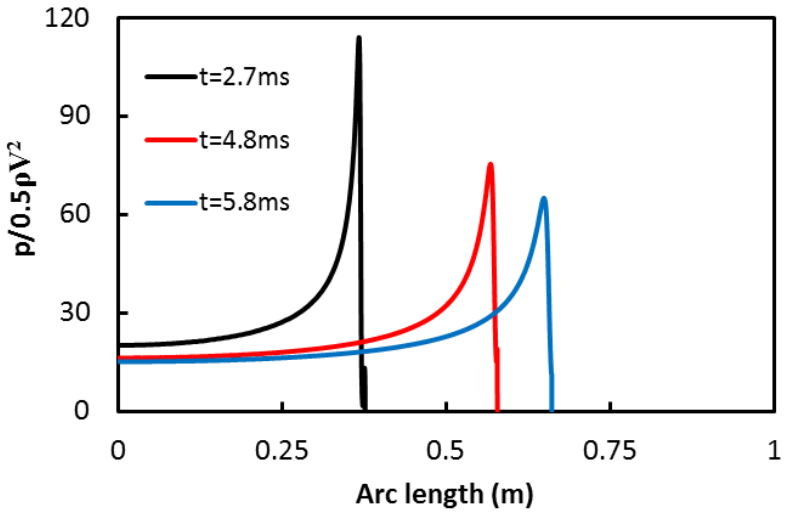

e. R=5m

Fig. 20 Variation of pressure on the rigid circular hulls of different radii

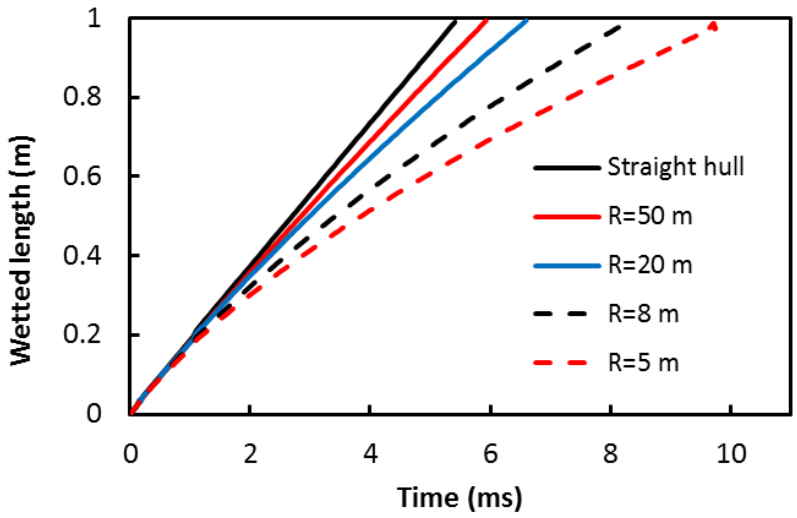

Fig. 21 Time history of wetted length for rigid circular hulls of different radii

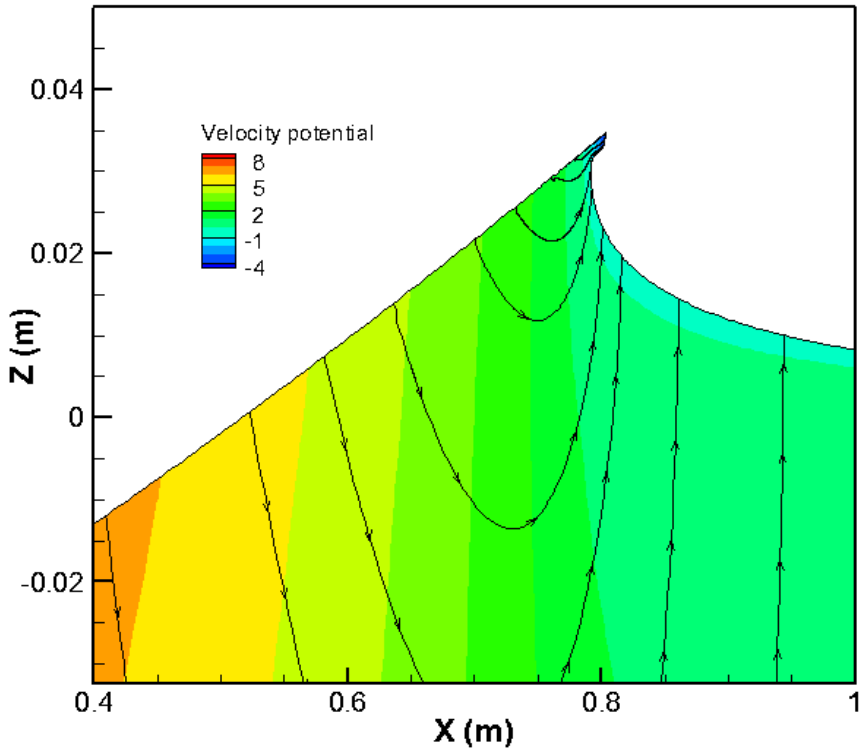

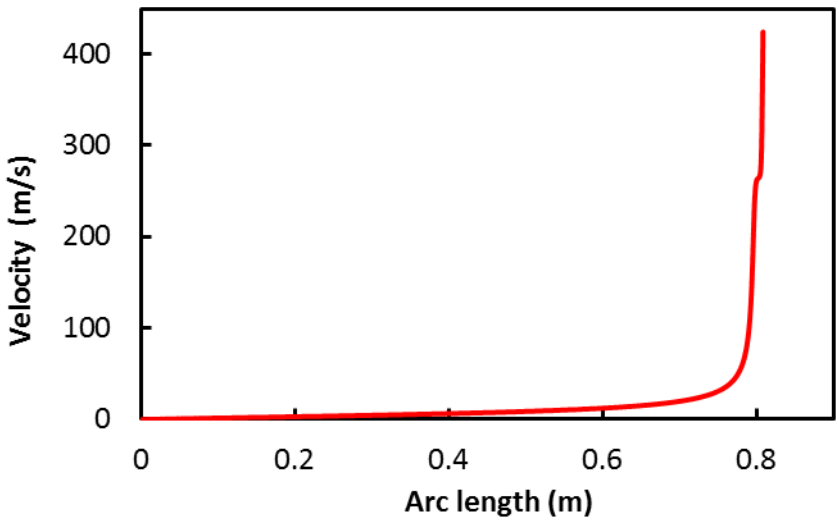

Fig. 22 At t = 5.2 ms, for water slamming of the rigid circular hull of radius R=20 m, velocity potential and streamlines (top) and variation of tangential velocity of fluid particles contacting the hull (bottom).

Table 3 Normailized peak pressure when the wetted length equals 1 m

	Straight hull	R=50m	R=20m	R=8m	R=5m
$\frac{P^{max}}{0.5\rho V^2}$	320	263	156	72.3	44.4

4. Conclusions

We have used the boundary element method to analyze transient 2-dimensional deformations of homogeneous, incompressible and inviscid water assumed to undergo irrotational deformations. The velocity potential is a solution of the Laplace equation defined on the fluid domain. Strategies to determine the evolution of free surface of water and the wetted length of a hull that impacts initially stationary water have been developed. The developed code has been verified by the method of manufactured solutions. Four initial-boundary-value problems involving water slamming of straight wedge with and without considering gravitational effects on the wedge, a ship bow section, and circular hulls have been studied. For the first three problems, the pressure

distribution on the wetted length and shapes of water jets near the edge of the wetted length have been found to compare well with either the experimental or the analytical or the numerical results of other investigators. For circular and straight hulls the pressure distribution on the hull can be viewed as a pressure wave traveling along the hull; the peak pressure in the wave occurs at its leading edge which is close to the terminus of the wetted length and the pressure distribution is uniform in its wake.

Appendix: Boundary conditions on Ψ

The auxiliary function Ψ and operator $\frac{D_B}{Dt}$ can be defined as

$$\Psi = \frac{D_B \varphi}{Dt} = \frac{\partial \varphi}{\partial \mathrm{t}} + \mathbf{V} \cdot \nabla \varphi \tag{A.1.a}$$

$$\frac{D_B}{Dt} = \frac{\partial}{\partial \mathrm{t}} + \mathbf{V} \cdot \nabla \tag{A.1.b}$$

As the fluid is assumed to be incompressible and its deformations irrotational, and $\boldsymbol{V}$ equals the translational velocity of a rigid body (no rotation), we have the following equations.

$$\nabla^2 \varphi = 0 \tag{A.2.a}$$

$$\nabla \times \nabla \varphi = \mathbf{0} \tag{A.2.b}$$

$$\nabla \cdot \mathbf{V} = 0 \tag{A.2.c}$$

$$\nabla \times \mathbf{V} = \mathbf{0} \tag{A.2.d}$$

Applying the Laplace operator to Bernoulli's Eq. (5), we get

$$-\nabla^2 \left(\frac{\partial \varphi}{\partial \mathrm{t}} + \mathbf{V} \cdot \nabla \varphi \right) + \nabla^2 (\mathbf{V} \cdot \nabla \varphi) + \nabla^2 \left(\frac{1}{2} |\nabla \varphi|^2 + \frac{\mathrm{p} - \mathrm{p_a}}{\rho} \right) = 0 \tag{A.3.a}$$

We note that

$$\nabla^2 (\mathbf{V} \cdot \nabla \varphi) = \mathbf{V} \cdot \nabla (\nabla^2 \varphi) = 0 \tag{A.3.b}$$

$$\nabla^2 \left(\frac{1}{2} |\nabla \varphi|^2 + \frac{\mathrm{p} - \mathrm{p_a}}{\rho} \right) = \nabla \cdot \left(\nabla \varphi \cdot \nabla \nabla \varphi + \nabla \frac{\mathrm{p} - \mathrm{p_a}}{\rho} \right) = \nabla \cdot \left(\frac{\partial \nabla \varphi}{\partial \mathrm{t}} \right) = 0 \tag{A.3.c}$$

Applying the Laplace operator to Eq. (A.1.a) and using Eq. (A.3), we obtain

$$\nabla^2\Psi = \nabla^2\left(\frac{\partial\varphi}{\partial \mathrm{t}} + \mathbf{V}\cdot\nabla\varphi\right) = 0 \tag{A.4}$$

In order to prove the relation

$$\frac{\partial\Psi}{\partial n} = \frac{\partial}{\partial n}\left(\frac{D_B\varphi}{Dt}\right) = \frac{D_B}{Dt}\left(\frac{\partial\varphi}{\partial n}\right) \tag{A.5}$$

We assume that $\frac{D_B}{Dt}(\boldsymbol{n})$ is small, and note that

$$\frac{D_B}{Dt}\left(\frac{\partial\varphi}{\partial n}\right) = \boldsymbol{n}\cdot\left(\frac{\partial\nabla\varphi}{\partial \mathrm{t}} + \mathbf{V}\cdot\nabla\nabla\varphi\right) = \boldsymbol{n}\cdot\left(\frac{\partial\nabla\varphi}{\partial \mathrm{t}} + \nabla(\mathbf{V}\cdot\nabla\varphi)\right)$$

$$= \boldsymbol{n}\cdot\nabla\left(\frac{\partial\varphi}{\partial \mathrm{t}} + \mathbf{V}\cdot\nabla\varphi\right) = \frac{\partial}{\partial n}\left(\frac{D_B\varphi}{Dt}\right) \tag{A.6}$$

Substituting from Eq. (4) into Eq. (A.5), the boundary condition on the solid body is given by

$$\frac{\partial\Psi}{\partial n} = \frac{D_B}{Dt}\left(\frac{\partial\varphi}{\partial n}\right) = \frac{D_B}{Dt}(-\boldsymbol{V}\cdot\boldsymbol{n}) = -\dot{\boldsymbol{V}}\cdot\boldsymbol{n} \tag{A.7}$$

The boundary condition of zero normal velocity of the fluid on the symmetry axis and the truncation boundaries requires that

$$\frac{\partial\Psi}{\partial n} = \frac{D_B}{Dt}\left(\frac{\partial\varphi}{\partial n}\right) = 0 \tag{A.8}$$

Substituting from Eq. (A.1.a) into Eq. (5), the boundary condition on the free surface can be written as

$$\Psi = \frac{\partial\varphi}{\partial \mathrm{t}} + \mathbf{V}\cdot\nabla\varphi = -\left(-\frac{\partial\varphi}{\partial \mathrm{t}} + \frac{1}{2}|\nabla\varphi|^2\right) + \mathbf{V}\cdot\nabla\varphi + \frac{1}{2}|\nabla\varphi|^2 = \mathbf{V}\cdot\nabla\varphi + \frac{1}{2}|\nabla\varphi|^2 \tag{A.9}$$

References

1. Faltinsen O.M., *Sea loads on ships and offshore structures.*1993, Cambridge, UK: Cambridge University press.

2. Von Karman T., *The impact on seaplane floats during landing.* NASA, 1929(TN-321).
3. Wagner H., *Über Stoß - und Gleitvorgänge an der Oberfläche von Flüssigkeiten.* ZAMM - Journal of Applied Mathematics and Mechanics/Zeitschrift für Angewandte Mathematik und Mechanik, 1932. **12**(4): p. 193-215.
4. Dobrovol'Skaya Z., *On some problems of similarity flow of fluid with a free surface.* Journal of Fluid Mechanics, 1969. **36**(04): p. 805-829.
5. Zhao R. and O. Faltinsen, *Water entry of two-dimensional bodies.* Journal of Fluid Mechanics, 1993. **246**(1): p. 593-612.
6. Zhao R., O. Faltinsen, and J. Aarsnes. *Water entry of arbitrary two-dimensional sections with and without flow separation*. in *Twenty-first Symposium on NAVAL HYDRODYNAMICS*. 1996.
7. Mei X., Y. Liu, and D.K.P. Yue, *On the water impact of general two-dimensional sections.* Applied Ocean Research, 1999. **21**(1): p. 1-15.
8. Yettou E.M., A. Desrochers, and Y. Champoux, *A new analytical model for pressure estimation of symmetrical water impact of a rigid wedge at variable velocities.* Journal of fluids and structures, 2007. **23**(3): p. 501-522.
9. Donguy B., B. Peseux, L. Gornet, and E. Fontaine. *Three-dimensional hydroelastic water entry: preliminary results*. in *Proceedings of the 11th International Offshore and Polar Engineering Conference*. 2001. Stavanger, Norway.
10. Stenius I., A. Rosén, and J. Kuttenkeuler, *Explicit FE-modelling of fluid-structure interaction in hull-water impacts.* International Shipbuilding Progress, 2006. **53**(2): p. 103-121.
11. Oger G., M. Doring, B. Alessandrini, and P. Ferrant, *Two-dimensional SPH simulations of wedge water entries.* Journal of Computational Physics, 2006. **213**(2): p. 803-822.
12. Lin M.C. and T.Y. Ho, *Water-entry for a wedge in arbitrary water depth.* Engineering analysis with boundary elements, 1994. **14**(2): p. 179-185.
13. Battistin D. and A. Iafrati, *Hydrodynamic loads during water entry of two-dimensional and axisymmetric bodies.* Journal of fluids and structures, 2003. **17**(5): p. 643-664.
14. Sun H., *A Boundary Element Method applied to strongly nonlinear wave-body interaction problems*, 2007, Ph.D dissertation, Norwegian University of Science and Technology: Trondheim, Norwegian.
15. Sun H. and O.M. Faltinsen, *Water impact of horizontal circular cylinders and cylindrical shells.* Applied Ocean Research, 2006. **28**(5): p. 299-311.
16. Sun H. and O.M. Faltinsen, *Water entry of a bow-flare ship section with roll angle.* Journal of Marine Science and Technology, 2009. **14**(1): p. 69-79.
17. Qin Z. and R.C. Batra, *Local slamming impact of sandwich composite hulls.* International Journal of Solids and Structures, 2009. **46**(10): p. 2011-2035.
18. Das K. and R.C. Batra, *Local water slamming impact on sandwich composite hulls.* Journal of fluids and structures, 2011. **27**(4): p. 523-551.
19. Stenius I., A. Rosén, and J. Kuttenkeuler, *Hydroelastic interaction in panel-water impacts of high-speed craft.* Ocean Engineering, 2010. **38**(2-3): p. 371-381.
20. Lu C., Y. He, and G. Wu, *Coupled analysis of nonlinear interaction between fluid and structure during impact.* Journal of fluids and structures, 2000. **14**(1): p. 127-146.

21. Panciroli R., S. Abrate, G. Minak, and A. Zucchelli, *Hydroelasticity in water-entry problems: Comparison between experimental and SPH results.* Composite Structures, 2011.
22. Charca S., B. Shafiq, and F. Just, *Repeated slamming of sandwich composite panels on water.* Journal of Sandwich Structures and Materials, 2009. **11**: p. 409-424.
23. Charca S. and B. Shafiq, *Damage assessment due to single slamming of foam core sandwich composites.* Journal of Sandwich Structures and Materials, 2010. **12**: p. 97-112.
24. Hu Z.H., X.D. He, J. Shi, R.G. Wang, and H.J. Liu, *Study on Delamination Problems of Composite Hull Structures under Slamming Loads.* Polymers & Polymer Composites, 2011. **19**(4-5): p. 433-437.
25. Van Paepegem W., C. Blommaert, I. De Baere, J. Degrieck, G. De Backer, J. De Rouck, J. Degroote, J. Vierendeels, S. Matthys, and L. Taerwe, *Slamming wave impact of a composite buoy for wave energy applications: Design and large‐scale testing.* Polymer Composites, 2011. **32**(5): p. 700-713.
26. Aureli M., C. Prince, M. Porfiri, and S.D. Peterson, *Energy harvesting from base excitation of ionic polymer metal composites in fluid environments.* Smart Materials and Structures, 2010. **19**: p. 015003.
27. Paris F. and J. Cañas, *Boundary element method: fundamentals and applications.*1997, New York: Oxford University Press
28. Greco M., *A two-dimensional study of green-water loading*, 2001, Ph.D dissertation, Norwegian University of Science and Technology: Trondheim, Norwegian.
29. Longuet-Higgins M.S. and E. Cokelet, *The deformation of steep surface waves on water. I. A numerical method of computation.* Proceedings of the Royal Society of London. A. Mathematical and Physical Sciences, 1976. **350**(1660): p. 1-26.
30. Young Y., *Time-dependent hydroelastic analysis of cavitating propulsors.* Journal of fluids and structures, 2007. **23**(2): p. 269-295.
31. Batra R.C. and X.Q. Liang, *Finite dynamic deformations of smart structures.* Computational mechanics, 1997. **20**(5): p. 427-438.
32. Das K., *Analysis of instabilities in microelectromechanical systems, and of local water slamming*, 2009, Ph.D dissertation, Virginia Polytechnic Institute and State University: Blacksburg, VA.
33. Aarsnes J., *Drop test with ship sections–effect of roll angle.* Marintek report, 1996. **603834**(01).
34. Arai M. and K. Matsunaga, *A numerical and experimental study of bow flare slamming.* Journal of the Society of Naval Architects of Japan, 1989. **166**: p. 343-353.

Chapter 4: Delamination in Sandwich Hulls due to Local Water Slamming Loads

Abstract

We study delamination in a sandwich hull due to transient finite plane strain elastic deformations caused by local water slamming loads and use the boundary element method to analyze deformations of water and the finite element method to scrutinize deformations of the hull. The cohesive zone model is used to study delamination initiation and propagation. The fluid is assumed to be incompressible and inviscid, and its deformations irrotational. A layer-wise third order shear and normal deformable plate/shell theory is employed to simulate hull's deformations by considering all geometric nonlinearities and taking hull's material to be St. Venant–Kirchhoff. The Rayleigh damping is introduced to account for structural damping that reduces oscillations in the pressure acting on the hull/water interface. Results have been computed for deformable sandwich hulls with face sheets made of fiber reinforced composites and the core of soft materials. The effect of the hull curvature on the hydrodynamic pressure acting on the hull/water interface has been delineated. Strain energies of deformation in the core and the face sheets have been computed to determine which modes of deformation are dominant in the core and the face sheets. It is shown that the consideration of geometric nonlinearities significantly increases the peak hydrodynamic pressure, the shape of the free surface of water adjacent to the hull, and the delamination length. The delamination occurs in mode-II and it reduces the hydroelastic pressure acting on the hull surface and hence alters its deformations.

Key Words: Water slamming, curved sandwich hull, geometric nonlinearities, delamination

1. Introduction

Local water slamming is characterized by large hydrodynamic loads of short duration which can cause significant structural damage, e.g., see Faltinsen [1]. The water entry of a V-shape wedge of small dead rise angle β was studied by von Kármán [2]. The conservation of linear momentum and the concept of added mass were employed to

analyze the water entry problem. Subsequently, Wagner [3] generalized von Kármán's work by including effects of water splash-up on a body with a small deadrise angle β. Sedov [4] extended Wagner's work to large deadrise angles. Correction factors to Wagner's solution to consider 3-D effects were proposed by Yu [5]. Bisplinghoff and Doherty [6] conducted 2-D experiments and showed that Wagner's solution overestimated effects of the piled-up water.

Cointe [7] used the method of asymptotic expansions and extended Wagner's theory to oblique impacts and initially curved free surfaces. Howison et al. [8] extended Cointe's work to axisymmetric and 3-D problems. Donguy et al. [9] used the finite element method (FEM) to analyze fluid-structure interaction (FSI) problems and found that Cointe's and Howison et al.'s solutions over-predict the maximum pressure. Shiffman and Spencer [10, 11] investigated the vertical impact of spheres and cones on water and developed the exact solution for a cone impacting water at normal incidence. A solution for the linearized problem involving the impact on water of a body at an arbitrary angle was developed by Trilling [12]. Schnitzer [13] presented an approximate method for computing the water impact loads and pressure distribution on elliptic cylinders during oblique impacts.

Review articles [14, 15] by Szebehely and Basin suggest that efforts should be concentrated on non-linear free surface boundary conditions and the hydroelastic aspects of the impact. Similarity solutions for water slamming of a rigid wedge were developed by Dobrovol'skaya [16] for $\beta > 30^{\circ}$ and by Zhao and Faltinsen [17] for $4^{\circ} \leq \beta \leq 81^{\circ}$. Zhao et al. [18] generalized Wagner's solution for arbitrary values of β and numerically solved the problem with the boundary integral method. Effects of jet flow were neglected and computed results were found to agree well with the corresponding experimental findings. Mei et al. [19] analytically and numerically solved two-dimensional water impact problems for wedges and circular cylinders including effects of jet flow. Yettou et al. [20] experimentally measured hydrodynamic pressures acting on rigid wedges during their free fall into stationary water and analytically solved the problem. Miloh [21, 22] derived expressions of the slamming force for water entry of rigid spheres and results agreed well with the available experimental data. Seddon and

Moatamedi [23] reviewed the water entry problem with focus on the water landing of spacecraft.

Fluid motion of water entry problems have been simulated by several numerical methods such as the FEM [9, 24], the FEM with Arbitrary-Lagrange-Euler (ALE) formulation [25], smoothed particle hydrodynamics (SPH) method [26] and the boundary element method (BEM) [17], [27], [28]. Zhao and Faltinsen [17] analyzed the water entry of a rigid wedge using the BEM and compared computed results with those obtained by the similarity method. Lin and Ho [27] used the BEM to study the influence of the water depth on the slamming pressure acting on a rigid wedge. They found that the maximum impact pressure is higher for shallow water than that for deep water which agreed with their experimental observations. Battistin and Iafrati [28] used the BEM to simulate two-dimensional water entry problems of arbitrary shaped bodies.

In practical water slamming problems, the hull is curved and deformable. Hull's deformations affect the motion of the fluid and the hydroelastic pressure acting on the fluid/solid interface. Sun [29] and Sun and Faltinsen [30, 31] numerically analyzed water slamming problems for arbitrary geometries using the BEM for studying deformations of the water that was modeled as non-viscous and incompressible, and the modal analysis technique for deformations of the cylindrical shell. They considered effects of gravity and flow separation from the solid surface. Qin and Batra [32] studied the hydroelastic problem using $\{3,2\}$-order plate theory for a sandwich hull of small deadrise angle and modified Wagner's water impact theory to consider the fluid structure interaction (FSI) during slamming. The plate theory incorporates the transverse shear and the transverse normal deformations of the core, but not of the face sheets which were modeled as Kirchhoff plates. Nila et al. [33] experimentally studied the water slamming of rigid and deformable bodies, and used the high speed Particle Image Velocimetry (PIV) technique to determine features of the fluid flow around the slammed bodies. The experimentally found velocity field, except in the spray root region, was found to agree well with the corresponding analytical and numerical results.

We note that a typical sandwich structure is composed of stiff face sheets and a flexible core, and the slamming pressure is highly localized. One should consider

transverse normal and transverse shear deformations especially when damage and failure of the composite hull are to be delineated. Das [34] and Das and Batra [35] studied the water slamming of deformable sandwich hulls using the commercial FE software LSDYNA with the ALE formulation. They considered all geometric nonlinearities when studying hull's deformations, assumed the fluid to be compressible, accounted for inertia effects in the fluid and the solid, and examined delamination between the core and the face sheets. They pointed out that boundary conditions at the fluid/solid interface were not well satisfied since the fluid penetrated into the rigid hull. The pressure distribution on the wetted hull surface was found to be oscillatory. Stenius et al. [36] used LSDYNA to study hydroelastic effects for deformable hulls considering different boundary conditions, impact velocities, deadrise angles, membrane effects and hull materials. Lu et al. [37] employed the coupled BEM and the FEM for studying hydroelastic effects with the hull modeled as a Timoshenko beam. Panciroli et al. [38] experimentally and numerically analyzed the water slamming of linear elastic wedges. The experimental results for different values of the panel thickness, deadrise angle and entry velocity were compared with those obtained by using the SPH formulation in LSDYNA. As pointed out by Oger et al. [26], 20 million particles are needed to correctly predict the pressure on the wedge. Experimental results for the failure of deformable sandwich composite panels including core shear, delamination and damage of the face sheets due to water slamming are reported in [39, 40]. Hu et al. [41] approximated the slamming pressure by equivalent bending moment to study delamination of a composite hull using the FE software ANSYS and the cohesive zone model (CZM). In [42] we studied deformations of the fluid by the BEM and focused on delineating how hull curvature affected the pressure distribution on curved rigid hulls.

Here we study delamination of a sandwich hull due to water slamming loads and use coupled BE and FE methods. The BEM is used to analyze deformations of the fluid that is modeled as incompressible and inviscid and whose deformations are assumed to have null vorticity. Finite transient deformations of the curved sandwich hull are analyzed by the FEM and employing a third order shear and normal deformable plate/shell theory (TSNDT), accounting for all geometric nonlinearities, and considering the hull material to be St. Venant-Kirchhoff. Deformations of the hull and the water are

coupled by requiring the continuity of the pressure and the normal component of velocity at the water/hull interface. The Rayleigh damping is used to account for damping of the structure that reduces oscillations in the hydrodynamic pressure on the solid/fluid interface. The CZM is incorporated in the TSNDT to study delamination initiation and growth due to water slamming.

The rest of the paper is organized as follows. In Section 2 we formulate the problem by considering all geometric nonlinearities and coupling between fluid's and structure's deformations. Numerical methods used to solve the hydroelastic problem are summarized in Section 3. Results for several water slamming problems of deformable sandwich hulls and delamination in a sandwich hull are described in Section 4. Conclusions of this work are summarized in Section 5.

2. Formulation of the Problem

A schematic sketch of the problem studied is shown in Fig. 1. At time t = 0, the ship hull keel impacts at normal incidence with vertically downward velocity V stationary water occupying the semi-infinite domain $Z \leq 0$ when rectangular Cartesian coordinates (X, Y, Z) fixed to the earth are used to describe deformations of the fluid. We use curvilinear material coordinates attached to the hull to identify its particles, and simplify the problem by assuming that the hull dimension in the Y-direction is much greater than that in the X- and Z-directions so that a plane strain state of deformation in the XZ-plane can be assumed and the problem can be solved as 2-dimensional (2-D). Furthermore, we assume that the hull geometry is symmetrical about the plane X = 0 and it initially impacts water along the line X = Z = 0. Thus deformations of water in the region $X \geq 0$ and $Z \leq 0$ and of the right-half of the hull are analyzed.

We note that the hydrodynamic load which accounts for hull's deformations is highly localized; thus the slamming problem is idealized as that of a deformable sandwich wedge entering water with a uniform vertically downward velocity (see Fig. 1). We account for finite deformations of the hull, and derive equations governing deformations of the hull and the water from balance laws of mass, linear momentum and moment of momentum, the strain-displacement relations appropriate for finite

deformations, and constitutive relations. An additional source of nonlinearity is the *a priori* unknown length of the wetted surface which is a nonlinear function of hull's deformations, and the deformed shape of the free surface of water. Of course, the shape of the free surface of water is to be determined as a part of the solution of the problem.

2.1 Equations governing deformations of the fluid

For hull speeds of the order of 10 m/s, viscous effects in water are often neglected. Also, the compressibility of water most likely plays a noticeable role only for a very short duration after the hull contacts the water. We thus assume the water to be incompressible

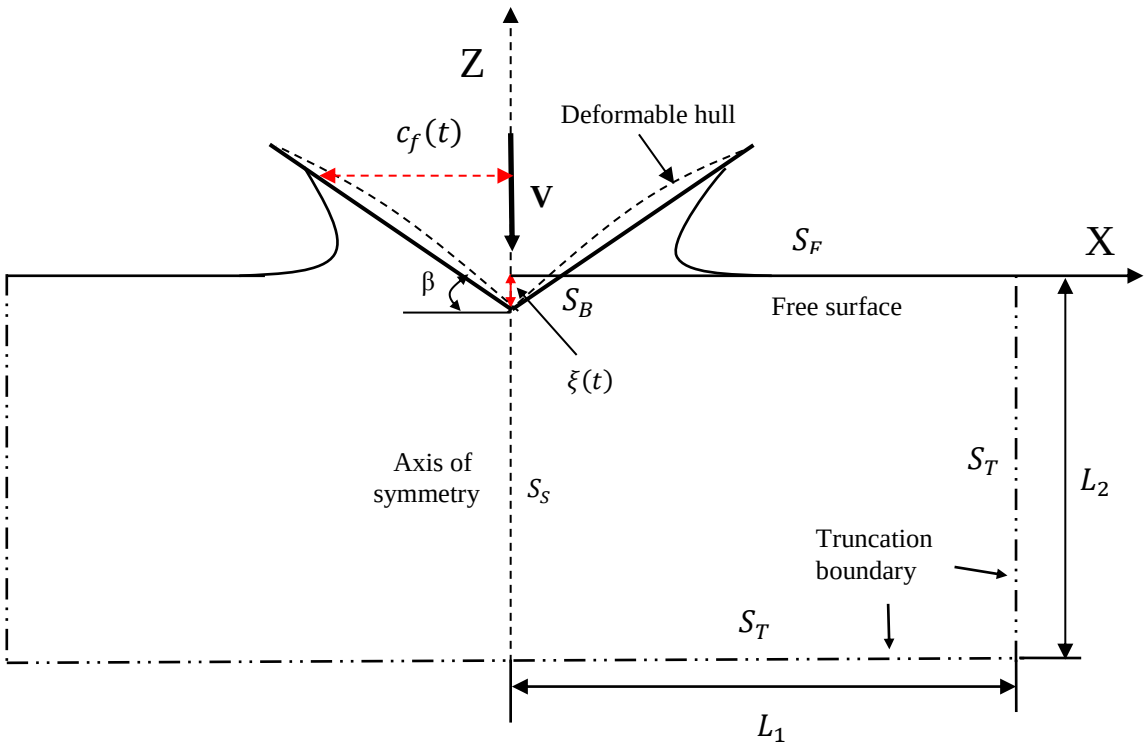

Fig. 1 Schematic sketch of the water slamming problem studied

and its deformations to be irrotational. The assumption of null vorticity implies that there exists a velocity potential φ such that velocity $\boldsymbol{v} = -\nabla\varphi$, where ∇ is the spatial gradient operator in the XZ-plane. The assumption of incompressibility requires that φ satisfy the Laplace equation:

$$\frac{\partial^2\varphi}{\partial Z^2} + \frac{\partial^2\varphi}{\partial X^2} = 0 \qquad \text{in the water domain.} \tag{1}$$

In the absence of gravity force, the balance of linear momentum for an inviscid fluid requires that

$$\rho \frac{D\boldsymbol{v}}{Dt} = -\nabla p \tag{2}$$

where ρ is the mass density of water, D/Dt the total time derivative, and the hydrostatic pressure p is determined by solving Eq. (2) under the following boundary conditions.

$$p = p_a, \ \frac{\mathrm{DX}}{\mathrm{Dt}} = -\frac{\partial \varphi}{\partial \mathrm{X}}, \frac{\mathrm{DZ}}{\mathrm{Dt}} = -\frac{\partial \varphi}{\partial \mathrm{Z}}, \ \frac{\mathrm{D}\varphi}{\mathrm{Dt}} = -\frac{1}{2}|\nabla \varphi|^2 \text{ on the free surface of water} \tag{3.a}$$

$$|\boldsymbol{v}| \to 0 \text{ as } (\mathrm{X}^2 + \mathrm{Z}^2)^{1/2} \to \infty \text{ for } \mathrm{X} > 0 \text{ and } \mathrm{Z} \leq 0 \tag{3.b}$$

$$\frac{\partial \varphi}{\partial \mathrm{X}} = 0 \ \text{ on } \mathrm{X} = 0 \tag{3.c}$$

Here p_a is the atmospheric pressure. In writing boundary condition (3.a) we have tacitly neglected the surface tension effect. These equations imply that the velocity of a point on the free surface equals that of the fluid particle instantaneously occupying it. Eq. $(3.a)_4$ following from Eq. $(3.a)_1$ and the Bernoulli Eq. (5) is used to update the function φ on the free surface after every time step. Ideally one should specify in Eq. (3.b) the rate of decay of the speed of water at infinity. However, we do not do so since the domain occupied by the fluid will be truncated to a finite one when numerically solving the problem. The boundary condition (3.c) follows from the assumption that deformations are symmetric about the plane X = 0. At the fluid/hull interface the non-penetration of the fluid into the solid is satisfied if

$$\frac{\partial \varphi}{\partial \mathrm{n}} = -\dot{\boldsymbol{U}} \cdot \boldsymbol{n} \tag{4}$$

where $\dot{\boldsymbol{U}}$ is velocity of the hull particle and $\boldsymbol{n}$ is a unit vector normal to the fluid/hull interface (pointing into hull).

Recalling that $\boldsymbol{v} = -\nabla\varphi$, Eq. (2) can be integrated to give the following Bernoulli equation

$$\mathrm{p} - \mathrm{p_a} = -\rho\left(-\frac{\partial \varphi}{\partial \mathrm{t}} + \frac{1}{2}|\nabla \varphi|^2\right) \tag{5}$$

2.2 Equations governing deformations of sandwich hull

2.2.1 Kinematics

Because of the assumption of plane strain deformations we model the hull as a 2-D curved beam schematically shown in Fig. 2. In the reference configuration, we describe the position of a material point $\mathcal{p}$ by using orthogonal curvilinear coordinate axes y_1, y_2, y_3 with y_1-axis along the tangent to the mid-surface of the beam, y_2-axis pointing into the plane of the paper, and y_3-axis pointing along the local thickness

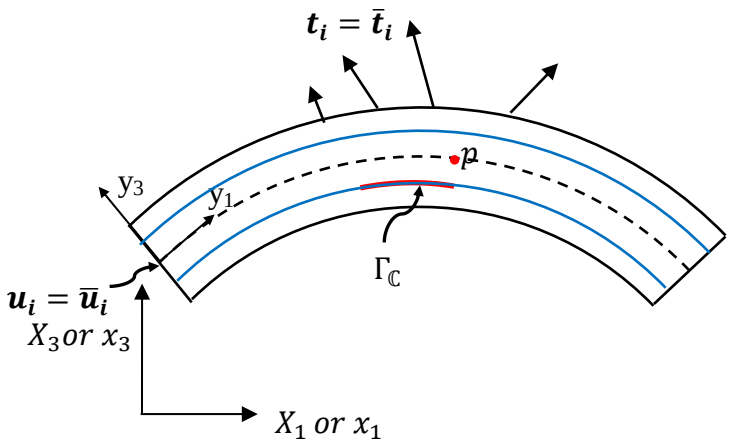

(a)

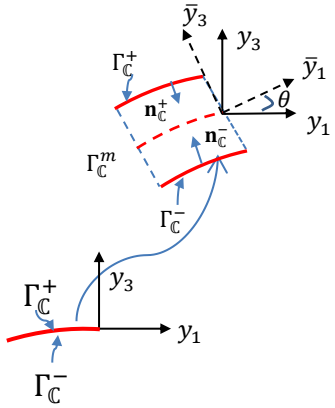

(b)

Fig. 2 Schematic sketches of a curved beam (a) and of cohesive interface $\Gamma_{\mathbb{C}}$ (b). X_2-, x_2- , y_2- and $\bar{y}_2$ -axes pointing into the plane of the paper are not shown in the Fig.

direction. The coordinate axes y_1, y_2, y_3 move with the downward instantaneous velocity $\boldsymbol{V}$ (rigid translation, no rotation). Let position vectors, with respect to fixed rectangular Cartesian coordinate axes, of point $\mathscr{p}$ in the current and the reference configurations be $\boldsymbol{x}$ and $\boldsymbol{X}$, respectively. The y_2-axis is parallel to the x_2-(or the y-) and X_2-(or the Y-) axes. The displacement $\boldsymbol{U}$ of point $\mathscr{p}$ is given by

$$\boldsymbol{U} = \boldsymbol{u} + \boldsymbol{u}' = \boldsymbol{x} - \boldsymbol{X} \tag{6}$$

where $\boldsymbol{u}'$ is the displacement of the origin of the curvilinear coordinate axes y_1, y_2, y_3 and is only a function of time t, and $\boldsymbol{u}$ is the displacement relative to axes y_1, y_2, y_3. The displacement, velocity and acceleration of point $\mathscr{p}$ relative to axes y_1, y_2, y_3 are hereafter called relative or vibrational displacement, velocity and acceleration, respectively. The translational velocity and acceleration of the origin of the curvilinear coordinate axes y_1, y_2, y_3 are $\boldsymbol{V}$ and $\dot{\boldsymbol{V}}$, respectively.

Components, G_{ij}, of the metric tensor in the reference configuration are given by

$$G_{ij} = \boldsymbol{A}_i \cdot \boldsymbol{A}_j \,, \;\; \boldsymbol{A}_i = \frac{\partial \boldsymbol{X}}{\partial y_i} \tag{7}$$

For orthogonal curvilinear coordinate axes G_{ij} is non-zero only when $i = j$. We set

$$H_1 = \sqrt{G_{11}} \,, \quad H_2 = \sqrt{G_{22}} = 1, \quad H_3 = \sqrt{G_{33}} = 1, \;\; \tilde{e}_i = \frac{\boldsymbol{A}_i}{H_{(i)}} \text{ (no sum on } i\text{).} \tag{8}$$

The ordered set $(\tilde{e}_1, \tilde{e}_2, \tilde{e}_3)$ form orthonormal base vectors for the curvilinear coordinate axes in the reference configuration. We note that

$$H_1 = \left(1 + \frac{y_3}{R}\right), \;\; \frac{\partial \tilde{e}_1}{\partial y_1} = -\frac{\tilde{e}_3}{R} \,, \;\; \frac{\partial \tilde{e}_3}{\partial y_1} = \frac{\tilde{e}_1}{R} \tag{9}$$

where R is the radius of curvature of the point $(y_1, y_2, 0)$ on the mid-surface of the beam.

Physical components of the deformation gradient, $\boldsymbol{F}$, are given by

$$[F] = \begin{bmatrix} 1 + \frac{1}{H_1}\left(\frac{\partial u_1}{\partial y_1} + \frac{u_3}{R}\right) & 0 & \frac{\partial u_1}{\partial y_3} \\ 0 & 1 & 0 \\ \frac{1}{H_1}\left(\frac{\partial u_3}{\partial y_1} - \frac{u_1}{R}\right) & 0 & 1 + \frac{\partial u_3}{\partial y_3} \end{bmatrix} \tag{10}$$

The Green-St. Venant strain tensor, $\boldsymbol{E}$, defined by

$$\boldsymbol{E} = \frac{1}{2}(\boldsymbol{F}^T\boldsymbol{F} - \mathbf{1}), \tag{11}$$

where $\mathbf{1}$ is the identity tensor, has the following non-zero physical components:

$$E_{11} = \frac{1}{H_1}\left(\frac{\partial u_1}{\partial y_1} + \frac{u_3}{R}\right) + \frac{1}{2{H_1}^2}\left[\left(\frac{\partial u_1}{\partial y_1} + \frac{u_3}{R}\right)^2 + \left(\frac{\partial u_3}{\partial y_1} - \frac{u_1}{R}\right)^2\right]$$

$$E_{33} = \frac{\partial u_3}{\partial y_3} + \frac{1}{2}\left[\left(\frac{\partial u_1}{\partial y_3}\right)^2 + \left(\frac{\partial u_3}{\partial y_3}\right)^2\right] \tag{12}$$

$$2E_{13} = \frac{1}{H_1}\left(\frac{\partial u_3}{\partial y_1} - \frac{u_1}{R}\right) + \frac{\partial u_1}{\partial y_3} + \frac{1}{H_1}\left[\frac{\partial u_3}{\partial y_3}\left(\frac{\partial u_3}{\partial y_1} - \frac{u_1}{R}\right) + \frac{\partial u_1}{\partial y_3}\left(\frac{\partial u_1}{\partial y_1} + \frac{u_3}{R}\right)\right]$$

We note that $\boldsymbol{E}$ incorporates all nonlinearities including the von Kármán nonlinearity, and is valid for finite (or large) deformations of the beam.

2.2.2 Kinetics

The in-plane displacements (u_1, u_3) of a point are governed by the following equations expressing the balance of linear momentum written in the Lagrangian description of motion using physical components $T_{11}, T_{13}, T_{31}, T_{33}$, of the first Piola-Kirchhoff stress tensor [43] .

$$\rho_0\ddot{u}_1 = \frac{1}{H_1}\frac{\partial T_{11}}{\partial y_1} + \frac{1}{H_1}\frac{\partial (H_1 T_{13})}{\partial y_3} + \frac{1}{H_1 R}T_{31} + f_1 \tag{13.a}$$

$$\rho_0\ddot{u}_3 = \frac{1}{H_1}\frac{\partial T_{31}}{\partial y_1} + \frac{1}{H_1}\frac{\partial (H_1 T_{33})}{\partial y_3} - \frac{1}{H_1 R}T_{11} + f_3 \tag{13.b}$$

$$u_i(y_1, y_3, 0) = u_i^0(y_1, y_3) \tag{13.a}$$

$$\dot{u}_i(y_1, y_3, 0) = \dot{u}_i^0(y_1, y_3) \tag{13.b}$$

$$T_{ij}N_j^t = \bar{t}_i(y_1, y_3, t) \quad \text{on } \Gamma_\mathrm{t} \tag{13.c}$$

$$u_i(y_1, y_3, t) = \bar{u}_i(y_1, y_3, t) \text{ on } \Gamma_\mathrm{u} \tag{13.d}$$

$$T_{ij}N_j^{\mathbb{C}+} = \bar{f}_i^{\mathbb{C}+},\ T_{ij}N_j^{\mathbb{C}-} = \bar{f}_i^{\mathbb{C}-} \text{ on } \Gamma_\mathbb{C} \tag{13.e}$$

$$\bar{f}_1^{\mathbb{C}-} = \hat{a}(\mathbb{R}_{11}\sigma_\mathrm{t} + \mathbb{R}_{31}\sigma_\mathrm{n})\ ,\ \bar{f}_3^{\mathbb{C}-} = \hat{a}(\mathbb{R}_{13}\sigma_\mathrm{t} + \mathbb{R}_{33}\sigma_\mathrm{n}),\ \bar{f}_i^{\mathbb{C}+} = -\bar{f}_i^{\mathbb{C}-} \text{ on } \Gamma_\mathbb{C} \tag{13.f}$$

$$[\mathbb{R}] = \begin{bmatrix} \cos\theta & 0 & \sin\theta \\ 0 & 1 & 0 \\ -\sin\theta & 0 & \cos\theta \end{bmatrix} \tag{13.g}$$

In Eq. (13) indices i and j equal 1 and 3, a repeated index implies summation over the range of the index, f_1 and f_3 are components of the body force per unit reference volume along the y_1- and the y_3- axes, respectively, ρ_0 the mass density in the reference configuration, and $\ddot{u}_i = \frac{\partial^2 u_i}{\partial t^2}$. The initial displacement u_i^0 and the initial velocity $\dot{u}_i^0$ are known functions of y_1 and y_3. $\boldsymbol{N}^t$ is a unit outward normal in the reference configuration at a point on the boundary Γ_t where surface tractions are prescribed as $\bar{t}_i$. On boundary Γ_u, displacements are prescribed as $\bar{u}_i$. $\boldsymbol{N}^{\mathbb{C}\pm}$ is the outward unit normal on the corresponding interface $\Gamma_{\mathbb{C}}^{\pm}$, $\hat{a}$ equals the area into which a unit surface area in the reference configuration is deformed, $\mathbb{R}_{ij}$ the rotation matrix, θ the angle between y_1- and $\bar{y}_1$- axes, $\bar{f}_i^{\mathbb{C}\pm}$ the traction on the cohesive interface $\Gamma_{\mathbb{C}}^{\pm}$, and σ_t and σ_n the tangential and the normal tractions, respectively, on the cohesive interface in the current configuration. Tractions σ_t and σ_n are related to jumps in displacements on the cohesive interface as discussed in subsection 2.2.4. As unit normals at corresponding points on the upper and the lower surfaces of a cohesive interface may not be parallel to each other, we use a mean cohesive interface $\Gamma_{\mathbb{C}}^m$ (see Fig. 2) to find surface tractions and jumps in the tangential and the normal displacements on the cohesive interface. Accordingly, we introduce local coordinate axes $\bar{y}_1$ and $\bar{y}_3$, respectively, along the tangent and the normal to the deformed mean cohesive interface $\Gamma_{\mathbb{C}}^m$. The unit outward normal $\mathbf{n}_{\mathbb{C}}^{\pm}$ on $\Gamma_{\mathbb{C}}^{\pm}$ in the current configuration is found from values of the deformation gradient on the corresponding interface. We assume that the rotation angle θ of the mean cohesive interface $\Gamma_{\mathbb{C}}^m$ equals the average of the rotation angles of unit normals $\mathbf{n}_{\mathbb{C}}^{\pm}$. The deformed area $\hat{a}$ of the mean cohesive interface $\Gamma_{\mathbb{C}}^m$ is taken equal to the average of areas into which unit areas on $\Gamma_{\mathbb{C}}^+$ and $\Gamma_{\mathbb{C}}^-$ are deformed. We note that tractions on $\Gamma_{\mathbb{C}}^+$ and $\Gamma_{\mathbb{C}}^-$ are equal and opposite.

Using the transformation matrix $\mathbb{R}_{ij}$, the jump displacements δ_t and δ_n, of corresponding points on $\Gamma_{\mathbb{C}}^+$ and $\Gamma_{\mathbb{C}}^-$ are given by

$$\delta_t = \mathbb{R}_{1j}\left(u_j^+(y_1, y_3, t) - u_j^-(y_1, y_3, t)\right) \text{ on } \Gamma_{\mathbb{C}},\ j = 1, 3 \tag{14.a}$$

$$\delta_n = \mathbb{R}_{3j}\left(u_j^+(y_1, y_3, t) - u_j^-(y_1, y_3, t)\right) \text{ on } \Gamma_{\mathbb{C}},\ j = 1, 3 \tag{14.b}$$

where $u_i^+(y_1, y_3, t)$ and $u_i^-(y_1, y_3, t)$ represent, respectively, displacements of a point on $\Gamma_{\mathbb{C}}^+$ and $\Gamma_{\mathbb{C}}^-$ with respect to y_1 and y_3 coordinate axes, and δ_t and δ_n equal jumps in the tangential and the normal displacements of corresponding points on $\Gamma_{\mathbb{C}}^+$ and $\Gamma_{\mathbb{C}}^-$ with respect to $\bar{y}_1$ and $\bar{y}_3$ coordinate axes on the mean cohesive interface $\Gamma_{\mathbb{C}}^m$.

Initially the hull is assumed to move with a uniform velocity **V** along the negative Z-axis and have null vibrational displacement and velocity, i.e.,

$$\dot{\boldsymbol{u}}(y_1, y_3, 0) = \mathbf{0}, \boldsymbol{u}(y_1, y_3, 0) = \mathbf{0} \tag{15}$$

We assume that the left and the right edges of the hull are undeformed during the water slamming process. Thus $u_i(0, y_3, t) = 0, u_i(\mathcal{L}, y_3, t) = 0,\ i = 1, 3$, on the left and the right edges of the hull. On the bottom surface $\Gamma_t(t)$ (or $y_3 = y_{3b}$) of the hull that contacts water

$$T_{ij}N_j = p\,\hat{a}\,n_i(y_1, y_{3b}, 0),\ \ \frac{\partial \varphi}{\partial n} = -(\dot{\boldsymbol{u}} + \boldsymbol{V}) \cdot \boldsymbol{n} \tag{16. a, b}$$

and

$$T_{ij}N_j = 0 \quad \text{on } \Gamma_f \tag{17}$$

Here Γ_f is the part of the bottom surface of the hull not contacting water and also the entire top surface of the hull**,** and $\dot{\boldsymbol{u}}$ the vibrational velocity of the wetted hull surface. We note that in Eqs. (16), T_{ij} is computed from deformations of the hull and p from deformations of the water. Furthermore, $\boldsymbol{N}$ is a unit outward normal at a point on $\Gamma_t(t)$ of the hull in the undeformed configuration, n_i is the component of the unit normal $\boldsymbol{n}$ to the hull surface in the deformed configuration, and $\hat{a}$ equals the area into which a unit area on the hull surface in the reference configuration is deformed. Thus $\boldsymbol{n}$ and $\hat{a}$ depend upon deformations of the hull. For an inviscid fluid the tangential surface traction vanishes. Also, the tangential velocities of the fluid and the solid particles instantaneously contacting each other may be discontinuous. We note that Eqs. (16. a, b) imply the continuity of surface tractions and the normal component of velocity on the interface

$\Gamma_t(t)$ between the hull and the water, and $\Gamma_t(t)$ is to be determined as a part of the solution of the problem. The continuity of surface tractions on $\Gamma_t(t)$ enables one to solve the FSI problem if $\Gamma_t(t)$ were known. The continuity of the normal component of velocity expressed by Eq. (16. b) is needed to find $\Gamma_t(t)$. Should the pressure p at a point on $\Gamma_t(t)$ become tensile, then the fluid cannot be contacting the hull at that point. That is, the fluid separates from the hull at that point and the surfaces become traction free. For problems studied herein, this situation did not arise.

2.2.3 Constitutive relations

We assume that the beam material is St. Venant-Kirchhoff for which the strain energy density, W, is given by

$$W = \frac{1}{2} E_{ij} C_{ijkl} E_{kl}, C_{ijkl} = C_{klij} = C_{jikl} \tag{18}$$

Here $\boldsymbol{C}$ is the fourth-order elasticity tensor having 21 independent components for a general anisotropic material. The strain energy density for the St. Venant-Kirchhoff material reduces to that of a Hookean material if the finite strain tensor $\boldsymbol{E}$ is replaced in Eq. (18) by the strain tensor for infinitesimal deformations. The material with the strain energy density given by Eq. (18) is often called neo-Hookean. Batra [44] has compared the response of four elastic materials for which a stress tensor is a linear function of an appropriate strain tensor (e.g., the Cauchy stress tensor is a linear function of the Almansi-Hamel strain tensor).

For a nonlinear elastic material, physical components of the second Piola-Kirchhoff stress tensor $\boldsymbol{S}$ are related to $\boldsymbol{E}$ by

$$S_{ij} = \frac{\partial W}{\partial E_{ij}} = C_{ijkl} E_{kl} \tag{19}$$

For plane strain deformations of an orthotropic material with the material principal axes coincident with the coordinate axes (y_1, y_2, y_3), Eq. (19) reduces to

$$\begin{Bmatrix} S_{11} \\ S_{33} \\ S_{13} \end{Bmatrix} = \begin{bmatrix} C_{1111} & C_{1133} & 0 \\ C_{3311} & C_{3333} & 0 \\ 0 & 0 & C_{1313} \end{bmatrix} \begin{Bmatrix} E_{11} \\ E_{33} \\ 2E_{13} \end{Bmatrix} \tag{20.a}$$

$$C_{1111} = \frac{1-\nu_{23}\nu_{32}}{E_2E_3\mathcal{D}},\ C_{3333} = \frac{1-\nu_{12}\nu_{21}}{E_1E_2\mathcal{D}},\ C_{1133} = C_{3311} = \frac{\nu_{31}+\nu_{21}\nu_{32}}{E_2E_3\mathcal{D}},\ C_{1313} = G_{13} \tag{20.b}$$

$$\mathcal{D} = \frac{1}{E_1E_2E_3}\begin{vmatrix} 1 & -\nu_{21} & -\nu_{31} \\ -\nu_{12} & 1 & -\nu_{32} \\ -\nu_{13} & -\nu_{23} & 1 \end{vmatrix} \tag{20.c}$$

Here E_1, E_2 and E_3 equal Young's moduli along the y_1-, the y_2- and the y_3-axes, respectively, G_{13} is the shear modulus in the y_1y_3-plane, $\upsilon_{12}, \upsilon_{13}$ and υ_{23} are Poisson's ratios.

Recalling that

$$\boldsymbol{T} = \boldsymbol{FS} \tag{21}$$

where $\boldsymbol{T}$ is the 1st Piola-Kirchhoff stress tensor, we get

$$\begin{bmatrix} T_{11} & T_{13} \\ T_{31} & T_{33} \end{bmatrix} = \begin{bmatrix} F_{11}S_{11} + F_{13}S_{13} & F_{11}S_{13} + F_{13}S_{33} \\ F_{31}S_{11} + F_{33}S_{13} & F_{31}S_{13} + F_{33}S_{33} \end{bmatrix} \tag{22}$$

Substitution for $\boldsymbol{F}$ from Eq. (10) into Eq. (22), for $\boldsymbol{E}$ from Eq. (12) into Eq. (20) and the result into Eq. (22) gives expressions for $\boldsymbol{T}$ in terms of displacements u_1 and u_3 and the four elastic constants C_{1111}, C_{1133}, C_{3333}, and C_{1313}. We note that constitutive relations (19) and (21) are materially objective, i.e., are invariant under a rigid body motion superimposed upon the present configuration.

The true stress or the Cauchy stress, $\boldsymbol{\sigma}$, is related to the 1st Piola-Kirchhoff stress by

$$\boldsymbol{\sigma} = \frac{1}{J}\boldsymbol{T}\boldsymbol{F}^T, \tag{23}$$

where J is the determinant of deformation gradient $\boldsymbol{F}$. Thus $\boldsymbol{\sigma}$ is a more involved function of displacement gradients than either $\boldsymbol{T}$ or $\boldsymbol{S}$.

We now substitute in Eq. (13) for the first Piola-Kirchhoff stress $\boldsymbol{T}$, and solve the resulting nonlinear coupled partial differential equations (PDEs) for u_1 and u_3 under pertinent initial and boundary conditions. These PDEs involve 2nd order derivatives of u_1 and u_3 with respect to y_1, y_3 and time. Thus C^0 basis functions can be used to numerically solve the boundary value problem for the sandwich hull.

2.2.4 Cohesive zone model

2.2.4.1 Mode-I or mode-II deformations

We first describe the CZM for mode-I and mode-II deformations, and then for mixed-mode deformations. We postulate the traction-separation relations depicted in Figs. 3a and 3b for mode-I and mode-II deformations, respectively.

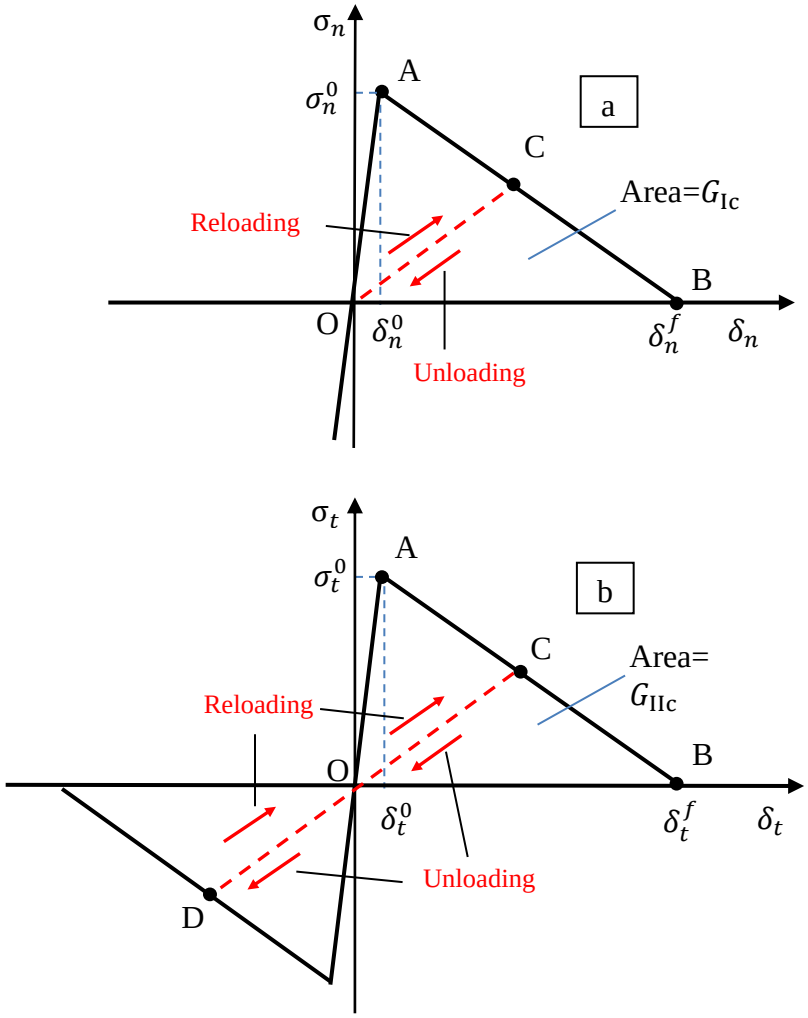

Fig. 3 Traction-separation relations at cohesive interface; (a) mode-I, (b) mode-II

For relative normal (tangential) displacement δ_n (δ_t) of adjoining points on the two sides of the interface less than δ_n^0 (δ_t^0) corresponding to point A in Fig. 3a (Fig. 3b), the traction-separation relation represented by straight line OA is completely reversible. For monotonically increasing values of δ_n (δ_t) greater than δ_n^0 (δ_t^0) the traction-separation relation is given by straight line AB. For $\delta_n = \delta_n^f$ $(\delta_t = \delta_t^f)$ there is complete separation

(sliding) at the interface for mode-I (mode-II) deformations. For mode-I deformations, the separated surfaces are traction free and for mode-II deformations the sliding surfaces are assumed to be smooth or frictionless. Should the relative displacement δ_n (δ_t) exceeding δ_n^0 (δ_t^0) but less than δ_n^f (δ_t^f) begin to decrease, then the traction-separation relation follows the path CO for δ_n and COD for δ_t. The area of the triangle OAB equals the critical strain energy release rate (SERR) G_{Ic} (G_{IIc}) for mode-I (mode-II) deformations. Values of G_{Ic} (G_{IIc}) and σ_n^0 (σ_t^0) characterize the interface. Here σ_n^0 (σ_t^0) equals the interface strength for mode-I (mode-II) deformations. The slope, k_s, of straight line OA is estimated. Then

$$\sigma_i = k_s \delta_i , \quad i = t , n \tag{24.a}$$

$$\delta_i^0 = \frac{\sigma_i^0}{k_s}, \; i = t, n \tag{24.b}$$

and k_s is called the initial interface stiffness.

Thus, the delamination initiates when $\sigma_n = \sigma_n^0$ ($\sigma_t = \sigma_t^0$), and complete separation (sliding) occurs when

$$\delta_n^f = \frac{2G_{Ic}}{\sigma_n^0}, \; \delta_t^f = \frac{2G_{IIc}}{\sigma_t^0} \tag{25}$$

for pure mode-I (mode-II) deformations.

The interface stiffness k_s should be such that it does not make the system of simultaneous equations to be solved ill-conditioned and effectively prevents interpenetration between two contacting layers when compressive normal traction acts on the interface. For a beam of thickness H we use the relation

$$k_s = \frac{H}{\mathcal{K}} \max(\sigma_n^0, \sigma_t^0) \tag{26}$$

to find k_s, and set the nondimensional parameter $\mathcal{K} = 10^{-9}$.

2.2.4.2 Mixed mode deformations

For mixed-mode deformations, $\delta_n > 0$ and $\delta_t \neq 0$. We follow the approach of Ref. [45], and postulate that the delamination at a point on the interface initiates when

$$\left(\frac{\sigma_n}{\sigma_n^0}\right)^2 + \left(\frac{\sigma_t}{\sigma_t^0}\right)^2 = 1 \tag{27}$$

and complete separation occurs when

$$\left(\frac{G_I}{G_{Ic}}\right)^2 + \left(\frac{G_{II}}{G_{IIc}}\right)^2 = 1 \tag{28}$$

Here σ_n and σ_t are the normal and the tangential tractions on the interface under mixed-mode deformations. Similarly, G_I (G_{II}) are SERR for mode-I (mode-II) deformations for mixed-mode loading.

We define the equivalent mixed-mode relative displacement δ_e by

$$\delta_e = \sqrt{(\delta_t)^2 + (\delta_n)^2} = \frac{\delta_t}{\mu}\sqrt{1+\mu^2} = \delta_n\sqrt{1+\mu^2} \tag{29}$$

where $\mu\delta_n = \delta_t$, and note that $\mu = 0$ for mode-I, and $\mu \to \infty$ for mode-II deformations .

Assuming that under mixed-mode loading, the interface stiffness for the tangential and the normal traction-separation modes also equals k_s, then substituting for σ_n and σ_t in terms of δ_t and δ_n into Eq. (27), the separation will initiate when

$$\left(\frac{\delta_n}{\sigma_n^0}\right)^2 + \left(\frac{\delta_t}{\sigma_t^0}\right)^2 = 1/(k_s)^2 \tag{30}$$

or equivalently,

$$\delta_e^0 = \delta_t^0\delta_n^0\sqrt{\frac{1+\mu^2}{(\delta_t^0)^2+(\mu\delta_n^0)^2}} \tag{31}$$

where δ_t^0 and δ_n^0 are given by Eq. (24.b). We evaluate the mode-mixity ratio μ at every point on the interface and note that it can vary from point to point. However, at a point μ is assumed to stay fixed from separation initiation to separation completion.

In order to find the value δ_e^f of δ_e at complete separation, we assume that the effective traction–effective separation relation under mixed-mode loading is also triangular, i.e., is similar to that for mode-I and mode-II loadings. Thus values of G_I and G_{II} at complete separation are given by

$$G_I(1+\mu^2) = \frac{k_s \delta_e^0 \, \delta_e^f}{2}, \; G_{II} = \mu^2 G_I \tag{32}$$

Substitution from Eq. (32) into Eq. (28) gives

$$\delta_e^f = \frac{2(1+\mu^2)}{k_s \delta_e^0}\left[\left(\frac{1}{G_{Ic}}\right)^2 + \left(\frac{\mu^2}{G_{IIc}}\right)^2\right]^{-1/2} \tag{33}$$

Because of the assumption of μ staying constant at a point, should unloading occur for $\delta_e^0 < \delta_e < \delta_e^f$, the unloading curve follows a path similar to the straight line CO in Fig. 3a for mode-I deformations.

2.2.5 Displacement field for the TSNDT

For 2-D problems being studied here, we model the hull as a sandwich beam having three layers and denote displacements of a point in the top, the central, and the bottom layers by superscripts *t*, *c* and *b*, respectively. With the origin of the curvilinear coordinate axes located at the geometric centroid of the rectangular cross-section (e.g., see Fig. 4), we assume the following displacement field in the beam.

$$u_\alpha^c(y_1, y_3, t) = \sum_{i=0}^{3} (y_3)^i \, u_{\alpha i}^c(y_1, t), \qquad \alpha = 1,3, \qquad |y_3| \le h^c \tag{34.a}$$

$$u_\alpha^t(y_1, y_3, t) = u_\alpha^c(y_1, h^c, t) + u_{\alpha 0}^t + \sum_{i=1}^{3} \left((y_3)^i - (h^c)^i\right) u_{\alpha i}^t(y_1, t), \quad \alpha = 1,3, \qquad h^c \le y_3 \le h^c + h^t \tag{34.b}$$

$$u_\alpha^b(y_1, y_3, t) = u_\alpha^c(y_1, -h^c, t) - u_{\alpha 0}^b + \sum_{i=1}^{3} \left((y_3)^i - (-h^c)^i\right) u_{\alpha i}^b(y_1, t), \quad \alpha = 1,3, \quad -(h^b + h^c) \le y_3 \le -h^c \tag{34.c}$$

Here u_{10}^c and u_{30}^c are, respectively, the axial and the transverse displacements of a point on the beam mid-surface, $u_{\alpha i}^c, u_{\alpha i}^t$ and $u_{\alpha i}^b$ ($\alpha = 1,3, \;\; i = 1,2,3$) may be interpreted as generalized axial and transverse displacements of a point, and $u_{\alpha 0}^t$ and $u_{\alpha 0}^b$ ($\alpha = 1,3$) represent jumps in displacements between adjoining points on the top and the bottom interfaces, respectively, when there is delamination. The top (bottom) interface is between the core and the top (bottom) face sheet. Displacements δ_n and δ_t at the

interface between the top layer and the core appearing in Eq. (24.a) are related to the displacement field $u_\alpha(y_1, y_3, t)$ by substituting from Eq. (34) into Eq. (14). Thus

$$\delta_t = \mathbb{R}_{1\alpha} u^t_{\alpha 0},\ \delta_n = \mathbb{R}_{3\alpha} u^t_{\alpha 0},\ \alpha = 1,3,\ \text{summed on } \alpha \tag{35}$$

We are unable to analytically solve the above formulated nonlinear problem; thus we analyze it numerically.

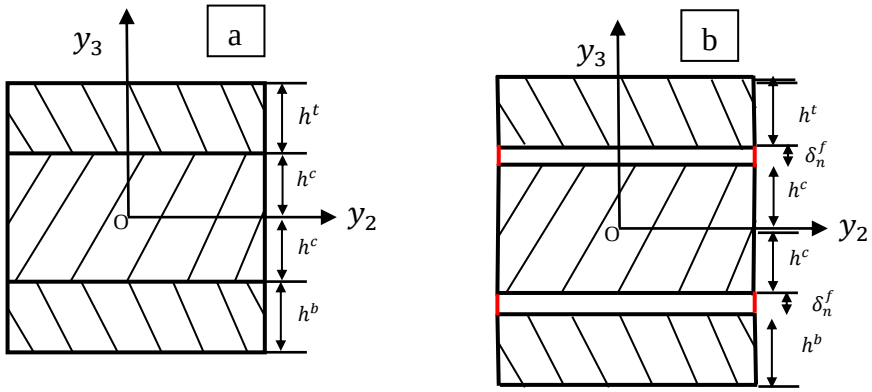

Fig. 4 Cross-section of a 3-layer beam ((a) before delamination, (b) after separation)

3. Numerical Solution of the Problem

3.1 Analysis of fluid's deformations by the boundary element method (BEM)

We use the BEM to solve Laplace Eq. (1) and truncate the domain occupied by the fluid to lengths L_1 and L_2 in the X- and the Z- directions, respectively. Values of L_1 and L_2 will be determined iteratively to compute a converged solution near the hull/water interface.

Using Green's second identity, the velocity potential at point *j* in the fluid (either in the interior or on the boundary) can be written as [46] :

$$c(j)\varphi(j) = \int_{\partial D} G(\boldsymbol{\xi}, j)\frac{\partial \varphi(\boldsymbol{\xi})}{\partial n} ds(\boldsymbol{\xi}) - \int_{\partial D} \varphi(\boldsymbol{\xi})\frac{\partial G(\boldsymbol{\xi}, j)}{\partial n} ds(\boldsymbol{\xi}) \tag{36}$$

where $G(\boldsymbol{\xi}, j) = \ln r(\boldsymbol{\xi}, j)$, $r(\boldsymbol{\xi}, j)$ is the distance between source point $\boldsymbol{\xi}$ on the fluid boundary and point *j* , c(j) is a constant, and D equals the region occupied by the fluid.

We note that c, φ, D and $\boldsymbol{n}$ vary with time t; this dependence is not exhibited to simplify the notation. Noting that Eq. (36) holds for a constant velocity potential, we get

$$c(j) = \int_{\partial D} \frac{\partial G(\boldsymbol{\xi},j)}{\partial n} ds(\boldsymbol{\xi}) \tag{37}$$

The integral Eq. (36) is converted into a system of coupled simultaneous linear algebraic equations by using piecewise linear basis functions, i.e., the boundary of the fluid domain is discretized by using 2-node 1-D elements. Integrals in Eq. (36) are numerically evaluated by using 6 Gauss points in each element. Thus Eq. (36) can be written as

$$[H]\begin{Bmatrix} \varphi^F \\ \varphi^B \\ \varphi^{T+S} \end{Bmatrix} = [G]\begin{Bmatrix} \frac{\partial \varphi^F}{\partial n} \\ \frac{\partial \varphi^B}{\partial n} \\ \frac{\partial \varphi^{T+S}}{\partial n} \end{Bmatrix} \tag{38}$$

where elements of matrices $[H]$ and $[G]$ depend upon coordinates of nodes, and superscripts F, B, T and S on a quantity represent, respectively, its value at a node on the free surface, the hull, the truncation boundaries and the axis of symmetry.

Recalling that at time *t* we know at every point on the fluid boundary either φ or $\frac{\partial \varphi}{\partial n}$ we can solve for the other variable at that point. Transforming unknowns in Eq. (38) to the left hand side, we rewrite it as

$$[A]\begin{Bmatrix} \frac{\partial \varphi^F}{\partial n} \\ \varphi^B \\ \varphi^{T+S} \end{Bmatrix} = [B]\begin{Bmatrix} \varphi^F \\ \frac{\partial \varphi^B}{\partial n} \\ \frac{\partial \varphi^{T+S}}{\partial n} \end{Bmatrix} \tag{39}$$

In writing Eq. (39) we have used boundary condition (4) and taken the velocity of the hull particles to be known.

After Eq. (39) has been solved we know φ and $\frac{\partial \varphi}{\partial n}$ at every point on the fluid boundary at time *t*. Thus the tangential derivative $\frac{\partial \varphi}{\partial s}$ of φ at points on the boundary ∂D

can be computed; here s is the arc length along ∂D. Combining $\frac{\partial \varphi}{\partial s}$ with the computed $\frac{\partial \varphi}{\partial n}$ on ∂D, the gradient vector $\nabla\varphi$ at points on the hull/water interface and on the free surface of water is determined. The free surface profile, and values of φ at points on the free surface are updated using Eq. (3.a). Eq. (36) is used to determine the velocity potential φ at any point in the fluid domain.

The term $\frac{\partial \varphi}{\partial \mathrm{t}}$ needed to determine the pressure field in the fluid domain from Eq. (5) is found by introducing a new variable Ψ defined by

$$\Psi = \frac{\partial \varphi}{\partial t} + \mathbf{V} \cdot \nabla\varphi \tag{40}$$

It has been proved by Greco [47] that Ψ also satisfies the 2-D Laplace equation

$$\frac{\partial^2 \Psi}{\partial X^2} + \frac{\partial^2 \Psi}{\partial Z^2} = 0 \tag{41}$$

Following Sun [29] and deferring details to the Appendix, boundary conditions for Ψ are

$$\Psi = \mathbf{V} \cdot \nabla\varphi + \frac{1}{2}|\nabla\varphi|^2 \qquad \text{on the free surface} \tag{42.a}$$

$$\frac{\partial \Psi}{\partial \mathrm{n}} = -\boldsymbol{n} \cdot \dot{\mathbf{V}} - \boldsymbol{n} \cdot \ddot{\boldsymbol{u}} - \mathbf{V} \cdot \nabla(\boldsymbol{n} \cdot \dot{\boldsymbol{u}}) \qquad \text{on the fluid/solid interface} \tag{42.b}$$

$$\frac{\partial \Psi}{\partial n} = 0 \qquad \text{on the axis of symmetry and on truncation boundaries} \tag{42.c}$$

Here $\dot{\mathbf{V}}$ is the acceleration of the rigid body motion, and $\ddot{\boldsymbol{u}}$ the vibrational acceleration of particles on the hull surface.

At every time *t*, the boundary value problem defined by Eqs. (41) and (42) is numerically solved by the BEM. The algebraic equation for the determination of Ψ and $\frac{\partial \Psi}{\partial n}$ at boundary points is

$$[A]\begin{Bmatrix} \frac{\partial \Psi^{\mathrm{F}}}{\partial n} \\ \Psi^{\mathrm{B}} \\ \Psi^{\mathrm{T+S}} \end{Bmatrix} = [B]\begin{Bmatrix} \Psi^{\mathrm{F}} \\ \frac{\partial \Psi^{\mathrm{B}}}{\partial n} \\ \frac{\partial \Psi^{\mathrm{T+S}}}{\partial n} \end{Bmatrix} \tag{43}$$

where matrices $[A]$ and $[B]$ are the same as those in Eq. (39). Knowing Ψ and φ, from Eq. (39), $\frac{\partial \varphi}{\partial t}$ can be evaluated at all points on the fluid boundary including those on the fluid/solid interface. This approach avoids finding $\frac{\partial \varphi}{\partial t}$ by the backward difference method at the expense of solving Eq. (43). Recall that the value of φ at any point in the fluid domain is found from Eqs. (36) and (37).

3.2 Analysis of the motion of free surface of water

The thickness of the water layer between the free surface and the hull near the terminus of the wetted length of the hull becomes very small and necessitates using extremely small time steps for analyzing subsequent deformations of the FSI problem. As explained in [42] for a rigid hull, we cut the thin jet, smoothen the free surface, re-mesh it and derive values of variables at the newly generated nodes by interpolating and extrapolating from those at nodes on the previous mesh. We numerically integrate Eq. (3.a) to find the motion of free surface of water.

3.3 Analysis of hull's deformations by the finite element method

We refer the reader to [48] for derivation of the governing equations, boundary conditions for the TSNDT, and a weak formulation of the initial-boundary-value problem (IBVP). By introducing the stiffness proportional Rayleigh damping to account for structural damping that reduces high frequency vibrations of the hull, we get the following system of coupled nonlinear ordinary differential equations (ODEs) for finding hull's deformations.

$$\boldsymbol{M}\ddot{\boldsymbol{d}} + \boldsymbol{C}\dot{\boldsymbol{d}} + \boldsymbol{K}(\boldsymbol{d})\boldsymbol{d} = \boldsymbol{F}^{ext} + \boldsymbol{F}^{c} \tag{44.a}$$

$$\boldsymbol{F}^{ext} = \int_0^{\ell} [\Phi(\mathrm{y}_1, -h^b - h^c)]^T \begin{Bmatrix} -F_{31} \\ F_{11} \end{Bmatrix} (\mathrm{p} - \mathrm{p_a}) H_1 d\mathrm{y}_1 + \boldsymbol{F}^{rig} \tag{44.b}$$

$$\boldsymbol{F}^{rig} = -\int_{-h^b-h^c}^{h^b+h^c} \int_0^{\mathcal{L}} [\Phi]^T \begin{Bmatrix} \dot{V}_1 \\ \dot{V}_3 \end{Bmatrix} \rho_0 H_1 d\mathrm{y}_1 \mathrm{d}\,\mathrm{y}_3 \tag{44.c}$$

$$\boldsymbol{F}^{c} = \int_0^{\mathcal{L}} ([\Phi(\mathrm{y}_1, h^{c-})] - [\Phi(\mathrm{y}_1, h^{c+})])^T \begin{Bmatrix} \bar{f}_1^{\mathbb{C}-} \\ \bar{f}_3^{\mathbb{C}-} \end{Bmatrix} H_1 d\mathrm{y}_1 + \int_0^{\mathcal{L}} ([\Phi(\mathrm{y}_1, -h^{c-})] - [\Phi(\mathrm{y}_1, -h^{c+})])^T \begin{Bmatrix} \bar{f}_1^{\mathbb{C}-} \\ \bar{f}_3^{\mathbb{C}-} \end{Bmatrix} H_1 d\mathrm{y}_1 \tag{44.d}$$

$$\boldsymbol{C} = \alpha \boldsymbol{K}(\boldsymbol{d}(0)) \tag{44.e}$$

Here $\boldsymbol{M}$ is the mass matrix, $\boldsymbol{C}$ the damping matrix defined by Eq. (44.e), α the Rayleigh coefficient, $\boldsymbol{K}(\boldsymbol{d})$ the stiffness matrix, $\boldsymbol{d}$ the vector of generalized displacements of nodes on hull's centroidal axis and ℓ the arc length of the fluid structure interface in the reference configuration. Furthermore, F_{31} and F_{11} are components of the deformation gradient, $[\Phi]$ defined in Eq. (42) of [49] is the matrix of the FE basis functions, $\boldsymbol{F}^{ext}$ is force vector defined by Eq. (44.b) in which the pressure exerted by the fluid on the hull is denoted by p, and p_a is the atmospheric pressure. The integration in Eq. (44.b) extends over the fluid/hull interface, and $\boldsymbol{F}^{rig}$ is the inertia force vector due to rigid body acceleration of the hull. The force vector $\boldsymbol{F}^{c}$ represents tractions on the cohesive interface, and $h^{c\pm}$ equals the value of y_3 on $\Gamma_{\mathbb{C}}^{\pm}$. We note that the damping matrix $\boldsymbol{C}$ is assumed to be proportional to the value of the stiffness matrix at time t = 0.

We first discuss how to find the rigid body motion of the hull, and then vibrational displacements of hull particles. Assuming $V(t)$ is the projection of the rigid body velocity $\boldsymbol{V}$ along the Z-direction and $\dot{V}(t)$ is the corresponding acceleration, the rigid body acceleration of the hull in the Z-direction can be calculated from

$$M^{*}\dot{V}(t) = F_Z - M^{*}g \tag{45.a}$$

$$F_Z = -M_a^{*}\dot{\mathrm{V}} + F_Z^{'} \tag{45.b}$$

Here M^{*} is the total mass of the hull, g the acceleration due to gravity, and F_Z the total upward force due to water slamming. We note that F_Z is an implicit function of the acceleration of fluid particles contacting the hull. We decompose it into two parts: the upward force $F_Z^{'}$ without considering acceleration of fluid particles and $M_a^{*}\dot{\mathrm{V}}$ that depends upon the acceleration of fluid particles abutting the hull. The quantity M_a^{*}, given by Eq. (51), is called the added mass.

The numerical solution may diverge when the added mass M_a^* is greater than the total mass of the body. Recall that the water slamming pressure is a function of the acceleration of solid particles on the solid/fluid interface. Young [50] analyzed the hydroelastic problem for propulsors by coupled BE and FE methods and obtained the added mass matrix from the solution of the fluid problem by the BEM. We separate the pressure term (e.g, see Eq. (49.a)) due to acceleration and calculate the added mass effect for rigid body motion and vibration of the solid body. We have thus successfully simulated the free drop of a light weight rigid wedge and a rigid ship bow section in [42], and FSI of a deformable flat and curved hull in this paper.

Substituting for $\frac{\partial \Psi^{\mathrm{B}}}{\partial n}$ from Eqs. (42.b) and (42.c) into Eq. (43) we get

$$[A]\begin{Bmatrix} \frac{\partial \Psi^{\mathrm{F}}}{\partial n} \\ \Psi^{\mathrm{B}} \\ \Psi^{\mathrm{T+S}} \end{Bmatrix} = [B]\begin{Bmatrix} \Psi^{\mathrm{F}} \\ -\boldsymbol{n}\cdot\ddot{\boldsymbol{u}} - \boldsymbol{n}\cdot\dot{\mathbf{V}} - \boldsymbol{n}\cdot\nabla(\boldsymbol{n}\cdot\dot{\boldsymbol{u}}) \\ 0 \end{Bmatrix} \tag{46}$$

With the notation

$$[\mathbb{Q}] = \begin{bmatrix} \mathbb{Q}_{11} & \mathbb{Q}_{12} & \mathbb{Q}_{13} \\ \mathbb{Q}_{21} & \mathbb{Q}_{22} & \mathbb{Q}_{23} \\ \mathbb{Q}_{31} & \mathbb{Q}_{32} & \mathbb{Q}_{33} \end{bmatrix} = [A]^{-1}[B]$$

we write

$$\{\Psi^{\mathrm{B}}\} = [\mathbb{Q}_{21} \quad \mathbb{Q}_{22} \quad \mathbb{Q}_{23}]\begin{Bmatrix} \Psi^{\mathrm{F}} \\ -\boldsymbol{n}\cdot\ddot{\boldsymbol{u}} - \boldsymbol{n}\cdot\dot{\mathbf{V}} - \boldsymbol{n}\cdot\nabla(\boldsymbol{n}\cdot\dot{\boldsymbol{u}}) \\ 0 \end{Bmatrix} = \{\Psi_1^{\mathrm{B}}\} + \{\Psi_2^{\mathrm{B}}\} + \{\Psi_3^{\mathrm{B}}\} \tag{47}$$

where

$$\{\Psi_1^{\mathrm{B}}\} = -[\mathbb{Q}_{22}]\{\boldsymbol{n}\cdot\ddot{\boldsymbol{u}}\}, \quad \{\Psi_2^{\mathrm{B}}\} = -[\mathbb{Q}_{22}]\{\boldsymbol{n}\cdot\dot{\mathbf{V}}\} \tag{48}$$

$$\{\Psi_3^{\mathrm{B}}\} = [\mathbb{Q}_{21} \quad \mathbb{Q}_{22} \quad \mathbb{Q}_{23}]\begin{Bmatrix} \Psi^{\mathrm{F}} \\ -\boldsymbol{n}\cdot\nabla(\boldsymbol{n}\cdot\dot{\boldsymbol{u}}) \\ 0 \end{Bmatrix}$$

The coefficient matrix $[\mathbb{Q}]$ is derived from matrices A and B appearing in the BE formulation of the fluid problem.

By combining Eqs. (40), (5) and (48), we get following equations for the pressure acting on the solid/fluid interface:

$$\mathrm{p} - \mathrm{p_a} = -\rho\left(-\Psi^{\mathrm{B}} + \mathbf{V}\cdot\nabla\varphi + \frac{1}{2}|\nabla\varphi|^2\right) = \mathrm{p}_1 + \mathrm{p}_2 + \mathrm{p}_3 \tag{49.a}$$

$$\mathrm{p}_1 = \rho\Psi_1^{\mathrm{B}} = -\rho[\overline{\mathbb{Q}}_{22}]\{\boldsymbol{n}\cdot\ddot{\boldsymbol{u}}\} = -\rho[\overline{\mathbb{Q}}_{22}][\mathbb{C}]\ddot{\boldsymbol{d}} \tag{49.b}$$

$$\mathrm{p}_2 = \rho\Psi_2^{\mathrm{B}} = -\rho[\overline{\mathbb{Q}}_{22}]\{n_Z\}\dot{\boldsymbol{V}} \tag{49.c}$$

$$\mathrm{p}_3 = -\rho\left(-\Psi_3^{\mathrm{B}} + \mathbf{V}\cdot\nabla\varphi + \frac{1}{2}|\nabla\varphi|^2\right) \tag{49.d}$$

$$\overline{\mathbb{Q}}_{22}(j) = \mathbb{Q}_{22}(i,j)\left(\frac{s_{i+1}-s}{s_{i+1}-s_i}\right) + \mathbb{Q}_{22}(i+1,j)\left(\frac{s-s_i}{s_{i+1}-s_i}\right), j = 1,\mathcal{N} \tag{49.e}$$

Here p_1 is the pressure due to vibrational acceleration of the deformable solid body, p_2 the pressure due to rigid body acceleration, p_3 the pressure without considering acceleration of the rigid body motion and vibration, and $\{n_Z\}$ the component of the unit normal to the fluid/solid interface along the Z-axis with the unit normal pointing out of the fluid. The coefficient matrix $\overline{\mathbb{Q}}_{22}$ for point $\mathscr{p}$ between nodes i and $i+1$ is evaluated by using Eq. (49.e) in which s, s_i and s_{i+1} are, respectively, the arc length of point $\mathscr{p}$, node i and node $i+1$, and $\mathcal{N}$ equals the number of nodes of the fluid part of the fluid/structure interface. The matrix $[\mathbb{C}]$ transforms the acceleration $\ddot{\boldsymbol{d}}$ in curvilinear coordinates to $\{\boldsymbol{n}\cdot\ddot{\boldsymbol{u}}\}$. We note that nodes for the BE and the FE meshes in the fluid and the solid domains on the solid/fluid interface need not coincide with each other, and we find values of a quantity at the desired location by either interpolating or extrapolating values at points where they are known.

Integrating component of the pressure in the Z-direction over the solid/fluid interface gives the total Z-force acting on the hull. Thus using Eq. (45.b) we get

$$F_Z = \int_0^{\ell}(\mathrm{p}_1 + \mathrm{p}_2 + \mathrm{p}_3)n_Z\mathrm{H}_1\mathrm{dy}_1 = -M_a^*\dot{\mathrm{V}} + F_Z^{'} \tag{50}$$

where

$$M_a^* = \int_0^{\ell}\rho n_Z[\overline{\mathbb{Q}}_{22}]\{n_Z\}\mathrm{H}_1\mathrm{dy}_1\,, \qquad F_Z^{'} = \int_0^{\ell}(\mathrm{p}_1 + \mathrm{p}_3)n_Z\mathrm{H}_1\mathrm{dy}_1 \tag{51}$$

Substitution from Eq. (50) into Eq. (45.a) gives

$$(M^* + M_a^*)\dot{V}(t) = F_Z^{'} - M^* g \tag{52}$$

Eq. (52) is numerically integrated by using the following algorithm:

$$(M^* + M_a^*)\dot{V}^{n+1} = F_Z^{'}(t_{n+1}) - M^* g \tag{53.a}$$

$$V^{n+1} = V^n + \frac{1}{2}\left(\dot{V}^{n+1} + \dot{V}^n\right)\delta t \tag{53.b}$$

$$\xi^{n+1} = \xi^n + V^n \delta t + \frac{1}{2}\dot{V}^n \delta t^2 \tag{53.c}$$

where

$$V^{n+1} = V\,(t_{n+1})\,,\ \xi^{n+1} = \xi\,(t_{n+1}) \tag{54}$$

Here ξ is the submergence, shown in Fig. 1, of the solid body apex with respect to the undisturbed water surface. The velocity and acceleration of the solid body apex is assumed to be equal to the rigid body motion velocity and acceleration since the edge at the apex is assumed not to deform. The acceleration of the rigid body motion can be evaluated from Eq. (52), and the rigid body displacement and velocity are updated by using, respectively, the forward and the central difference methods; e.g., see Eqs. (53.b) and (53.c).

Using Eq. (49.a), we write the force vector in Eq. (44) as

$$\begin{aligned} \boldsymbol{F}^{ext} &= \int_0^{\ell} [\Phi(\mathrm{y}_1, -h^b - h^c)]^T \begin{Bmatrix} -F_{31} \\ F_{11} \end{Bmatrix} (p_1 + p_2 + p_3) H_1 d\mathrm{y}_1 + \boldsymbol{F}^{rig} \\ &= -\mathbf{M}_{\mathrm{a}} \ddot{\boldsymbol{d}} + \boldsymbol{F}^{pre} + \boldsymbol{F}^{rig} \end{aligned} \tag{55}$$

where

$$\boldsymbol{F}^{pre} = \int_0^{\ell} [\Phi(\mathrm{y}_1, -h^b - h^c)]^T \begin{Bmatrix} -F_{31} \\ F_{11} \end{Bmatrix} (p_2 + p_3) H_1 d\mathrm{y}_1 \tag{56.a}$$

$$\mathbf{M}_{\mathrm{a}} = \int_0^{\ell} [\Phi(\mathrm{y}_1, -h^b - h^c)]^T \begin{Bmatrix} -F_{31} \\ F_{11} \end{Bmatrix} \rho[\overline{\mathbb{Q}}_{22}]\,[\mathbb{C}] H_1 d\mathrm{y}_1 \tag{56.b}$$

Here $\mathbf{M}_a$ is called the added mass matrix due to vibrational motion of the hull and $\boldsymbol{F}^{pre}$ is the external force vector due to the slamming pressure without considering vibrational acceleration. We note that Qin and Batra [32] used a semi-analytical approach for studying fluid's deformations and found an expression for the added mass matrix.

Thus the equation of motion (44.a) of the solid body becomes

$$(\mathbf{M}+\mathbf{M}_a)\ddot{\boldsymbol{d}}+\boldsymbol{C}\dot{\boldsymbol{d}}+K(\boldsymbol{d})\boldsymbol{d}=\boldsymbol{F}^{pre}+\boldsymbol{F}^{rig}+\boldsymbol{F}^{c} \tag{57}$$

Equation (57) is used to update the vibrational acceleration, velocity and deformations of the solid body. It is integrated by using the conditionally stable central-difference method, i.e., the following algorithm:

$$\boldsymbol{d}^{n+1}=\boldsymbol{d}^{n}+\delta t\dot{\boldsymbol{d}}^{n}+\frac{\delta t^2}{2}\ddot{\boldsymbol{d}}^{n} \tag{58.a}$$

$$\left(\mathbf{M}+\mathbf{M}_a+\frac{\delta t}{2}\boldsymbol{C}\right)\ddot{\boldsymbol{d}}^{n+1}=\boldsymbol{F}^{rig}(t_{n+1})+\boldsymbol{F}^{pre}(t_{n+1})+\boldsymbol{F}^{c}(t_{n+1})-\boldsymbol{K}(\boldsymbol{d}^{n+1})\boldsymbol{d}^{n+1}-\boldsymbol{C}\left(\dot{\boldsymbol{d}}^{n}+\frac{\delta t}{2}\ddot{\boldsymbol{d}}^{n}\right) \tag{58.b}$$

$$\dot{\boldsymbol{d}}^{n+1}=\dot{\boldsymbol{d}}^{n}+\frac{\delta t}{2}\left(\ddot{\boldsymbol{d}}^{n+1}+\ddot{\boldsymbol{d}}^{n}\right) \tag{58.c}$$

where

$$\boldsymbol{d}^{n+1}=\boldsymbol{d}\,(t_{n+1}) \tag{59}$$

The flow chart for iteratively solving the FSI problem is given in Fig. 5. Using the known solution at time t_n, $\ddot{\boldsymbol{d}}^{n+1}$, $\dot{\boldsymbol{d}}^{n+1}$, $\dot{\boldsymbol{V}}^{n+1}$ and $\boldsymbol{V}^{n+1}$ can be evaluated by using Eqs. (58) and (53). These quantities are used to update φ and Ψ for the next iteration. The iterative process is terminated when the normalized difference of computed total pressure between two successive iterations is less than the prescribed tolerance of 10^{-4}. The normalized difference of pressure between iterations $I+1$ and I is defined as $\int_0^{\ell}|p_4^{I+1}-p_4^{I}|ds\,/\int_0^{\ell}|p_4^{I+1}|ds$ where $p_4^{I}=\mathrm{p}-\mathrm{p_a}$ is total pressure on the wedge at iteration I. The procedure discussed above to analyze the FSI problem is called the added mass method.

The critical time step size δt_s to compute a stable solution for the structure part is determined by finding the maximum frequency, ω_{max} , of free vibrations and taking $\delta t_s \leq \delta t_{crit}$, $\Delta t_{crit} = 2/\omega_{max}$. Ideally, ω_{max} should be found after every time step since frequencies of a structure change as it is deformed. The accuracy of the solution can be improved by taking $\delta t_s \ll \delta t_{crit}$ but at the cost of increasing the computational time.

Results presented in Section 4 have been computed with a consistent mass matrix and $\delta t_s = 0.9\delta t_{crit}$ for a linear problem but $\delta t_s = 0.5\delta t_{crit}$ for a nonlinear problem. For the nonlinear problems, ω_{max} found from analyzing frequencies of the undeformed beam is used to ascertain δt_{crit}. $\mathbf{M}_{\mathrm{a}}$ is not considered when evaluating ω_{max}.

As mentioned in [42] , the time step δt_f for integrating, with respect to time, Eq. (3) for fluid's deformation is given by

$$\delta t_f = \frac{h_{min} 2 tan\beta}{V \pi \gamma_t} \tag{60}$$

where h_{min} is minimum element length near the jet tip, γ_t is assigned values between 2 and 20; here we use γ_t= 5. For the water slamming of a curved hull shown in Fig. 14, we choose β as the minimum of the local deadrise angles at nodes on the hull/fluid interface, slope of the free water surface at nodes on it, and the local angle at the jet tip. The time step δt for the FSI analysis equals the smaller of δt_f and δt_s.

3.4 Verification of the code

The verification of the FE software for analyzing hull's deformations is described in [51] and the verification of FE software for delamination analysis is discussed in [48]. The developed BEM software has been verified in [42] by using the method of manufactured solutions (e.g., see the material just preceding and following Eq. 20 of [52]). The coupling between the two software is verified by analyzing problems for rigid hulls and comparing computed results with those available in the literature, e.g., see [42].

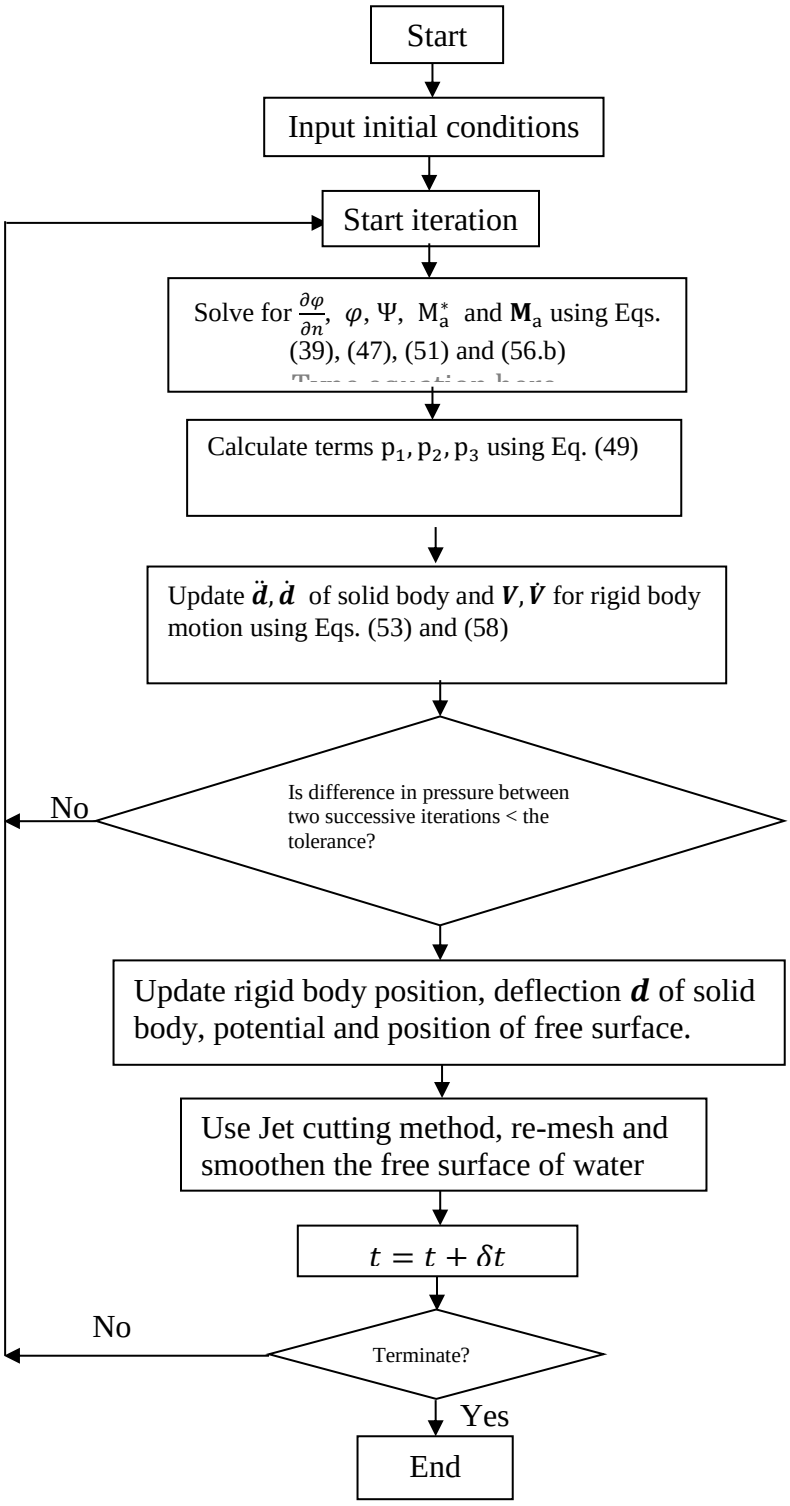

Fig. 5 Flow chart for the analysis of the FSI problem by the coupled BE-FE method.

4. Example Problems

We discretize the fluid domain boundary into two-node elements with node numbers starting from point $\mathcal{C}$ in Fig. 6 and going counter-clockwise ($\mathcal{CDEAB C}$), and denote the length of element *j* with nodes *j* and *j+1* by h_j. Non-uniform meshes are used to discretize the free surface of water near the jet tip $\mathcal{A}$, fluid boundary $\mathcal{AB}$ on the hull and fluid boundary $\mathcal{BC}$ on the symmetry axis. In Fig. 6 the free surface of water near the wedge edge is exhibited in which points $\mathcal{A}$ and $\mathcal{B}$ are, respectively, points of intersection between the free surface and the hull, and the hull and the symmetry axis. The length, h_j, of element j on the free surface boundary $\mathcal{EA}$ for mesh 1 is chosen according to the following empirical criteria.

$$h_j = \begin{cases} d_{34}\,, & \bar{N}_{\mathcal{A}} - 100 \le j < \bar{N}_{\mathcal{A}} \\ \min\left(d_{33}, 1.05^{\bar{N}_A - 100 - j} d_{34}\right), & j < \bar{N}_{\mathcal{A}} - 100 \text{ and } \zeta_{\mathcal{A}j} \le 1.0\mathcal{L} \\ d_{32}, & 1.0\mathcal{L} < \zeta_{\mathcal{A}j} \le 2.0\mathcal{L} \\ d_{31}, & \zeta_{\mathcal{A}j} > 2.0\mathcal{L} \end{cases} \tag{61}$$

$$d_{31} = L_1/40\,,\ d_{32} = 1/75,\ d_{33} = d_{32}/5,\ d_{34} = d_{32}/b_r$$

Here b_r is the mesh refinement parameter whose value depends upon the deadrise angle, $\zeta_{\mathcal{A}j}$ is the arc length between points $\mathcal{A}$ and *j*, and $\bar{N}_{\mathcal{A}}$ is the node number of point $\mathcal{A}$.

A non-uniform mesh with element size h_j given by Eq. (61) is used to discretize the water surface $\mathcal{AB}$ contacting the hull with smaller elements near points $\mathcal{A}$ and $\mathcal{B}$ than those elsewhere.

$$h_j = \begin{cases} d_{34}\,, & \bar{N}_{\mathcal{A}} \le j \le \bar{N}_{\mathcal{A}} + 100 \\ \min\left(d_{32}, 1.05^{j - (\bar{N}_A + 100)} d_{34}\right), & j > \bar{N}_{\mathcal{A}} + 100 \text{ and } \zeta_{\mathcal{A}j} \le \zeta_{\mathcal{AB}} - 0.1\mathcal{L} \\ 0.5 d_{32}\,, & j > \bar{N}_{\mathcal{A}} + 100 \text{ and } \zeta_{\mathcal{A}j} > \zeta_{\mathcal{AB}} - 0.1\mathcal{L} \end{cases} \tag{62}$$

It is clear that this scheme generates finer meshes near points $\mathcal{A}$ and $\mathcal{B}$. The length h_j of element *j* on the axis of symmetry $\mathcal{BC}$ is taken to be given by

$$h_j = \min\left(d_{31}, 1.2^{j - \bar{N}_{\mathcal{B}}} h_{\bar{N}_{\mathcal{B}} - 1}\right). \tag{63}$$

Here $\bar{N}_{\mathcal{B}}$ is the node number of point $\mathcal{B}$. The element length on the truncation boundaries $\mathcal{CD}$ and $\mathcal{DE}$ equals d_{31}. Lengths of elements for mesh 2 are the same as those for mesh 1 except that $d_{31} = L_1/80$ and $d_{32} = 1/150$; thus the element length for mesh 2 is one-half of that for mesh 1 in most of the region on the boundary. Unless otherwise specified, results presented below have been computed with mesh 2 and $b_r = 20$.

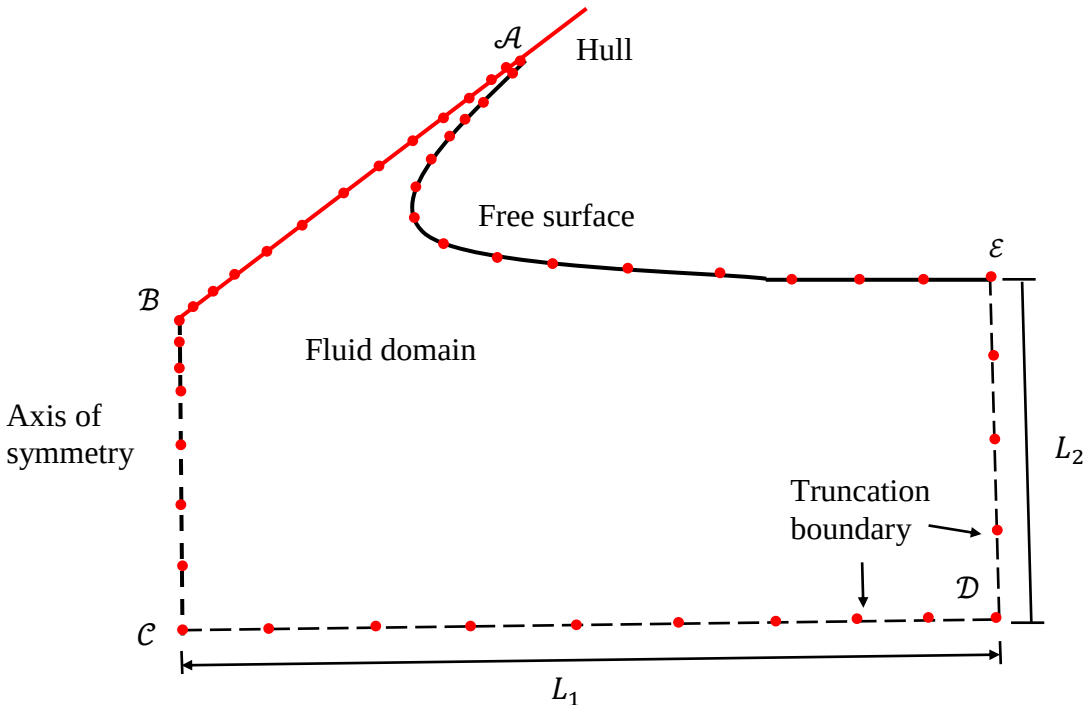

Fig. 6 Discretization of the boundary of the fluid domain into elements

4.1 Water slamming of linear elastic straight sandwich hull

We now analyze deformations of a clamped-clamped linear elastic straight sandwich hull of length $\mathcal{L} = 1$ m, thickness of each face sheet $h^b = h^t = 1.2$ cm, core thickness $2h^c = 3.0$ cm, and downward impact velocity = 10 m/s. Effects of gravity have been neglected. Values of material parameters are listed in Table 1. The mass density assigned to face sheets includes the dead weight of the ship. The sandwich beam is divided into 60 uniform 2-node elements along the y_1-axis, the fluid domain is discretized using mesh 2 with b_r = 40, and L_1 and L_2 are set equal to 15 m. As shown in [47] through numerical experiments these values of b_r, L_1 and L_2 give converged results. The time steps used to compute results found by using the criterion discussed in Section

3.3 equaled 0.19 μs, 0.37 μs, 0.53 μs for deadrise angle, β = 5°, 10°, and 14°, respectively

For the hull of initial deadrise angle 5° we set the Rayleigh damping coefficient $\alpha = 5 \times 10^{-6}$. As should be clear from the time history of the pressure at $y_1 = 0.35$ m plotted in Fig. 7, oscillations in the pressure have been significantly diminished, and the difference in results computed with $\alpha = 5\times10^{-6}$ and 5×10^{-7} is miniscule. The pressure computed without using the added mass method exhibits oscillations at t = 4 ms whereas that with the added mass method does not. Results presented below have been computed with the added mass method.

In Fig. 8 the presently computed time histories of the deflection of the hull centroid for three different values of the initial deadrise angle are compared with those found by Das and Batra [35] who used LSDYNA and by Qin and Batra [32] who employed a semi-analytical approach. Solutions from the three methods are close to each other for initial deadrise angles of 5° and 10°, but differences among them are large for initial deadrise angle of 14°. Results obtained by using the three meshes for the hull of initial deadrise angle 14° plotted in Fig. 9 suggest that they are essentially unchanged and are closer to the results from the coarse rather than the fine mesh employed by Das and Batra [35]. We note that Qin and Batra [32] assumed small values of the initial deadrise angle of the hull. The deformed shapes at $t = 5.47$ ms of the mid-surface of the hull of initial deadrise angle $= 5°$ computed by the three methods plotted in Fig. 10 are close to each other, with percentage difference, $100 \int_0^{\mathcal{L}} |u_3 - u_3^{pre}| ds \,/\, \int_0^{\mathcal{L}} |u_3^{pre}| ds$, equal to 10 % and 6.2 % , respectively, for solutions of u_3 given in [32] and [35]. Here, u_3^{pre} is the presently computed value of u_3.

Fig. 11 exhibits time histories of the slamming pressure at locations $y_1 = 0.24$, 0.35 and 0.57 m of the hull of initial deadrise angle $= 5°$, and Fig. 12 shows the pressure variations on the hull at times t = 2.72, 4.79 and 5.75 ms. The peak pressure predicted by the present method is very high and qualitatively resembles that given by Qin and Batra's [32] semi-analytical approach, and it is much higher than that found in [35] using LSDYNA. We note that in the modified Wagner's theory employed in [32]

the pressure field is singular and its peak value is approximated. Except for the peak pressure, the three methods give results that are close to each other.

The strain energy density is computed by using Eq. (18). Contributions to the strain energy density due to the transverse shear strain, the axial strain and the transverse normal strain equal, respectively, $C_{1313}{E_{13}}^2$, $\frac{1}{2}C_{1111}{E_{11}}^2$ and $\frac{1}{2}C_{3333}{E_{33}}^2$. Taking the hull dimension in the y_2-direction as 1 m, strain energy densities stored in the core and the two face sheets at t = 2.74 ms and 6.02 ms are plotted in Fig. 13 along with those from Das and Batra [35]. The core of the sandwich hull absorbs significant amount of energy due to transverse shear deformations which agrees with that reported by Qin and Batra [32] and Das and Batra [35]. Hull's deformations were assumed to be infinitesimal in [32] but all geometric nonlinearities were considered in [35]. We have listed in Table 2 salient features of solutions of the water slamming problem using the FE software LSDYNA and the present coupled BE-FE approach.

Table 1 Values of material parameters of the sandwich hull

	C_{1111} (GPa)	C_{1133} (GPa)	C_{3333} (GPa)	C_{1313} (GPa)	Mass density (kg/m^3)
Face sheet	140.3	3.77	9.62	7.10	31,400
Core	3.77	1.62	3.77	1.08	150

Table 2 Comparison of LSDYNA and coupled BE-FE approaches for the water slamming problem

	LSDYNA	BE-FE methods
Fluid penetrates into solid	Yes	No
Oscillations in pressure on the hull	Yes	No
Results depend on contact algorithm	Yes	No
Computation of water jet	Difficult	Easy
Assumptions for fluid deformations	Compressible and no restrictions on fluid's deformations	Incompressible and irrotational
Evaluation of deformations at a point in the fluid domain	Easy	Difficult

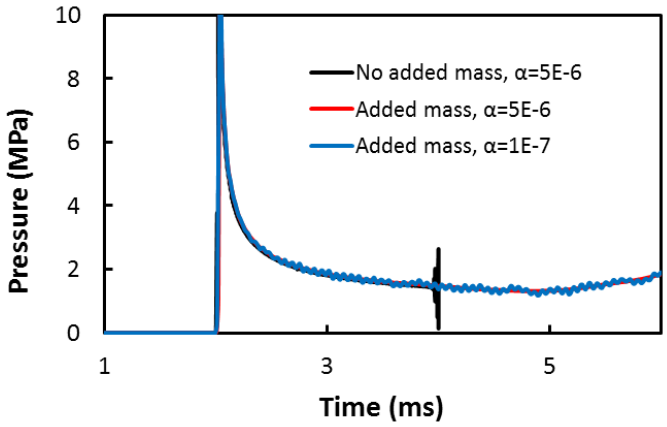

Fig. 7 For initial impact speed = 10 m/s and deadrise angle = 5^o, time histories of the pressure on the hull at $y_1 = 0.35$ m for two values of the damping ratio, and with and without adding mass due to acceleration of particles on the hull surface. The three curves overlap each other.

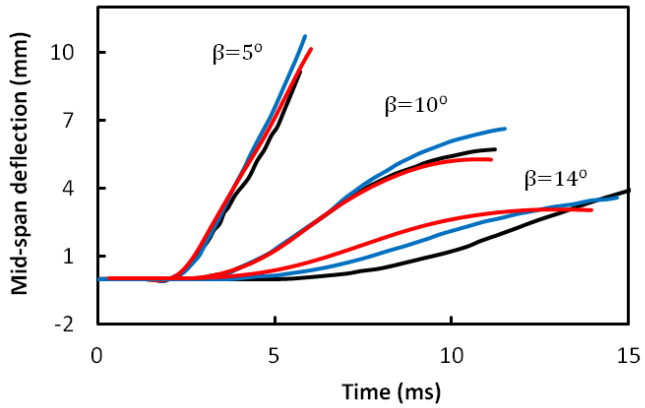

Fig. 8 For initial impact speed = 10 m/s, time histories of the hull centroid deflection for initial deadrise angle = 5^o, 10^o and 14^o. Black, blue and red curves represent results from Qin and Batra [32] , Das and Batra [35], and the present work, respectively.

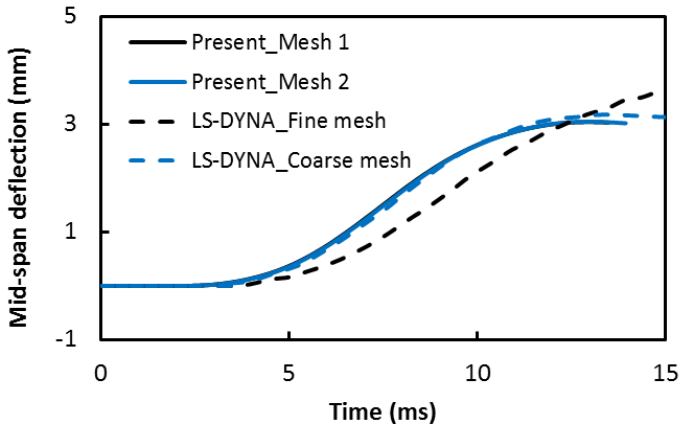

Fig. 9 For initial deadrise angle $= 14^{\circ}$ and initial impact speed = 10 m/s, time histories of the hull centroid deflection found by using different meshes. Results from FE meshes 1 and 2 are indistinguishable from each other in the plots. Curves marked LSDYNA denote results from Das and Batra [35] .

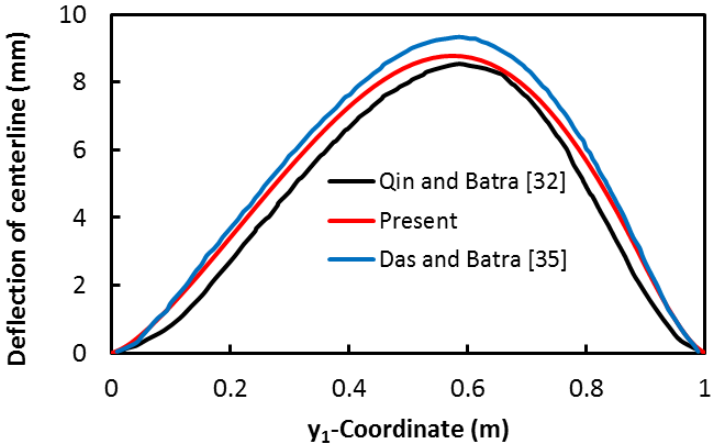

Fig. 10 At t = 5.471 ms after impact, deformed shapes of the mid-surface of the hull computed by the three methods.

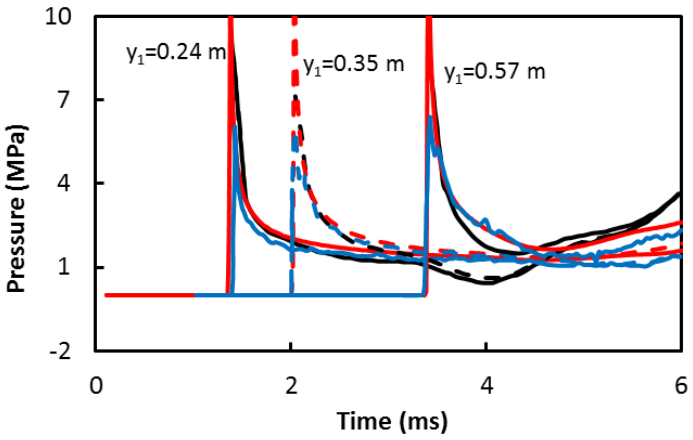

Fig. 11 Time histories of the pressure at three locations of the hull of initial deadrise angle 5^0; black, blue and red curves represent results from Qin and Batra [32], Das and Batra [35], and the present method, respectively.

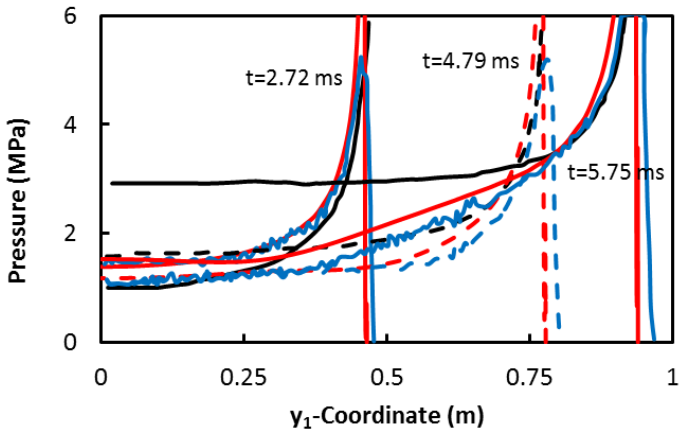

Fig. 12 Pressure distribution on the hull of initial deadrise angle = 5^o at t = 2.72, 4.79 and 5.75 ms. Black, blue and red curves represent results computed, respectively, by Qin and Batra [32], Das and Batra [35], and the present method**.**

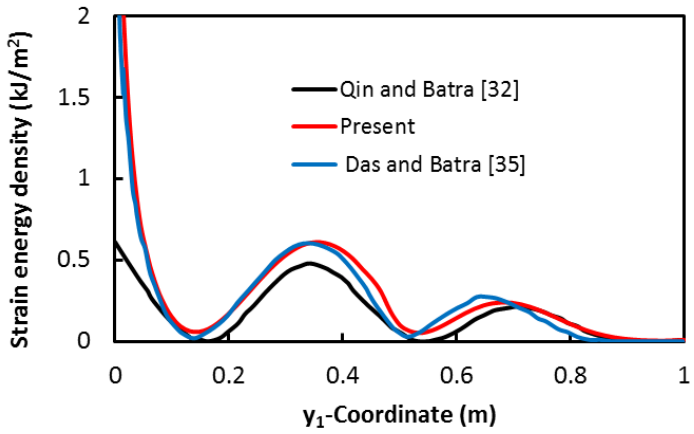

a. At t = 2.74 ms, the spatial variation of the strain energy density in the face sheets.

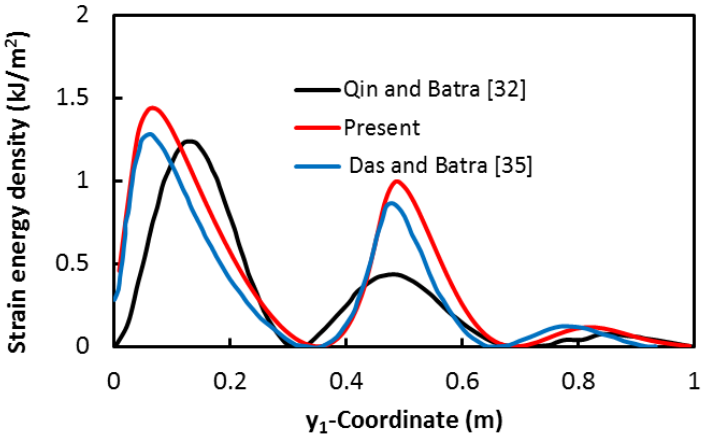

b. At t = 2.74 ms, spatial variation of the strain energy density due to the transverse shear strain in the core

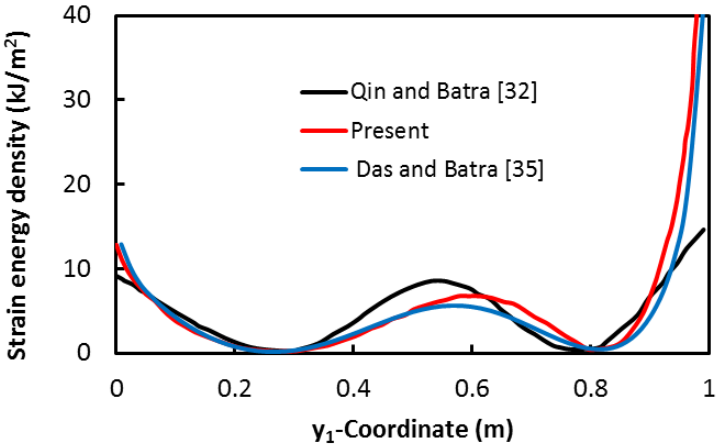

c. At t = 6.02 ms, variation of total strain energy density in the two face sheets along the hull span

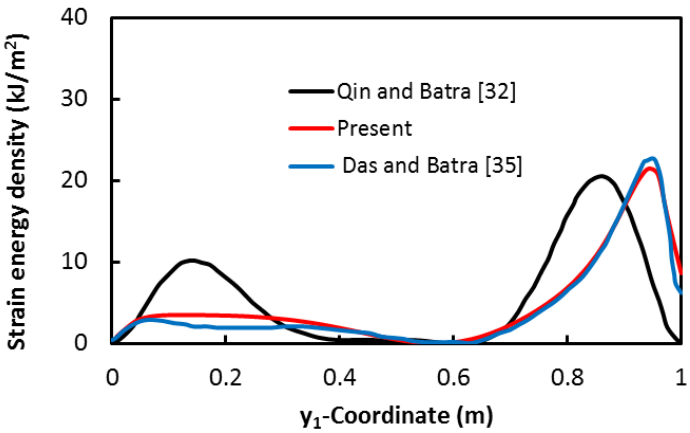

d. At t = 6.02 ms, variation along the hull span of the strain energy density in the core due to transverse shear strain

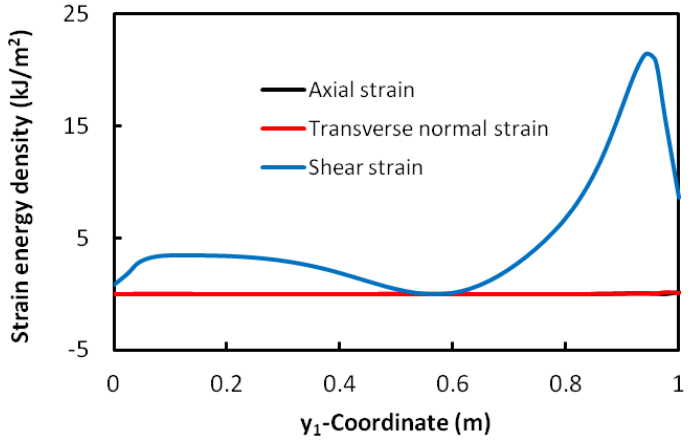

e. At t = 6.02 ms, variation along the hull span of the strain energy density in the core due to different strain components. The curve for the axial strain coincides with that for the transverse shear strain.

Fig. 13 Variation of the strain energy density in the face sheets and the core along the hull span when t = 2.74 ms and 6.02 ms (initial deadrise angle = 5^{o}).

4.2 Water slamming of linear elastic circular sandwich hull

Sun and Faltinsen [30] have considered hydroelastic effects in analyzing deformations of circular shells made of steel and aluminum. They studied deformations of the fluid by the BEM and those of shells by the modal analysis. Here we analyze transient plane strain deformations of a circular sandwich hull with mid-surface radius equal to R, deadrise angle $\beta = 5^{\circ}$at the initial point of impact (e.g., see Fig. 14), both

edges rigidly clamped, and values of material parameters the same as those of the straight sandwich hull studied above. The length $\mathcal{L}$ equals the arc length of the curved beam.

From time histories of the hull centroid deflection for different values of R displayed in Fig. 15, it is transparent that with an increase in the value of R, the centroidal deflection approaches that of a straight hull as it should. Also, at a fixed time, the deflection increases with an increase in R which could be due to the dependence upon R of the wetted length and of the pressure distribution. We have exhibited in Fig. 16 the variation of the hydroelastic pressure on curved and straight hulls at t = 2.72, 4.79 and 5.75 ms. It is clear that the curvature of the hull noticeably affects the magnitude of the peak pressure and the pressure distribution on the hull. The peak pressure on the circular hull is considerably less than that on the flat hull. As deformations of the hull are infinitesimal the maximum difference in the hydrodynamic pressure on rigid and deformable hulls is small. Both for circular and flat hulls, the pressure distribution on the hull can be viewed as a traveling wave with the peak pressure acting at the just wetted point, the pressure rapidly decreasing in its wake, and staying uniform over a significant part of the wetted length.

At t = 6.02 ms and four values of R, variations of the strain energy density in the core and the face sheets along the hull span plotted in Fig. 17 reveal that at a point on the hull the strain energy densities in the core and the face-sheets decrease with a decrease in the value of R. When the entire hull has been wetted, the strain energy densities due to the transverse shear stain in the core and the total strain energy in the face sheets at points near the right edge are significantly larger than those at points near the left edge of the hull possibly due to the peak pressure acting near the right edge. Values of the strain energy densities at a point decrease with a decrease in the value of R.

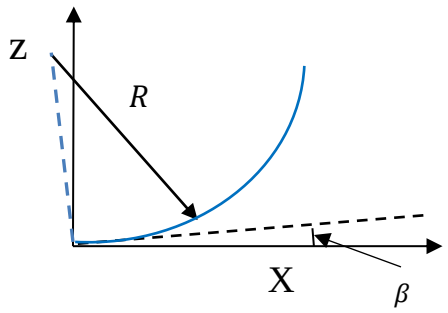

Fig. 14 Sketch of the undeformed circular hull, and of the local deadrise angle at the point of impact.

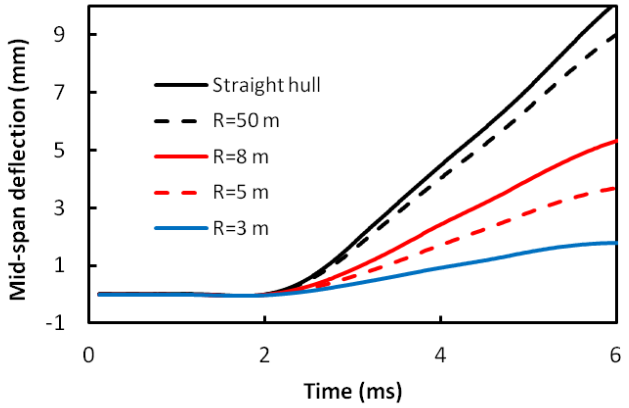

Fig. 15 Time histories of the deflection of the mid-span of the hull.

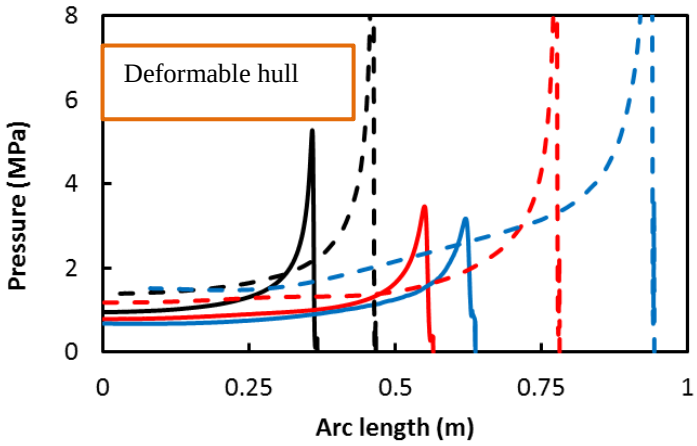

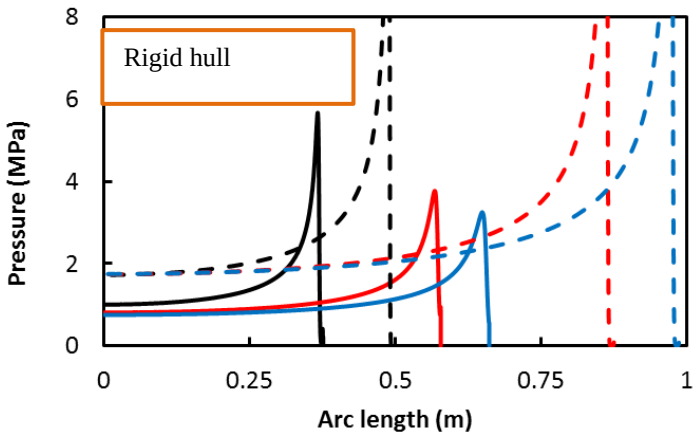

Fig. 16 Pressure distribution on the deformable and rigid hulls at different times; Solid (dashed) curves represent pressure distribution on the circular (straight) hull of $R = 5\ m$ (infinity). Black, red and blue curves represent results at t = 2.72 ms, 4.79 ms and 5.75ms, respectively.

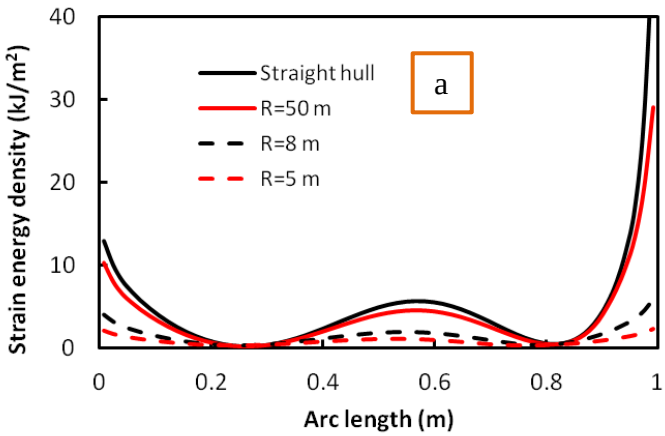

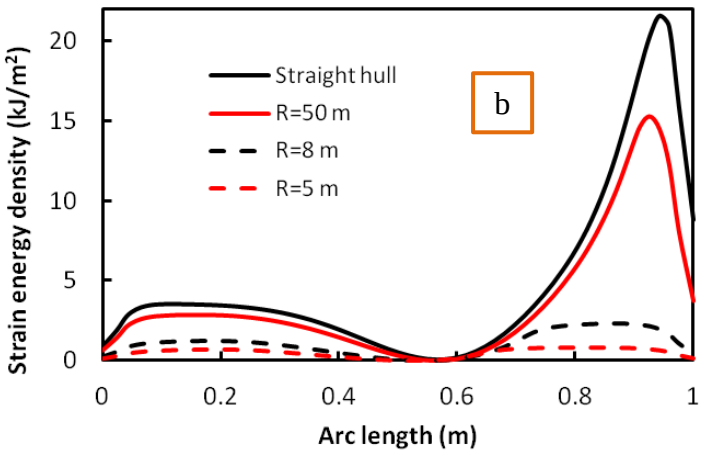

Fig. 17 For different radii of the circular hull and t = 6.02 ms, variation along the hull span of (a) the strain energy density due to transverse shear strain in the core, and (b) the total strain energy density in the face sheets.

4.3 Water slamming of straight sandwich hull made of St. Venant-Kirchhoff material

Two water slamming problems have been simulated to delineate the influence on the hydrodynamic pressure acting on a sandwich hull of geometric nonlinearities and hull stiffness. For problem 1 values of elastic constants are the same as those for the hull studied in subsection 4.1, and for problem 2, values of all elastic parameters have been reduced by a factor of 10 and the mass density reduced to $2{,}000\ \mathrm{kg/m^3}$. For problem 2 we set $h^t = h^b = 6$ mm , $h^c = 7.5$ mm, and $\mathcal{L} = 1\ m$. The fundamental frequency for the beam of problems 1 and 2 without considering added mass and deformation of the beam are 110 and 101 Hz, respectively. The deadrise angle and the downward velocity of the hull for both problems equal 10° and 10 m/s, respectively. The BE mesh 2 described at the beginning of Section 4 with the mesh refinement number b_r = 20 has been used. Effects of geometric nonlinearities are considered only for problem 2. The time steps used to compute results equaled 0.75 μs for both problems.

Time histories of the hull centroid deflection are plotted in Fig. 18. For problem 2, the maximum percentage difference $100|w_{lin} - w_{non}|/w_{lin}$ between the hull centroid deflections with (w_{non}) and without (w_{lin}) considering geometric nonlinearities is 32.5%. The time histories of centroidal deflections for the two linear problems suggest that the hull of problem 1 is considerably stiffer than that of problem 2 even though their fundamental frequencies are only 9% different. Recall that the fundamental frequency also depends upon the mass density, the hull thickness and the elastic moduli. From results for the two linear problems we deduce that the peak pressure on the stiffer hull that deflects less is nearly 80% more than that on the flexible hull. At a fixed value of time the wetted length is larger for the stiffer hull than that for the flexible hull.

Fig. 19 exhibits time histories of the hydrodynamic pressure on the hull at three different locations with arc length in the deformed shape equal to 0.24, 0.35, 0.57 m and Fig. 20 shows the pressure variations on the hull at times t = 2.72 ms and 8.01 ms. These results suggest that the consideration of geometric nonlinearities significantly increases

the maximum hydroelastic pressure acting on the hull. For example, at x = 0.57 m, the peak hydroelastic pressures at t ≅ 9 ms for the nonlinear problem equals 1.4 times that for the linear problem. It could be due to the fact that the stiffness of the hull considering geometrically nonlinear deformations is more than that of the identical hull for which geometric nonlinearities are not considered. At x = 0.57 m, the peak hydrostatic pressure occurs sooner for the nonlinear problem than that for the linear problem. The traveling wave like behavior of the hydroelastic pressure is unaffected by the consideration of geometric nonlinearities.

Time histories of the maximum value of an element of the mass matrix **M** and the added mass matrix $\mathbf{M}_a$ for problem 2 considering infinitesimal deformations are exhibited in Fig. 21. It is clear that the added mass matrix increases significantly with an increase in the area of the contact surface between the hull and water. We note that the added mass matrix is due to the vibrational motion of the hull since its rigid body acceleration is null.

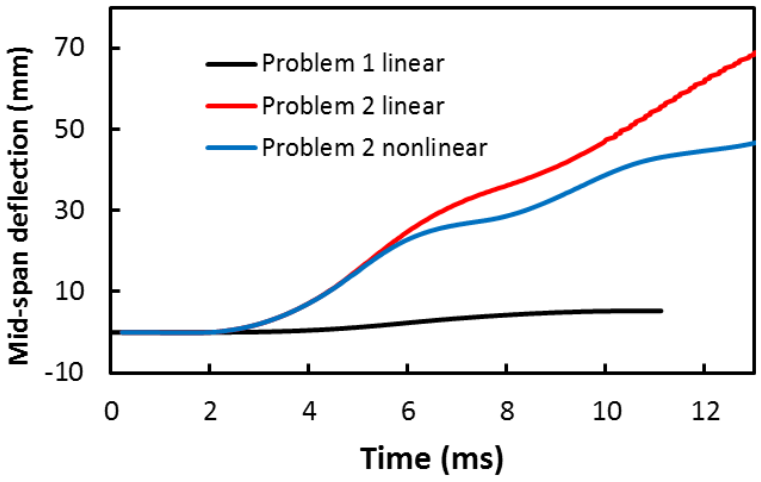

Fig. 18 Time histories of the hull centroid deflection.

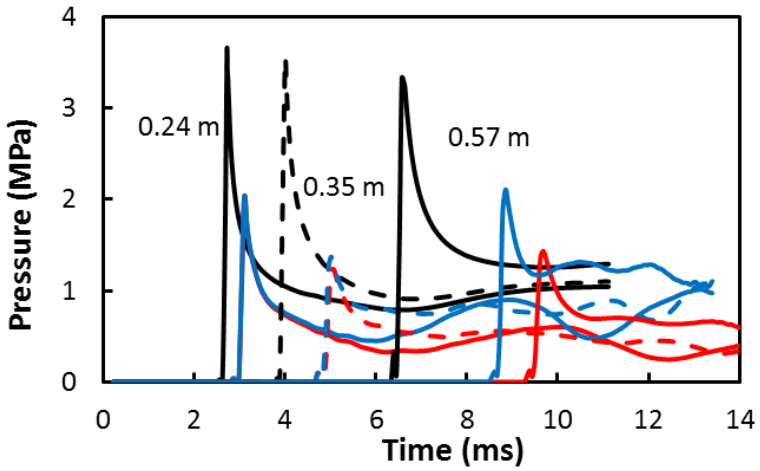

Fig. 19 Time histories of the hydroelastic pressure on the hull at three points with arc length in the deformed shape equal to 0.24 m,0.35 m and 0.57 m. Black, red and blue curves represent results for linear problem 1, linear problem 2 and nonlinear problem 2, respectively.

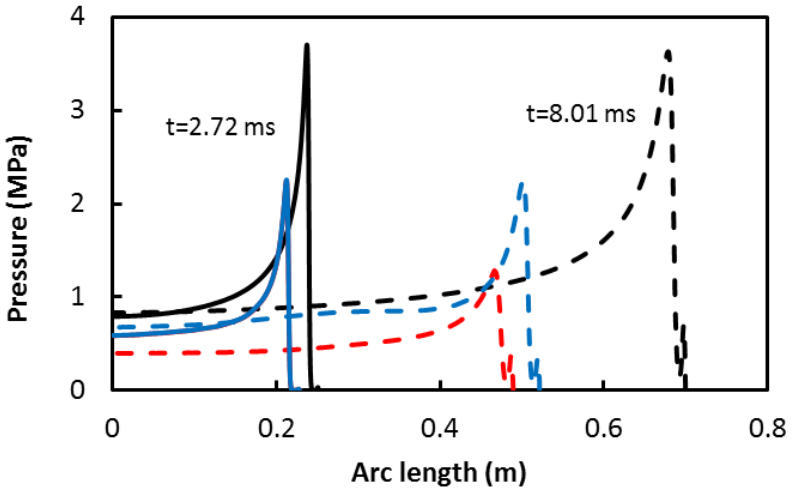

Fig. 20 Distribution of the hydroelastic pressure on the hull at t = 2.72 and 8.01 ms. Black, red and blue curves represent results for linear problem 1, linear problem 2 and nonlinear problem 2, respectively. At t = 2.72 ms, the red curve overlaps the blue curve as the geometric nonlinear effect is insignificant when deformations are infinitesimal.

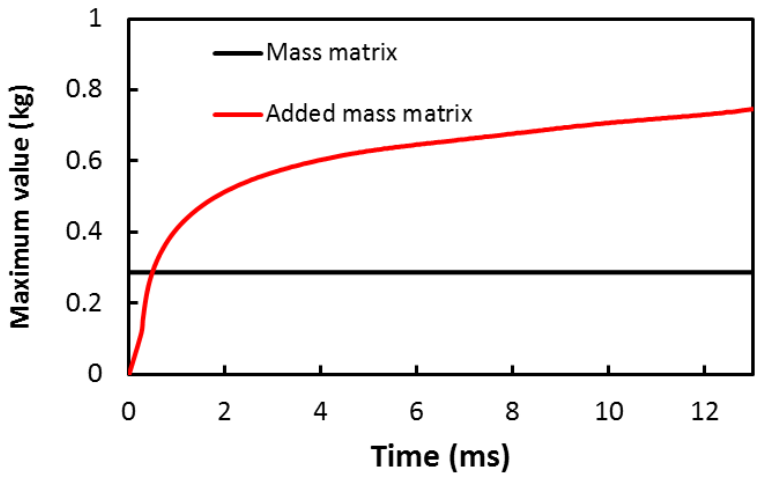

Fig. 21 Time history of the maximum value of an element of the mass matrix **M** and added mass matrix $\mathbf{M}_a$ for linear problem 2.

4.4 Delamination in linear elastic straight sandwich hull due to water slamming loads

We now analyze two problems involving delamination initiation and growth in a clamped-clamped linear elastic straight sandwich hull of length $\mathcal{L} = 1$ m. The hull is divided into 81 uniform 2-node elements along the y_1-axis. The fluid domain is discretized using mesh 2 described at the beginning of Section 4 with the mesh refinement number $b_r = 40$ and 20, respectively, for problems 1 and 2. For problem 1, the geometric and material parameters, and the entry velocity are the same as those for the hull studied in subsection 4.1 and the deadrise angle $\beta = 5°$. We assume that the interface strength parameters have values $\sigma_t^0 = \sigma_n^0 = 1$ MPa , $\mathrm{G_{Ic}} = 625\ \mathrm{Jm^{-2}}$, $\mathrm{G_{IIc}} = 418\ \mathrm{Jm^{-2}}$. Delamination in the hull of problem 1 has been studied by Das and Batra [35] using LSDYNA and the above listed values of parameters. For problem 2, we assume that the thickness of each face sheet, $h^b = h^t = 2$ cm, core thickness, $2h^c = 6.0$ cm, downward impact velocity = 10 m/s and deadrise angle β = 10°. The face sheets and the core are assumed to be made of GRP and PVC foam (H200), respectively, and the interface parameters have values, $\sigma_t^0 = 3.5$ MPa , $\sigma_n^0 = 7.1$ MPa , $\mathrm{G_{Ic}} = 625\ \mathrm{Jm^{-2}}$, $\mathrm{G_{IIc}} = 418\ \mathrm{Jm^{-2}}$. The material properties for the face sheets and the experimental value of the critical interface SERR for mode II delamination are taken from [53]. Values of the critical interface SERR for mode I delamination and the mass density of the GRP are not provided in [53], and these have been taken from [54] and [55], respectively. Values of

material parameters for the core and the interface strength are taken from [56]. These values are listed in Table 3. The time steps used to compute results for problems 1 and 2 equaled 0.19 μs and 0.75 μs, respectively.

Table 3 Values of material parameters of the sandwich hull

	C_{1111} (GPa)	C_{1133} (GPa)	C_{3333} (GPa)	C_{1313} (GPa)	Mass density (kg/m^3)
Face sheet	13.4	2.40	5.92	1.92	1,850
Core	0.307	1.62	0.0923	0.107	200

For problem 1, we compare the presently computed results with those of [35] obtained by using LSDYNA and the stress criterion given by Eq. (27) to predict the delamination and failure of the interface. When using the stress criterion the failure occurs instantaneously when the criterion is satisfied. Fig. 22 exhibits time histories of the deflection of the hull centroid with and without considering delamination. It is clear that the presently computed results are close to those of [35], and the hull centroid deflection considering delamination is larger than that without accounting for delamination. The sandwich hull's stiffness decreases subsequent to the onset of delamination.

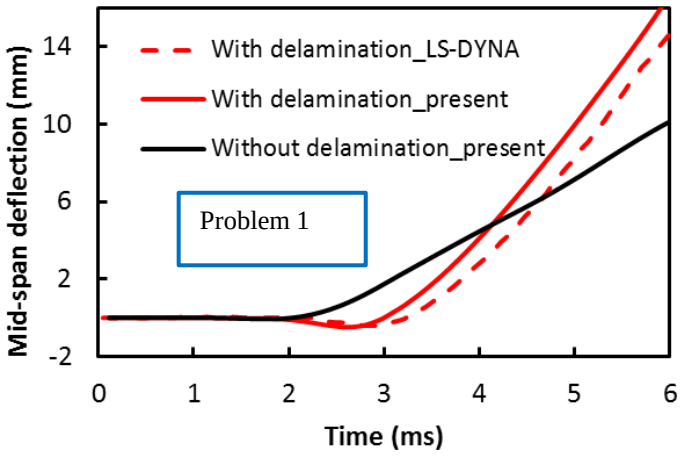

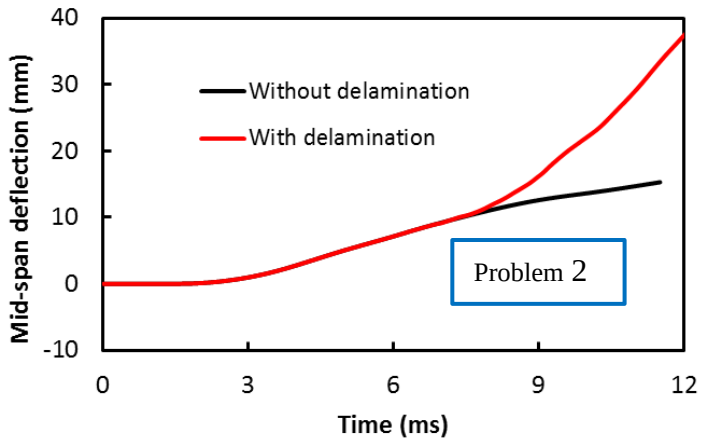

Fig. 22 Time histories of the deflection of the straight hull centroid with and without considering delamination

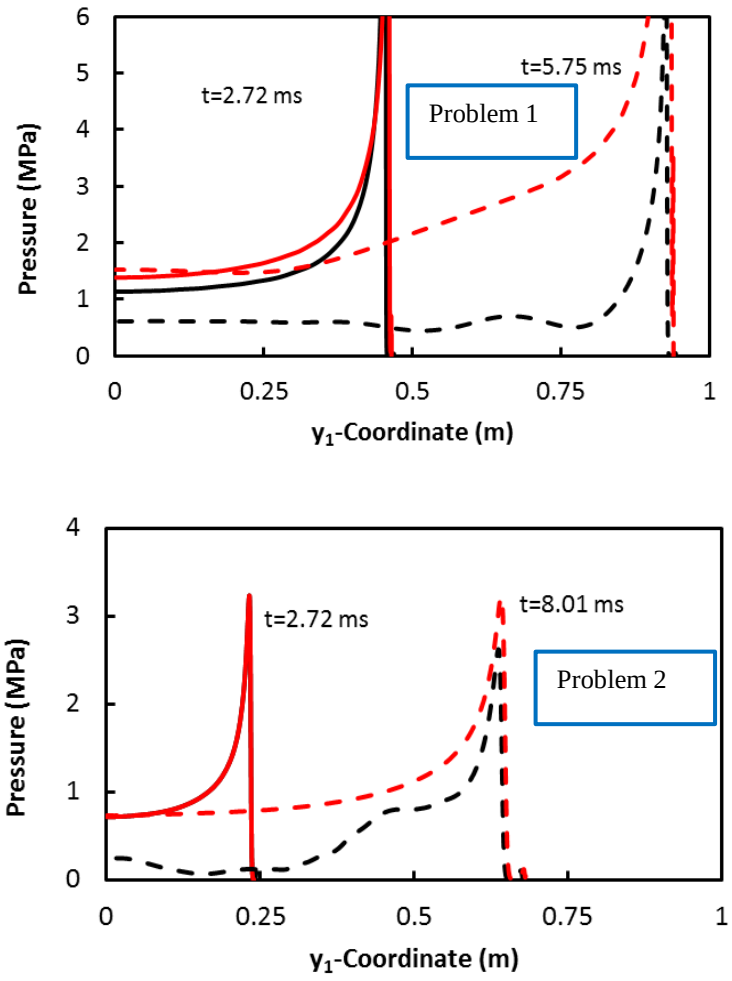

Fig. 23 Distribution of the hydroelastic pressure on the hull at two different times. Black and red curves represent results with and without considering delamination, respectively. The red and black curves at t = 2.72 ms for problem 2 overlap as the beam has not been delaminated at this time.

The variations of the hydroelastic pressure on the hull surface for two values of time are shown in Fig. 23. Consistent with the results presented in Figs. 16 and 19 the hydroelastic pressure on a delaminated hull is less than that on the corresponding in-tact hull because the hull stiffness is reduced due to delamination.

In order to determine from where and when delamination initiates first, we define the separation index, ω, by

$$\omega = \sqrt{\left(\frac{G_I}{G_{Ic}}\right)^2 + \left(\frac{G_{II}}{G_{IIc}}\right)^2} \ , \tag{64}$$

It equals 1 at a point when complete delamination has occurred there. In Figs. 24 and 25, we have plotted the variation of ω versus time t and y_1-coordinate on the two interfaces for problems 1 and 2, respectively. We note that ω equals the square root of the left hand side of Eq. (28), $G_I = \int \sigma_n d\delta_n \ and \ G_{II} = \int \sigma_t d\delta_t$ and have taken the hull width (dimension in the y_2-direction) equal to 1 m. It is clear that the complete delamination first occurs on both interfaces at points close to the left edge or near $y_1 = 0$ at about t = 3.6 and 6.5 ms, respectively, for problems 1 and 2, and propagates to the right edge of the beam on both interfaces. At t = 6 ms, there are some regions of the hull on both interfaces for problem 1 that have not completely delaminated. However, for problem 2 the entire interfaces have been delaminated.

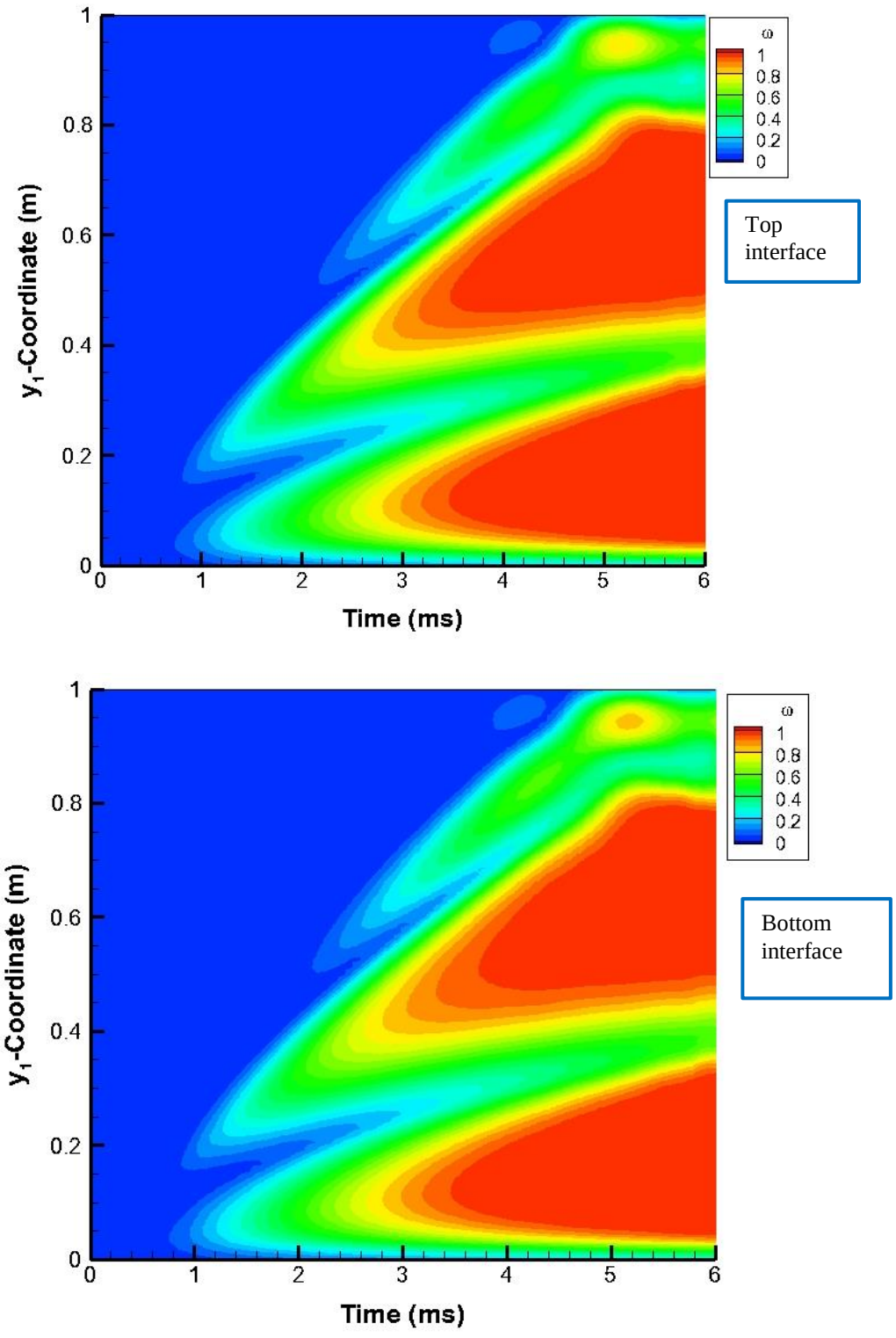

Fig. 24 Variation of the separation index ω with y_1-coordinate and time, on the top and the bottom interfaces for problem 1.

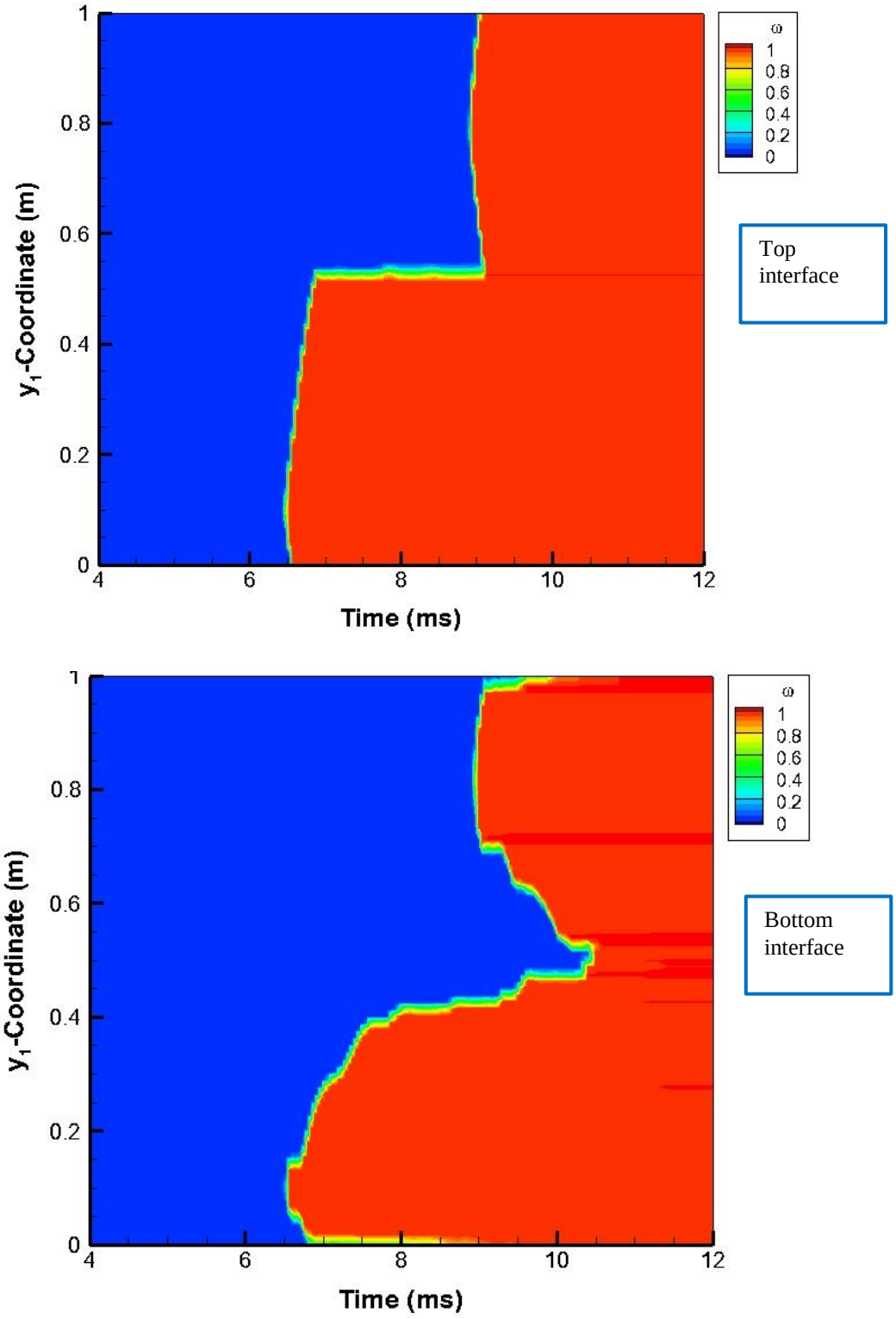

Fig. 25 Variation of the separation index ω with y_1-coordinate and time, on the top and the bottom interfaces for problem 2.

For problem 2, the two interfaces are delaminated at different rates with the top and the bottom interfaces completely delaminated at approximately t = 9.1 and 10.5 ms, respectively. The delamination rate is higher for problem 2 than that for problem 1 because there are large regions where the transverse shear stress nearly equals the critical shear stress of 3.5 MPa as shown in Fig. 26. The delamination process is unstable for problem 2 as evidenced by the sharp increases followed by arrests in the delamination lengths. Also, at t = 9 ms, a large portion of both interfaces near the right edge is delaminated very rapidly.

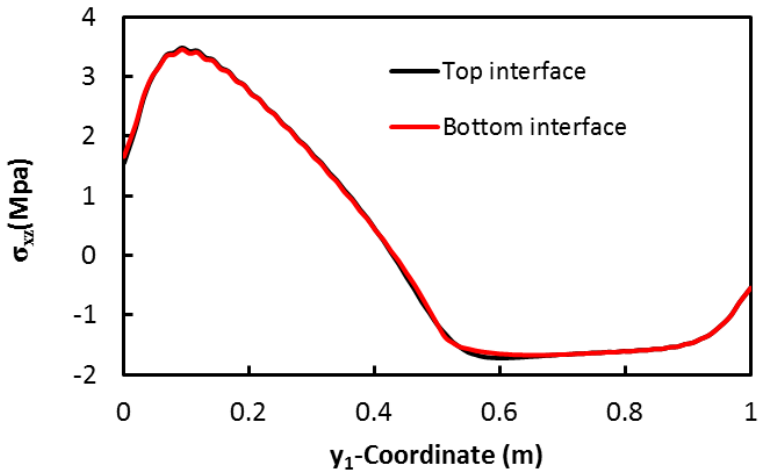

Fig. 26 Distribution of the transverse shear stress σ_{xz} on the top and the bottom interfaces at t = 6.3 ms for problem 2.

In order to delineate the mode of delamination for problems 1 and 2, we have exhibited in Figs. 27 and 28 the distribution of the SERRs, G_I and G_{II} , versus time t and the y_1-coordinate on the two interfaces. For both problems, the value of G_I is negligible as compared to that of G_{II} and the maximum values of G_I/G_{II} equal 0.07 and 0.19, respectively, for problems 1 and 2. It is evident that the SERR G_{II} increases slowly after delamination initiation for problem 1. However, it increases rapidly after the delamination initiation for problem 2.

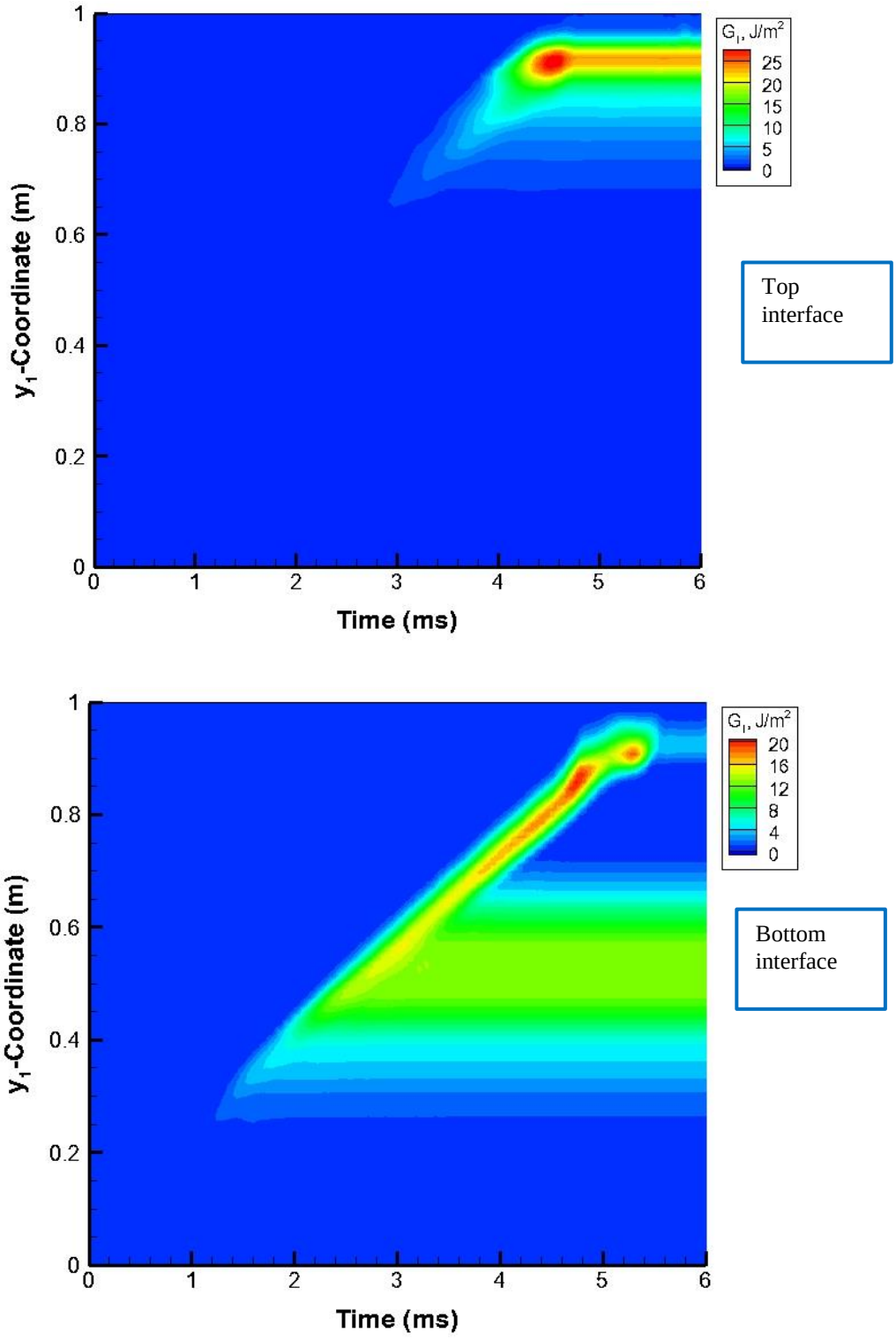

Fig. 27 Variation of the SERR G_I with y_1-coordinate and time, on the top and the bottom interfaces for problem 1.

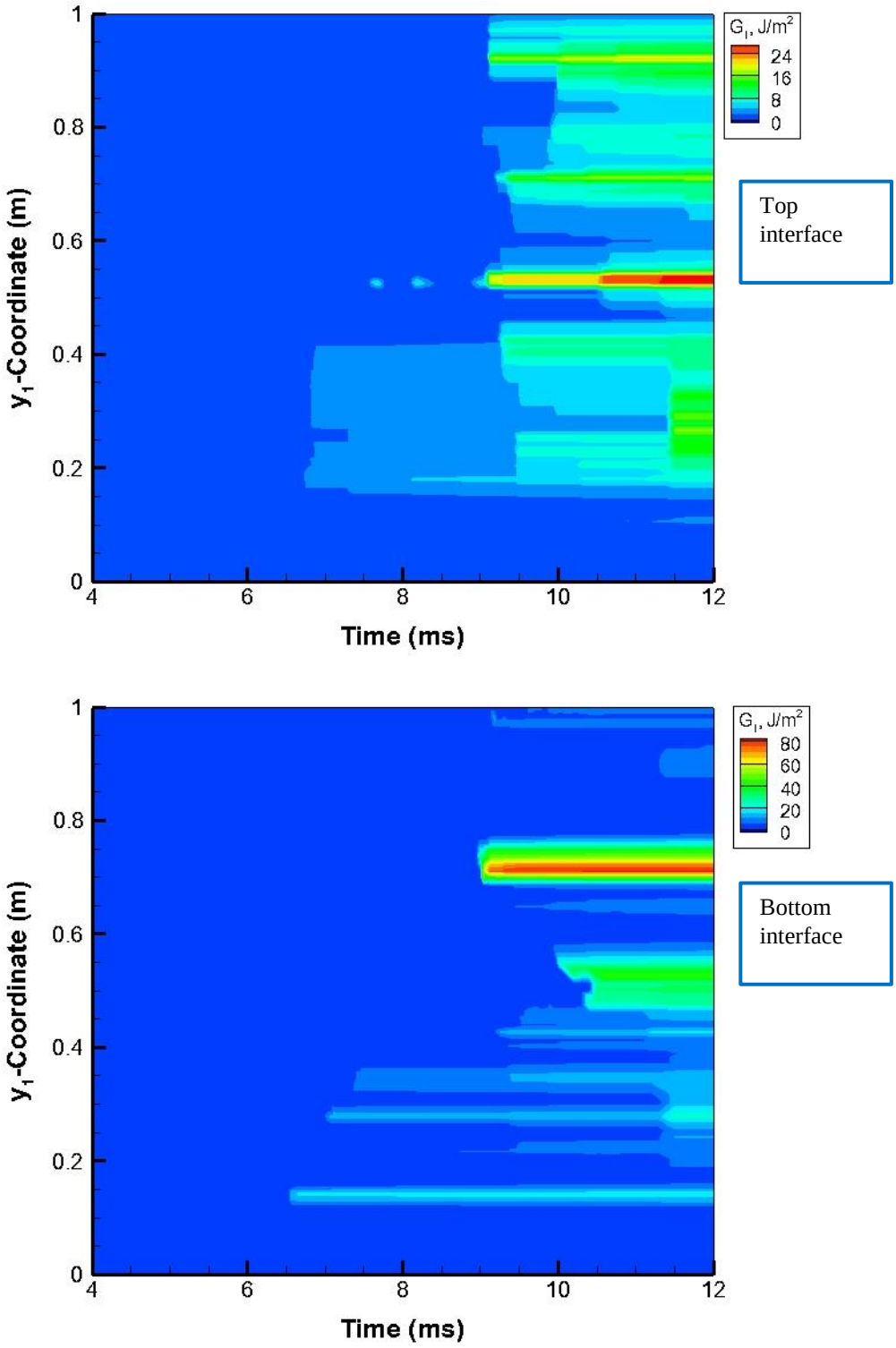

Fig. 28 Variation of the SERR G_I with y_1-coordinate and time, on the top and the bottom interfaces for problem 2.

Time histories of the strain energy W_e and the kinetic energy W_k of the hull, the external work W_p done by the water slamming pressure and of the energy W_d dissipated during delamination are exhibited in Fig. 29. The energies W_e and W_k are evaluated by integrating over the hull domain the elastic energy density W (cf. Eq. 18) and the kinetic energy density, respectively. The work W_p of water slamming pressure equals $\iint (p - p_a) H_1 d\Delta dy_1$, and the energy W_d of delamination equals $\int_{\Gamma_{\mathbb{C}}} (G_{Ic} + G_{IIc})\, H_1 dy_1$. Here Δ is the normal deflection of the hull, and $\Gamma_{\mathbb{C}}$ are the two cohesive interfaces between face sheets and the core. The energy dissipated during the delamination process is a miniscule part of the total work done by external forces. Discontinuities in the time histories of the elastic strain energy for problem 2 at about t = 6.5 and 9 ms are due to the unstable growth of delamination. The time history of the percentage difference $100\big(W_p - W_e - W_d - W_k\big)/W_p$ is shown in Fig. 30. The percentage difference is large for small values of time due to the small value of W_p that appears in the denominator, e.g., see Fig. 29. For problem 1, the percentage difference $100\big(W_p - W_e - W_d - W_k\big)/W_p$ is about 1% for t > 2 ms signifying that the balance of energy is well satisfied. For problem 2, the percentage difference $100\big(W_p - W_e - W_d - W_k\big)/W_p$ is about 30% after delamination has initiated. Oscillations in the error in the energy balance are due to the unstable delamination process for problem 2 as shown in Fig. 25.

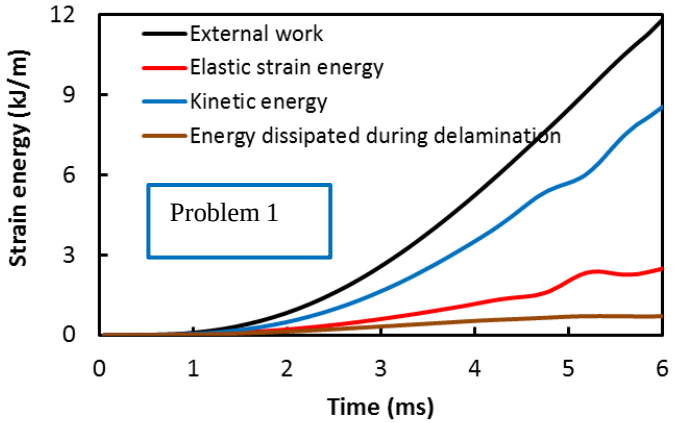

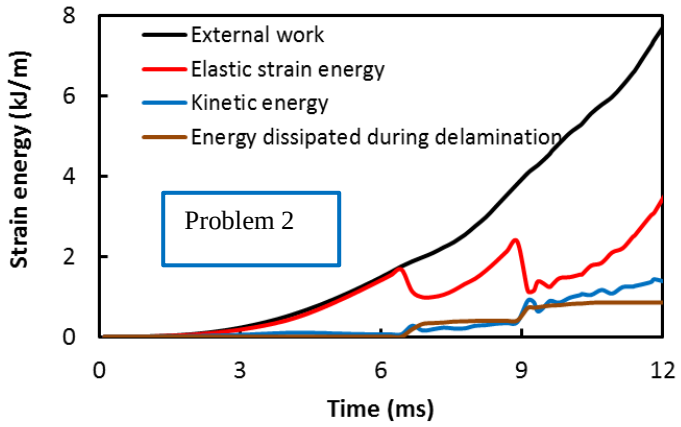

Fig. 29 Time histories of the work done by external forces, strain energy stored in the hull, kinetic energy and energy dissipated during delamination.

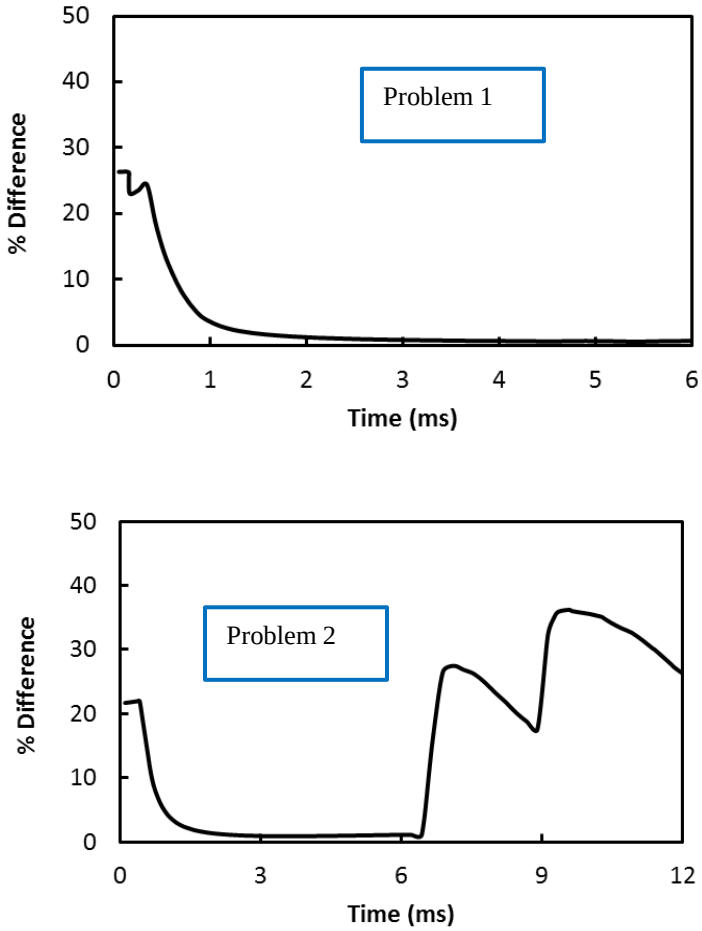

Fig. 30 Time history of the percentage difference, $100(W_p - W_e - W_d - W_k)/W_p$

In Fig. 31 we have plotted the deformed shapes of the hull at t = 6 ms and 12 ms, respectively, for problems 1 and 2. The deformed shapes are not symmetric about the mid-section because the hydroelastic pressure acting on the hull is non-uniform. The corresponding deformed configurations of a line PQRS initially perpendicular to the centroidal axis are exhibited in Fig. 32. Segments PQ, QR and RS in the bottom face sheet, the core and the top face sheet are deformed, respectively, into P'Q', Q"R" and R'S'. Since the entire interfaces have been delaminated for problem 2, the hull is now composed of three separate beams connected at the edges.

Time histories of the total strain energies of the face sheets and the core are plotted in Figs. 33 and 34. For problem 1, the strain energy stored in the core is comparable to that required to deform the face sheets. For problem 2, the elastic strain energy in the core is larger than that in the face sheets. The energy absorbed in the core decreases dramatically when delamination is considered. Prior to the onset of delamination, the strain energy in the core is mainly due to transverse shear strain. However, subsequent to delamination the strain energy of deformation is mainly due to the axial strain.

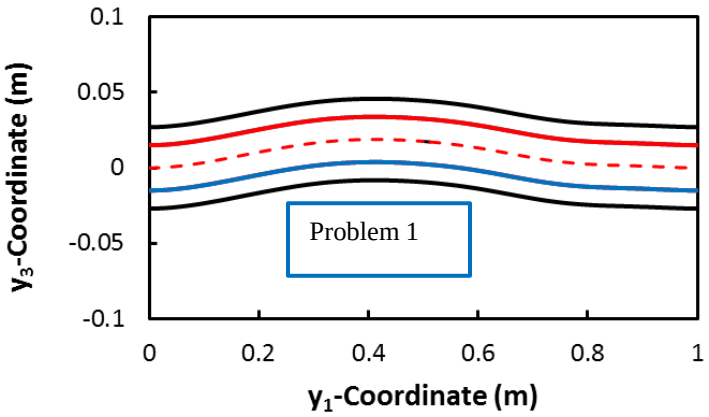

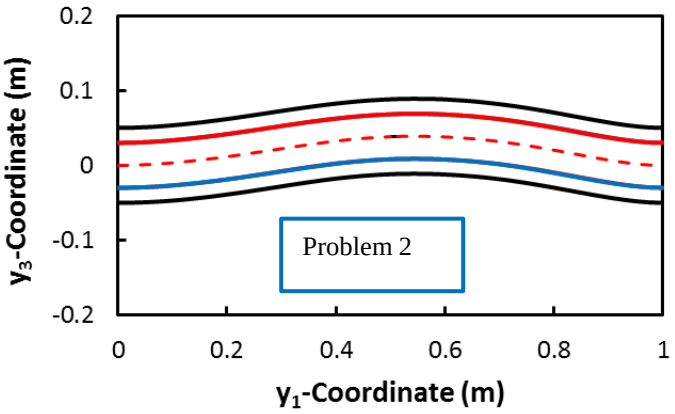

Fig. 31 Deformed shape of the sandwich hull when t = 6 ms and 12 ms, respectively, for problems 1 and 2.

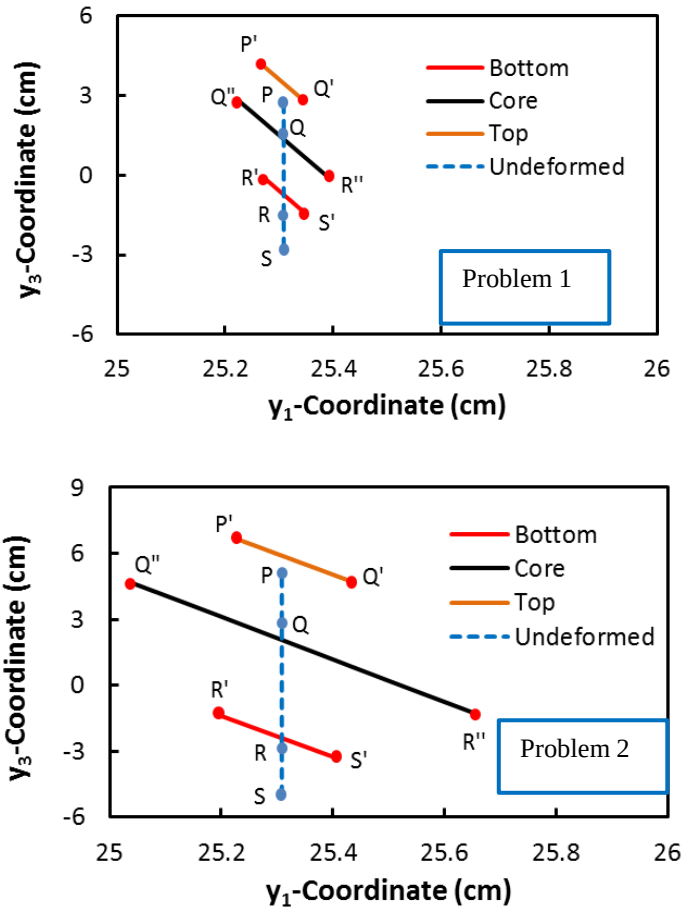

Fig. 32 Deformed configurations of a line initially perpendicular to the centroidal axis at $y_1 = 25.3$ cm when t = 6 ms and 12 ms, respectively, for problems 1 and 2.

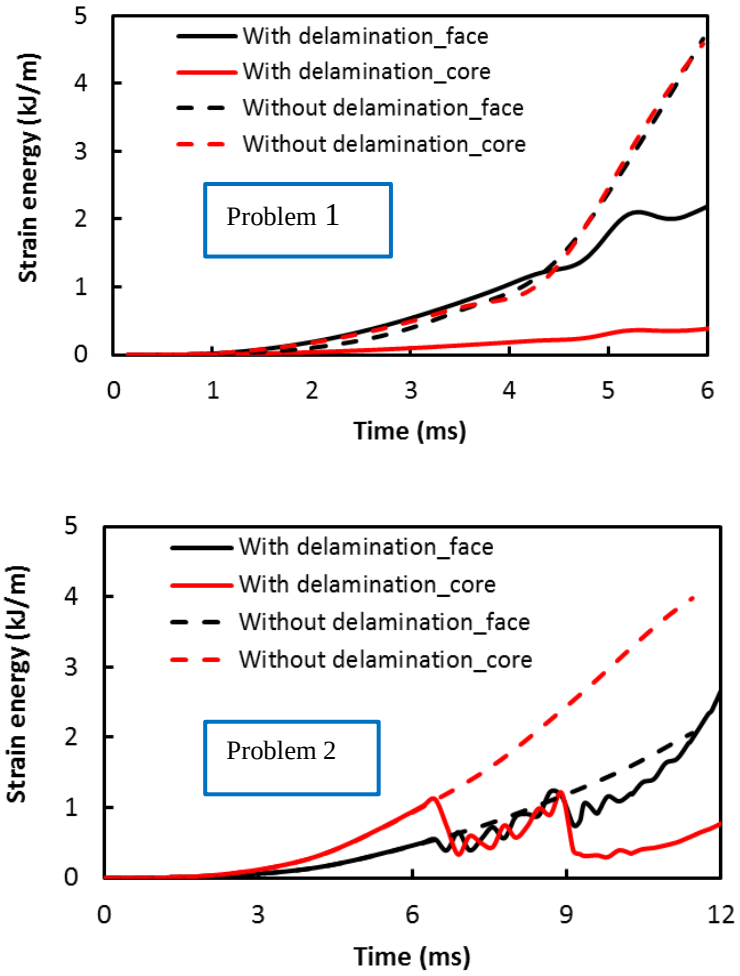

Fig. 33 Time histories of the total energy in the face sheets and the core.

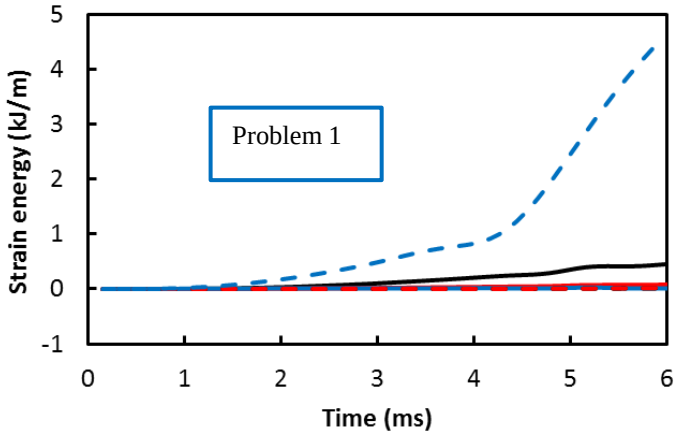

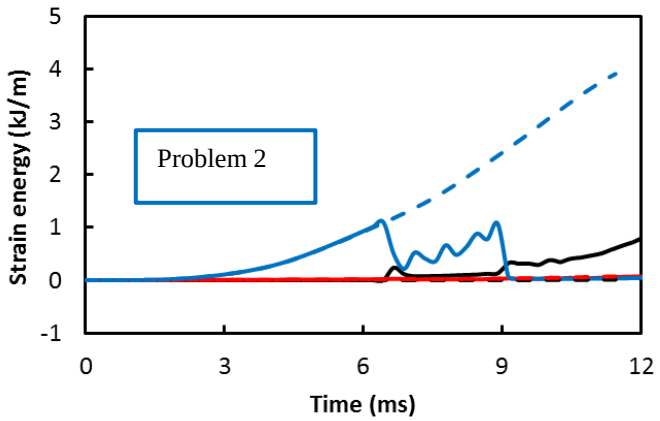

Fig 34 Time histories of the total energy in the core due to different components of strain. The solid curves and dashed curves represent results with and without considering delamination, respectively. Black, red and blue curves represent the energy due to axial strain, transverse normal strain, and shear strain, respectively.

5. Conclusions

Water slamming of deformable straight and curved hulls has been studied using coupled boundary and finite element methods. The boundary element method (BEM) has been employed to analyze deformations of the fluid, and the finite element method (FEM) coupled with a third order shear and normal deformable plate/shell theory (TSNDT) has been used to study hydroelastic problems for hulls with and without considering all geometric nonlinearities. When studying effects of geometric nonlinearities the hull material is taken to be St. Venant-Kirchhoff. The computed results for the deformable hull agree with those found by Das and Batra [35] who used the commercial FE software LSDYNA. These suggest that the assumptions of water being incompressible and its deformations being irrotational do not noticeably influence the hydroelastic effects. The consideration of geometric nonlinearities significantly increases the maximum hydrodynamic pressure experienced by the hull. However, it does not affect the traveling wave like behavior of the hydroelastic pressure acting on the hull. We have also analyzed delamination in two linear elastic sandwich hulls subjected to water slamming loads. In both problems the delamination occurred at the two interfaces between the core and the face sheets due to mode-II deformations. Whereas in one problem, the delamination propagated smoothly and stably, in the other problem the delamination

growth was unstable. Factors which results in stable and unstable mode-II delamination growth will be analyzed in a future study.

Appendix: Boundary Conditions on Ψ

The auxiliary function Ψ and operator $\frac{D_B}{Dt}$ are defined as

$$\Psi = \frac{D_B\varphi}{Dt} = \frac{\partial\varphi}{\partial \mathrm{t}} + \mathbf{V}\cdot\nabla\varphi \tag{A.1.a}$$

$$\frac{D_B}{Dt} = \frac{\partial}{\partial \mathrm{t}} + \mathbf{V}\cdot\nabla \tag{A.1.b}$$

As the fluid is assumed to be incompressible and its deformations irrotational, and $\boldsymbol{V}$ equals the translational velocity of a rigid body, we have following equations for the velocity potential φ.

$$\nabla^2\varphi = 0 \tag{A.2.a}$$

$$\nabla\times\nabla\varphi = \mathbf{0} \tag{A.2.b}$$

$$\nabla\cdot\mathbf{V} = 0 \tag{A.2.c}$$

$$\nabla\times\mathbf{V} = \mathbf{0} \tag{A.2.d}$$

Applying the Laplace operator to Bernoulli's Eq. (5), we get

$$-\nabla^2\left(\frac{\partial\varphi}{\partial \mathrm{t}} + \mathbf{V}\cdot\nabla\varphi\right) + \nabla^2(\mathbf{V}\cdot\nabla\varphi) + \nabla^2\left(\frac{1}{2}|\nabla\varphi|^2 + \frac{\mathrm{p}-\mathrm{p_a}}{\rho}\right) = 0 \tag{A.3.a}$$

We note that

$$\nabla^2(\mathbf{V}\cdot\nabla\varphi) = \mathbf{V}\cdot\nabla(\nabla^2\varphi) = 0 \tag{A.3.b}$$

$$\nabla^2\left(\frac{1}{2}|\nabla\varphi|^2 + \frac{\mathrm{p}-\mathrm{p_a}}{\rho}\right) = \nabla\cdot\left(\nabla\varphi\cdot\nabla\nabla\varphi + \nabla\frac{\mathrm{p}-\mathrm{p_a}}{\rho}\right) = \nabla\cdot\left(\frac{\partial\nabla\varphi}{\partial \mathrm{t}}\right) = 0 \tag{A.3.c}$$

Applying the Laplace operator to Eq. (A.1.a) and using Eq. (A.3), we obtain

$$\nabla^2\Psi = \nabla^2\left(\frac{\partial\varphi}{\partial \mathrm{t}} + \mathbf{V}\cdot\nabla\varphi\right) = 0 \tag{A.4}$$

In order to prove the relation

$$\frac{\partial\Psi}{\partial n} = \frac{\partial}{\partial n}\left(\frac{D_B\varphi}{Dt}\right) = \frac{D_B}{Dt}\left(\frac{\partial\varphi}{\partial n}\right) \tag{A.5}$$

we assume that $\frac{D_B}{Dt}(\boldsymbol{n})$ is small, and note that

$$\frac{D_B}{Dt}\left(\frac{\partial\varphi}{\partial n}\right) = \boldsymbol{n}\cdot\left(\frac{\partial\nabla\varphi}{\partial \mathrm{t}} + \mathbf{V}\cdot\nabla\nabla\varphi\right) = \boldsymbol{n}\cdot\left(\frac{\partial\nabla\varphi}{\partial \mathrm{t}} + \nabla(\mathbf{V}\cdot\nabla\varphi)\right)$$

$$= \boldsymbol{n}\cdot\nabla\left(\frac{\partial\varphi}{\partial \mathrm{t}} + \mathbf{V}\cdot\nabla\varphi\right) = \frac{\partial}{\partial n}\left(\frac{D_B\varphi}{Dt}\right) \quad \text{(A.6)}$$

Substituting from Eq. (4) into Eq. (A.5), the boundary condition on the solid body is given by

$$\frac{\partial\Psi}{\partial n} = \frac{D_B}{Dt}\left(\frac{\partial\varphi}{\partial n}\right) = \frac{D_B}{Dt}(-\boldsymbol{V}\cdot\boldsymbol{n} - \boldsymbol{n}\cdot\dot{\boldsymbol{u}}) = -\dot{\boldsymbol{V}}\cdot\boldsymbol{n} - \ddot{\boldsymbol{u}} - \boldsymbol{V}\cdot\nabla(\boldsymbol{n}\cdot\dot{\boldsymbol{u}}) \quad \text{(A.7)}$$

The boundary condition of zero normal velocity of the fluid on the symmetry axis and the truncation boundaries requires that

$$\frac{\partial\Psi}{\partial n} = \frac{D_B}{Dt}\left(\frac{\partial\varphi}{\partial n}\right) = 0 \quad \text{(A.8)}$$

Substituting from Eq. (A.1.a) into Eq. (5), the boundary condition on the free surface of water can be written as

$$\Psi = \frac{\partial\varphi}{\partial \mathrm{t}} + \mathbf{V}\cdot\nabla\varphi = -\left(-\frac{\partial\varphi}{\partial \mathrm{t}} + \frac{1}{2}|\nabla\varphi|^2\right) + \mathbf{V}\cdot\nabla\varphi + \frac{1}{2}|\nabla\varphi|^2 = \mathbf{V}\cdot\nabla\varphi + \frac{1}{2}|\nabla\varphi|^2 \quad \text{(A.9)}$$

References

1. Faltinsen O.M., *Sea loads on ships and offshore structures.*1993, Cambridge, UK: Cambridge University press.
2. Von Karman T., *The impact on seaplane floats during landing.* NASA, 1929(TN-321).
3. Wagner H., *Über Stoß - und Gleitvorgänge an der Oberfläche von Flüssigkeiten.* ZAMM - Journal of Applied Mathematics and Mechanics/Zeitschrift für Angewandte Mathematik und Mechanik, 1932. **12**(4): p. 193-215.
4. Sedov L., *The impact of a solid body floating on the surface of an incompressible fluid*, in *CAHI*1934: Moscow.
5. Yu Y.T., *Virtual masses of rectangular plates and parallelepipeds in water.* Journal of Applied Physics, 1945. **16**(11): p. 724-729.
6. Bisplinghoff R.L. and C.S. Doherty, *Some studies of the impact of vee wedges on a water surface.* Journal of the Franklin Institute, 1952. **253**(6): p. 547-561.
7. Cointe R. *Two-dimensional water-solid impact*. in *International Offshore Mechanics and Arctic Engineering Symposium (OMAE), 6th*. 1989.
8. Howison S.D., J.R. Ockendon, and S.K. Wilson, *Incompressible water-entry problems at small deadrise angles.* Journal of Fluid Mechanics, 1991. **222**(1): p. 215-230.

9. Donguy B., B. Peseux, L. Gornet, and E. Fontaine. *Three-dimensional hydroelastic water entry: preliminary results*. in *Proceedings of the 11th International Offshore and Polar Engineering Conference*. 2001. Stavanger, Norway.
10. Shiffman M. and D.C. Spencer, *The force of impact on a sphere striking a water surface (second approximation)*, A.M. Panel, Editor 1945, NEW YORK UNIV NY COURANT INST OF MATHEMATICAL SCIENCES.
11. Shiffman M. and D. Spencer, *The force of impact on a cone striking a water surface (vertical entry).* Communications on pure and applied mathematics, 1951. **4**(4): p. 379-417.
12. Trilling L., *The impact of a body on a water surface at an arbitrary angle.* Journal of Applied Physics, 1950. **21**(2): p. 161-170.
13. Schnitzer E. and M.E. Hathaway. *Estimation of hydrodynamic impact loads and pressure distributions on bodies approximating elliptical cylinders with special reference to water landings of helicopters*. 1953.
14. Szebehely V.G. and E.D.T.M. Basin. *Progress in theoretical and experimental studies of ship slamming*. in *Proceedings of the First Conference on Ships and Waves Research*. 1955. University of California, USA.
15. Szebehely V., *Hydrodynamic impact.* Applied mechanics reviews, 1959. **12**(5): p. 297-300.
16. Dobrovol'Skaya Z., *On some problems of similarity flow of fluid with a free surface.* Journal of Fluid Mechanics, 1969. **36**(04): p. 805-829.
17. Zhao R. and O. Faltinsen, *Water entry of two-dimensional bodies.* Journal of Fluid Mechanics, 1993. **246**(1): p. 593-612.
18. Zhao R., O. Faltinsen, and J. Aarsnes. *Water entry of arbitrary two-dimensional sections with and without flow separation*. in *Twenty-first Symposium on NAVAL HYDRODYNAMICS*. 1996.
19. Mei X., Y. Liu, and D.K.P. Yue, *On the water impact of general two-dimensional sections.* Applied Ocean Research, 1999. **21**(1): p. 1-15.
20. Yettou E.M., A. Desrochers, and Y. Champoux, *A new analytical model for pressure estimation of symmetrical water impact of a rigid wedge at variable velocities.* Journal of fluids and structures, 2007. **23**(3): p. 501-522.
21. Miloh T., *On the oblique water-entry problem of a rigid sphere.* Journal of engineering mathematics, 1991. **25**(1): p. 77-92.
22. Miloh T., *On the initial-stage slamming of a rigid sphere in a vertical water entry.* Applied Ocean Research, 1991. **13**(1): p. 43-48.
23. Seddon C.M. and M. Moatamedi, *Review of water entry with applications to aerospace structures.* International journal of impact engineering, 2006. **32**(7): p. 1045-1067.
24. Anghileri M. and A. Spizzica. *Experimental validation of finite element models for water impacts*. in *Proceedings of the Second International Crash Users Seminar*. 1995. Cranfield,UK.
25. Stenius I., A. Rosén, and J. Kuttenkeuler, *Explicit FE-modelling of fluid-structure interaction in hull-water impacts.* International Shipbuilding Progress, 2006. **53**(2): p. 103-121.

26. Oger G., M. Doring, B. Alessandrini, and P. Ferrant, *Two-dimensional SPH simulations of wedge water entries.* Journal of Computational Physics, 2006. **213**(2): p. 803-822.
27. Lin M.C. and T.Y. Ho, *Water-entry for a wedge in arbitrary water depth.* Engineering analysis with boundary elements, 1994. **14**(2): p. 179-185.
28. Battistin D. and A. Iafrati, *Hydrodynamic loads during water entry of two-dimensional and axisymmetric bodies.* Journal of fluids and structures, 2003. **17**(5): p. 643-664.
29. Sun H., *A Boundary Element Method applied to strongly nonlinear wave-body interaction problems*, 2007, Ph.D dissertation, Norwegian University of Science and Technology: Trondheim, Norwegian.
30. Sun H. and O.M. Faltinsen, *Water impact of horizontal circular cylinders and cylindrical shells.* Applied Ocean Research, 2006. **28**(5): p. 299-311.
31. Sun H. and O.M. Faltinsen, *Water entry of a bow-flare ship section with roll angle.* Journal of Marine Science and Technology, 2009. **14**(1): p. 69-79.
32. Qin Z. and R.C. Batra, *Local slamming impact of sandwich composite hulls.* International Journal of Solids and Structures, 2009. **46**(10): p. 2011-2035.
33. Nila A., S. Vanlanduit, S. Vepa, D. Van Nuffel, W. Van Paepegem, J. Degroote, and J. Vierendeels, *High Speed Particle Image Velocimetry Measurements During Water Entry of Rigid and Deformable Bodies*, in *16th Int Symp on Applications of Laser Techniques to Fluid Mechanics*2012: Lisbon, Portugal.
34. Das K., *Analysis of instabilities in microelectromechanical systems, and of local water slamming*, 2009, Ph.D dissertation, Virginia Polytechnic Institute and State University: Blacksburg, VA.
35. Das K. and R.C. Batra, *Local water slamming impact on sandwich composite hulls.* Journal of fluids and structures, 2011. **27**(4): p. 523-551.
36. Stenius I., A. Rosén, and J. Kuttenkeuler, *Hydroelastic interaction in panel-water impacts of high-speed craft.* Ocean Engineering, 2010. **38**(2-3): p. 371-381.
37. Lu C., Y. He, and G. Wu, *Coupled analysis of nonlinear interaction between fluid and structure during impact.* Journal of fluids and structures, 2000. **14**(1): p. 127-146.
38. Panciroli R., S. Abrate, G. Minak, and A. Zucchelli, *Hydroelasticity in water-entry problems: Comparison between experimental and SPH results.* Composite Structures, 2011.
39. Charca S., B. Shafiq, and F. Just, *Repeated slamming of sandwich composite panels on water.* Journal of Sandwich Structures and Materials, 2009. **11**: p. 409-424.
40. Charca S. and B. Shafiq, *Damage assessment due to single slamming of foam core sandwich composites.* Journal of Sandwich Structures and Materials, 2010. **12**: p. 97-112.
41. Hu Z.H., X.D. He, J. Shi, R.G. Wang, and H.J. Liu, *Study on Delamination Problems of Composite Hull Structures under Slamming Loads.* Polymers & Polymer Composites, 2011. **19**(4-5): p. 433-437.
42. Xiao J. and R.C. Batra, *Local water slamming of curved rigid hulls* International Journal of Multiphysics 2012. **6**(3): p. 305-339.
43. Saada A.S., *Elasticity: theory and applications.*1993, Malabar,FL: Krieger.
44. Batra R.C., *Elements of continuum mechanics.*2006: AIAA.

45. Camanho P.P. and C.G. Dávila, *Mixed-mode decohesion finite elements for the simulation of delamination in composite materials.* NASA-Technical Paper, 2002. **211737**.
46. París F. and J. Cañas, *Boundary element method: fundamentals and applications.*1997, New York: Oxford University Press
47. Greco M., *A two-dimensional study of green-water loading*, 2001, Ph.D dissertation, Norwegian University of Science and Technology: Trondheim, Norwegian.
48. Batra R.C. and J. Xiao, *Analysis of Post-buckling and Delamination in Laminated Composite Beams using CZM and Layer-wise TSNDT.* 2013.
49. Batra R.C. and J. Xiao, *Analysis of Post-buckling and Delamination in Laminated Composite Beams using CZM and Layer-wise TSNDT.*
50. Young Y., *Time-dependent hydroelastic analysis of cavitating propulsors.* Journal of fluids and structures, 2007. **23**(2): p. 269-295.
51. Batra R.C. and J. Xiao, *Finite deformations of curved laminated St. Venant-Kirchhoff beam using layer-wise third order shear and normal deformable beam theory (TSNDT)* Composite structures 2013. **97**: p. 147-164.
52. Batra R.C. and X.Q. Liang, *Finite dynamic deformations of smart structures.* Computational mechanics, 1997. **20**(5): p. 427-438.
53. Zenkert D., *Strength of sandwich beams with interface debondings.* Composite Structures, 1991. **17**(4): p. 331-350.
54. Berggreen C., B.C. Simonsen, and K.K. Borum, *Experimental and numerical study of interface crack propagation in foam-cored sandwich beams.* Journal of Composite Materials, 2007. **41**(4): p. 493-520.
55. *http://www.amiantit.com/media/pdf/brochures/Glass_Fibre_Reinforced_Products /files/Glass_Fibre_Reinforced_Products.pdf*.
56. DIAB, *Technical Manuals – Divinycell H, HT & HCP, DIAB AB*, 2000: Laholm, Sweden.

Chapter 5: Analysis of adiabatic shear bands in thermo-elasto-viscoplastic materials by using piece-wise discontinuous basis functions

Abstract

An adiabatic shear band (ASB) is narrow region of intense plastic deformation that forms when most metallic alloys and some polymers are deformed at high strain rates and there is not enough time for the heat generated due to plastic deformation to diffuse away to surroundings. The study of ASBs is important because an ASB is a precursor to shear/ductile fractures. Initial-boundary-value problems simulating the initiation and propagation of an ASB have been analyzed usually by the finite element method (FEM). Because of the large plastic strains involved, the FE mesh needs to be refined several times to delineate the ASB width. However, each refinement requires interpolation of data from nodes of the previous mesh to those of the new mesh which smoothens out sharp gradients in deformation fields. Here we propose using piecewise discontinuous basis functions for studying ASBs to capture sharp gradients in the solution variables across element boundaries, and study simple shearing deformations of a body composed of an isotropic and homogeneous thermo-elasto-viscoplastic material. The mathematical model of the problem has a system of coupled nonlinear partial differential equations and an inequality constraint for finding plastic strain rates. In the absence of an analytical solution of the problem, the computed solution is compared with the converged solution of the problem obtained with the FEM. It is found that indeed the discontinuous Galerkin method captures well the localization of deformation into narrow regions and gives results that agree with those available in the literature.

Key words: adiabatic shear band, shear strain localization; piecewise discontinuous basis functions

1. Introduction

An adiabatic shear band (ASB) refers to the localization of intense plastic deformation into a narrow region that forms in most metallic alloys when they are deformed at high strain rates in processes such as machining, explosive forming, shock impact loading, ballistic penetration, fragmentation, ore crushing, and metal shaping and forming. Whereas it is desirable

to delay the initiation and growth of ASBs in most structures, their occurrences in kinetic energy penetrators are promoted since it is believed that they enhance the penetration of the rod into a target by continuously making the penetrator nose shape conical. Several books [1-4] and review articles [5-7] have summarized earlier works on ASBs. Here we only mention that the phenomenon was experimentally discovered by Tresca [8] in 1878 and by Massey [9] in 1921 during high strain-rate compressive deformations of a steel block. As pointed out by Tresca and Massey, the dominant mode of deformation in an ASB is shearing. Numerical simulations of plane strain deformations of a block made of a thermo-elasto-viscoplastic material by Batra and Ko [10] and Batra and Hwang [11], amongst others, have shown that the tangential velocity is discontinuous across interfaces between the ASB and the material surrounding it. However, quantifying this discontinuity in the tangential velocity has been a challenge. We believe that numerically analyzing the problem by using piecewise discontinuous basis functions should enable one to capture this discontinuity. Accordingly, as a first step, we analyze here a simple shearing problem for a thermo-elasto-viscoplastic material.

We note that similar one-dimensional (1-D) problems have been analyzed by the finite element method (FEM) [12], and meshless methods using basis functions derived by the moving least squares (MLS) [13] and the modified smoothed particle hydrodynamics (MSPH) methods [14]. In each case, and as is done here, the Galerkin formulation of the problem is derived first. The goal of the present work is to show that discontinuous basis functions give as accurate numerical solution of the problem as the FE basis functions employed in [12]. The numerical technique employing the Galerkin formulation of the problem and piecewise discontinuous basis functions is usually called the Discontinuous Galerkin Method (DGM).

The DGM has been used by Reed and Hill [15] to study neutron transport, wave propagation and thermal transport problems. In a DGM [16] the shape functions are chosen so that either the field variable, or its derivatives or both, are discontinuous across inter-element boundaries. The relaxation of the inter-element continuity requirement permits several choices for incorporating different numerical fluxes to enhance the computational performance, and it has the potential of delineating sharp discontinuities in the solution variables. Both h- and p-adaptive mesh refinements can be used in the DGM, and the algorithm can be readily parallelized. Cockburn et al. [17] have summarized recent developments in the DGM, and its applications.

It is shown here that for simple shearing deformations of a thermo-elasto-viscoplastic body containing an inhomogeneity that makes deformations inhomogeneous, the DGM gives as accurate results as those obtained by using the FE, the MLS and the MSPH basis functions. We note that governing equations are highly nonlinear and the coupled ordinary differential equations in time obtained by using the DGM are stiff. The application of the DGM to 2-D problems simulating ASBs and cracks is left for a future study.

2. Formulation of the problem

We study torsional deformations of a thin-walled circular cylindrical steel tube clamped at the left end and twisted by applying a torque at the right end as shown in Fig. 1a. The problem has been experimentally studied by Marchand and Duffy [18] amongst others. Because of the small thickness of the tube, as was also done in interpreting the test data, we assume that deformations are essentially homogeneous through the tube thickness. In experiments the thin tube has small length as compared to its radius so that it does not buckle. As a first approximation deformations of an infinitesimal element ABCD can be regarded as simple shearing schematically shown in Fig. 1b. Batra and Kim [19] used a similar 1-D model for the problem except that they assumed the tube thickness to vary in the y-direction to simulate a machining defect. Here the effect of a defect is considered by perturbing deformations of the homogeneous specimen. We use rectangular Cartesian coordinate axes exhibited in Fig. 1b to describe deformations of the specimen.

We assume that the tube material is homogeneous and isotropic and account for its strain hardening, strain-rate hardening and thermal softening, and use rectangular Cartesian coordinate axes to describe its deformations. For simple shearing deformations, with material particles

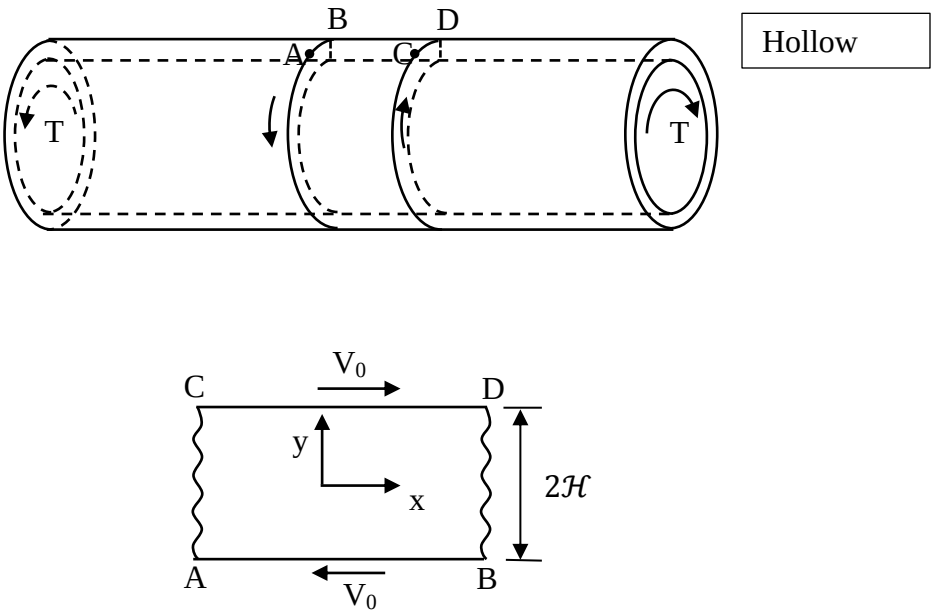

Fig.1 (a) A thin-walled tube deformed in torsion, the tube length has been exaggerated in the Fig. (b) 1-D model of simple shearing deformations

moving only in the x-direction, their y-coordinate does not change and all field variables (e.g., the x-velocity, the temperature, the shear stress) are taken to be functions of the space coordinate y and time t. Equations governing transient thermo-mechanical deformations of the body are (e.g., see [1-3]):

$$\rho\dot{v} = s_{,y} \ , \tag{1.a}$$

$$\rho\dot{e} = -q_{,y} + sv_{,y} \ , \tag{1.b}$$

$$\dot{\gamma} = \dot{\gamma}_e + \dot{\gamma}_p \ , \tag{1.c}$$

$$\dot{\gamma} = v_{,y} \ , \tag{1.d}$$

$$q = -\kappa\theta_{,y} \ , \tag{1.e}$$

$$\dot{s} = \mu\dot{\gamma}_e \ , \tag{1.f}$$

$$\rho\dot{e} = \rho c\dot{\theta} + s\dot{\gamma}_e \ , \tag{1.g}$$

$$\dot{\gamma}_p = \Lambda s \,, \tag{1.h}$$

$$k\dot{\psi} = s\dot{\gamma}_p \,, \tag{1.i}$$

$$k = k_0\left(1 + \frac{\psi}{\psi_0}\right)^n \,, \tag{1.j}$$

$$\Lambda = max\left\{0, \quad \left(\left(\frac{s}{k_0(1-a\theta)\left(1+\frac{\psi}{\psi_0}\right)^n}\right)^{1/m} - 1\right)\Big/ bs\right\}. \tag{1.k}$$

Here a superimposed dot indicates the material derivative with respect to time t, s the shear stress, ρ the mass density, v the velocity in x −direction, q the heat flux, γ the shear strain, γ_e the elastic shear strain, γ_p the plastic shear strain, θ the temperature rise, e the specific internal energy, κ the thermal conductivity, c the specific heat, ψ an internal variable, and μ the shear modulus. The parameter k describes the work hardening of the material, a is the thermal softening parameter, b and m are the strain-rate hardening parameters, ψ_0 and n are work hardening parameters, and k_0 is the yield stress in a quasi-static isothermal simple shear test. Since simple shearing deformations are isochoric (i.e., volume preserving) the mass density remains constant during the deformations.

Equations (1.a) and (1.b) describe, respectively, the balance of linear momentum and the balance of internal energy. Eq. (1.c) is the additive decomposition of the shear strain rate into its elastic and plastic parts, and Eq. (1.d) relates the shear strain rate to the velocity gradient. Eq. (1.e) is Fourier's law of heat conduction with the thermal conductivity, κ, taken to be independent of temperature, Eq. (1.f) is Hooke's law in the rate form, Eq. (1.g) is the constitutive relation for the specific internal energy, and Eq. (1.h) is the flow rule with the plastic multiplier, Λ, given by Eq. (1.j). The plastic multiplier Λ equals zero when the deformation is elastic and is positive for elasto-plastic deformations. The right-hand side of Eq. (1.i) describes working due to plastic deformations, and its left-hand side is the rate of evolution of the internal variable ψ. Eqs. (1.i) and (1.j) imply that $\dot{\psi}$ equals current plastic working divided by the current shear stress of the work-hardened material. For a perfectly plastic material, $\dot{\psi} = \dot{\gamma}_p$. From Eqs. (1.h) and (1.j) we conclude that the yield surface for the material is given by

$$s = k_0(1 - a\theta)\left(1 + \frac{\psi}{\psi_0}\right)^n \left(1 + b\dot{\gamma}_p\right)^m \ . \qquad (2)$$

Thus the yield (or the flow) stress increases due to strain and strain-rate hardening, and it decreases due to thermal softening.

Recall that the von Mises stress for simple shearing deformations equals $\sqrt{3}s$. The above-described model of a thermo-elasto-visco-plastic material is simplification to simple shear deformations of the constitutive relations for 3-D deformations described in [20]. For 3-D deformations, the time derivatives of vectors and tensors in Eq. (1) are replaced by their objective rates such as the Jaumann rate. Also, the flow rule given by Eq. (1.i) is replaced by the normality rule stating that the current value of the plastic part of the strain-rate tensor is along the normal to the current yield surface in the stress space, e.g., see [21]. The internal variable ψ can be interpreted as the effective plastic strain. Equations for 3-D deformations reduce to Eqs. (1) when the skew-symmetric part of the velocity gradient in the Eulerian description of motion vanishes. Since this is not the case for simple shearing deformations, Eqs. (1) can be considered as an approximate model of the simple shearing problem. The approach taken here is similar to that adopted in developing a beam or a plate theory wherein the assumed displacement field rules out satisfying all equations of the 3-D theory. For example, in the Euler-Bernoulli beam theory, both transverse normal strains and transverse normal stress equal zero which is not admissible in the 3-D theory. For simple shearing deformations, normal stresses acting on the top and the bottom surfaces of the specimen and hence in its interior have been tacitly assumed here to have negligible effect on its plastic deformations. These normal stresses for a nonlinear elastic body are generally proportional to square of the magnitude of the shear strain; e.g. see [22]. As shown in [19] this simple model gives results that qualitatively agree with experimental observations, and quantitatively are close to test results.

The shear stress versus the shear strain curves for homogeneous deformations of the material deformed at strain rates of 5 x 10^5/s and 5 x 10^8/s and uniform temperatures of 35.8^{o}C and 71.7^{o}C are shown in Fig. 2. For a given value of the shear strain, the difference in the shear

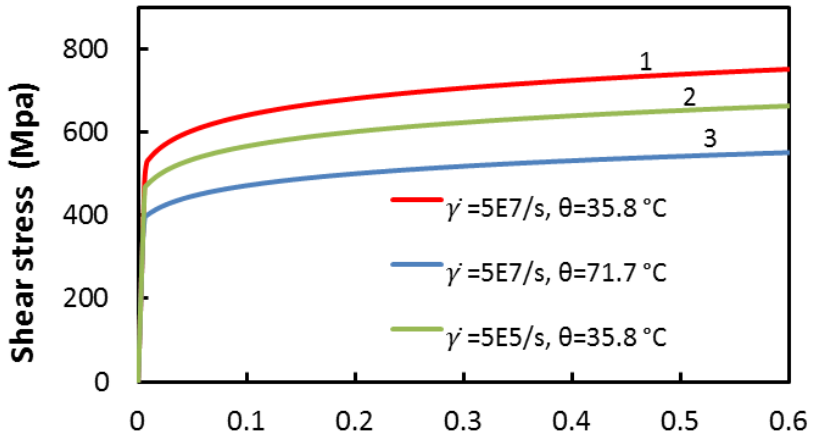

Fig. 2 Shear stress versus shear strain curves for the material studied at two strain rates and two temperatures.

stress between curves 1 and 3 is due to the strain rate hardening effect, and that between curves 1 and 2 is because of thermal softening. We note that the effect of thermal softening has been exaggerated because of an artificially large value assigned to a in Eq. (20) below. When $\theta = 1/a$ the yield surface shrinks to a point and plastic deformations can increase unboundedly. Thus computations should be stopped before the temperature rise equals $1/a$.

Pertinent initial and boundary conditions for the problem are taken to be the following:

$$v(y,0) = 0\,, \quad \theta\,(y,0) = 0, \tag{3.a}$$

$$v(-\mathcal{H},t) = -v_0\,, \quad v(\mathcal{H},t) = v_0\,, \quad \theta_{,y}(\pm\mathcal{H},t) = 0. \tag{3.b}$$

Thus the left and the right surfaces of the specimen are moved in equal and opposite directions with time-dependent speed v_0 in the x-direction, and these surfaces are thermally insulated. Initially the body is at rest and at a uniform temperature which is normalized to be zero.

We introduce the following non-dimensional variables indicated by a superimposed bar:

$$y = \mathcal{H}\overline{y}, \qquad \gamma = \overline{\gamma}, \qquad \psi = \overline{\psi}, \qquad v = \mathcal{H}\dot{\gamma}_0\overline{v}, \qquad t = \frac{\overline{t}}{\dot{\gamma}_0}\,,$$

$$s = k_0\overline{s}, \qquad k = k_0\overline{k}, \qquad \Lambda = \frac{\dot{\gamma}_0}{k_0}\overline{\Lambda}, \qquad b = \frac{\overline{b}}{\dot{\gamma}_0}\,, \qquad \mu = k_0\overline{\mu}, \tag{4}$$

$$\theta = \frac{k_0}{\rho c}\overline{\theta}, \qquad \rho = \frac{k}{H^2\dot{\gamma}_0^2}\overline{\rho}\,, \qquad \kappa = \rho c\dot{\gamma}_0\mathcal{H}^2\overline{\kappa}\,, \qquad a = \frac{\rho c}{k_0}\overline{a}.$$

Here $2\mathcal{H}$ equals the specimen height, and $\dot{\gamma}_0$ is the average shear strain rate. Substituting from Eq. (4) into Eq. (1) we get

$$\dot{\bar{v}} = \frac{1}{\bar{\rho}}\bar{s}_{,\bar{y}} \tag{5.a}$$

$$\dot{\bar{s}} = \bar{\mu}(\bar{v}_{,\bar{y}} - \overline{\Lambda}\bar{s}) \tag{5.b}$$

$$\dot{\bar{\theta}} = \overline{\kappa}q_{,\bar{y}} + \overline{\Lambda}\bar{s}^2 \tag{5.c}$$

$$q = \bar{\theta}_{,\bar{y}} \tag{5.d}$$

$$\dot{\bar{\psi}} = \frac{\overline{\Lambda}\bar{s}^2}{\left(1+\frac{\bar{\psi}}{\bar{\psi}_0}\right)^n} \tag{5.e}$$

$$\overline{\Lambda} = max\left\{0, \quad \left(\left(\frac{\bar{s}}{\left(1-\bar{a}\bar{\theta}\right)\left(1+\frac{\bar{\psi}}{\bar{\psi}_0}\right)^n}\right)^{1/m} - 1\right)\Big/\bar{b}\bar{s}\right\} \tag{5.f}$$

Here, q is the non-dimensional heat flux in the y-direction. In terms of non-dimensional variables, the form (e.g., see Eqs. (3.a) and (3.b)) of the initial and the boundary conditions is unchanged.

Because of boundary conditions (3.b) and initial conditions (3.a), we assume that the solution exhibits the following symmetry and anti-symmetry properties:

$$\begin{aligned} &\bar{v}(-\bar{y},\bar{t}) = -\bar{v}(\bar{y},\bar{t})\,, \;\; \bar{\theta}\,(-\bar{y},\bar{t}) = \bar{\theta}(\bar{y},\bar{t}) \\ &\bar{\psi}(-\bar{y},\bar{t}) = \bar{\psi}(\bar{y},\bar{t})\,, \quad \bar{s}(-\bar{y},\bar{t}) = \bar{s}(\bar{y},\bar{t}) \end{aligned} \tag{6}$$

Therefore, we solve the problem on the domain [0, 1] using the following boundary conditions:

$$\bar{v}(0,\bar{t}) = 0\;, \qquad \bar{v}(1,\bar{t}) = v_0\;, \qquad \bar{\theta}_{,\bar{y}}(0,\bar{t}) = 0\;, \qquad \bar{\theta}_{,\bar{y}}(1,\bar{t}) = 0\;. \tag{7}$$

3. Numerical solution of the IBVP

The IBVP formulated in Section 2 is numerically solved by using discontinuous basis functions. We first derive a weak formulation of the problem, and then describe the solution methodology.

3.1 Weak form

We discretize the problem domain [0, 1] into the union of $\mathbb{N}$ disjoint subdomains, $\Omega_j = [\bar{y}_j, \bar{y}_{j+1}]$, and call Ω_j the j^{th} element. Elements Ω_j and Ω_{j+1} share the common point $\bar{y} = \bar{y}_{j+1}$ called the $(j+1)^{th}$ node. Even though Eqs. (5.a) and (5.b) can be combined into one PDE involving second-order derivatives of $\bar{v}$ with respect to $\bar{t}$ and $\bar{y}$, we do not do so because it is difficult to define flux terms for first-order derivatives. The flux, $\hat{s}$, is a function of values of s on both sides of the inter-element node and the neighboring elements communicate information to each other through the flux terms which are defined in subsection 3.2. For the discontinuous basis functions, there are two different values s_j^+ and s_j^- of s at the inter-element node j defined below:

$$\bar{s}_j^+ = \lim_{\bar{y} \downarrow \bar{y}_j^+} \bar{s}(\bar{y}), \quad \bar{s}_j^- = \lim_{\bar{y} \uparrow \bar{y}_j^-} \bar{s}(\bar{y}) \tag{8}$$

where $\bar{y}_j^+$ and $\bar{y}_j^-$ are shown in Fig. 3.

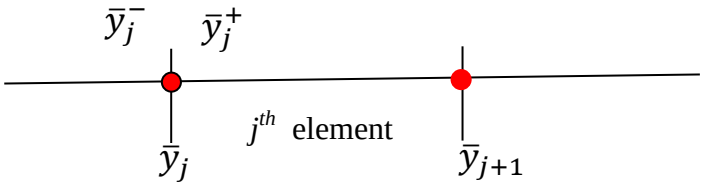

Fig. 3 Definitions of $\bar{y}_j^+$ and $\bar{y}_j^-$ at the j^{th} node

Multiplying both sides of Eqs. (5.a) - (5.e) by test functions ω_1, ω_2…, integrating the resulting equation on $\Omega_j = [\bar{y}_j, \bar{y}_{j+1}]$, and using the integration by parts formula, we get

$$\int_{\bar{y}_j}^{\bar{y}_{j+1}} \left(\omega_1 \dot{\bar{v}} + \frac{1}{\bar{\rho}} \bar{s} \frac{\partial \omega}{\partial \bar{y}} \right) dy + \frac{1}{\bar{\rho}} \hat{\bar{s}}_j \omega_1(\bar{y}_j) - \frac{1}{\bar{\rho}} \hat{\bar{s}}_{j+1} \omega_1(\bar{y}_{j+1}) = 0 \tag{9.a}$$

$$\int_{\bar{y}_j}^{\bar{y}_{j+1}} \left(\omega_2 \dot{\bar{s}} + \bar{\mu}\bar{v}\frac{\partial \omega_2}{\partial \bar{y}}\right) d\bar{y} + \bar{\mu}\hat{\bar{v}}_j \omega_2(\bar{y}_j) - \bar{\mu}\hat{\bar{v}}_{j+1}\omega_2(\bar{y}_{j+1}) = -\int_{\bar{y}_j}^{\bar{y}_{j+1}} \omega_2 \bar{\Lambda}\bar{s}\, d\bar{y} \tag{9.b}$$

$$\int_{\bar{y}_j}^{\bar{y}_{j+1}} \left(\omega_3 \dot{\bar{\theta}} + \bar{\kappa}\bar{q}\frac{\partial \omega_3}{\partial y}\right) d\bar{y} + \bar{\kappa}\hat{\bar{q}}_j \omega_3(\bar{y}_j) - \bar{\kappa}\hat{\bar{q}}_{j+1}\omega_3(\bar{y}_{j+1}) = \int_{\bar{y}_j}^{\bar{y}_{j+1}} \omega_3 \bar{\Lambda}\bar{s}^2\, d\bar{y} \tag{9.c}$$

$$\int_{\bar{y}_j}^{\bar{y}_{j+1}} \left(\omega_4 \bar{q} + \bar{\theta}\frac{\partial \omega_4}{\partial \bar{y}}\right) d\bar{y} + \hat{\bar{\theta}}_j \omega_4(\bar{y}_j) - \hat{\bar{\theta}}_{j+1}\omega_4(\bar{y}_{j+1}) = 0 \tag{9.d}$$

$$\int_{\bar{y}_j}^{\bar{y}_{j+1}} \omega_5 \dot{\bar{\psi}}\, d\bar{y} = \int_{\bar{y}_j}^{\bar{y}_{j+1}} \omega_5 \frac{\bar{\Lambda}\bar{s}^2}{\left(1+\frac{\bar{\psi}}{\bar{\psi}_0}\right)^n} d\bar{y} \tag{9.e}$$

The test function, $\omega_\ell, \ell = 1,2 \ldots,5$ is not the same in each equation, and values of the shear stress, $\bar{s}$, the velocity $\bar{v}$, the heat flux $\bar{q}$, and the temperature $\bar{\theta}$ at the element boundaries (i.e., nodes *j* and *j+1*) are replaced by the fluxes $\hat{s}$, $\hat{\bar{v}}$, $\hat{\bar{q}}$, and $\hat{\bar{\theta}}$.

On each element, the variables $\bar{s}$, $\bar{v}$, $\bar{q}$, $\bar{\theta}$ and $\bar{\psi}$ on Ω_j are approximated in terms of shape functions $\phi_1^{(j)}(\bar{y}), \phi_2^{(j)}(\bar{y}) \cdots \phi_{N_e}^{(j)}(\bar{y})$ for the j^{th} element as

$$\bar{s}_h^{(j)}(\bar{y},\bar{t}) = \sum_{i=1}^{N_e} \phi_i^{(j)}(\bar{y})\bar{s}_i^{(j)}(\bar{t}) \ , \bar{v}_h^{(j)}(\bar{y},\bar{t}) = \sum_{i=1}^{N_e} \phi_i^{(j)}(\bar{y})\bar{v}_i^{(j)}(\bar{t}) \ ,$$

$$\bar{q}_h^{(j)}(\bar{y},\bar{t}) = \sum_{i=1}^{N_e} \phi_i^{(j)}(\bar{y})\bar{q}_i^{(j)}(\bar{t}) \ , \bar{\theta}_h^{(j)}(\bar{y},\bar{t}) = \sum_{i=1}^{N_e} \phi_i^{(j)}(\bar{y})\bar{\theta}_i^{(j)}(\bar{t}) \ , \tag{10}$$

$$\bar{\psi}_h^{(j)}(\bar{y},\bar{t}) = \sum_{i=1}^{N_e} \phi_i^{(j)}(\bar{y})\bar{\psi}_i^{(j)}(\bar{t})$$

Here N_e equals the number of nodes on element Ω_j . N_e equals 2 and 3, respectively, for shape functions that are complete polynomials of degree 1 and 2. For N_e = 2 and 3, the shape functions are defined below.

$$\phi_1^{(j)}(\bar{y}) = \frac{1}{2}(1-\xi), \phi_2^{(j)}(\bar{y}) = \frac{1}{2}(1+\xi), \text{for } N_e = 2 \tag{11.a}$$

and

$$\phi_1^{(j)}(\bar{y}) = \frac{1}{2}\xi(1-\xi) \ , \phi_2^{(j)}(\bar{y}) = 1-\xi^2 \ , \ \phi_3^{(j)}(\bar{y}) = \frac{1}{2}\xi(1+\xi), \text{for } N_e = 3, \tag{11.b}$$

where

$$\xi = \frac{2\bar{y}-(\bar{y}_{j+1}+\bar{y}_j)}{(\bar{y}_{j+1}-\bar{y}_j)}. \tag{12}$$

For the problem being studied, there are $5 \times N_e$ unknowns for an element and the total number of unknowns equals $5 \times N_e \times \mathbb{N} + 10$ which includes unknowns at the boundaries.

For the test function ω_ℓ defined on the j^{th} element, we use the same basis functions as those for the trial solution, i.e.,

$$\omega_\ell = \sum_{i=1}^{N_e} \phi_i^{(j)}(\bar{y}) c_{\ell i}^{(j)} \tag{13}$$

where $c_{\ell i}^{(j)}$ are constants. Substitution from Eqs. (10) and (13) into Eqs. (9) and requiring that the resulting equations hold for all values of constants $c_{\ell 1}^{(j)}, c_{\ell 2}^{(j)} \cdots, c_{\ell N_e}^{(j)}$ gives the following set of coupled nonlinear ordinary differential equations (ODEs).

$$M_{li}^{(j)} \dot{\bar{v}}_i^{(j)} + \frac{1}{\bar{\rho}} K_{li}^{(j)} \bar{s}_i^{(j)} + \frac{1}{\bar{\rho}} \hat{\bar{s}}_j Q_{l1}^{(j)} - \frac{1}{\bar{\rho}} \hat{\bar{s}}_{j+1} Q_{l2}^{(j)} = 0 \tag{14.a}$$

$$M_{li}^{(j)} \dot{\bar{s}}_i^{j} + \bar{\mu} K_{li}^{(j)} \bar{v}_i^{(j)} + \bar{\mu} \hat{\bar{v}}_j Q_{l1}^{(j)} - \bar{\mu} \hat{\bar{v}}_{j+1} Q_{l2}^{(j)} = f_{l\bar{s}}^{(j)} \tag{14.b}$$

$$M_{li}^{(j)} \dot{\bar{\theta}}_i^{(j)} + \bar{\kappa} K_{li}^{(j)} q_i^{(j)} + \bar{\kappa} \hat{q}_j Q_{l1}^{(j)} - \kappa \hat{q}_{j+1} Q_{l2}^{(j)} = f_{l\bar{\theta}}^{(j)} \tag{14.c}$$

$$M_{li}^{(j)} q_i^{(j)} + K_{li}^{(j)} \bar{\theta}_i^{(j)} + \hat{\bar{\theta}}_j Q_{l1}^{(j)} - \hat{\bar{\theta}}_{j+1} Q_{l2}^{(j)} = 0 \tag{14.d}$$

$$M_{li}^{(j)} \dot{\bar{\psi}}_i^{(j)} = f_{l\bar{\psi}}^{(j)} \tag{14.e}$$

where

$$\begin{gathered} M_{li}^{(j)} = \int_{\bar{y}_j}^{\bar{y}_{j+1}} \phi_l^{(j)} \phi_i^{(j)} dy \;, K_{li}^{(j)} = \int_{\bar{y}_j}^{\bar{y}_{j+1}} \frac{d\phi_l^{(j)}}{dx} \phi_i^{(j)} d\bar{y} \,, Q_{l1}^{(j)} = \phi_l^{(j)}(\bar{y}_j) \,, Q_{l2}^{(j)} = \phi_l^{(j)}(\bar{y}_{j+1}) \\ f_{l\bar{s}}^{(j)} = -\int_{\bar{y}_j}^{\bar{y}_{j+1}} \phi_l^{(j)} \overline{\Lambda} \bar{s} d\bar{y} \;, f_{l\bar{\theta}}^{(j)} = \int_{\bar{y}_j}^{\bar{y}_{j+1}} \phi_l^{(j)} \overline{\Lambda} \bar{s}^2 d\bar{y} \;, f_{l\bar{\psi}}^{(j)} = \int_{\bar{y}_j}^{\bar{y}_{j+1}} \phi_l^{(j)} \frac{\overline{\Lambda} \bar{s}^2}{\left(1+\frac{\bar{\psi}}{\bar{\psi}_0}\right)^n} d\bar{y} \end{gathered} \tag{15}$$

The integrals for the mass matrix $M_{li}^{(j)}$ and the stiffness matrix $K_{li}^{(j)}$ are evaluated analytically, and those for the force vectors $f_{l\bar{s}}^{(j)}$, $f_{l\bar{\theta}}^{(j)}$ and $f_{l\bar{\psi}}^{(j)}$ numerically using 5 Gauss points. Thus the consistent mass matrix is used to find an approximate solution of the IBVP.

3.2 Choice of flux

Cockburn and Shu [23] have discussed fluxes for solution schemes using piecewise discontinuous basis functions. The choice of flux depends on the type (hyperbolic, parabolic, elliptic) of the equation. Eqs. (9.a) and (9.b) are hyperbolic, and we use the flux-vector splitting method, e.g., see Weinhart [24] (chapter 2), to find the flux at the inter-element boundary node *j* . That is, the flux $\hat{f}_j(u)$ for Eqs. (9.a) and (9.b) at the inter-element node *j* is given by

$$\hat{f}_j(u) = Au_j = P\lambda P^{-1}u = P(\lambda^+ + \lambda^-)P^{-1}u = \hat{f}_j(u)^+ + \hat{f}_j(u)^- \tag{16}$$

where

$$\hat{f}_j(u) = \begin{bmatrix} -\frac{1}{\bar{\rho}}\hat{\bar{s}}_j \\ -\bar{\mu}\hat{\bar{v}}_j \end{bmatrix},\ \lambda_i^{\pm} = \frac{\lambda_i \pm |\lambda_i|}{2},\quad A = \begin{bmatrix} 0 & -\frac{1}{\bar{\rho}} \\ -\bar{\mu} & 0 \end{bmatrix},\quad u = \begin{bmatrix} \bar{v} \\ \bar{s} \end{bmatrix}$$

$$\lambda^{\pm} = \begin{bmatrix} \lambda_1^{\pm} & 0 \\ 0 & \lambda_2^{\pm} \end{bmatrix},\ \lambda_1 = -\sqrt{\frac{\bar{\mu}}{\bar{\rho}}},\ \lambda_2 = \sqrt{\frac{\bar{\mu}}{\bar{\rho}}}, P = \begin{bmatrix} \frac{1}{\sqrt{\bar{\rho}\bar{\mu}}} & -\frac{1}{\sqrt{\bar{\rho}\bar{\mu}}} \\ 1 & 1 \end{bmatrix} \tag{17}$$

$$\hat{f}_j(u)^+ = P(\lambda^-)P^{-1}u_j^+\ ,\ \hat{f}_j(u)^- = P(\lambda^+)P^{-1}u_j^-,$$

λ and *P* are eigenvalues and eigenvectors of matrix A. We note that the magnitudes of λ_1 and λ_2 equal the shear wave speed, and $\sqrt{\bar{\rho}\bar{\mu}}$ equals the acoustic impedance for simple shear deformations of a linear elastic body.

Heat conduction Eqs. (9.c) and (9.d) are parabolic and the alternating upwind scheme, e.g., see Li [16], is used. That is,

$$\hat{q}_j = q_j^+\ ,\ \hat{\bar{\theta}}_j = \bar{\theta}_j^- \quad . \tag{18}$$

3.3 Satisfaction of boundary conditions

The essential boundary conditions at $\bar{y} = 0$ (node 1) and $\bar{y} = 1$ (node $\mathbb{N}l$), and natural boundary conditions of zero heat flux at these nodes are satisfied as follows.

$$\begin{aligned} &\bar{v}_1^+ = \bar{v}_1^- = 0,\ \ \bar{s}_1^+ = \bar{s}_1^-,\ \ \ q_1^+ = q_1^- = 0,\ \ \bar{\theta}_1^+ = \bar{\theta}_1^-,\ \ \bar{\psi}_1^+ = \bar{\psi}_1^- \\ &\bar{v}_{\mathbb{N}l}^+ = \bar{v}_{\mathbb{N}l}^- = \bar{v}_0\ ,\ \ \bar{s}_{\mathbb{N}l}^- = \bar{s}_{\mathbb{N}l}^+,\ \ \ q_{\mathbb{N}l}^+ = q_{\mathbb{N}l}^- = 0,\ \ \bar{\theta}_{\mathbb{N}l}^- = \bar{\theta}_{\mathbb{N}l}^+,\ \ \bar{\psi}_{\mathbb{N}l}^- = \bar{\psi}_{\mathbb{N}l}^+ \end{aligned} \tag{19}$$

3.4 ASB initiation criterion

Following Batra and Kim [12], an ASB is assumed to initiate at a material point when the shear stress there has dropped to 80% of its maximum value at that point, the material point is deforming plastically and deformations in its neighborhood are inhomogeneous. We recall that in Marchand and Duffy's [18] experimental work the torque dropped catastrophically when an ASB initiated. The drop in the shear stress is so rapid that a precise value of 80% or 70% of the maximum shear stress for the ASB initiation makes very little difference in the value of the ASB initiation time.

3.5 ASB width

In their torsional tests Marchand and Duffy [18] called the width, δ_{ASB}, of the intensely deformed region of uniform plastic strain as the ASB width. Batra and Kim [12] defined an edge of the ASB as the point where the effective plastic strain equaled 95% of that at the ASB center. Here the edge of the ASB is taken to be the point where the temperature equals 40% of the peak value of the temperature at the ASB center.

4. Computation and discussion of results

Following the common terminology the numerical scheme based on the above described Galerkin formulation of the problem employing piecewise discontinuous basis functions is called the Discontinuous Galerkin Method (DGM).

The coupled nonlinear ODEs (14) are integrated with respect to time *t* by using the subroutine LSODE taken from the ODEPACK developed by Radhakrishnan and Hindmarsh [25]. Results presented below have been calculated by setting MF = 20, ATOL $= 1 \times 10^{-7}$ and RTOL $= 1 \times 10^{-7}$ in LSODE. The parameter MF = 20 defines a choice of stiff solver method with internally computed full Jacobian, and parameters ATOL and RTOL equal the absolute and

the relative tolerances in the computed solution, respectively. The subroutine adjusts the time step adaptively to compute the solution within the prescribed tolerances.

Values assigned to non-dimensional parameters are:

$$\bar{\rho} = 3.928 \times 10^{-5}, \quad \bar{\mu} = 240.3\,, \quad \bar{a} = 0.4973\,,\ n = 0.09\,, \tag{20}$$

$$\bar{k} = 3.978 \times 10^{-5}, \quad \bar{\psi}_0 = 0.017\,, \quad m = 0.025\,, \quad \bar{b} = 5 \times 10^{6}.$$

These values are for typical steel with specimen of height 2.58 mm deformed at an average strain rate $\dot{\gamma}_0 = 500\ \mathrm{s}^{-1}$, except that the value of the thermal softening coefficient $\bar{a}$ has been enhanced to reduce the computational time. The temperature rise in $^0\mathrm{C}$ and the shear stress in MPa can be obtained by multiplying the corresponding non-dimensional values by 89.6 and 333, respectively. In order to reduce the computational time, transient deformations of a homogeneous specimen are studied first, and the homogeneous solution is perturbed when $\bar{\psi} = 0.1$, $\bar{\theta} = 0.1003$, and $\bar{\gamma} = 0.0692$. The time is reckoned from this instant of introducing the following perturbation in the uniform temperature and stress fields.

$$\bar{\theta}(\bar{y}, 0) = 0.1003 + 0.1(1 - \bar{y}^2)^9 e^{-5\bar{y}^2}\,, \tag{21}$$

$$\bar{s}(\bar{y}, 0) = \left(1 + \frac{0.1}{\bar{\psi}_0}\right)^n (1 - \bar{a}\bar{\theta}(\bar{y}, 0))\left(1 + \bar{b}\right)^m\ .$$

The second term on the right side of the temperature field represents the perturbation with a large value at the center $\bar{y} = 0$. The perturbation in the temperature dies out quickly with an increase in $\bar{y}$. The perturbation amplitude is purposely taken to be large to speed up the localization of deformation around the point $\bar{y} = 0$. The perturbation makes deformations of the specimen inhomogeneous, and the high temperature at points near $\bar{y} = 0$ softens the material more than that at other points of the specimen. This softer material deforms more rapidly which results in larger values of the energy dissipated due to plastic working and thus in a larger increase in the temperature. This self-feeding process makes deformations localize in a narrow region around $\bar{y} = 0$. The perturbation can be regarded as representing the effect of a defect at $\bar{y} = 0$, with its maximum value proportional to the strength of the defect.

In the absence of an analytical solution of the problem, the converged numerical solution, $\bar{s}(\bar{y},\bar{t})$, computed with the graded mesh

$$\text{Mesh1: } \bar{y}(j) = \left(\frac{j-1}{200}\right)^5, j = 1,2,\cdots,201 \tag{22}$$

and the FE code developed by Batra and Kim [12] is taken as the reference solution. Here $\bar{y}(j)$ is the $\bar{y}$-coordinate of node *j*.

In order to delineate the effect of the mesh size on the solution computed by the DGM and the FEM we used following meshes.

$$\text{Mesh 2 : } \bar{y}(j) = \left(\frac{j-1}{200}\right)^3, j = 1,2,\cdots,201 \quad \text{(Linear shape functions)}$$

$$\text{Mesh 3 : } \bar{y}(j) = \left(\frac{j-1}{100}\right)^2, j = 1,2,\cdots,101 \quad \text{(Linear shape functions)}$$

$$\text{Mesh4: } \bar{y}(j) = \begin{cases} \left(\frac{k-1}{50}\right)^2, j = 2k-1,\ k = 1,2,\cdots,51 \\ \frac{y(2k-1)+y(2k+1)}{2},\ j = 2k,\ k = 1,2,\cdots,50 \end{cases} \quad \text{(Linear shape functions)}$$

$$\bar{y}(j) = \left(\frac{j-1}{50}\right)^2, \quad j = 1,2,\cdots,51 \quad \text{(Quadratic shape functions)}$$

$$\text{Mesh 5: } \bar{y}(j) = \begin{cases} \left(\frac{k-1}{100}\right)^2, j = 2k-1,\ k = 1,2,\cdots,101 \\ \frac{\bar{y}(2k-1)+\bar{y}(2k+1)}{2},\ j = 2k,\ k = 1,2,\cdots,100 \end{cases} \quad \text{(Linear shape functions)} \tag{23}$$

$$\bar{y}(j) = \left(\frac{j-1}{100}\right)^2, j = 1,2,\cdots,101 \quad \text{(Quadratic shape functions)}$$

$$\text{Mesh 6: } \bar{y}(j) = \left(\frac{j-1}{100}\right)^3,\ j = 1,2,\cdots,101 \quad \text{(Quadratic shape functions)}$$

The meshes for the FEM are the same as those for the DGM with linear shape functions. The error in the solution $\bar{s}(\bar{y},\bar{t})$ is measured by the following expressions:

$$\eta(\bar{y},\bar{t}) = \frac{s(\bar{y},\bar{t}) - \tilde{s}(\bar{y},\bar{t})}{\tilde{s}(\bar{y},\bar{t})}, \qquad \eta_0 = \sup_{\substack{0 \le \bar{y} \le 1 \\ 0 \le \bar{t} \le T}} |\eta(\bar{y},\bar{t})| \tag{24}$$

where T equals the final time for the computation of the solution, and $\tilde{s}(\bar{y},\bar{t})$ is the reference shear stress.

Table 1 ASB initial time, error η_0, speed of unloading elastic wave, and the ASB width.

	ASB initiation time (μs)	η_0	Non-dimensional speed of unloading elastic wave	ASB width (μm)	Number of degrees of freedom
FEM_mesh1	60.47	--	2478	12.2	804
MLPG (MLS basis)[13]	60.45	0.378	2487	10.32	1604
MSPH [14]	60.56	0.0590	2473	10.32	1768
FEM_mesh3	60.46	0.105	2476	12.2	404
DGM_mesh2_linear	60.48	0.0597	2473	12.3	2010
DGM_mesh3_linear	60.47	0.378	2380	12.3	1010
DGM_mesh4_linear	60.47	0.770	2303	12.3	1010
DGM_mesh5_linear	60.47	0.171	2444	12.2	2010
DGM_mesh4_quadratic	60.47	0.548	2330	12.4	760
DGM_mesh5_quadratic	60.48	0.0906	2435	12.3	1510
DGM_mesh6_quadratic	60.48	0.0637	2475	12.3	1510

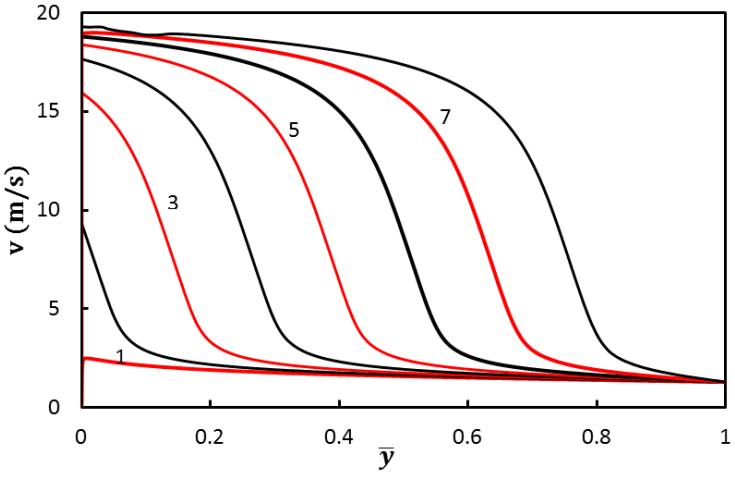

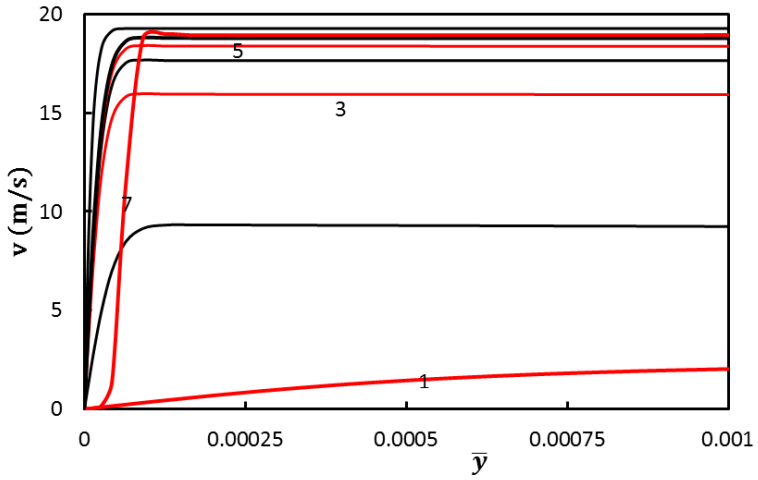

(a) Velocity

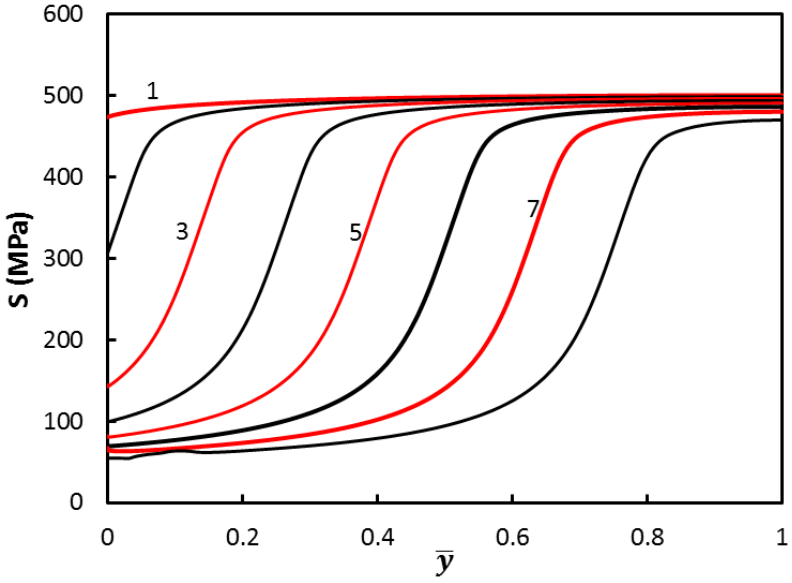

(b) Shear stress

Fig. 4 Comparison of the spatial variations of the velocity and the shear stress computed by the DGM using mesh 2; curves are plotted at intervals of 0.1 μs starting at t = 60.5 μs and curves labeled 1, 3, 5 and 7 represent solutions at t = 60.5, 60.7, 60.9 and 61.1 μs, respectively.

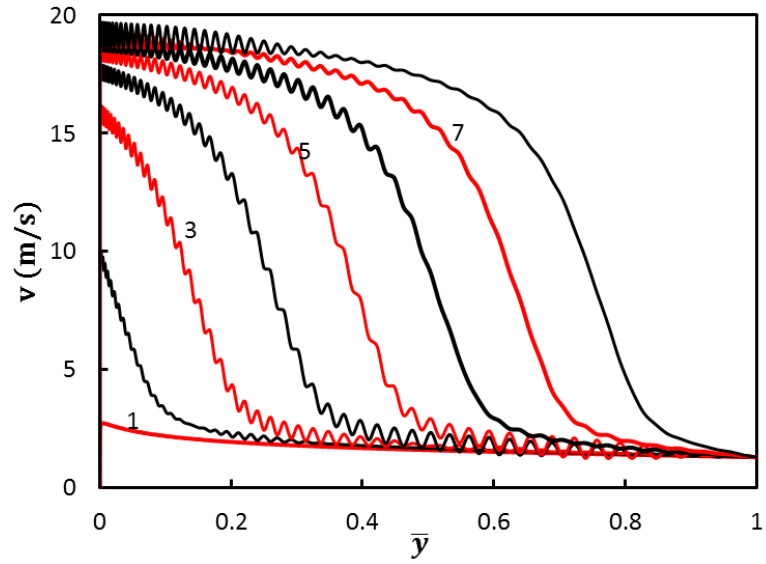

(a)

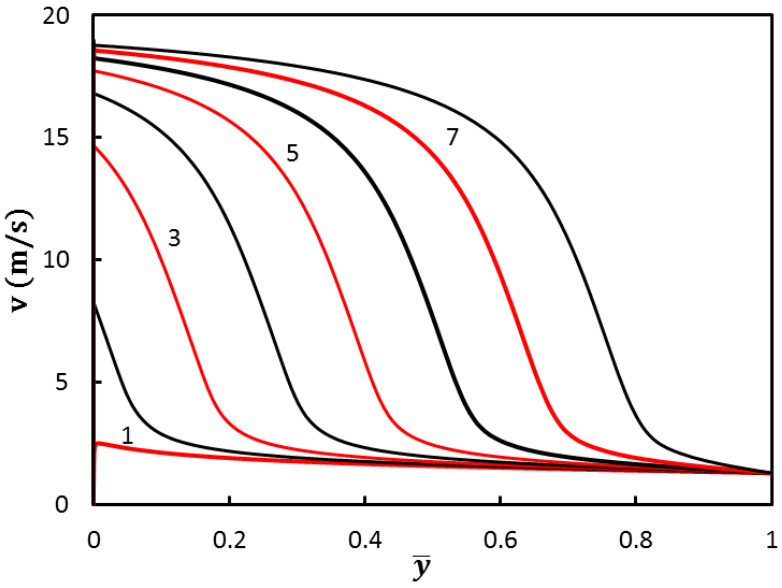

(b)

Fig. 5 Comparison of the spatial variations of the velocity computed by the FEM (a) and the DGM (b) using mesh 3; Curves are plotted at intervals of 0.1 μs starting at t = 60.5 μs and curves labeled 1, 3, 5 and 7 represent solutions at t = 60.5, 60.7, 60.9 and 61.1 μs, respectively

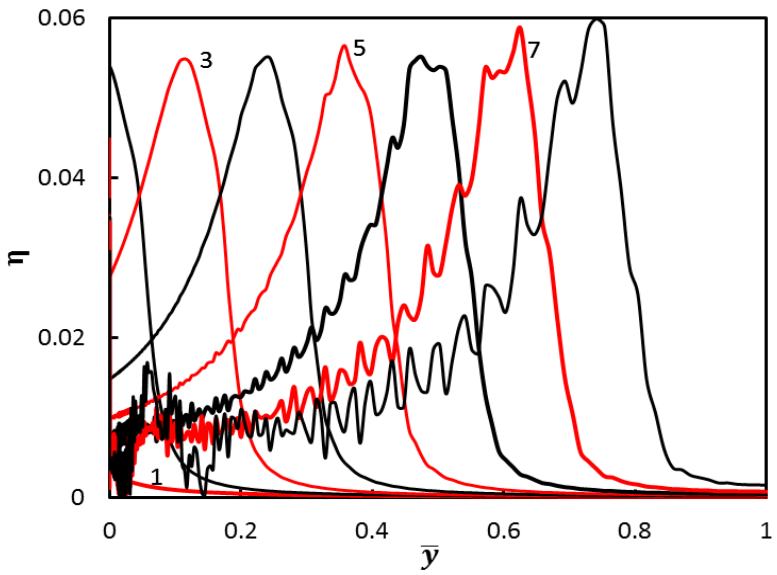

(a) Mesh 2 DGM

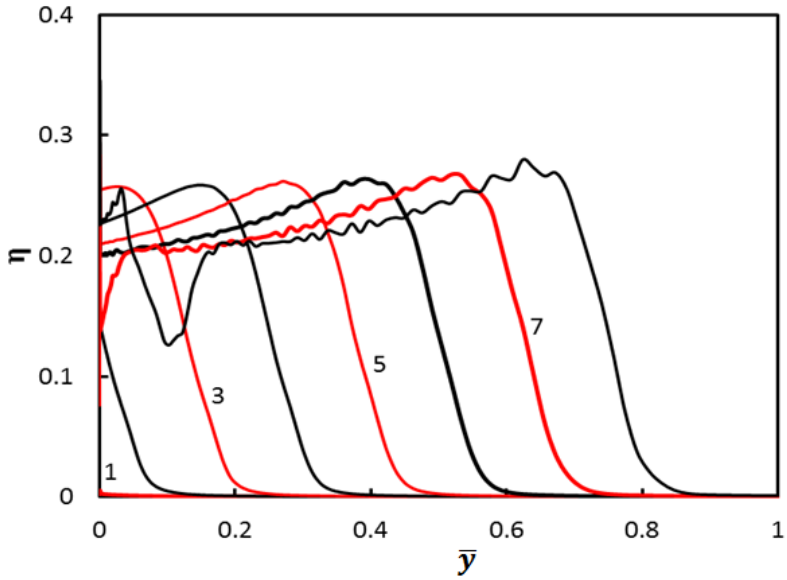

(b) Mesh 3 DGM

Fig. 6 Spatial distribution of the error in the shear stress using linear basis functions; curves are plotted at intervals of 0.1 μs starting at t = 60.5 μs and curves labeled 1, 3, 5 and 7 represent solutions at t = 60.5, 60.7, 60.9 and 61.1 μs, respectively.

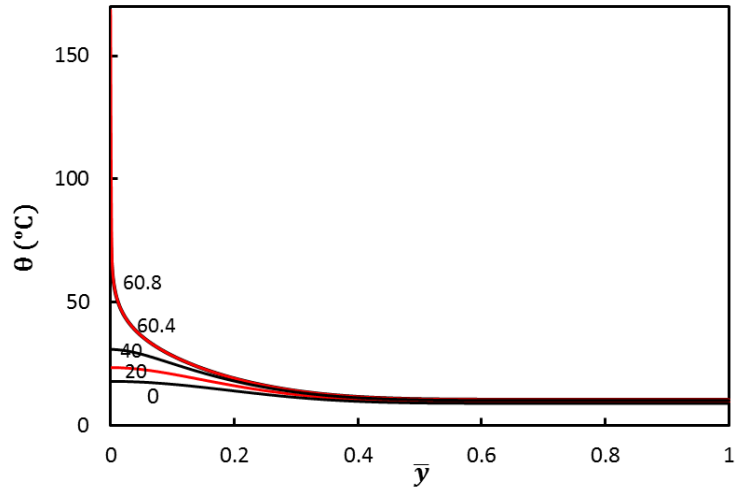

(a)

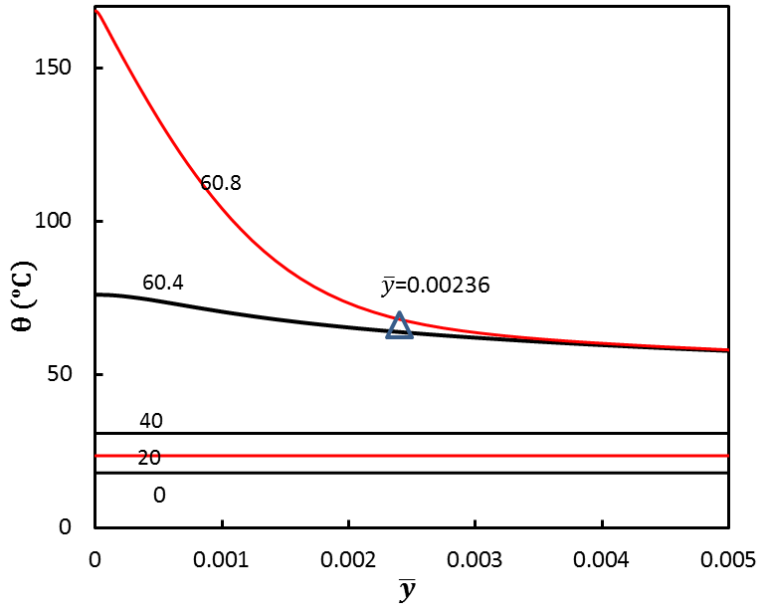

(b)

Fig. 7 Spatial distribution in the very small region near $\bar{y}$ = 0 of the temperature rise at times 0, 20, 40, 60.4 and 60.8 μs computed by the DGM using mesh 2 and linear basis functions. The symbol Δ denotes the point where the temperature equals 40% of its value at the specimen center, and is considered as the ASB edge.

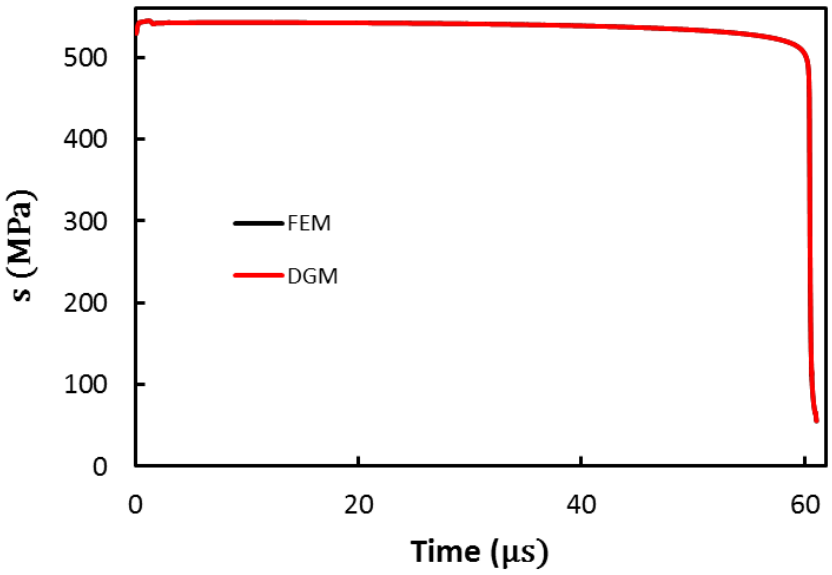

(a)

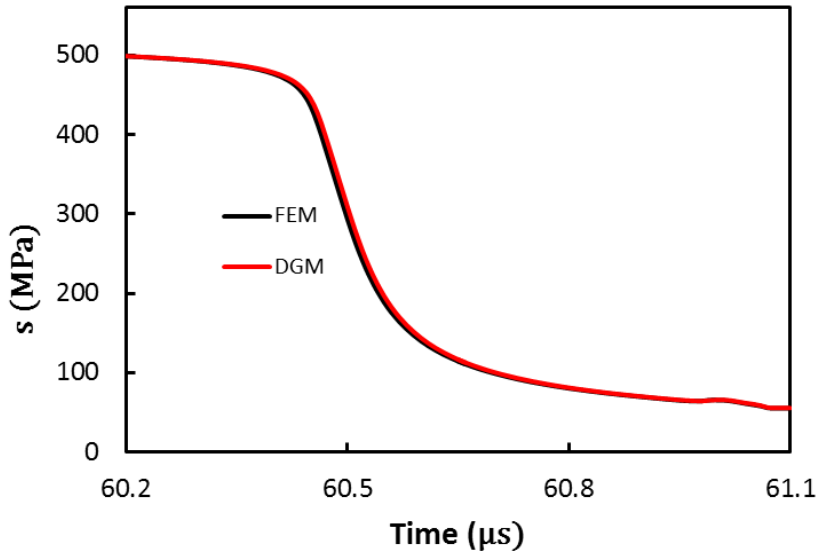

(b)

Fig. 8 Time histories of the shear stress, s, at $\bar{y} = 0$ computed by the DGM using mesh 2 and linear shape functions, and the FEM using mesh 1.

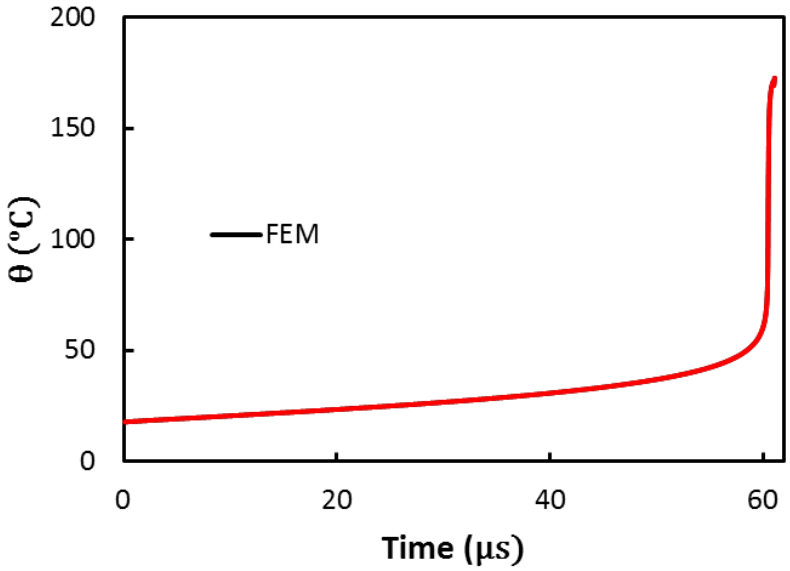

(a)

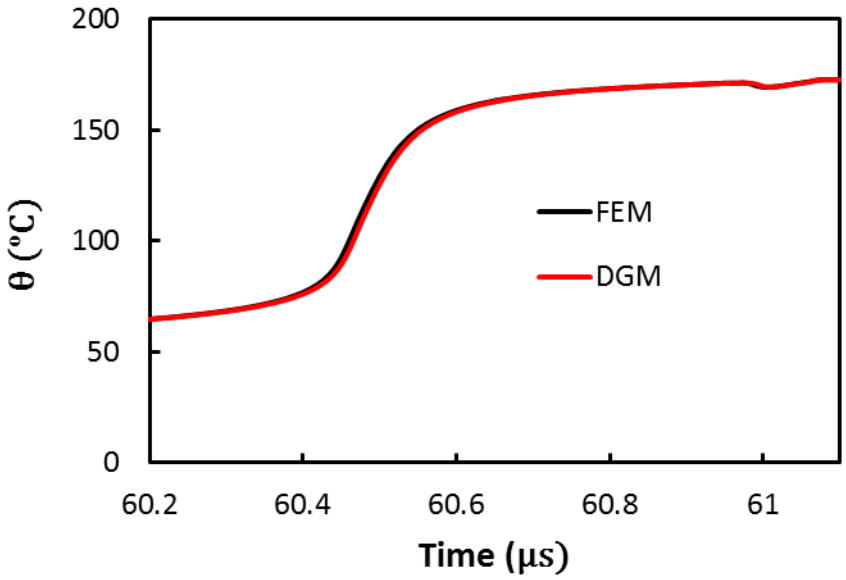

(b)

Fig. 9 Time history of the temperature rise at $\bar{y}$ = 0 computed by the DGM using mesh 2 and linear shape functions, and the FEM using mesh 1.

In Fig. 4 we have displayed spatial variations of the shear stress and the velocity at $t = 60.5,\ 60.6,\ 60.7,\ 60.8,\ 60.9,\ 60.10,\ 60.11,\ 60.12\ \mu s$ computed by the DGM using mesh 2 and linear shape functions. For t < 60 μs the shear stress is essentially uniform through the

specimen thickness. At t = 60.5 μs one can see that the shear stress at the specimen center is less than that at points away from it. The shear stress begins to drop rather rapidly at this instant which becomes evident from the values of s at $\bar{y}$ = 0 at subsequent time intervals of 0.1 μs, and the time history of s at $\bar{y}$ = 0 plotted in Fig. 8. Simultaneously with a catastrophic drop in s at $\bar{y}$ = 0, the temperature increases rapidly, and the velocity field exhibits a steep gradient at $\bar{y}$ = 0. Thus deformations localize in a narrow region around $\bar{y}$ = 0. The sharp drop in the shear stress at $\bar{y}$ = 0 results in an unloading elastic wave emanating from $\bar{y}$ = 0 and propagating outwards. The non-dimensional wave speed calculated from the shear stress values obtained with the FEM and the DGM equal 2478 and 2473, respectively. The analytical value of the wave speed, $\sqrt{\frac{\bar{\mu}}{\bar{\rho}}}$, is 2473.

The spatial variations of temperature at t = 0, 20, 40, 60.4 and 60.8 μs computed by the DGM using mesh 2 are shown in Fig. 7 and the evolution with time of the temperature at $\bar{y}$ = 0 is exhibited in Fig. 9. From the plots of the temperature rise in a small region near $\bar{y}$ = 0 exhibited in Fig. 7b, one can conclude that the temperature in this region rises very rapidly during the 0.4 μs interval starting at t = 60.4 μs. Thus the time for the ASB formation is of the order of 50 ns. Even though it is not transparent from plots of Fig. 7b, the boundary condition of zero heat flux at $\bar{y}$ = 0 is well satisfied. The edge of the ASB where the temperature rise equals 40% of that at the specimen center is marked with the symbol Δ in Fig. 7b. Thus the band width equals $2 \times 0.00236 \times 2580 = 12.18\, \mu m$.

In Fig. 5 we have displayed the spatial variations of the velocity at $t = 60.5,\ 60.6,\ 60.7,\ 60.8,\ 60.9,\ 60.10,\ 61.1,\ 61.2\ \mu s$ computed by the FEM and the DGM using mesh 3. We note that the spatial distributions of the velocity and the stress computed with the FEM and mesh 3 exhibit oscillations whereas those found using the DGM are smooth. The spatial distributions of the error η in the shear stresses computed by the DGM using meshes 2 and 3 are plotted in Fig. 6. Values of η corresponding to mesh 2 are smaller than those for mesh 3. The large values of η corresponding to solutions computed with mesh 3 are due to a slight mismatch in the values of the shear stresses at the same time computed by the two methods even though the time integration schemes are the same and the solutions have been computed for the same values of ATOL and RTOL.

Values of the ASB initiation time, the ASB width, the speed of the elastic unloading wave and the error in the shear stress computed by the two methods and several meshes listed in Table 1 reveal that the FEM and the DGM give results very close to each other. As for the FEM, the mesh size and the degree of complete polynomials in the shape functions for an element affects the solution accuracy for the DGM. The numerical solution with the DGM using mesh 6 with quadratic polynomial shape functions has the lowest error of 6% amongst the seven combinations of the mesh and the basis functions tried in this work.

The effort and the computational resources required to analyze the problem by the DGM and the FEM are compared in Table 2. As the DGM needs two unknowns for one variable at an inter-element node, the number of unknowns in the DGM with linear shape function is twice of that in the FEM using identical meshes. Thus the CPU time for the DGM is more than that for the FEM. However, the code based on the DGM is easy to parallelize because of the local formulation. Furthermore, in the DGM there is no assembly of matrices required. Adjerid et al. [26] have stated that the adaptive h- or p- refinement can be implemented at low computational cost in the DGM.

Table 2 Comparison of FEM and DGM.

	FEM	DGM
Simulation of solution discontinuity	Poor	Good
Assembly of global matrix	Required	Not required
h- and p- refinement effort	Extensive	Little
Implementation for parallel computing	Difficult	Easy
Number of variables	Small	Large
Compute 2^{nd} order spatial derivatives	Easy	Difficult
CPU time (201 nodes, 5 variables/node)	$\cong$ 1minute	$\cong$ 5minutes

5. Conclusions

Simple shearing deformations of a thermo-elasto-viscoplastic body have been analyzed by using the Galerkin formulation of the problem and basis functions that are discontinuous across inter-element boundaries. The deformations are found to localize into a narrow region of intense plastic deformation known as an adiabatic shear band (ASB). No artificial viscosity is introduced to smoothen out the numerical solution. The ASB width and the ASB initiation time are found to agree well with those computed by the finite element method (FEM) as well as other meshless methods using basis functions derived by the moving least squares approximation and the modified smoothed particle hydrodynamics method. For the same number of finite elements and nodes, the number of unknowns when using the discontinuous basis functions is twice of that in the FEM because of twice the number of unknowns at a node on an inter-element boundary. Since there is no assembly of equations required, the algorithm can be easily parallelized. It is shown that the technique can capture well the sharp gradients in the solution that require more work in the FEM.

Acknowledgement:

Authors are indebted to Professor Adjerid for helpful discussions on the use of the DGM for this problem.

References

1. Bai Y.L. and B. Dodd, *Adiabatic shear localization: occurrence, theories and applications.*1992: Pergamon Press Oxford, UK.
2. Dodd B. and Y.L. Bai, *Ductile Fracture and Ductility-with Applications to Metal working*, 1987, Academic Press, London.
3. Wright T.W., *The physics and mathematics of adiabatic shear bands.*2002, Cambridge, UK: Cambridge University Press.
4. Perzyna P., *Localization and fracture phenomena in inelastic solids.*1998: Springer.
5. Needleman A. and V. Tvergaard, *Finite element analysis of localization in plasticity*, in *Finite Elements: Special Problms in Solid Mechanics*, J.T. Oden and G.F. Carey, Editors. 1984, Prentice Hall, Englewood Cliffs. p. 94-157.
6. Zbib H.M., S. T.G., and R.C. Batra, *Analysis of Shear Bands in Simple Shearing Deformations of Nonpolar and Dipolar Viscoplastic Materials, in Material Instabilities.* Applied Mechanics Reviews, 1992. **45**(3(2)): p. S123 - S131.
7. Tomita Y., *Simulations of plastic instabilities in solid mechanics.* Applied mechanics reviews, 1994. **47**: p. 171-205.

8. Tresca H., *On further application of the flow of solids.* Proc. Inst. Mech. Engrs, 1878. **30**: p. 301-345.
9. Massey H.F. *The flow of metal during forging*. in *Proc. Manchester Assoc. Engrs*. 1921.
10. Batra R.C. and K.I. Ko, *An adaptive mesh refinement technique for the analysis of shear bands in plane strain compression of a thermoviscoplastic solid.* Computational mechanics, 1992. **10**(6): p. 369-379.
11. Batra R.C. and J. Hwang, *An adaptive mesh refinement technique for two-dimensional shear band problems.* Computational mechanics, 1993. **12**(4): p. 255-268.
12. Batra R.C. and C.H. Kim, *Adiabatic shear banding in elastic-viscoplastic nonpolar and dipolar materials.* International journal of plasticity, 1990. **6**(2): p. 127-141.
13. Batra R.C. and D. Spinello, *Analysis of adiabatic shear bands in heat‐conducting elastothermoviscoplastic materials by the meshless local Bubnov–Galerkin method.* Communications in Numerical Methods in Engineering, 2009. **25**(10): p. 1019-1040.
14. Batra R.C. and G.M. Zhang, *Analysis of adiabatic shear bands in elasto-thermo-viscoplastic materials by modified smoothed-particle hydrodynamics (MSPH) method.* Journal of Computational Physics, 2004. **201**(1): p. 172-190.
15. Reed W.H. and T.R. Hill, *TRIANGULARMESH METHODSFOR THE NEUTRONTRANSPORTEQUATION.* Los Alamos Report LA-UR-73-479, 1973.
16. Li B.Q., *Discontinuous finite elements in fluid dynamics and heat transfer.*2006: Springer-Verlag(London).
17. Cockburn B., G.E. Karniadakis, and C.W. Shu, *Discontinuous Galerkin methods. Theory, computation and applications., volume 11 of Lecture Notes in Computational Science and Engineering*, 2000, Springer-Verlag, Berlin.
18. Marchand A. and J. Duffy, *An experimental study of the formation process of adiabatic shear bands in a structural steel.* Journal of the Mechanics and Physics of Solids, 1988. **36**(3): p. 251-283.
19. Batra R.C. and C.H. Kim, *Analysis of shear banding in twelve materials.* International journal of plasticity, 1992. **8**(4): p. 425-452.
20. Batra R.C., *Steady state penetration of thermoviscoplastic targets.* Computational mechanics, 1988. **3**(1): p. 1-12.
21. Lubliner J., *Plasticity theory.* Vol. 15. 1990, New York: Macmillan
22. Batra R.C., *Elements of continuum mechanics.*2006: AIAA.
23. Cockburn B. and C.W. Shu, *TVB Runge-Kutta local projection discontinuous Galerkin methods of scalar for Conservation Laws II: General Framework.* Mathematics of Computation, 1989. **52**(186): p. 411-435.
24. Weinhart T., *A Posteriori Error Analysis of the Discontinuous Galerkin Method for Linear Hyperbolic Systems of Conservation Laws*, 2009, Ph.D dissertation, Virginia Polytechnic Institute and State University: Blacksburg,VA.
25. Radhakrishnan K., A.C. Hindmarsh, U.S.N. Aeronautics, and S. Administration, *Description and use of LSODE, the Livermore solver for ordinary differential equations.*1993: National Aeronautics and Space Administration, Office of Management, Scientific and Technical Information Program.
26. Adjerid S., K.D. Devine, J.E. Flaherty, and L. Krivodonova, *A posteriori error estimation for discontinuous Galerkin solutions of hyperbolic problems.* Computer methods in applied mechanics and engineering, 2002. **191**(11-12): p. 1097-1112.

Chapter 6: Conclusions

A third order shear and normal deformable beam theory (TSNDT) for analyzing finite deformations of a curved laminated beam made of a St. Venant-Kirchhoff material has been developed. It has been used in combination with the finite element method (FEM) to analyze static and dynamic deformations of straight and curved beams by considering all geometric nonlinear effects. Equations governing deformations of the beam are written in the Lagrangian description of motion using continuum mechanics principles, and a weak form of the governing equations has been derived. No shear correction factor is used, and stresses are derived from the displacement field and the constitutive relations without using any post-processing technique. The method of manufactured solutions has been used to verify the in-house developed software capable of analyzing static and dynamic problems. Furthermore, for both straight and curved beams, deflections and stresses computed using the TSNDT for linear and nonlinear theories agree very well with those obtained using the commercial FE software ABAQUS that analyzes plane strain deformations of the beam modeled as a continuum. For a curved beam made of a homogeneous and isotropic material and radius of curvature/beam thickness = 10, it is found that the maximum transverse deflections and axial stresses at critical points computed using the linear theory are nearly 60% and 40% more than those obtained from the nonlinear theory. However, the transverse shear stresses from the linear theory equal about 86% of those from the nonlinear theory. Thus a stress based failure criterion will predict premature failure of the beam if stresses are derived from the linear elasticity theory.

We have also used a cohesive zone model (CZM) and the TSNDT to analyze the delamination growth in a laminated composite beam, and compared our results with those available in the literature for four problems. Presently computed results for mode I, mode II and mixed mode deformations of straight and curved double cantilever beams (DCBs) have been found to agree well with those of other investigators including those obtained using the linear elastic fracture mechanics approach. We have also studied delamination growth in axial compression of an initially delaminated beam and found that local buckling ensues first and it is followed by global buckling. Because of the geometric nonlinearities considered, we could analyze the post-buckling response of the beam which is found to agree well that reported in the

literature. We have also studied the effect of inertia forces on the delamination growth in a predelaminated beam. It is found that for the applied axial strain rate of 40/s, the buckling load increases by 65% over that for the static problem, and the length of the unstably grown delaminated region decreases by 30%.

Water slamming of rigid and deformable straight and curved hulls has been studied using coupled boundary and finite element methods. The boundary element method (BEM) has been employed to analyze deformations of the fluid, and the finite element method (FEM) coupled with the TSNDT has been used to study hydroelastic problems for hulls with and without considering all geometric nonlinearities. When studying effects of geometric nonlinearities the hull material is taken to be St. Venant-Kirchhoff. The water is assumed to be inviscid and incompressible and undergo irrotational deformations. The Laplace equation for the velocity potential is numerically solved by the BEM with normal velocity and pressure assumed to be continuous across the interface between the hull and the water. The codes for the fluid and structure part have been separately verified by the method of manufactured solutions. We studied water slamming of rigid straight wedge with and without considering gravitational effects on the wedge, a rigid ship bow section, and rigid circular hull. For the first three problems, the pressure distribution on the wetted length and shapes of water jets near the edge of the wetted length have been found to compare well with either the experimental or the analytical or the numerical results of other investigators. The computed results for the water slamming of flat deformable are found to agree with those obtained by the commercial FE software LSDYNA. These suggest that the assumptions of water being incompressible and its deformations being irrotational do not noticeably influence the hydroelastic effects. The consideration of geometric nonlinearities significantly increases the maximum hydrodynamic pressure experienced by the hull. However, it does not affect the traveling wave like behavior of the hydroelastic pressure acting on the hull. We have also analyzed delamination in two linear elastic sandwich hulls subjected to water slamming loads. In both problems the delamination occurred at the two interfaces between the core and the face sheets due to mode-II deformations. Whereas in one problem, the delamination propagated smoothly and stably, in the other problem the delamination growth was unstable.

Simple shearing deformations of a thermo-elasto-viscoplastic body have been analyzed by using the Galerkin formulation of the problem and basis functions that are discontinuous across inter-element boundaries. In order to save computational resources, a homogeneous solution of the governing equations is perturbed to make the deformations inhomogeneous. The deformations are found to localize into a narrow region of intense plastic deformation known as an adiabatic shear band (ASB). No artificial viscosity is introduced to smoothen out the numerical solution. The ASB width and the ASB initiation time are found to agree well with those found by the finite element method (FEM) as well as other meshless methods using basis functions derived by the moving least squares approximation and the modified smoothed particle hydrodynamics method. For the same number of finite elements and nodes, the number of unknowns when using the discontinuous basis functions is twice of that in the FEM because of twice the number of unknowns at a node on the inter-elements boundary. Since there is no assembly of equations required, the algorithm can be easily parallelized. It is shown that the technique can capture well the sharp gradients in the solution that require more work in the FEM.